



The
University
Of
Sheffield.

Granular Pellet Deformation in a Shear Flow System through Experiment and Simulation

By:

Intan Soraya Shamsudin

*A thesis submitted in partial fulfilment of the requirements for the degree of Doctor of
Philosophy*

The University of Sheffield

Faculty of Engineering

Department of Chemical and Biological Engineering

Submission Date:

October 2020

Declaration

The work presented in this thesis is, to the best of my knowledge and belief, original, except as acknowledge in the text, and has not been submitted in whole or in part, for a degree at this or any other institution.

Intan Soraya Shamsudin

October 2020

Acknowledgements

I would like to express my tremendous gratitude to my supervisors, Dr Rachel Smith and Dr Jonathan Howse, for their guidance, patience, motivation. I would like to say a big thank you to my Post-Doctoral Research Associate, Dr Kate Pitt, for her time, guidance, support and contributions throughout my PhD journey. A special thanks to Dr Li Ge Wang and his colleagues at the University of Edinburgh, for their knowledge, advice and expertise in DEM simulations and C++ code file development.

A big thank you to Jonathan Phillips and his colleagues from Instron High Wycombe and Dr Colin Hare from University of Surrey for their technical help towards my research work. A special thanks to the technical and electronics staff in the Department of Chemical and Biological Engineering; Andy Patrick, Mario Dorna, Usman Younis, Oz McFarlene, Glynn Reynolds and Mark McIntosh, who helped to design and manufacture the annular shear cell. To my colleagues in Particle Technology Group; I am grateful for the friendship, companionship, care and fruitful discussions, which developed my critical thinking and problem-solving skills. I cherished every single one of you throughout my PhD study.

I would like to give a special thanks to my family. To my parents, Haji Shamsudin Abu Bakar and Hajah Khatijah Abdul Kadir for their belief in me, endless prayers, support, understanding, love and advice throughout my PhD journey. To my friends, I really appreciate the love, support, advice and time. I cherish every single moment with you.

Finally, thank you to the Majlis Amanah Rakyat (MARA) for the financial support.

Abstract

Attrition and breakage are particularly important rate process in the high shear granulation; however, they are still poorly understood and only limited studies have been reported in the literature. The wet granulation process possesses a high/rapid shear flow; however, the flow patterns can be complex, and there are no reliable methods to experimentally measure shear stresses in these granulators. In this study, both experimental and modelling techniques were used to investigate deformation of granular materials. Experimentally, an annular shear cell was used due to its relatively simple shear profiles. A computational model was also developed to gain information on the particle scale to help understand pellet deformation in the annular shear cell. The objectives of this work are: 1) to study the effect of material properties and operating parameters on wet granular pellet deformation in an annular shear cell; 2) to attempt to predict pellet deformation through DEM modelling and theoretical failure theory and 3) to correlate the experiments with prediction.

Granular pellets (composed of either lactose or ballotini glass beads with different viscosity of silicone oils) surrounded by background glass beads were chosen as the model materials. Young's modulus, plastic and elastic stiffness and yield stresses of the pellets were experimentally measured from two types of compression tests and used as the input materials in the DEM simulations. Annular shear cell experiments were tested for lactose 10cSt and ballotini 10cSt pellets (composed of lactose or ballotini glass beads with 0.01 Pa.s silicone oil) and sheared under shearing conditions; the effect of shear rate, normal pressure and size of background beads were investigated. The pellet deformation was evaluated based on two measures of deformation, degree of deformation through pellet elongation (%) and deformation fraction (%). The experimental results were compared to the Stokes deformation number, St_{def} and the range of critical Stokes deformation number, St_{def}^* were determined.

A "DEM unit shear cell", representing a small section of the annular shear cell, was developed using DEM simulations. A model of a DEM pellet was created by agglomerating multi-sphere particles in a cylindrical geometry, surrounded by background beads and sheared in between a stationary bottom plate and moving top plate. A linear elastic-plastic without adhesion was chosen as the contact force model. Deviatoric stress was computed to predict the deformation stress of the pellet. For analysis of von Mises failure theory, the computed von Mises stress was compared to yield stresses of the pellets at different compression speeds between 1 and 125.7 mm/s and the intersection times between the von Mises stress and yield stresses were determined to represent the predicted yielding time of the pellet. A correlation was made between the predicted yielding time and the experimental data of

lactose 10cSt and beads 10cSt pellets, e.g., pellet elongation (%) and deformation fraction (%) for operating parameters; shear rate, normal pressure and size of background beads.

Experimental pellet deformation in the annular shear cell showed increasing pellet elongation (%) and deformation fraction (%) for lactose 10cSt and beads 10cSt pellets can be obtained with increasing normal pressure, higher shear rate, larger background beads and longer shearing times. The Stokes deformation number, St_{def} has potential to be used as a predictor for some of the experiments results by changing the shear rate.

Results from the DEM simulations showed that the deviatoric and von Mises stresses increased with shearing time for all conditions studied. It was found that lactose 10cSt pellets had higher deviatoric stress with increasing shear rate, increasing normal pressure and decreasing size of background beads. Deviatoric stress of ballotini 10cSt pellets was increased with increasing normal pressure and decreasing size of background beads. Only small differences in the deviatoric stress of the ballotini pellets were observed for all the shear rates used. The von Mises failure theory predicted that lactose 10cSt pellets had decreasing yielding times with increasing shear rate, increasing normal pressure and decreasing size of background beads. The von Mises failure theory predicted that ballotini 10cSt pellets had decreasing yielding time with increasing normal pressure and decreasing size of background beads.

The results of pellet deformation prediction through DEM simulations and the experiments were indirectly correlated. The correlation was made between the predicted yielding time to the elongation and deformation fraction measured experimentally in the annual shear cell. It would be expected that higher predicted yielding time would result in lower experimentally measured deformation. There were some conditions where this expectation was met, overall, the model developed is a semi-prediction for the experimentally observed deformation.

In conclusion, a new method for investigating the pellet deformation is presented, using a combination of experiment, modelling and theoretical tools.

Table of Contents

Acknowledgements.....	iii
Abstract.....	iv
Table of Contents.....	vi
List of Figures	x
List of Tables	xvi
List of Symbols	xviii
1 Introduction	1
1.1 Introduction to granulation	1
1.2 Challenges in granulation breakage research.....	2
1.3 Research plan.....	3
1.4 Aim of the study.....	5
1.5 Objectives.....	5
1.6 Structure of the thesis	5
2 Literature review	6
2.1 Introduction	6
2.2 Granulation	6
2.2.1 Breakage studies in granulation.....	9
2.2.2 Granulation parameters affecting breakage.....	16
2.3 Shear cell testers.....	19
2.3.1 Stability condition of shear flow in an annular shear cell.....	22
2.4 Types of deformation.....	22
2.5 Stresses of 3D material	23
2.5.1 Determining the principal stresses	26
2.5.2 Deviator stress tensor	29
2.5.3 Deviatoric stress.....	32
2.6 Failure criterion theory	35
2.6.1 von Mises yield criterion.....	36
2.7 Numerical simulation of granular materials	38
2.7.1 Discrete Element Method (DEM) simulations	39
2.7.2 Principle of DEM simulations.....	40
2.7.3 Contact force models.....	41
2.7.4 Time-step, Δt	50
2.7.5 DEM simulations for shear flow and breakage studies	52
2.8 Summary	54
3 Experimental: Materials and methods.....	56
3.1 Introduction	56

3.2	Selection of materials and methods	56
3.3	Properties of powders and background beads	58
3.3.1	Morphology of powders	58
3.3.2	Particle size distributions	60
3.3.3	Density	64
3.4	Properties of liquid binder	65
3.4.1	Preparation of blue dyed silicone oil	65
3.4.2	Measuring the density of liquid binder	65
3.4.3	Measuring the viscosity of liquid binder	66
3.5	Formulation of different paste materials	68
3.5.1	Measuring volume of solid and density of solid	68
3.5.2	Calculating the void volume in the paste.....	69
3.5.3	Calculating liquid volume and air volume in the paste.....	69
3.5.4	Calculating the mass of the paste	70
3.5.5	Methods for making the paste.....	71
3.6	Formation of pellets.....	75
3.6.1	Properties of the pellets	76
3.6.2	Methods for making the pellets.....	76
3.7	Summary	77
4	Mechanical properties of granular pellets	78
4.1	Introduction	78
4.2	Experimental methodology.....	78
4.2.1	Quasi-static compression test.....	78
4.2.2	Dynamic compression test.....	80
4.3	Methods of analysis	82
4.3.1	Analysis of raw data from the compression test	82
4.3.2	Characterising the regions of the force-displacement curve from the quasi-static compression test.....	84
4.3.3	Measuring plastic and elastic stiffness of pellets from quasi-static compression test.....	91
4.3.4	Measuring Young's modulus of pellets from the quasi-static compression test.....	96
4.3.5	Measuring the yield stress of pellets from the dynamic compression test.....	98
4.4	Results and discussion	99
4.4.1	Plastic and elastic stiffness of pellets from the quasi-static compression test	99
4.4.2	Young's modulus of pellets from the quasi-static compression test.....	101
4.4.3	Yield stress of pellets from the dynamic compression test	103
4.5	Summary	108
5	Granular pellet deformation in an annular shear cell.....	109
5.1	Introduction	109

5.2	Materials and methods.....	109
5.2.1	Properties of the annular shear cell.....	112
5.2.2	Parameters for the experiments.....	114
5.2.3	Performing shearing in the annular shear cell.....	117
5.2.4	Analyses of the pellets	118
5.3	Results and Discussion	122
5.3.1	Deformation behavior of strongest pellets (lactose 10cSt pellets)	122
5.3.2	Deformation behavior of the weakest pellets (ballotini 10cSt pellets)	135
5.3.3	Pellet deformation and the Stokes deformation number, <i>Stdef</i> relationship	142
5.4	Summary	148
6	Predicting granular pellet deformation through DEM simulations and failure theory.....	149
6.1	Introduction	149
6.2	Designing and building the DEM unit shear cell	149
6.2.1	Periodic boundaries	150
6.2.2	Length and width of the DEM unit shear cell	150
6.2.3	Height of the DEM unit shear cell and simulation domain.....	153
6.3	Creating a DEM cylindrical pellet.....	154
6.4	Contact force models.....	155
6.5	Setup for DEM simulations	158
6.6	Pressure from the top plate of the DEM unit shear cell	158
6.7	Material properties for DEM simulations	159
6.7.1	Particle size distribution and mass of background beads for DEM simulations.....	159
6.7.2	Stiffness of pellets and background beads for DEM simulations.....	160
6.7.3	Young’s modulus of materials for DEM simulations	161
6.7.4	Shear modulus of materials for DEM simulations	162
6.7.5	Density of materials for DEM simulations	162
6.8	Interaction properties for DEM simulations	163
6.9	Parameters for DEM simulations.....	164
6.10	Processing and post processing for DEM simulations	166
6.11	Stress components from DEM simulations.....	169
6.12	Results and discussion	171
6.12.1	Steady-state condition in the DEM simulations.....	171
6.12.2	Deviatoric stress of the pellets.....	174
6.12.3	Analysis of von Mises failure theory	194
6.13	Summary	203
7	Relationship between experiment and prediction	206
7.1	Introduction	206
7.2	Results and discussion	207

7.2.1	Strongest pellets (lactose 10cSt pellets)	207
7.2.2	Weakest pellets (ballotini 10cSt pellets).....	211
7.3	Summary	214
8	Conclusions and Recommendations	215
8.1	Introduction	215
8.2	Research conclusion.....	216
8.3	Future works	217
9	References.....	219

List of Figures

Figure 1.1 Area of breakage zone in the granulator	1
Figure 1.2 Flow diagram of the problem statement and approaches	4
Figure 2.1 High shear mixer	6
Figure 2.2 Rate processes involved in the granulation process (Simon M. Iveson, Litster, et al., 2001)	7
Figure 2.3 Bumping flow (left) and roping flow (right) in vertical shaft mixers (Jim Litster and Bryan Ennis, 2004).....	8
Figure 2.4 Un-deformed agglomerate (left) and sheared deformed agglomerate (right) in opposite directions, surrounding by dry particulates medium (Khan & Tardos, 1997)	11
Figure 2.5 Defining critical Stokes deformation number based on the works of (Tardos et al., 1997). The fraction of surviving granules is indicated by f	14
Figure 2.6 Types of shear cell testers.....	20
Figure 2.7 Variation position of upper platen in z-direction over time for steady-state condition	22
Figure 2.8 Two types of deformation: brittle (left) and plastic (right).....	23
Figure 2.9 Stress state of a 3D material	24
Figure 2.10 a) Components of stress tensor are: b) hydrostatic stress tensor and c) deviator stress tensor	25
Figure 2.11 The state of stress of a material with original coordinate axes (left) and principal stress coordinate axes (right).....	27
Figure 2.12 Typical flow in DEM simulations (Vedachalam, 2011)	41
Figure 2.13 Contact force model in normal and tangential directions (Weerasekara et al., 2016)	42
Figure 2.14 Normal force - deformation relationship in linear spring model.....	43
Figure 2.15 Normal force – deformation relationship in non-linear Hertz contact model	44
Figure 2.16 Normal force – overlap relationship in the simplified Pasha’s linear elastic-plastic with adhesive contact model (Massih Pasha et al., 2014a).....	48
Figure 2.18 Process work flow	55
Figure 3.1 Images of 1 – 1.4 mm background beads	57
Figure 3.2 Images of 2 mm background beads	58
Figure 3.3 Image of ballotini glass beads	59
Figure 3.4 Image of MCC.....	59
Figure 3.5 Image of lactose	60
Figure 3.6 Frequency distribution curve for 1 – 1.4 mm background beads.....	61
Figure 3.7 Frequency distribution curve for 2 mm background beads.....	62
Figure 3.8 Modular Compact Rheometer MCR 502.....	67
Figure 3.9 The logarithmic plot of viscosity of blue dyed silicone oil solutions as a function of shear rate, at a constant temperature of 25°C.....	67
Figure 3.10 Hand-kneading the mixture in a plastic bag (left) and localization of liquid binder within powders (right)	71
Figure 3.11 Pre-mixing the mixture in a beaker (left) and uniform distribution of the liquid binder and powder (right)	71
Figure 3.12 Types of pellets	75
Figure 3.13 Custom-made die, bottom base, head puncher and spacer	77
Figure 4.1 Instron 5500R/1175 Universal Testing Machine.....	79
Figure 4.2 Image of pre-test pellet	79
Figure 4.3 Instron Electropuls E1000 testing machine	80
Figure 4.4 Initial position of the pellet before and after the dynamic compression test.....	82
Figure 4.5 Regions from the non-linear force-displacement curve based on (Mattucci & Cronin, 2015) works.....	85

Figure 4.6 Example of a non-linear force-displacement curve obtained from a ballotini 10cSt pellet with 10 N and compression speed of 0.02 mm/s	86
Figure 4.7 Bi-linear model from (Chandrashekar et al., 2008) works	87
Figure 4.8 Example of multi-curves fit model: toe to linear regions (left) and linear to traumatic regions (right) based on (Mattucci & Cronin, 2015) works	89
Figure 4.9 Bi-linear model on the loading force-displacement curve for a ballotini 10cSt pellet compressed with 10 N and compression speed of 0.02 mm/s.....	92
Figure 4.10 Multi-curves fit model on the loading force-displacement curve for a ballotini 10cSt pellet compressed with 10 N and compression speed of 0.02 mm/s.....	93
Figure 4.11 Linear regression fitted to the portion of the linear region of the loading force-displacement curve for a ballotini 10cSt pellet compressed with 10 N and compression speed of 0.02 mm/s.....	94
Figure 4.12 Multi-curves fit model on the unloading force-displacement curve for a ballotini 10cSt pellet compressed with 10 N and compression speed of 0.02 mm/s	95
Figure 4.13 Linear regression fitted to the portion of linear region of the unloading force-displacement curve for a ballotini 10cSt pellet compressed with 10 N and compression speed of 0.02 mm/s	95
Figure 4.14 Stress (Pa) versus strain (mm/mm) curve for a ballotini 10cSt pellet compressed with 10 N and compression speed of 0.02 mm/s.....	97
Figure 4.15 The linear region of the stress- strain curve using the multi-curves fit model for a ballotini 10cSt pellet compressed with 10 N and compression speed of 0.02 mm/s.....	97
Figure 4.16 Linear regression fitted to the portion of the linear region of the stress – strain curve for a ballotini 10cSt pellet compressed with 10 N and compression speed of 0.02 mm/s.....	98
Figure 4.17 Plastic and elastic stiffness of different types of pellets. Error bars represent the standard error values of a minimum of 3 measurements	99
Figure 4.18 Plastic and elastic stiffness for ballotini pellets with different viscosity of silicone oils. Error bars represent the standard error values of a minimum of 3 measurements	100
Figure 4.19 Young’s modulus of different types of pellets. Error bars represent the standard error values of a minimum of 3 measurements	101
Figure 4.20 Young’s modulus for ballotini pellets with different viscosity of silicone oils. Error bars represent the standard error values of a minimum of 3 measurements.....	102
Figure 4.21 Stress (Pa) versus strain (mm/mm) curve for ballotini 10cSt pellets. Load cell of 50 N and compression speeds from 1 to 125.7 mm/s	104
Figure 4.22 Stress (Pa) versus strain (mm/mm) curve for ballotini 50cSt pellets. Load cell of 50 N and compression speeds from 1 to 125.7 mm/s	104
Figure 4.23 Stress (Pa) versus strain (mm/mm) curve for ballotini 100cSt pellets. Load cell of 50 N and compression speeds from 1 to 125.7 mm/s	105
Figure 4.24 Stress (Pa) versus strain (mm/mm) curve for ballotini 1000cSt pellets. Load cell of 50 N and compression speeds from 1 to 125.7 mm/s	105
Figure 4.25 Stress (Pa) versus strain (mm/mm) curve for lactose 10cSt pellets. Load cell of 50 N and compression speeds from 1 to 125.7 mm/s	106
Figure 4.26 Stress (Pa) versus strain (mm/mm) curve for lactose 10cSt pellets. Load cells of 50 N and 100 N and compression speed of 125.7 mm/s	106
Figure 5.1 Flow diagram of experimental work	111
Figure 5.2 Load force, top lid and bottom base of the annular shear cell.....	112
Figure 5.3 Shear cell controller box (left) and motor and power system (right).....	113
Figure 5.4 Schematic diagram of the annular shear cell: Top view of the bottom base (Top) and side view with top lid and bottom base (Bottom)	113
Figure 5.5 The surfaces of the top lid (left) and bottom base (right) with 60 grit sandpaper.....	114
Figure 5.6 Position of the pellet at the centre in the trough of the annular shear cell and the specific radius of the annular shear cell, r *(r_i =Inner radius and r_o = outer radius).....	115

Figure 5.7 Position of pellets and proportion of background beads in the bottom base (left) and after addition of the remaining background beads (right).....	118
Figure 5.8 Ballotini 10cSt pellets flattened/fragmented (left) and lactose 10cSt pellets elongated (right)	119
Figure 5.9 Ballotini 10cSt pellets retained on the 4 mm sieve at 0 sec (left) and 100 sec (right)	119
Figure 5.10 Lactose 10cSt pellets retained on the 4 mm sieve at 0 sec (left) and 100 sec (right)	120
Figure 5.11 Measurement setup in ImageJ for length of the longest diagonal for lactose 10cSt pellets at 0 sec (left) and 100 sec (right)	121
Figure 5.12 Shape of lactose 10cSt pellets beads before loading the top lid.....	123
Figure 5.13 Shape of lactose 10cSt pellets with 1-1.4 mm beads after uplifting the top lid.....	123
Figure 5.14 Shape of lactose 10cSt pellets with 2 mm beads after uplifting top lid	124
Figure 5.15 Pellet elongation, Ep , versus shear rate for lactose 10cSt pellets with a top lid pressure of 2000 Pa and 1-1.4 mm background beads. Error bars represent the standard error of 4 measurements	125
Figure 5.16 Images of lactose 10cSt pellets with shearing time with a top lid pressure of 2000 Pa and 1-1.4 mm background beads for conditions: 5.03/s (bottom) and 40.21/s (top)	126
Figure 5.17 Pellet elongation, Ep , versus shear rate for lactose 10cSt pellets with a top lid pressure of 2000 Pa and 2 mm background beads. Error bars represent the standard error of 4 measurements	128
Figure 5.18 Images of lactose 10cSt pellets with shearing time, with a top lid pressure of 2000 Pa and 2 mm background beads for conditions: 5.03/s (bottom) and 40.21/s (top).....	129
Figure 5.19 Pellet elongation, Ep , versus normal pressure for lactose 10cSt pellets with a shear rate of 40.21/s and 1-1.4 mm background beads. Error bars represent the standard error of 4 measurements	131
Figure 5.20 Images of lactose 10cSt pellets with shearing time, at a shear rate of 40.21/s and 1-1.4 mm background beads for conditions: 383 Pa (bottom), 600 Pa (middle) and 2000 Pa (top)	132
Figure 5.21 Pellet elongation, Ep , versus size of background beads for lactose 10cSt pellets with a shear rate of 40.21/s and a top lid pressure of 2000 Pa. Error bars represent the standard error of 4 measurements	133
Figure 5.22 Images of lactose 10cSt pellets with shearing time, using a shear rate of 40.21/s and a top lid pressure of 2000 Pa for conditions: 1-1.4 mm beads (bottom) and 2 mm beads (top)	134
Figure 5.23 Shape of ballotini 10cSt pellets with 1-1.4 mm beads before loading top lid	135
Figure 5.24 Shape of ballotini 10cSt pellets with 1-1.4 mm beads after uplifting the top lid	136
Figure 5.25 Deformation fraction, FD , versus shear rate for ballotini 10cSt pellets with a top lid pressure of 2000 Pa and 1-1.4 mm background beads. Error bars represent the standard error s of 4 measurements	137
Figure 5.26 Images of ballotini 10cSt pellets with shearing time, with a top lid pressure of 2000 Pa and 1-1.4 mm background beads for conditions: 5.03/s (bottom) and 40.21/s (top)	138
Figure 5.27 Deformation fraction, FD , versus normal pressure for ballotini 10cSt pellets with a shear rate of 40.21/s and 1-1.4 mm background beads. Error bars represent the standard error of 4 measurements	140
Figure 5.28 Images of ballotini 10cSt pellets with shearing time, with a shear rate of 40.21/s and 1-1.4 mm background beads for conditions: 383 Pa (bottom), 600 Pa (middle) and 2000 Pa (top).....	141
Figure 5.29 Pellet elongation, Ep , and Stokes deformation number, $Stdef$, relationship for lactose 10cSt pellets at shear rates of 5.03/s and 40.21/s, a top lid pressure of 2000 Pa, 1-1.4 mm background beads and uniaxial compression speeds between 1 mm/s and 125.7 mm/s. Error bars represent the standard error of 4 measurements.....	143
Figure 5.30 Pellet elongation, Ep , and Stokes deformation number, $Stdef$, relationship for lactose 10cSt pellets at shear rates of 5.03/s and 40.21/s, a top lid pressure of 2000 Pa, 2 mm background beads and uniaxial compression speeds between 1 mm/s and 125.7 mm/s. Error bars represent the standard error of 4 measurements.....	145

Figure 5.31 Deformation fraction, FD , and Stokes deformation number, St_{def} , relationship for ballotini 10cSt pellets at shear rates of 5.03/s and 40.21/s, a top lid pressure of 2000 Pa, 1-1.4 mm background beads and uniaxial compression speeds between 1 mm/s and 125.7 mm/s. Error bars represent the standard error of 4 measurements.....	147
Figure 6.1 Sections of the annular shear cell and the DEM unit shear cell	150
Figure 6.2 Length in the x-direction and width in the y-direction for the DEM unit shear cell.....	152
Figure 6.3 Height in the z-direction for the DEM unit shear cell	154
Figure 6.4 (a) Experimentally produced pellet; (b) 3D geometry of the pellet; (c) 3D meshes of the pellet in DEM simulations and (d) 3D model of the pellet in DEM simulations	155
Figure 6.5 Normal force – overlap relationship in the modified version of Simplified Pasha’s model: linear elastic-plastic without adhesive contact model	157
Figure 6.6 The DEM unit shear cell was built within the simulation domain box (red lines). The top plate was able to move and apply pressure in the z-direction and to shear in the x-direction.	168
Figure 6.7 Position of the cylindrical pellet surrounded by the background beads from side view (left) and front view (right).....	168
Figure 6.8 Stress components acting on the pellet	169
Figure 6.9 Top plate position in the z-axis over shearing time for lactose 10cSt pellets with different size of background beads, shear rate of 40.21/s and top plate pressure of 2000 Pa	172
Figure 6.10 Top plate pressure over shearing time for lactose 10cSt pellets with different size of background beads, shear rate of 40.21/s and top plate pressure of 2000 Pa	173
Figure 6.11 Position of lactose 10cSt pellet in the z-axis over the shearing time. Conditions for shear rate of 40.21/s and top plate pressure of 2000 Pa.....	174
Figure 6.12 Deviatoric stress versus time for lactose 10cSt pellet with different background beads, shear rate of 40.21/s and top plate pressure of 2000 Pa	175
Figure 6.13 Stress σ_{xx} over time for lactose 10cSt pellets with variation of size of background beads, shear rate of 40.21/s and top plate pressure of 2000 Pa	177
Figure 6.14 Stress σ_{xy} over time for lactose 10cSt pellets with variation of size of background beads, shear rate of 40.21/s and top plate pressure of 2000 Pa	177
Figure 6.15 Stress σ_{xz} over time for lactose 10cSt pellets with of variation size of background beads, shear rate of 40.21/s and top plate pressure of 2000 Pa	178
Figure 6.16 Stress σ_{yx} over time for lactose 10cSt pellets with variation of size of background beads, shear rate of 40.21/s and top plate pressure of 2000 Pa	178
Figure 6.17 Stress σ_{yy} over time for lactose 10cSt pellets with variation of size of background beads, shear rate of 40.21/s and top plate pressure of 2000 Pa	179
Figure 6.18 Stress σ_{yz} over time for lactose 10cSt pellets with variation of size of background beads, shear rate of 40.21/s and top plate pressure of 2000 Pa	179
Figure 6.19 Stress σ_{zx} over time for lactose 10cSt pellets with variation of size of background beads, shear rate of 40.21/s and top plate pressure of 2000 Pa	180
Figure 6.20 Stress σ_{zy} over time for lactose 10cSt pellets with variation of size of background beads, shear rate of 40.21/s and top plate pressure of 2000 Pa	180
Figure 6.21 Stress σ_{zz} over time for lactose 10cSt pellets with variation of size of background beads, shear rate of 40.21/s and top plate pressure of 2000 Pa	181
Figure 6.22 Deviatoric stress versus time for ballotini 10cSt pellets with different size of background beads, shear rate of 40.21/s and top plate pressure of 2000 Pa.....	182
Figure 6.23 Stress σ_{xx} over time for ballotini 10cSt pellets with variation of size of background beads, shear rate of 40.21/s and top plate pressure of 2000 Pa	184
Figure 6.24 Stress σ_{xy} over time for ballotini 10cSt pellets with variation of size of background beads, shear rate of 40.21/s and top plate pressure of 2000 Pa	184
Figure 6.25 Stress σ_{xz} over time for ballotini 10cSt pellets with variation of size of background beads, shear rate of 40.21/s and top plate pressure of 2000 Pa	185

Figure 6.26 Stress σ_{yx} over time for ballotini 10cSt pellets with variation of size of background beads, shear rate of 40.21/s and top plate pressure of 2000 Pa	185
Figure 6.27 Stress σ_{yy} over time for ballotini 10cSt pellets with variation of size of background beads, shear rate of 40.21/s and top plate pressure of 2000 Pa	186
Figure 6.28 Stress σ_{yz} over time for ballotini 10cSt pellets with variation of size of background beads, shear rate of 40.21/s and top plate pressure of 2000 Pa	186
Figure 6.29 Stress σ_{zx} over time for ballotini 10cSt pellets with variation of size of background beads, shear rate of 40.21/s and top plate pressure of 2000 Pa	187
Figure 6.30 Stress σ_{zy} over time for ballotini 10cSt pellets with variation of size of background beads, shear rate of 40.21/s and top plate pressure of 2000 Pa	187
Figure 6.31 Stress σ_{zz} over time for ballotini 10cSt pellets with variation of size of background beads, shear rate of 40.21/s and top plate pressure of 2000 Pa	188
Figure 6.32 Deviatoric stress versus time for lactose 10cSt pellets with different shear rates, top plate pressure of 2000 Pa and 1-1.4 mm background beads	189
Figure 6.33 Deviatoric stress versus time for ballotini 10cSt pellets with different shear rates, top plate pressure of 2000 Pa and 1-1.4 mm background beads	190
Figure 6.34 Deviatoric stress versus time for lactose 10cSt pellets with different normal pressures, shear rate of 40.21/s and 1-1.4 mm background beads.....	191
Figure 6.35 Deviatoric stress versus time for ballotini 10cSt pellets with different normal pressures, shear rate of 40.21/s and 1-1.4 mm background beads.....	192
Figure 6.36 Deviatoric stress versus time for ballotini powder and different viscosity silicone oils, shear rate of 5.03/s, top plate pressure of 2000 Pa and 2 mm background beads	193
Figure 6.37 Deviatoric stress versus time for 0.01 Pa.s silicone oil and two types of powders, shear rate of 40.21/s, top plate pressure of 2000 Pa and 1-1.4 mm background beads	194
Figure 6.38 von Mises stress versus time for lactose 10cSt pellets with different sizes of background beads, shear rate of 40.21/s and top plate pressure of 2000 Pa.....	196
Figure 6.39 von Mises stress versus time for ballotini 10cSt pellets with different background beads, shear rate of 40.21/s and top plate pressure of 2000 Pa	197
Figure 6.40 von Mises stress versus time for lactose 10cSt pellets with different shear rates, top plate pressure of 2000 Pa and 1-1.4 mm background beads	199
Figure 6.41 von Mises stress versus time for lactose 10cSt pellets with different normal pressures, shear rate of 40.21/s and 1-1.4 mm background beads.....	201
Figure 6.42 von Mises stress versus time for ballotini 10cSt pellets with different normal pressures, shear rate of 40.21/s and 1-1.4 mm background beads.....	202
Figure 7.1 Predicted yielding time versus shear rate for lactose 10cSt pellets with a top lid pressure of 2000 Pa and 1-1.4 mm background beads.	207
Figure 7.2 Pellet elongation versus predicted yielding time for lactose 10cSt pellets with different shear rates, normal pressure of 2000 Pa and 1-1.4 mm background beads. Error bars represent the standard error of 4 measurements	208
Figure 7.3 Predicted yielding time versus normal pressure for lactose 10cSt pellets with a shear rate of 40.21/s and 1-1.4 mm background beads.	209
Figure 7.4 Pellet elongation versus predicted yielding time for lactose 10cSt pellets with different normal pressures, shear rate of 40.21/s and 1-1.4 mm background beads. Error bars represent the standard error of 4 measurements.....	209
Figure 7.5 Predicted yielding time versus size of background beads for lactose 10cSt pellets with a shear rate of 40.21/s and a top lid pressure of 2000 Pa.....	210
Figure 7.6 Pellet elongation versus predicted yielding time for lactose pellets with different size of background beads, shear rate of 40.21/s and normal pressure of 2000 Pa. Error bars represent the standard error of 4 measurements.....	211
Figure 7.7 Predicted yielding time versus shear rate for ballotini 10cSt pellets with a top lid pressure of 2000 Pa and 1-1.4 mm background beads.	212

Figure 7.8 Deformation fraction versus predicted yielding time for ballotini 10cSt pellets with different shear rates, normal pressure of 2000 Pa and 1-1.4 mm background beads. Error bars represent the standard error of 4 measurements..... 212

Figure 7.9 Predicted yielding time versus normal pressure for ballotini 10cSt pellets with a shear rate of 40.21/s and 1-1.4 mm background beads..... 213

Figure 7.10 Deformation fraction versus predicted yielding time for ballotini 10cSt pellets with different normal pressures, shear rate of 40.21/s and 1-1.4 mm background beads. Error bars represent the standard error of 4 measurements..... 214

List of Tables

Table 2.1 A range of values of critical Stokes deformation number St_{def}^*	15
Table 2.2 Summary of breakage studies in granulators	16
Table 2.3. Relationship between minimum viscosity of silicone oil and mean particle size of non-porous calcium carbonate particles to produce robust granules	17
Table 2.4. Summary of granulation parameters studied	18
Table 2.5 Experimental studies for annular shear cell and Couette cell	21
Table 2.6. Example of input properties in the simplified Pasha’s model.....	49
Table 2.7 DEM simulations for shear flow and breakage studies in selected types of equipment/techniques	53
Table 3.1 List of materials and methods.....	56
Table 3.2 Particle size distribution for background beads using the sieve method	61
Table 3.3 Particle size properties of powders using laser diffraction.....	63
Table 3.4 Density of powders	65
Table 3.5 Densities of background beads	65
Table 3.6 Densities of liquid binder	66
Table 3.7 Viscosity of liquid binder	68
Table 3.8 Ballotini glass beads paste formulations.....	72
Table 3.9 Lactose paste formulations	73
Table 3.10 MCC paste formulations.....	73
Table 3.11 Selected formulations of the different pastes	74
Table 3.12 List of properties of the pellets	76
Table 4.1 Set-up conditions for the dynamic compression test	81
Table 4.2 Plastic and elastic stiffness of pellets using the quasi-static compression test	100
Table 4.3 Young’s modulus of pellets using the quasi-static compression test	102
Table 4.4 Yield stress of pellets using the dynamic compression test.....	107
Table 5.1 Specifications of the annular shear cell	112
Table 5.2 Variable parameters for annular shear cell experiments	114
Table 5.3 Variation of the shear rate of the top lid	116
Table 5.4 Variation of the pressure of the top lid.....	116
Table 5.5 Mass of background beads for the experiments	117
Table 6.1 Pressure, mass and area of the top plate	158
Table 6.2 Scale and percentage of mass for background beads 1-1.4 mm in DEM simulations	160
Table 6.3 Scale and percentage of mass for background beads 2 mm in DEM simulations	160
Table 6.4 Stiffness of pellets and background beads in the DEM simulations	161
Table 6.5 Young’s modulus of pellets for DEM simulations	161
Table 6.6 Density of pellets for DEM simulations	162
Table 6.7 Densities of background beads for DEM simulations	163
Table 6.8 Interaction properties for all cases	163
Table 6.9 Parameters for DEM simulations	164
Table 6.10 Properties of background beads for DEM simulations	164
Table 6.11 Shear rates from top plate of the DEM unit shear cell	166
Table 6.12 Example extracted data of stress components from DEM simulations	170
Table 6.13 Relationship between size of beads and amount of background beads for making up the height of the DEM unit shear cell	181
Table 6.14 Yield stresses of lactose 10cSt pellets for different compression speeds	195
Table 6.15 Yield stresses of ballotini 10cSt pellets for different compression speeds.....	195
Table 6.16 Intersection times for von Mises stress and yield stresses of lactose pellets with different sizes of background beads, shear rate of 40.21/s and top plate pressure of 2000 Pa.....	196

Table 6.17 Intersection times for von Mises stress and yield stresses of ballotini 10cSt pellets with different size of background beads, shear rate of 40.21/s and top plate pressure of 2000 Pa	197
Table 6.18 Intersection times for von Mises stress and yield stresses of lactose 10cSt pellets with different shear rates, top plate pressure of 2000 Pa and 1-1.4 mm background beads.....	199
Table 6.19 Intersection times for von Mises stress and yield stresses of ballotini 10cSt pellets with different shear rates, top plate pressure of 2000 Pa and 1-1.4 mm background beads.....	200
Table 6.20 Intersection times for von Mises stress and yield stresses of lactose 10cSt pellets with different normal pressures, shear rate of 40.21/s and 1-1.4 mm background beads.....	201
Table 6.21 Intersection times for von Mises stress and yield stresses of ballotini 10cSt pellets with different normal pressures, shear rate of 40.21/s and 1-1.4 mm background beads.....	203
Table 7.1 List of operating parameters for correlation between experimental data analysis from annular shear cell experiments and predicted from DEM simulations	206

List of Symbols

Symbols	Meaning
St_{def}	Stokes deformation number
Y	Granule dynamic yield strength
P_G	Granule density
U	Average relative granule collision velocity
F_B	Breakage fraction
N_0	Original number of granules placed in the granulator
N_s	Number of surviving granules at the end of experiment
ΔT	Time-step
ΔT_{CR}	Rayleigh time-step
T_{START}	Time for simulation to start
T_{END}	Time for simulation to end
R_i	Radius of particle 1
R_j	Radius of particle 2
C	Skin distance
P_i	Particle 1
P_j	Particle 2
F_n	Linear normal contact force
k_n	Linear normal spring stiffness (constant value)
δ_n	Deformation/ overlap in linear normal direction
C_n	Linear normal dashpot (damping coefficient)
v_n	Linear relative velocity in normal direction
F_{nl}	Nonlinear normal Hertz contact force
k_{nl}	Nonlinear normal contact force
δ_{nl}	Deformation/ overlap in nonlinear normal direction
U	Poisson's ratio for particle 1 and 2
D	Distance between the centers of the two particles
R^*	Effective particle radius
E^*	Effective Young's modulus (elastic moduli)
R	Radii for particle 1 and 2
E	Young's modulus (elastic moduli) for particle 1 and 2
C_{nl}	Nonlinear normal damping coefficient
v_{nl}	Nonlinear relative velocity
μ	Friction coefficient
F_c	Resultant normal and tangential contact forces
F_{nc}	Resultant non-contact forces (van der Waals force, liquid bridges force)
ϵ	Coefficient of restitution
v_f	Final velocity (after impact)
v_i	Initial velocity (before impact)
NP	Number of total particles to be inserted
PR	Particle rate
ΔT	Time-step

Symbols	Meaning
St_{def}	Stokes deformation number
Y	Granule dynamic yield strength
P_G	Granule density
U	Average relative granule collision velocity
F_B	Breakage fraction
N_0	Original number of granules placed in the granulator
N_s	Number of surviving granules at the end of experiment
ΔT	Time-step
ΔT_{CR}	Rayleigh time-step
T_{START}	Time for simulation to start
T_{END}	Time for simulation to end
R_i	Radius of particle 1
R_j	Radius of particle 2
C	Skin distance
P_i	Particle 1
P_j	Particle 2
F_n	Linear normal contact force
k_n	Linear normal spring stiffness (constant value)
δ_n	Deformation/ overlap in linear normal direction
C_n	Linear normal dashpot (damping coefficient)
v_n	Linear relative velocity in normal direction
F_{nl}	Nonlinear normal Hertz contact force
k_{nl}	Nonlinear normal contact force
δ_{nl}	Deformation/ overlap in nonlinear normal direction
U	Poisson's ratio for particle 1 and 2
D	Distance between the centers of the two particles
R^*	Effective particle radius
E^*	Effective Young's modulus (elastic moduli)
R	Radii for particle 1 and 2
E	Young's modulus (elastic moduli) for particle 1 and 2
C_{nl}	Nonlinear normal damping coefficient
v_{nl}	Nonlinear relative velocity
μ	Friction coefficient
F_c	Resultant normal and tangential contact forces
F_{nc}	Resultant non-contact forces (van der Waals force, liquid bridges force)
ϵ	Coefficient of restitution
v_f	Final velocity (after impact)
v_i	Initial velocity (before impact)
NP	Number of total particles to be inserted
PR	Particle rate
ΔT	Time-step
DEM	Discrete Element Method
COR	Coefficient of restitution
HPMC	hydroxypropylmethylcellulose

1 Introduction

1.1 Introduction to granulation

Granulation is a process of forming granules by the addition of a liquid binder into a continually agitated powder system (Simon M. Iveson, Litster, et al., 2001; Le et al., 2009). It plays an important role in the processing of pharmaceuticals, agricultural products, minerals and specialty chemicals (Pandey et al., 2013; Pathare et al., 2011). Wetting and nucleation, consolidation and growth, and attrition and breakage are the three rate processes occurring in the granulation process (Ennis Litster, J.D., 1997; Simon M. Iveson, Litster, et al., 2001; Mort & Tardos, 1999). Wetting and nucleation involve the initial contact between particles and binder solution to form granule nuclei. A combination of compaction (densification), coalescence and layering of granules may be involved in the consolidation and growth mechanism. During attrition and breakage, granules are broken due to granule-granule impacts, wear, granule impact with the impeller blade and the chopper within the granulator, or during subsequent product handling (Simon M. Iveson, Litster, et al., 2001; Kano et al., 2014).

In the high shear granulation process, the high shear within the powder bed and impacts with the impeller or chopper contribute to wet granule breakage (L. X. Liu et al., 2009; Rachel M Smith et al., 2010). The presence of agitation in the granulator results in the development of both shear and impact forces at high speed (Chitu et al., 2011b; L. X. Liu et al., 2009). Moreover, a high probability of breakage occurs through very high shear in the powder bed close to the impeller (L. X. Liu et al., 2009) as shown in Figure 1.1.

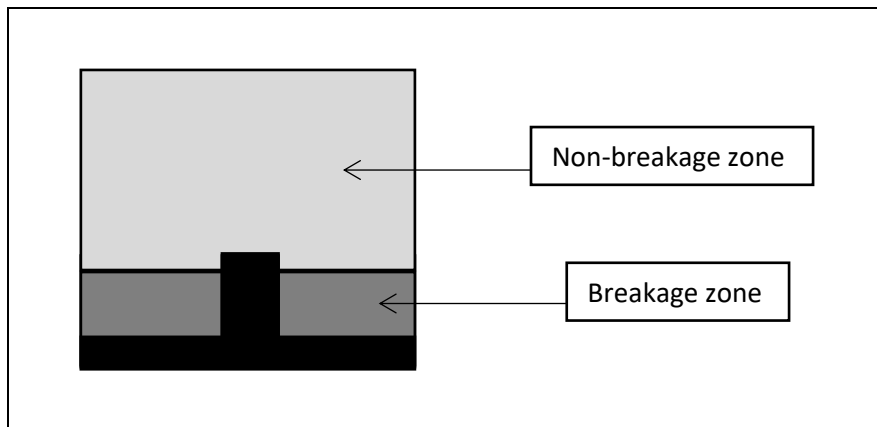


Figure 1.1 Area of breakage zone in the granulator

1.2 Challenges in granulation breakage research

Of all the aforementioned three rate processes, many studies have considered the wetting, nucleation, consolidation and growth mechanisms. However, limited research has been conducted into breakage and attrition and, therefore, there still remains a knowledge gap concerning this mechanism. Moreover, the study of breakage is challenging as the three rate processes often occur simultaneously during the granulation process. The presence of the internal flow pattern, bumping and roping flows in granulation, creates a random movement of the granules, resulting in granular materials falling near the granulator wall and difficulty in controlling the position of the granules. According to (Lekhal Girard, K.P., Brown, M.A., Kiang, S., Glasser, B.J., Khinast, J.G., 2003; Lekhal Girard, K.P., Brown, M.A., Kiang, S., Khinast, J.G., Glasser, B.J., 2004), breakage and agglomeration are very sensitive to the flow patterns and they greatly influence the final granule size.

In addition, shear and impact forces occur simultaneously in granulation which makes it difficult to identify which forces contribute to breakage. A few attempts to decouple both of the forces has been performed through experiment by previous works: 1) pre-formed granules outside the granulator and granulating the granules with a non-granulating cohesive sand mixture as the shearing (L. X. Liu et al., 2009; Rachel M Smith et al., 2010), and 2) a flat plate impeller has been used to minimize the impact in the granulator (Knight et al., 2001; Rachel M Smith et al., 2010). By using these approaches, the shear stress can be directly transmitted to the granules in the absence of nucleation and growth and, therefore, formulation and operational parameters that may contribute to granule breakage can be directly explored.

Although the aforementioned approaches have been taken, there are still knowledge gaps which need to be addressed. By assuming shear force is the primary force developed in the system and granules are shearing within the bed powder, the granules can break by different mechanisms, i.e. shearing, compression, fragmentation or a combination of them. For this reason, the shape of the granules can be elongated, flattened, fragmented or combination of these. Moreover, the application of different granulation parameters and the emergent of behaviour/properties of the granules would affect the breakage process. These are the focus of this research, and the approach is described in the following section.

1.3 Research plan

As shown in Figure 1.1, it is expected that breakage primarily occurs in a zone close to the impeller. Several approaches for this current study are described in this section.

As described in Section 1.2, the granular flow in the granulation process involves a complex system. A simple shear flow system was considered in this study due to its ability to generate simple, high shear flows, and a custom-made annular shear cell was developed and manufactured in-house. This shear cell has the ability to operate in a rapidly high shearing conditions between 15 rpm and 120 rpm.

Advancements of computer processing speeds have made computational simulations an effective alternative tool to study and understand granular flow, e.g. within granulators. They have become more popular both within research and in the industrial world. The use of numerical simulations provides a cost-effective method compared to experiments as no physical materials and process equipment are required. For this study, the pellet deformation was predicted by the combination of simulations to examine the stress applied to pellets under simple shear, and a suitable failure theory, i.e. von Mises failure theory.

Validation with experiments is needed to ensure it is realistic for predicting the flow behaviour of a certain process. For this purpose, the results from simulations were linked to the experiments so that the simulations results can be the representative of the experiment results. The flow diagram of the problem statement and approaches taking in this work is illustrated in Figure 1.2. Further details are given within specific chapters.

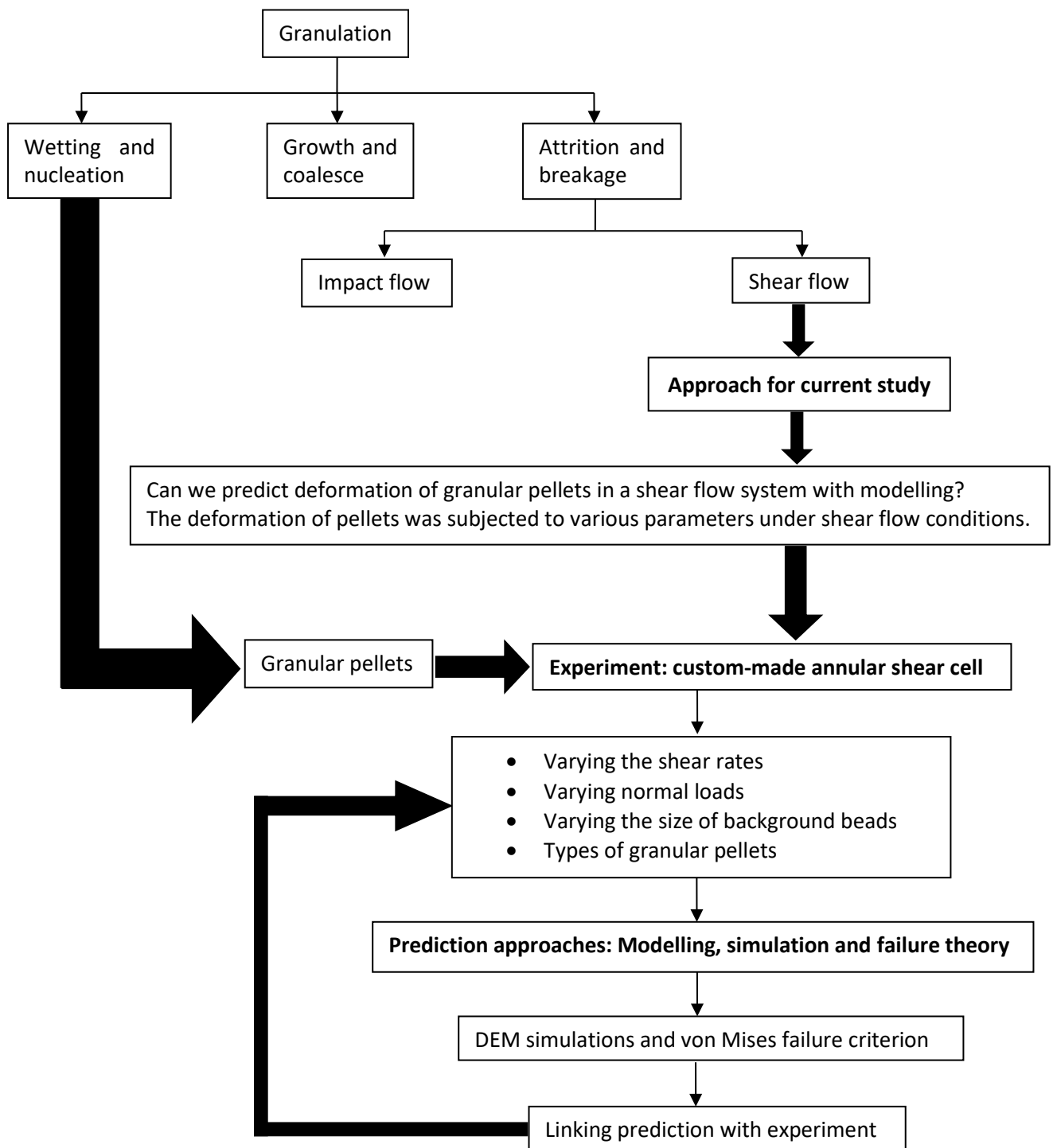


Figure 1.2 Flow diagram of the problem statement and approaches

1.4 Aim of the study

The aim of this research is to further understanding of wet granule breakage, and to develop a predictive model for granular pellet deformation in an annular shear cell.

1.5 Objectives

For achieving the aim above, the following objectives were identified:

- To characterize pellet deformation through experiments in an annular shear cell
- To predict granular pellet deformation through Discrete Element Method (DEM) simulations and theoretical failure criterion
- To correlate the experimental results with predictions results

1.6 Structure of the thesis

Chapter 2 presents a literature review regarding granulation, shear cell testers, stresses for 3D material and selected failure theory. In addition, DEM simulations and the chosen contact model for DEM simulations are discussed. In Chapter 3, the materials used and general methods for this research are described. Chapter 4 describes the mechanical properties of the granular pellet measured through compression tests. In Chapter 5, experiments in the annular shear cell were carried out. Pellet deformation under different operating parameters were characterised. The experimental results from annular shear cell will be used for modelling in DEM simulations. Predictive approaches with modelling and failure theory are given in Chapter 6. The design of the DEM unit shear cell using DEM simulations and other conditions related to the DEM unit shear cell are also explained. A relationship between experimental results and predictions is presented in Chapter 7. Conclusions and planning for future works of this thesis are given in Chapter 8.

2 Literature review

2.1 Introduction

This chapter gives a review on granulation, breakage in granulation and parameters affecting the granulation. Moreover, a short review of the types of shear cell and other properties related to shear flow are discussed in this chapter. It is followed by an examination of the stresses on 3D materials, the relationship with failure of material and models for predicting the deformation of materials. The chapter ends with a review of modelling and simulation using DEM simulations and the application of DEM simulations in several works of shear flow and breakage.

2.2 Granulation

In wet granulation processes, liquid binder is added to dry powders as they are agitated in a tumbling drum, fluidized bed, high shear mixer or similar device (Simon M. Iveson, Litster, et al., 2001). High shear mixers are the most widely used for a number of reasons; their capacity to process wet and sticky materials, their ability to spread viscous binders, they are less sensitive to operating conditions than tumbling granulators, and they produce small (<2 mm) and high density granules (Snow et al., 1997). A diagram of a high shear mixer and its components is shown in Figure 2.1.

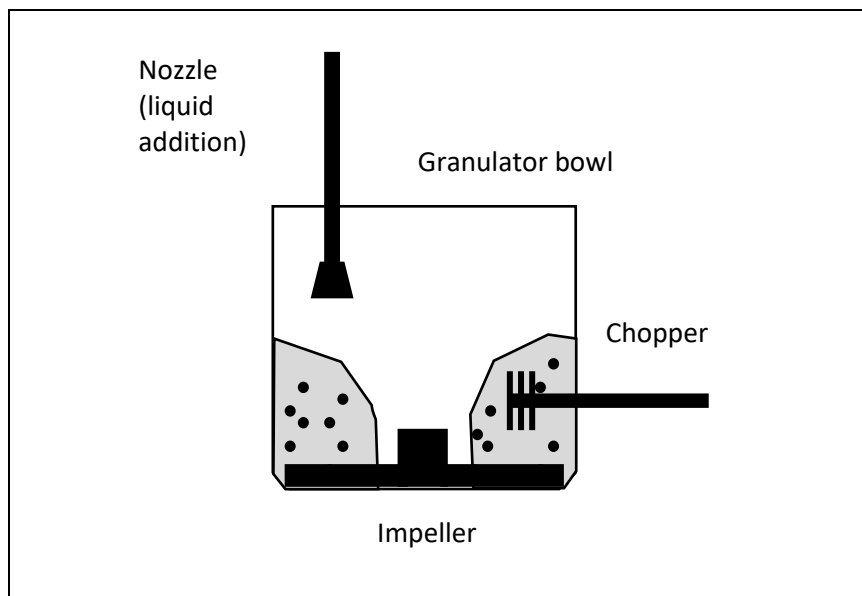


Figure 2.1 High shear mixer

There are three rate processes in the granulation process, 1) wetting and nucleation; 2) consolidation and growth and 3) attrition and breakage as shown in Figure 2.2 (Simon M. Iveson, Litster, et al., 2001; Mort & Tardos, 1999; Snow et al., 1997).

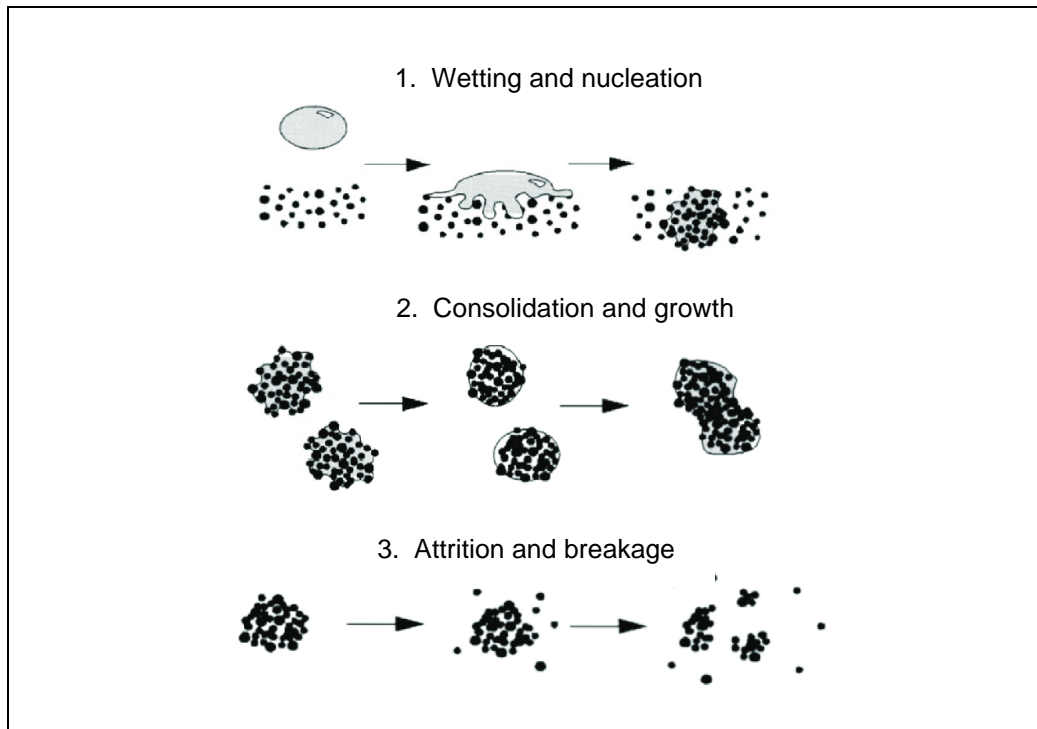


Figure 2.2 Rate processes involved in the granulation process (Simon M. Iveson, Litster, et al., 2001)

In the wetting and nucleation mechanism, the interaction between powder and liquid binder can be by means of distribution or immersion. Distribution occurs as the small size of liquid droplet disperses into the powder and liquid bridges are formed between the particles. In contrast, immersion occurs when the particles enter the droplet due to the larger size of liquid droplet than the particles. In the consolidation and growth mechanism, collisions between two or more granules, granules and feed powder, or granules and the equipment occur. This phenomenon leads granules to grow in size due to coalescence and/or layering. However, the granule size can be decreased slightly at first due to initial compaction with an increase in density. In the third mechanism, attrition and breakage, wet or dried granules can be continuously broken due to impact, wear, or compaction in the granulator by impeller blades and the chopper or during subsequent product handling (Simon M. Iveson, Litster, et al., 2001; Kano et al., 2014).

In a high shear mixer, mixing, wetting and massing can be performed simultaneously in a few minutes. Strong, dense and relatively more spherical granules can be generated by a high shear mixer compared to other granulation techniques due to the high contact between the mass of fine powder and binder (Franceschinis et al., 2014). The process is facilitated by the agitation of the impeller moving from low to high speeds. The mixture of the wetted powders undergoes densification due to the compaction forces imposed by the impeller and agglomeration due to contact via shear forces. A chopper may be included in the high shear mixer to cut down the large agglomerates into smaller fragments and promote densification at a high speed (Chitu et al., 2011a; Reynolds et al., 2005)

Granular shear flow in the high shear mixer can be both bumping and roping flow (Figure 2.3). According to (Litster et al., 2002) and (Nakamura et al., 2013), the internal flow pattern at the lower impeller tip speed exhibited “bumping flow. The surface of the powder bed remains horizontal and the powder bed bumps up and down with little vertical circulation as the impeller blade passes underneath. The internal flow pattern at the higher impeller tip speed was changed to “roping flow”, which is toroidal particle flow with a vertical circulation consisting of upward flow along the vessel wall and downward flow near the centre of the vessel.

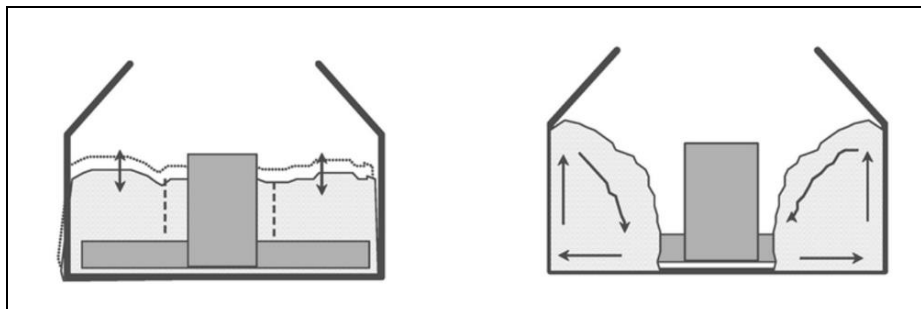


Figure 2.3 Bumping flow (left) and roping flow (right) in vertical shaft mixers (Jim Litster and Bryan Ennis, 2004)

A change in the dimensionless shear rate influences the transition of the internal particle flow pattern. According to (Nakamura et al., 2013), by increasing the ranges of the dimensionless shear rate, the internal particle flow pattern changes from the bumping flow to the roping flow. Moreover, within the constant region of the dimensionless shear rate (the plateau curve has achieved), the internal particle flow pattern remained in the roping flow. This indicates the granulation process is in a steady state condition.

2.2.1 Breakage studies in granulation

According to (Knight et al., 2000a; L. X. Liu et al., 2009; Reynolds et al., 2005; Rachel M. Smith & Litster, 2012; Jonathan Brett Wade, 2013), the importance of breakage are: a) allowing the improvement of the process design and specification; b) enhancing the distribution of viscous binder homogeneously for controlling the final granule size distribution; c) providing information of the behaviour of granules for further processing, handling and transporting conditions and d) as a product quality tool to access the properties of final granules e.g. strength of the granules.

In the past, granule breakage has been analysed in several ways such as visualization/ morphology test, breakage fraction, degree of elongation and linking with a predictive model; Stokes deformation number. The methods and findings are explained in the following sections.

2.2.1.1 Visualization/ morphology test

Studies by (Eliassen et al., 1998, 1999) have investigated granule breakage through visualization of the changes in granule size distribution. (Knight et al., 1998) found a persistent bimodal distribution of granule size throughout the granulation process after the addition of binder liquid. Changes in granule size distribution were observed as the mixing time was prolonged. This indicates that the content of coarse granules decreased and the content of fine granules increased with mixing time. In addition, they found a reduction in the size of granules and growth behaviour with all binder addition methods. They suggest that the changes in size distribution gave significant evidence for the presence of granule breakage (Knight et al., 1998).

On the other hand, (Knight et al., 2000a) carried out a morphology test to observe the change in granule shape due to changes in the impeller speed. From the test, spherical shaped granules were found at lower impeller speed. However, the use of higher impeller speed results in irregular shaped granules. This shows that the impeller speed has a significant effect on granule shape. Moreover, these findings indicate that impeller speed is a critical parameter that influences the size enlargement process, by which it can limit the growth of the granules due to the breakage of the large granules into small fragments. The persistent phenomenon of a bimodal size distribution with time after the addition of the binder represents the breakage of large granules into small fragments. A reduction in the fraction of large granules at high impeller speed was observed.

Additionally, (Simon M. Iveson, Litster, et al., 2001) suggested the changes in granule size distribution could be due to the increase in impeller speed as a result of high impact velocity occurring within the granulator. These high collision rates cause the rebound of the colliding granules, thus probably leading to the reduction of the coalescence of granules and changes in the granule size distribution.

2.2.1.2 Breakage fraction

(L. X. Liu et al., 2009; Rachel M. Smith et al., 2010) have introduced a 'breakage only' granulation technique. It is used to measure the amount of granules which break in the granulator. In this method, an amount of pre-formed granules was deposited into the high shear mixer with a non-granulating cohesive sand mixture. The non-granulating cohesive sand mixture does not agglomerate with the granules. Instead, the sand mixture acts as a medium for minimising granule growth in the granulator. In this way, breakage of the granules would not be influenced by the other two rate mechanisms; nucleation and growth. The granule breakage can be characterised using a simple mathematical expression, breakage fraction, F_B as shown in Equation 2.1 (R M Smith, 2007).

$$F_B(\%) = \frac{N_0 - N_s}{N_0} \times 100 \quad \text{Equation 2.1}$$

Where

F_B =	Breakage fraction	(%)
N_0 =	Original number of granules placed in the granulator	(-)
N_s =	Number of surviving granules at the end of experiment	(-)

2.2.1.3 Degree of elongation

(Khan & Tardos, 1997) have measured the degree of agglomerate deformation by introducing the degree of elongation, E . The range of values of E were obtained experimentally between 1 (for zero deformation) and 1.5 (for highly deformed agglomerates). From the work, they suggested that degree of elongation, E can be used as a measurement of the agglomerate's tendency to break. A low value of E would imply a low tendency towards breakage, whereas a high value of E indicates a high tendency towards breakage. The degree of elongation, E is defined in Equation 2.2. Figure 2.4 shows images of an agglomerate sheared in opposite directions, surrounding by a dry particulate medium (Khan & Tardos, 1997).

$$E = \frac{l}{d_0} \quad \text{Equation 2.2}$$

Where:

$E =$	Degree of elongation	(-)
$d_0 =$	Diameter of the original un-deformed (spherical) agglomerate	(m)
$l =$	Major axis of the deformed agglomerate	(m)

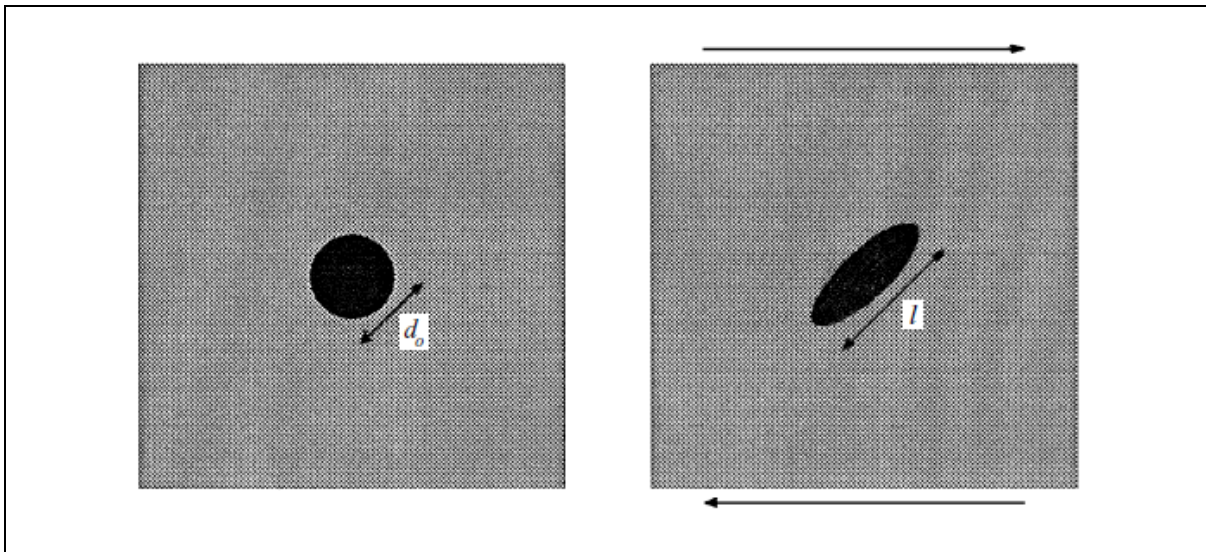


Figure 2.4 Un-deformed agglomerate (left) and sheared deformed agglomerate (right) in opposite directions, surrounding by dry particulates medium (Khan & Tardos, 1997)

2.2.1.4 Stokes deformation number

The experimental results of granule breakage can be correlated to a parameter called the Stokes deformation number, St_{def} (S M Iveson & Litster, 1998; Simon M. Iveson et al., 2003; Simon M. Iveson, Wauters, et al., 2001; L. X. Liu et al., 2009; Tardos et al., 1997; Van Den Dries et al., 2003a). (S M Iveson & Litster, 1998; Tardos et al., 1997) defined Stokes deformation number, St_{def} as the comparison between the externally applied kinetic energy on the granules with the energy required for deformation of the granules (Equation 2.3). The energy required for deformation was referred to the strength of the granules, which was usually obtained from the static and dynamic conditions.

$$St_{def} = \frac{\text{Externally applied kinetic energy}}{\text{Energy required for deformation}} \quad \text{Equation 2.3}$$

Based on an agglomerate breakage study by (Tardos et al., 1997), several outcomes could be obtained when the agglomerates are exposed to a constant shear field such as: 1) no agglomerates could break; 2) some agglomerates could break and 3) all agglomerates could break, by which all depend on the Stokes deformation number. Moreover, the agglomerates in the system were believed to be completely broken/deformed when the Stokes deformation number, St_{def} was greater than a critical Stokes deformation number, St_{def}^* .

(Bouwman et al., 2006a) used the Stokes deformation number to predict wet granule breakage. In this case, St_{def} was expressed as the ratio between the externally applied kinetic energy on the granules and the energy dissipated by the liquid bonds between the particles. According to (Simon M. Iveson, Litster, et al., 2001; Tardos et al., 1997), Stokes deformation number is the ratio of the impact kinetic energy of the wet granules just before collision to the characteristic work done in a collision to plastically deform the granules.

A mathematical expression of Stokes deformation number based on the works of (Simon M. Iveson, Litster, et al., 2001) is given in Equation 2.4. The input parameter of granule dynamic yield stress was used to represent the dynamic strength of the granules. They believed that the dynamic strength of the granules determines breakage behaviour in the granulator. For this purpose, they suggested that the dynamic strength of the granules is closely related to the fraction of surviving granules at a certain period of granulation time. Therefore, the Stokes deformation number was defined as the ratio of the impact energy to the granule dynamic strength, which then can be used to predict the granule breakage.

$$St_{def} = \frac{\rho_g U_o^2}{2Y_g} \quad \text{Equation 2.4}$$

Where:

ρ_g =	Granule density	(kg/m ³)
U_o =	Relative velocity between moving granules	(m/s)
Y_g =	Granule dynamic yield stress	(Pa) or (kg.m.m ⁻² .s ⁻²)

In Equation 2.4, the relative velocity between moving granules, U_o is difficult to predict for equipment other than high shear mixers. For example, the powder flow field in tumbling drums and high shear mixers have agitators or paddles which make the flow field very complicated and difficult to model. Due to this reason, a rough estimation for the relative velocity between moving granules, U_o has been made by considering the granule diameter and average shear rate in the equipment (Equation 2.5).

$$U_o = a\gamma \quad \text{Equation 2.5}$$

By substituting and combining the Equations 2.4 and 2.5, the Stokes deformation number can be further expressed in Equation 2.6.

$$St_{def} = \frac{\rho_g a^2 \gamma^2}{2Y_g} \quad \text{Equation 2.6}$$

Where:

ρ_g =	Granule density	(kg/m ³)
U_o =	Relative velocity between moving granules	(m/s)
a =	Granule diameter	(m)
γ =	Average shear rate in the granulator	(1/s)
Y_g =	Granule dynamic yield stress	(Pa) or (kg.m.m ⁻² .s ⁻²)

However, the relative velocity between moving particles, U_o have been interchangeably used with the representative collision velocity v_c (Bouwman et al., 2006a; Knight et al., 2001). The representative collision velocity, v_c was assumed to be 15-20% of the impeller tip speed. It has been used as a fixed value assumption in the calculation of Stokes deformation number, St_{def} (Kayrak-Talay et al., 2013; Knight et al., 2001; L. X. Liu et al., 2009). The definition of Stokes deformation number represents the relationship between formulation properties, liquid binder properties and operating conditions. Stokes deformation number with the input parameter of representative collision velocity is given in Equation 2.7.

$$St_{def} = \frac{\rho_g v_c^2}{2Y_g} \quad \text{Equation 2.7}$$

Where:

- ρ_g = Granule density (kg/m³)
 v_c = Representative collision velocity in the granulator and represents the process intensity (m/s)
 Y_g = Granule dynamic yield stress (Pa) or (kg.m.m⁻².s⁻²)

Figure 2.5 describes the use of Stokes deformation number for predicting the deformation and breakup of granules in a constant – shear Couette device by (Tardos et al., 1997). The granule deformation parameter, D was plotted as a function of the Stokes deformation number. D was defined as $(L-B)/(L+B)$, where L and B are the major and minor axis. Three distinct regions can be seen in the plot of Stokes deformation number, St_{def} . The left-hand side refers to the non-breakage or moderate deformation area. The right-hand side is the totally breakage area. In the middle region, the transition between the two can be clearly seen, involving some breakage with high deformation. The breakage of the granules occurs if the stresses of the granules exceed some critical Stokes deformation number, $St_{def} > St_{def}^*$. As shown in Figure 2.5, an approximate value of 0.2 has been marked as the critical Stokes deformation number, indicating none of the granules survived; all the granules have been destroyed.

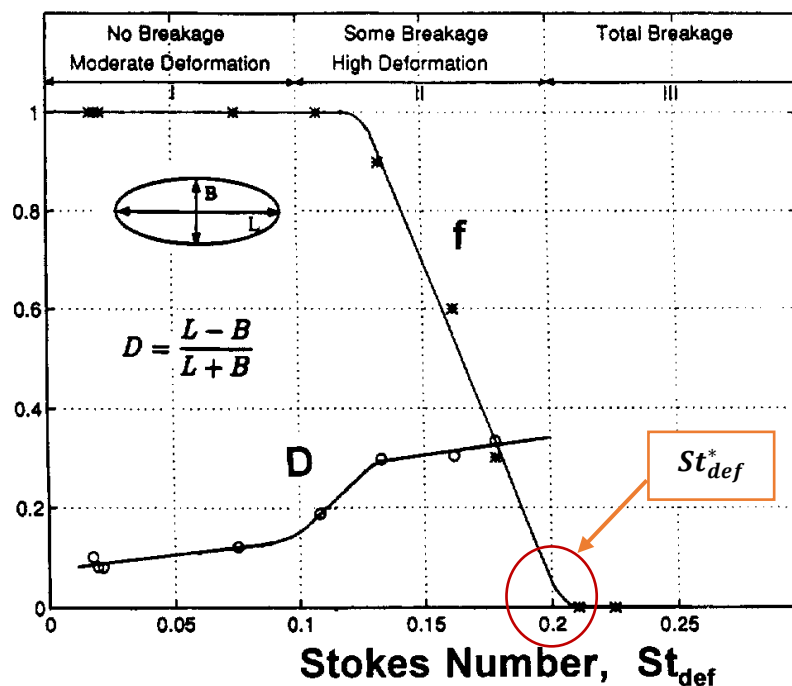


Figure 2.5 Defining critical Stokes deformation number based on the works of (Tardos et al., 1997). The fraction of surviving granules is indicated by f

Table 2.1 lists the values of the critical Stokes deformation number obtained from the previous studies. (Simon M. Iveson, Litster, et al., 2001) found a Stokes deformation number of approximately 0.04 clearly divided two regions between the breakage behaviour and no breakage behaviour. (Van Den Dries et al., 2003a) have set a value of 0.01 as the critical Stokes Deformation number St_{def}^* . According to (J. B. Wade et al., 2015), the calculated Stokes deformation number can give a good prediction of the breakage probability for each formulation. In their study, a value of 0.2 was proposed as the critical Stokes deformation number St_{def}^* . (L. X. Liu et al., 2009) have compared the breakage fraction obtained from experiments in high shear mixer with the Stokes deformation number St_{def}^* , defined as the ratio of kinetic energy over the granule dynamic strength. A similar value of 0.2 was obtained for the critical Stokes deformation number St_{def}^* . They have used this value as a criterion for granule breakage in a high shear mixer. Table 2.1, shows that different values of the critical Stokes deformation number, St_{def}^* could be obtained, depending on the granule properties and mixer geometry and flow patterns. This indicates the influence of the material properties and operating parameters. Moreover, the value of critical Stokes deformation number, St_{def}^* can be determined directly from the same graph of Stokes deformation number, St_{def} .

Table 2.1 A range of values of critical Stokes deformation number St_{def}^*

Critical Stokes deformation number St_{def}^*	References
0.04	(Simon M. Iveson, Litster, et al., 2001)
0.01	(Van Den Dries et al., 2003b)
0.2	(J. B. Wade et al., 2015)
0.2	(L. X. Liu et al., 2009)
0.2	(Tardos et al., 1997)
0.45	(Davis, 2016)
0.3	(Rachel M. Smith et al., 2010)

An experimental granule breakage study by (Van Den Dries et al., 2003b) considered a Stokes deformation number model and a breakage number (%) as part of the analysis. The granule breakage can be detected through the addition of coloured dye to give tracer granules or liquid in the granulator. Both the Stokes deformation number model and breakage number (%) were used to determine the extent of breakage and predict the granule breakage. Table 2.2 lists some of the experimental breakage studies in granulators using different measurement techniques.

Table 2.2 Summary of breakage studies in granulators

Techniques of measurements	References
Visualization through changes in granule mean size and granule size distribution	(Knight et al., 1998) (Eliassen et al., 1998) (Eliassen et al., 1999) (Knight et al., 2000b) (Simon M. Iveson, Litster, et al., 2001) (L. X. Liu et al., 2009) (Rachel M. Smith et al., 2010)
Addition of coloured dyes to create tracer granules or liquid	(Van Den Dries et al., 2003a) (Pearson et al., 2001) (Ramaker et al., 1998) (Vonk et al., 1997)
Correlated the experimental findings with the Stokes deformation number, St_{def}	(Moreno et al., 2003) (Antonyuk et al., 2006) (Z. Ning et al., 1997) (Seyedi Hosseininia & Mirghasemi, 2007) (Seyedi Hosseininia & Mirghasemi, 2006) (S M Iveson & Litster, 1998) (Simon M. Iveson et al., 2003) (Simon M. Iveson, Wauters, et al., 2001) (Van Den Dries et al., 2003a) (L. X. Liu et al., 2009) (Tardos et al., 1997)

2.2.2 Granulation parameters affecting breakage

There are a number of studies of the granulation parameters which influence the granulation process and properties of the final granules. This review is limited to the parameters that are important for breakage and, therefore, relevant to the current study. The effect of impeller speed in a high agitation intensity mixer has been investigated by (Knight et al., 2000b). It was found that high impeller speed increases granule breakage. In addition, there was a relationship between impeller speed, granule porosity, granule breakage and granule strength as studied by (Van Den Dries et al., 2003a). They suggested that an increase of impeller speed could increase the granule breakage, which eventually promotes the continuously exchange of primary particles between the granules. Moreover, granule breakage with a continuous exchange of particles can overcome the poor homogeneity of granules, which often occurs in high shear granulation. Granules that remain intact during the granulation process may undergo layering resulting in inhomogeneous granules (Van Den Dries et al., 2003a). (Rachel M. Smith et al., 2010) studied the effect of impeller speed, and found greater granule breakage at 750 rpm than 500 rpm.

The effect of impeller shape has been studied by (Schaefer et al., 1993). Curved impeller blades give rise to smooth granules of spherical shape while planar impeller blades give irregular shapes. Moreover, studies by (Rachel M. Smith et al., 2010) have suggested that changing the impeller shape from a bevelled blade to a flat plate could reduce the amount of granule breakage.

The viscosity of the binder is important in understanding the granulation mechanisms and the strength of the resulting granules. (Keningley et al., 1997) found a relationship between a minimum viscosity silicone oil and the size of non-porous calcium carbonate particles in order to produce robust granules (Table 2.3). In order to produce successfully formed granules, a minimum viscosity of 0.01 Pa s was necessary for mean particle sizes of 8 μm , 0.1 Pa s for particles with a mean size of 50 to 80 μm and 1 Pa s for particles with a mean particle size of 230 μm . From the results, it shows that the use of high viscosity of silicone oil is linearly proportional with the size of mean particle size.

Table 2.3. Relationship between minimum viscosity of silicone oil and mean particle size of non-porous calcium carbonate particles to produce robust granules

Minimum viscosity (Pa.s)	Mean particle sizes (μm)
0.01	8
0.1	50 to 80
1	230

In addition, previous studies found that increasing the viscosity of silicone oil above a certain critical value leads to the opposite effect, i.e. increasing viscosity increased granule breakage (Mills et al., 2000). They found that the viscosity of silicone oil could affect the granulation mechanisms. The use of lower viscosity of silicone oil might lead to the layering growth mechanism in granulation. However, coalescence was the predominant mechanism at higher viscosity of silicone oil especially when smaller and spherical particles were used.

An experimental study in laboratory scale high shear mixers by (Chitu et al., 2011a) has investigated the effect of liquid binder properties on torque curves, granule growth kinetics, wet mass consistency and dry granule strength. The binders used were aqueous solutions of polyvinylpyrrolidone (PVP) and hydroxypropylmethylcellulose (HPMC) at viscosities of 0.5 %, 1 %, 3 % and 13 % (wt/wt). The strength of the granules was evaluated through uniaxial compression tests using a Texture Analyser mechanical testing machine. From their study, the use of low viscosity binders resulted in improved wet mass

consistency and produced high dry granule strength. On the other hand, the use of high viscosity binders also produced high wet mass consistency but lower dry granule strength.

The granulation parameters, e.g. process and formulation parameters that are commonly studied in granulation processes are listed in Table 2.4. The selection of the parameters for the current research is described at the end of this chapter in Section 2.8.

Table 2.4. Summary of granulation parameters studied

No	Granulation parameters	References
1	Binder viscosity	(Cavinato et al., 2010) (B. M. J. Tan et al., 2014) (Johansen & Schafer, 2001) (J. B. Wade et al., 2015) (Schæfer et al., 2004) (Realpe & Velázquez, 2008) (L. X. Liu et al., 2009)
2	Binder surface tension	(Cavinato et al., 2010) (L. X. Liu et al., 2009)
3	Binder content e.g. liquid to solid (L/S) ratio	(Chitu et al., 2011a) (Franceschinis et al., 2014) (Bouwman et al., 2006a) (L. X. Liu et al., 2009) (Rachel M. Smith et al., 2010) (M. X. L. Tan & Hapgood, 2012) (Realpe & Velázquez, 2008) (Mangwandi et al., 2015)
4	Binder addition rate	(B. M. J. Tan et al., 2014) (Bouwman et al., 2006a)
5	Binder addition method e.g. pouring, spraying and melting	(Osborne et al., 2011) (B. M. J. Tan et al., 2014)
6	Contact angle between binder and primary particle (°)	(Cavinato et al., 2010) (Mangwandi et al., 2015)
7	Primary particle size and shape of powder	(Johansen & Schafer, 2001) (L. X. Liu et al., 2009) (M. X. L. Tan & Hapgood, 2012) (Schæfer et al., 2004) (MacKaplow et al., 2000) (Realpe & Velázquez, 2008)
8	Granulator capacity e.g. different mass fill and bowl size	(Cavinato et al., 2013) (Chitu et al., 2011a) (Cheng et al., 2012)

9	Granulation time	(Cavinato et al., 2010) (Jiang et al., 2015) (Bouwman et al., 2006a) (Y. Liu et al., 2014) (Saito et al., 2011)
10	Impeller tip speed (m/s) and impeller rotational speed (rpm)	(Cavinato et al., 2010) (Chitu et al., 2011a) (Franceschinis et al., 2014) (Knight et al., 2001) (Bouwman et al., 2006a) (Rachel M. Smith et al., 2010) (Saito et al., 2011) (M. X. L. Tan & Hapgood, 2012) (Van Den Dries et al., 2003a) (J. B. Wade et al., 2015)
11	Impeller shape and design	(Knight et al., 2001) (Smith Liu, L.A.X., Litster, J.D., 2010) (Schaefer et al., 1993)
12	Impeller clearance e.g. distance from bottom wall of the bowl	(Cavinato et al., 2013)
13	Chopper size	(Chitu et al., 2011a)
14	Chopper speed	(Chitu et al., 2011a) (Bouwman et al., 2006a)

2.3 Shear cell testers

In order to develop a suitable method or equipment for studying the pellet deformation under shear condition, a review of shear cell testers is necessary and will be presented in this section. The shear flow behaviour and shear properties of a material, e.g. failure of a granular material due to shear rates, can be studied by using several shear cell testers; translational shear cell, annular shear cell and rheometer shear cell (Figure 2.6). The shear cell testers enable measurement of the flow properties of the bulk powder under the application of relatively large consolidation stresses. The bed particles are uniformly loaded under shear cell testing, which make it easier to determine the internal stresses within the bed.

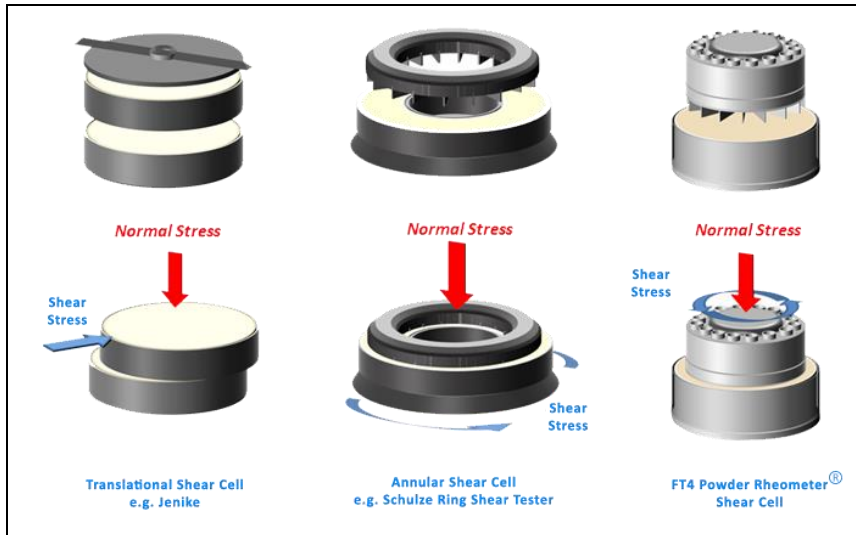


Figure 2.6 Types of shear cell testers

The translational shear cell type such as Jenike shear cell device has been extensively used for measuring the shear properties of the material. It requires the cell lid to apply the normal stress and lift to shear to produce the shear stress. Some of the drawbacks of this apparatus and technique are: 1) It requires the sample particles to be in size less than 3 mm, which results in limited shear displacement; 2) It requires preparation of the sample prior to the shear consolidation and 3) It requires major principal stresses of less than 1 psi or 6 kPa. As a result of this relatively low cell normal load, the lifting of the cell lid would cause the non-uniformity of the stress distribution.

The annular shear cell type has been widely used to study the fundamental flow of granular material and is able to estimate the yield strength of the flowing material in a confined system. A minimum shear stress is required to initiate the shear flow of the granular material. The granular material dilates during shearing, dependant on the magnitude of the normal stress subjected to the material. The more stress exerted on the particles, the denser the particles are compacted. As a result, it is harder for them to slide over one another. The particles would fail whenever the failure zone has occurred (Clyens & Johnson, 1977).

In an annular shear cell, the particles are sheared by a stationary upper platen and a rotating lower platen, with stationary inner and outer cylindrical walls (Schwedde, 2003; X. Wang et al., 2012b). The advantages of annular shear cell are: 1) The sample preparation is easier; 2) It gives unlimited shear displacement; 3) It gives a uniform load distribution and ensures a uniform shear rate is produced and 4) The shear flow can be in quasi-static, intermediate or rapid flow behaviour.

According to (X. Wang et al., 2012b), most of the previous works on the annular shear cell are mainly based on experimental approaches and have focused on attrition behaviour, external stress profile and transport property measurements. Moreover, the annular shear cell can only provide macroscopic scale information of the particle flow. The particle scale information is difficult to obtain through physical experiments. For this reason, it cannot produce much particle scale information which is useful to give a better understanding of the working principle of the shear cell devices.

On the other hand, the Couette cell has similar configuration to the annular shear cell except for its rotating cylindrical walls and stationary platens (X. Wang et al., 2012b). The rheometer shear cell such as the FT4 Powder Rheometer has a similar mechanism as the annular shear cell, except that the top part of the rheometer is rotated rather than the bottom part. Table 2.5 lists some of the experimental studies in annular shear cell and Couette cell. The types of measurements from these two shear cell testers were considered for current study.

Table 2.5 Experimental studies for annular shear cell and Couette cell

No.	Type of shear cell testers	Types of measurements	References
1	Annular shear cell	Attrition, shear stress	(Paramanathan & Bridgwater, 1983a) (Paramanathan & Bridgwater, 1983b) (Neil & Bridgwater, 1994) (Neil & Bridgwater, 1999) (C. Hare & Ghadiri, 2015) (Hanes & Inman, 1985) (Savage & Sayed, 1984) (Ghadiri et al., 2000a) (Bridgwater et al., 2003) (Zemin Ning & Ghadiri, 2006) (Orlando & Shen, 2012)
		Granular shear flows	(C. Liao et al., 2017a) (C. C. Liao et al., 2015) (Ji et al., 2009) (S.-S. Hsiau & Shieh, 1999)
		Stresses and transport phenomena	(S.-S. Hsiau & Shieh, 1999) (S. S. Hsiau & Yang, 2002) (S.-S. Hsiau & Yang, 2005)
2	Couette cell	Granular shear flows	(Tardos et al., 2003) (S. S. Hsiau et al., 2005)

2.3.1 Stability condition of shear flow in an annular shear cell

(X. Wang et al., 2012a) have simulated sheared granular material in an annular shear cell. Based on their study, once the velocities and normal pressure of the platens reached the pre-set values, the bulk properties of the system, e.g. the system volume fraction, were closely monitored. The variation in position of upper platen in z-direction over time was evaluated to determine the steady-state in the system (Figure 2.7). They assumed the system was steady when these properties only showed minor fluctuations around constant values and were independent of time.

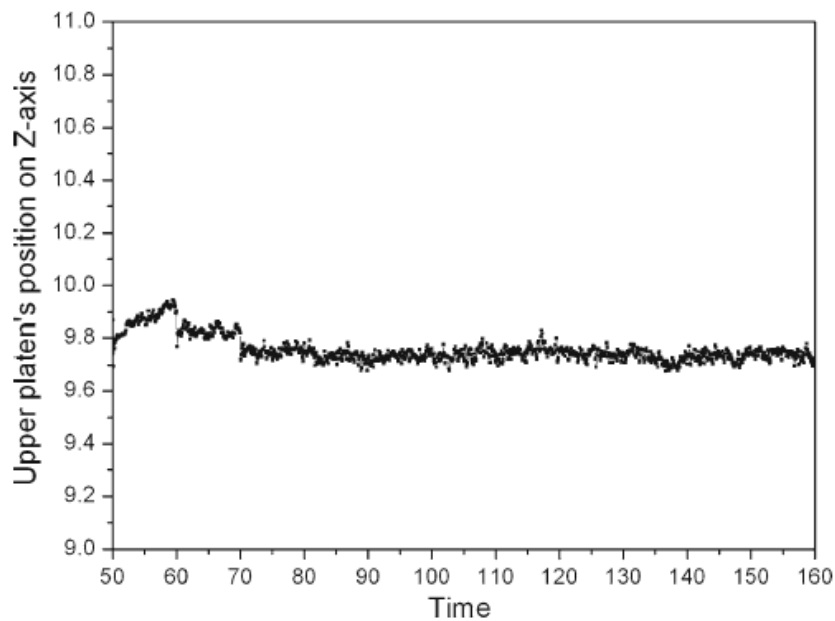


Figure 2.7 Variation position of upper platen in z-direction over time for steady-state condition

2.4 Types of deformation

The high shear flow contributes to the high rate of deformation (high shear rate), which is responsible for the plastic deformation of the materials and indicates a large permanent deformation of the material. According to (Rachel M. Smith & Litster, 2012), the material enables to fail in plastic deformation by producing high shear rate. On the other hand, materials that fail with little plastic deformation are said to be brittle. (Rachel M. Smith & Litster, 2012) have categorized the deformation or complete breakage into two types: brittle and plastic deformation. Figure 2.8 shows an example of brittle and plastic deformation observed clearly from the compression test based on (Rachel M. Smith & Litster, 2012) study.

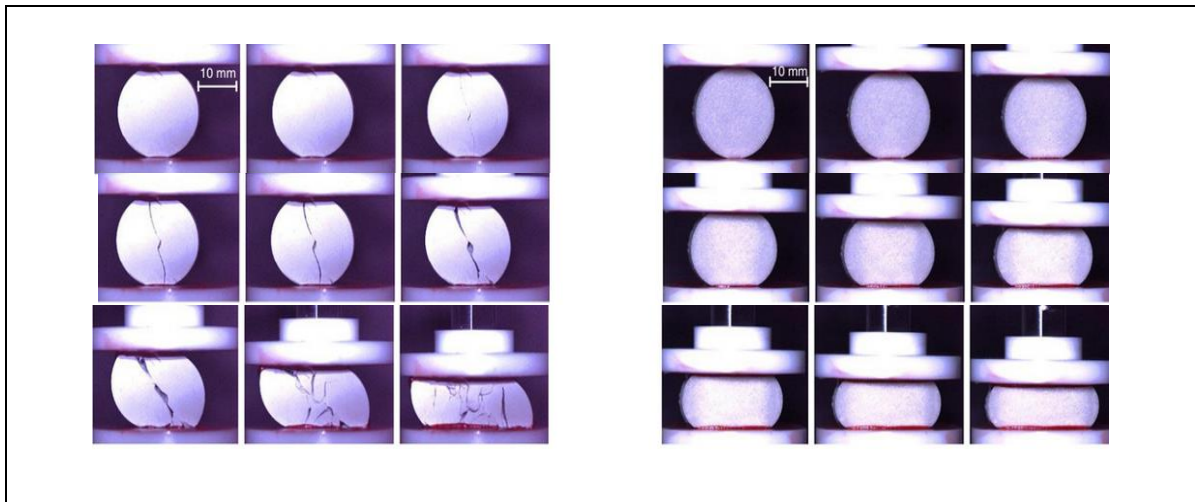


Figure 2.8 Two types of deformation: brittle (left) and plastic (right)

Both brittle and plastic deformations can be influenced by the types of materials for formulations. In a compression test, a ductile material yields and produces large plastic deformation when it experiences stresses beyond the elastic limit. Whereas, a brittle material results in failure with little plastic deformation.

2.5 Stresses of 3D material

As shown in Figure 2.9, the stress state of a 3D material can be represented by normal stress components and the shear stress components. The normal stress components are σ_{xx} , σ_{yy} and σ_{zz} . The shear stress components are σ_{xy} , σ_{yx} , σ_{xz} , σ_{zx} , σ_{zy} and σ_{yz} . These normal and shear stress components can be defined by the stress tensor, σ_{ij} , and relative to a chosen coordinate system by a matrix as shown in Equation 2.8.

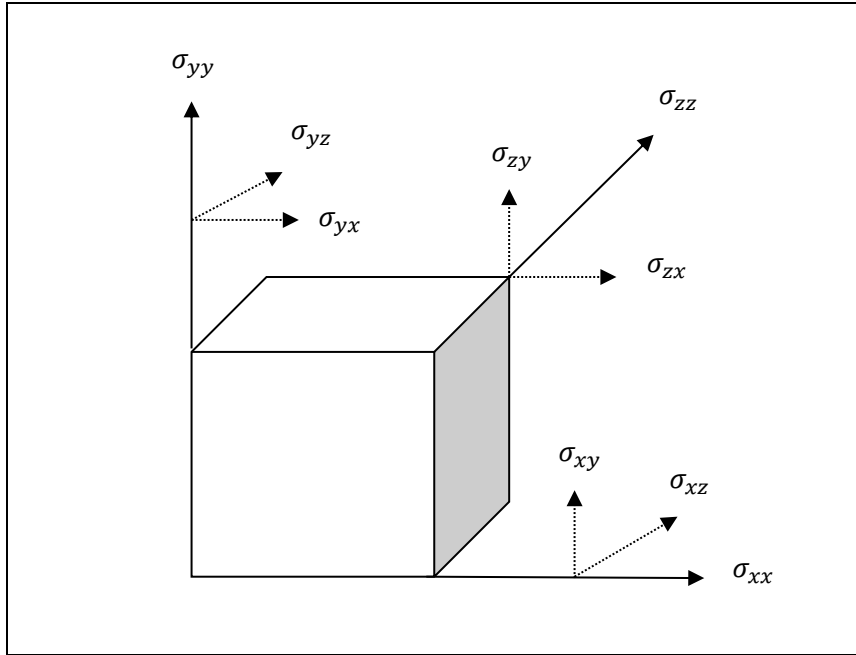


Figure 2.9 Stress state of a 3D material

$$\sigma_{ij} = \begin{pmatrix} \sigma_{xx} & \sigma_{xy} & \sigma_{xz} \\ \sigma_{yx} & \sigma_{yy} & \sigma_{yz} \\ \sigma_{zx} & \sigma_{zy} & \sigma_{zz} \end{pmatrix}$$

Equation 2.8

From the stress tensor, σ_{ij} , it can be further categorised into two parts; hydrostatic stress tensor σ_h and deviator stress tensor s_{ij} (Chen & Saleeb, 1994). The hydrostatic stress tensor σ_h can be defined as one-third of the trace of the stress tensor. The hydrostatic stress tensor results in volume change without distortion. It is associated with the dilatational (reduction or expansion) effects.

On the contrary, the deviator stress tensor s_{ij} , is the stress that is not equal from all directions and deviates from the mean stress. It is the difference between the state of stress and the hydrostatic stress tensor. It produces a distortion effect without a change in volume. As a result, distortion of the material (change in shape) is observed. The relationship between the stress tensor, hydrostatic stress tensor and deviator stress tensor is given in Figure 2.10 and Equation 2.9. The schematic diagram is given for understanding purposes, and does not represent the actual volume.

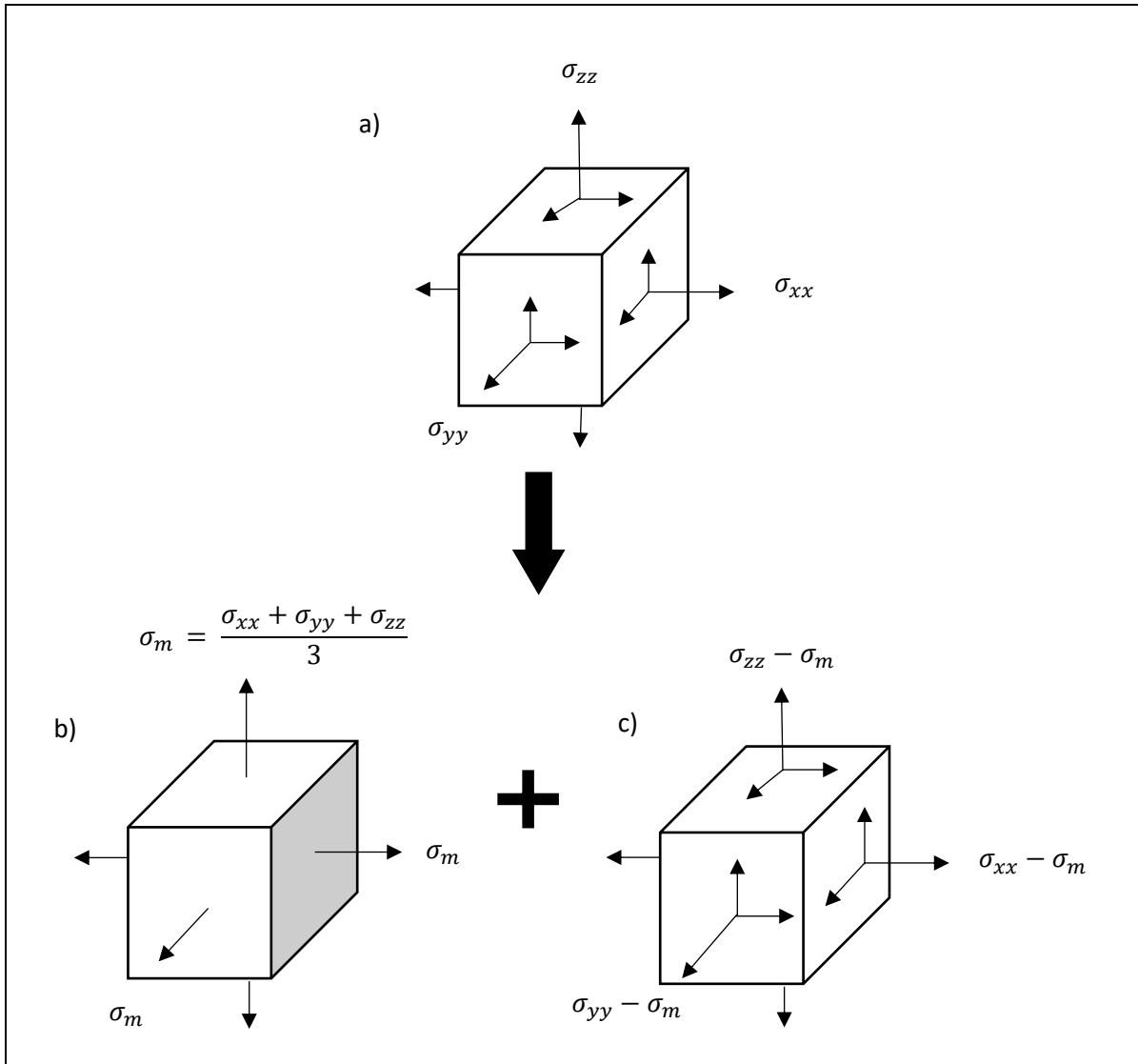


Figure 2.10 a) Components of stress tensor are: b) hydrostatic stress tensor and c) deviator stress tensor

$$\sigma_{ij} = s_{ij} + \sigma_h \quad \text{Equation 2.9}$$

The hydrostatic stress tensor, σ_h has the elements of mean stress, σ_m and the Kronecker delta δ_{ij} (Equations 2.10 to 2.13)

$$\sigma_h = \sigma_m \delta_{ij} \quad \text{Equation 2.10}$$

$$\delta_{ij} = \begin{bmatrix} 1 & 0 & 0 \\ 0 & 1 & 0 \\ 0 & 0 & 1 \end{bmatrix} \quad \text{Equation 2.11}$$

$$\delta_{ij} = 0 \text{ if } i \neq j \quad \text{Equation 2.12}$$

$$\delta_{ij} = 1 \text{ if } i = j \quad \text{Equation 2.13}$$

Where

σ_{ij} =	Stress tensor	(N/m ²) or (Pa)
s_{ij} =	Deviator stress tensor	(N/m ²) or (Pa)
σ_h =	Hydrostatic stress tensor	(N/m ²) or (Pa)
σ_m =	Mean stress	(N/m ²) or (Pa)
δ_{ij} =	Kronecker delta	(-)

The mean stress, σ_m (Equation 2.14) gives an equal amount of stresses in the three normal directions.

$$\sigma_m = \frac{\sigma_{xx} + \sigma_{yy} + \sigma_{zz}}{3} \quad \text{Equation 2.14}$$

The deviator stress tensor, s_{ij} is defined by the subtracting the hydrostatic stress tensor from the state of stress (Equations 2.15 and 2.16).

$$s_{ij} = \sigma_{ij} - \sigma_h \quad \text{Equation 2.15}$$

$$s_{ij} = \sigma_{ij} - \sigma_m \delta_{ij} \quad \text{Equation 2.16}$$

2.5.1 Determining the principal stresses

It is useful to describe the model of a material independent from the coordinate system relative to the material. By definition, regardless of the rotation of the model of the material, it should be independent of the coordinate system selected. The relationship between the stress state of a material, original coordinate axes, principal stresses of stress tensor, σ_1 , σ_2 and σ_3 and the principal stress coordinate axes is shown in Figure 2.11.

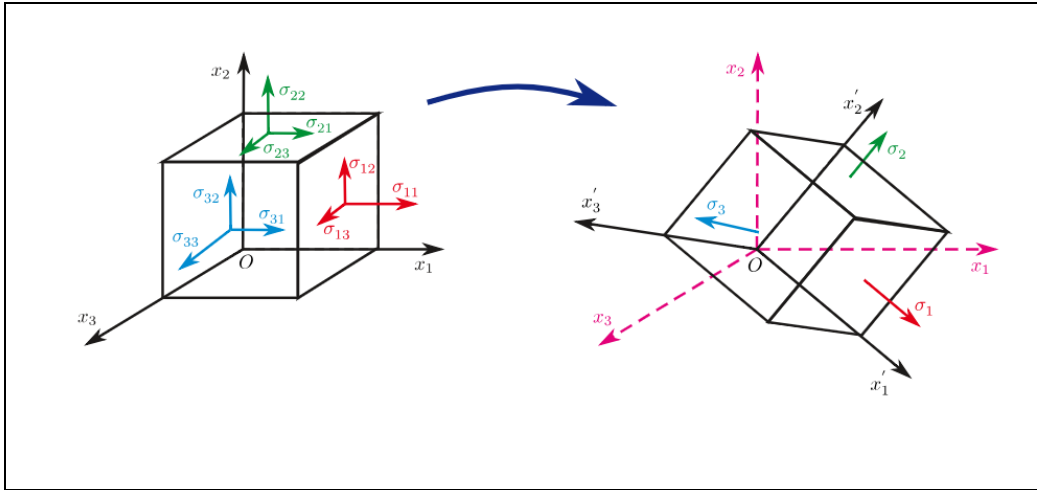


Figure 2.11 The state of stress of a material with original coordinate axes (left) and principal stress coordinate axes (right)

On the left side in Figure 2.11, the model of a material (in terms of stress tensor) is relative to the selected coordinate axes (x_1 , x_2 and x_3 direction). By transforming the stress state of the material in terms of principal stresses of stress tensor, σ_1 , σ_2 and σ_3 (right side in Figure 2.11), the model material is independent to the direction of the original coordinate system. Instead, it follows the direction of the new coordinate system known as principal stress coordinate axes, x'_1 , x'_2 and x'_3 . The model material and the stress state of the material is expressed in terms of principal stresses of stress tensor.

The above transformation of stress state to principal stresses of stress tensor requires solving the polynomial equation (Equation 2.17) (Chen & Saleeb, 1994). In order to obtain the values of σ from the polynomial equation, a set of three coefficients I_1 , I_2 and I_3 must be computed. They are three invariants of stress tensor, known as first invariant of stress tensor I_1 , second invariant of stress tensor I_2 and third invariant of stress tensor I_3 . The obtained three roots, σ_1 , σ_2 and σ_3 , are the three possible magnitudes of normal stress with zero shear stress, known as principal stresses of stress tensor.

$$\sigma^3 - I_1\sigma^2 + I_2\sigma - I_3 \quad \text{Equation 2.17}$$

Where

I_1 =	First invariant of stress tensor	(-)
I_2 =	Second invariant of stress tensor	(-)
I_3 =	Third invariant of stress tensor	(-)
σ =	Three values of principal stresses of stress tensor	(N/m ²) or (Pa)

2.5.1.1 Invariants of stress tensor

The three invariants of the stress tensor, I_1 , I_2 and I_3 are defined as follows. The first invariant of stress tensor, I_1 is the sum of the diagonal terms of σ_{ij} (Equation 2.18).

$$I_1 = \sigma_{xx} + \sigma_{yy} + \sigma_{zz} \quad \text{Equation 2.18}$$

The second invariant of stress tensor, I_2 is the sum of cofactors of diagonal terms of σ_{ij} (Equations 2.19 to 2.20).

$$I_2 = \begin{vmatrix} \sigma_{xx} & \sigma_{xy} \\ \sigma_{yx} & \sigma_{yy} \end{vmatrix} + \begin{vmatrix} \sigma_{yy} & \sigma_{yz} \\ \sigma_{zy} & \sigma_{zz} \end{vmatrix} + \begin{vmatrix} \sigma_{xx} & \sigma_{xz} \\ \sigma_{zx} & \sigma_{zz} \end{vmatrix} \quad \text{Equation 2.19}$$

For the case of simple shear, two possibilities can be obtained. The stresses are equal in magnitude but in different directions. These shear stresses follow $\sigma_{xy} = \sigma_{yx}$, $\sigma_{xz} = \sigma_{zx}$ and $\sigma_{yz} = \sigma_{zy}$. I_2 can be calculated using Equation 2.20.

$$I_2 = \sigma_{xx}\sigma_{yy} + \sigma_{yy}\sigma_{zz} + \sigma_{xx}\sigma_{zz} - \sigma_{xy}^2 - \sigma_{yz}^2 - \sigma_{zx}^2 \quad \text{Equation 2.20}$$

Or else, the stresses are different both in magnitudes and directions. These shear stresses follow $\sigma_{xy} \neq \sigma_{yx}$, $\sigma_{xz} \neq \sigma_{zx}$ and $\sigma_{yz} \neq \sigma_{zy}$. In this case, I_2 can be calculated using Equation 2.21.

$$I_2 = \sigma_{xx}\sigma_{yy} + \sigma_{yy}\sigma_{zz} + \sigma_{xx}\sigma_{zz} - \sigma_{xy}\sigma_{yx} - \sigma_{yz}\sigma_{zy} - \sigma_{zx}\sigma_{xz} \quad \text{Equation 2.21}$$

The third invariant of stress tensor, I_3 is the determinant of σ_{ij} , $I_3 = \det(\sigma_{ij})$ (Equations 2.22 to 2.23).

$$I_3 = \begin{vmatrix} \sigma_{xx} & \sigma_{xy} & \sigma_{xz} \\ \sigma_{yx} & \sigma_{yy} & \sigma_{yz} \\ \sigma_{zx} & \sigma_{zy} & \sigma_{zz} \end{vmatrix} \quad \text{Equation 2.22}$$

$$I_3 = \sigma_{xx} \begin{vmatrix} \sigma_{yy} & \sigma_{yz} \\ \sigma_{zy} & \sigma_{zz} \end{vmatrix} - \sigma_{xy} \begin{vmatrix} \sigma_{yx} & \sigma_{yz} \\ \sigma_{zx} & \sigma_{zz} \end{vmatrix} + \sigma_{xz} \begin{vmatrix} \sigma_{yx} & \sigma_{yy} \\ \sigma_{zx} & \sigma_{zy} \end{vmatrix} \quad \text{Equation 2.23}$$

For the case of simple shear, two possibilities can be obtained. The shear stresses follow $\sigma_{xy} = \sigma_{yx}$, $\sigma_{xz} = \sigma_{zx}$ and $\sigma_{yz} = \sigma_{zy}$. I_3 can be calculated using Equation 2.24.

$$I_3 = \sigma_{xx} \sigma_{yy} \sigma_{zz} + 2\sigma_{xy} \sigma_{yz} \sigma_{zx} - \sigma_{xy}^2 \sigma_{zz} - \sigma_{yz}^2 \sigma_{xx} - \sigma_{zx}^2 \sigma_{yy} \quad \text{Equation 2.24}$$

Or else, the shear stresses follow $\sigma_{xy} \neq \sigma_{yx}$, $\sigma_{xz} \neq \sigma_{zx}$ and $\sigma_{yz} \neq \sigma_{zy}$. These stresses are different both in magnitudes and directions. I_3 can be calculated using Equation 2.25.

$$I_3 = \sigma_{xx} \sigma_{yy} \sigma_{zz} + \sigma_{xy} \sigma_{yz} \sigma_{zx} + \sigma_{xz} \sigma_{yx} \sigma_{zy} - \sigma_{xx} \sigma_{yz} \sigma_{zy} - \sigma_{xy} \sigma_{yx} \sigma_{zz} - \sigma_{xz} \sigma_{zx} \sigma_{yy} \quad \text{Equation 2.25}$$

By solving the polynomial equation (refer to Equation 2.17), the three values of σ can be obtained. However, only the real values of principal stresses of stress tensor, σ_1 , σ_2 and σ_3 were chosen for further analysis. They are σ_1 = maximum principal stress, σ_2 = intermediate principal stress and σ_3 = minimum principal stress.

2.5.2 Deviator stress tensor

The deviator stress tensor described earlier is the component of stress tensor that responsible for the distortion of the material, e.g. changing the shape of the material. In this study, particular attention has been given to the deviator stress tensor (Equation 2.26) as deformation was evaluated in term of the shape changing. It can be represented by 3x3 matrix form (Equations 2.27 to 2.29).

$$s_{ij} = \sigma_{ij} - \sigma_m \delta_{ij} \quad \text{Equation 2.26}$$

$$s_{ij} = \begin{bmatrix} \sigma_{xx} & \sigma_{xy} & \sigma_{xz} \\ \sigma_{yx} & \sigma_{yy} & \sigma_{yz} \\ \sigma_{zx} & \sigma_{zy} & \sigma_{zz} \end{bmatrix} - \sigma_m \begin{bmatrix} 1 & 0 & 0 \\ 0 & 1 & 0 \\ 0 & 0 & 1 \end{bmatrix} \quad \text{Equation 2.27}$$

By substituting the Kronecker delta, the deviator stress tensor is given in Equations 2.28 and 2.29.

$$s_{ij} = \begin{bmatrix} (\sigma_{xx} - \sigma_m) & \sigma_{xy} & \sigma_{xz} \\ \sigma_{yx} & (\sigma_{yy} - \sigma_m) & \sigma_{yz} \\ \sigma_{zx} & \sigma_{zy} & (\sigma_{zz} - \sigma_m) \end{bmatrix} \quad \text{Equation 2.28}$$

$$s_{ij} = \begin{bmatrix} s_{11} & s_{12} & s_{13} \\ s_{21} & s_{22} & s_{23} \\ s_{31} & s_{32} & s_{33} \end{bmatrix} \quad \text{Equation 2.29}$$

2.5.2.1 Invariants of deviator stress tensor

The coefficients of J_1 , J_2 and J_3 , are the invariants of deviator stress tensor, which are derived from the deviator stress tensor. A similar derivation is followed as used for invariants of stress tensor (refer to section 2.5.1.1). They are known as first invariant of deviator stress tensor, J_1 , second invariant of deviator stress tensor J_2 and third invariant of deviator stress tensor J_3 . For computing the three invariants of deviator stress tensor, the polynomial equation (Equation 2.30) must be solved. The three roots, s_1 , s_2 and s_3 obtained are the three principal stresses of deviator stress tensor. For the case of computing the three invariants of deviator stress tensor, the minus sign convention (-) must be taking into consideration.

$$s^3 - J_1 s^2 - J_2 s - J_3 \quad \text{Equation 2.30}$$

Where

J_1 =	First invariant of deviator stress tensor	(-)
J_2 =	Second invariant of deviator stress tensor	(-)
J_3 =	Third invariant of deviator stress tensor	(-)
s =	Principal stresses for deviator stress tensor	(Pa)

Among the three invariants of the deviator stress tensor, the second invariant of deviator stress tensor, J_2 plays an important role for describing the failure criteria of a material. Due to this reason, the second invariant of deviator stress tensor J_2 has been given particularly attention in this study. The second invariant of deviator stress, J_2 is computed by summing the cofactors of diagonal terms. It can be expressed in different forms such as in terms of 1) components of stress tensor, σ_{ij} , 2) principal stresses of stress tensor, σ_1 , σ_2 and σ_3 , 3) components of deviator stress tensor, s_{ij} and 4) principal stresses of deviator stress tensor, s_1 , s_2 and s_3 .

For this current work, the derivation of the second invariant of deviator stress, J_2 has been limited to two forms only: in terms of components of stress tensor, σ_{ij} and principal stresses of stress tensor, σ_1 , σ_2 and σ_3 . The other two forms to derive the second invariant of deviator stress, J_2 can be found in (Chen & Saleeb, 1994). The derivation of second invariant of deviator stress tensor, J_2 (in terms of components of stress tensor, σ_{ij}) can be calculated using Equations 2.31 to 2.35.

$$s_{ij} = \sigma_{ij} - \sigma_m \delta_{ij} \quad \text{Equation 2.31}$$

$$s_{ij} = \begin{bmatrix} \sigma_{xx} & \sigma_{xy} & \sigma_{xz} \\ \sigma_{yx} & \sigma_{yy} & \sigma_{yz} \\ \sigma_{zx} & \sigma_{zy} & \sigma_{zz} \end{bmatrix} - \sigma_m \begin{bmatrix} 1 & 0 & 0 \\ 0 & 1 & 0 \\ 0 & 0 & 1 \end{bmatrix} \quad \text{Equation 2.32}$$

$$s_{ij} = \begin{bmatrix} (\sigma_{xx} - \sigma_m) & \sigma_{xy} & \sigma_{xz} \\ \sigma_{yx} & (\sigma_{yy} - \sigma_m) & \sigma_{yz} \\ \sigma_{zx} & \sigma_{zy} & (\sigma_{zz} - \sigma_m) \end{bmatrix} \quad \text{Equation 2.33}$$

$$J_2 = \begin{vmatrix} (\sigma_{xx} - \sigma_m) & \sigma_{xy} \\ \sigma_{yx} & (\sigma_{yy} - \sigma_m) \end{vmatrix} + \begin{vmatrix} (\sigma_{yy} - \sigma_m) & \sigma_{yz} \\ \sigma_{zy} & (\sigma_{zz} - \sigma_m) \end{vmatrix} \\ + \begin{vmatrix} (\sigma_{xx} - \sigma_m) & \sigma_{xz} \\ \sigma_{zx} & (\sigma_{zz} - \sigma_m) \end{vmatrix} \quad \text{Equation 2.34}$$

$$J_2 = (\sigma_{xx} - \sigma_m)(\sigma_{yy} - \sigma_m) + (\sigma_{yy} - \sigma_m)(\sigma_{zz} - \sigma_m) \\ + (\sigma_{xx} - \sigma_m)(\sigma_{zz} - \sigma_m) - \sigma_{xy}\sigma_{yx} - \sigma_{yz}\sigma_{zy} - \sigma_{zx}\sigma_{xz} \quad \text{Equation 2.35}$$

For the case of non-simple shear, the components of shear stresses remain unchanged. It follows that $\sigma_{xy} \neq \sigma_{yx}$, $\sigma_{xz} \neq \sigma_{zx}$ and $\sigma_{yz} \neq \sigma_{zy}$. These stresses are different both in magnitudes and directions. By solving the Equation 2.35 and considering the minus sign convention (-) (see Equation 2.30), the second invariant of deviator stress tensor, J_2 (in terms of components of stress tensor, σ_{ij}) can be calculated using Equations 2.36 and 2.37.

$$J_2 = \frac{1}{3} (\sigma_{xx}^2 + \sigma_{yy}^2 + \sigma_{zz}^2 + \sigma_{xx}\sigma_{yy} + \sigma_{yy}\sigma_{zz} + \sigma_{xx}\sigma_{zz}) + \sigma_{xy}\sigma_{yx} + \sigma_{yz}\sigma_{zy} \\ + \sigma_{zx}\sigma_{xz} \quad \text{Equation 2.36}$$

$$J_2 = \frac{1}{6} [(\sigma_{xx} + \sigma_{yy})^2 + (\sigma_{yy} + \sigma_{zz})^2 + (\sigma_{zz} + \sigma_{xx})^2] + \sigma_{xy}\sigma_{yx} + \sigma_{yz}\sigma_{zy} \\ + \sigma_{zx}\sigma_{xz} \quad \text{Equation 2.37}$$

The second invariant of deviator stress tensor, J_2 (in terms of principal stresses of stress tensor, σ_1 , σ_2 and σ_3) can be calculated using Equations 2.38 to 2.44.

$$s_{ij} = \sigma_{ij} - \sigma_m \delta_{ij} \quad \text{Equation 2.38}$$

$$s_{ij} = \begin{bmatrix} \sigma_1 & 0 & 0 \\ 0 & \sigma_2 & 0 \\ 0 & 0 & \sigma_3 \end{bmatrix} - \sigma_m \begin{bmatrix} 1 & 0 & 0 \\ 0 & 1 & 0 \\ 0 & 0 & 1 \end{bmatrix} \quad \text{Equation 2.39}$$

$$s_{ij} = \begin{bmatrix} (\sigma_1 - \sigma_m) & 0 & 0 \\ 0 & (\sigma_2 - \sigma_m) & 0 \\ 0 & 0 & (\sigma_3 - \sigma_m) \end{bmatrix} \quad \text{Equation 2.40}$$

$$J_2 = \begin{vmatrix} (\sigma_1 - \sigma_m) & 0 \\ 0 & (\sigma_2 - \sigma_m) \end{vmatrix} + \begin{vmatrix} (\sigma_2 - \sigma_m) & 0 \\ 0 & (\sigma_3 - \sigma_m) \end{vmatrix} + \begin{vmatrix} (\sigma_1 - \sigma_m) & 0 \\ 0 & (\sigma_3 - \sigma_m) \end{vmatrix} \quad \text{Equation 2.41}$$

$$J_2 = (\sigma_1 - \sigma_m)(\sigma_2 - \sigma_m) + (\sigma_2 - \sigma_m)(\sigma_3 - \sigma_m) + (\sigma_1 - \sigma_m)(\sigma_3 - \sigma_m) \quad \text{Equation 2.42}$$

By solving the above Equation 2.42 and considering the minus sign convention (-) (see Equation 2.30), the second invariant of deviator stress tensor, J_2 (in terms of principal stresses of stress tensor) is shown in Equation 2.43.

$$J_2 = \frac{1}{3}(\sigma_1^2 + \sigma_2^2 + \sigma_3^2 + \sigma_1\sigma_2 + \sigma_2\sigma_3 + \sigma_1\sigma_3) \quad \text{Equation 2.43}$$

It can also be expressed by factoring the second invariant of deviator stress tensor, J_2 (Equation 2.44).

$$J_2 = \frac{1}{6}[(\sigma_1 + \sigma_2)^2 + (\sigma_2 + \sigma_3)^2 + (\sigma_3 + \sigma_1)^2] \quad \text{Equation 2.44}$$

2.5.3 Deviatoric stress

The deviatoric stress, σ_D is often expressed based on the relationship given in Equations 2.45 to 2.48. The equations suggest that yielding of a material begins when the second invariant of deviator stress tensor, J_2 reaches a critical value, k , known as the yield stress of the material in pure shear. By substituting the value of J_2 , the deviatoric stress, σ_D can then be expressed in terms of components of stress tensor, σ_{ij} and principal stresses of stress tensor, σ_1 , σ_2 and σ_3 (Equations 2.49 to 2.52).

$$J_2 - k^2 = 0 \quad \text{Equation 2.45}$$

$$J_2 = k^2 \quad \text{Equation 2.46}$$

$$k = \sqrt{J_2} \quad \text{Equation 2.47}$$

$$\sigma_D = \sqrt{J_2} \quad \text{Equation 2.48}$$

Deviatoric stress, σ_D is expressed in terms of components of stress tensor, σ_{ij} (Equations 2.49 and 2.50)

$$\sigma_D = \sqrt{\frac{1}{3} (\sigma_{xx}^2 + \sigma_{yy}^2 + \sigma_{zz}^2 + \sigma_{xx}\sigma_{yy} + \sigma_{yy}\sigma_{zz} + \sigma_{xx}\sigma_{zz}) + \sigma_{xy}\sigma_{yx} + \sigma_{yz}\sigma_{zy} + \sigma_{zx}\sigma_{xz}} \quad \text{Equation 2.49}$$

$$\sigma_D = \sqrt{\frac{1}{6} [(\sigma_{xx} + \sigma_{yy})^2 + (\sigma_{yy} + \sigma_{zz})^2 + (\sigma_{zz} + \sigma_{xx})^2] + \sigma_{xy}\sigma_{yx} + \sigma_{yz}\sigma_{zy} + \sigma_{zx}\sigma_{xz}} \quad \text{Equation 2.50}$$

Deviatoric stress, σ_D is expressed in terms of principal stresses of stress tensor, σ_1 , σ_2 and σ_3 (Equations 2.51 and 2.52).

$$\sigma_D = \sqrt{\frac{1}{3} (\sigma_1^2 + \sigma_2^2 + \sigma_3^2 + \sigma_1\sigma_2 + \sigma_2\sigma_3 + \sigma_1\sigma_3)} \quad \text{Equation 2.51}$$

$$\sigma_D = \sqrt{\frac{1}{6} [(\sigma_1 + \sigma_2)^2 + (\sigma_2 + \sigma_3)^2 + (\sigma_3 + \sigma_1)^2]} \quad \text{Equation 2.52}$$

Where

J_2 =	Second invariant of deviator stress tensor	(N/m ²) or (Pa)
σ_D =	Deviatoric stress	(N/m ²) or (Pa)
k =	Yield stress of the material in pure shear	(N/m ²) or (Pa)
σ_1 =	Maximum principal stress	(N/m ²) or (Pa)
σ_2 =	Intermediate principal stress	(N/m ²) or (Pa)
σ_3 =	Minimum principal stress	(N/m ²) or (Pa)

It has been reported that the aforementioned expression of deviatoric stress has been used by previous researchers to describe the deformation of a material. For instance, (Luding, 2008) has proposed a deviatoric stress equation based on the normal component of stresses in the system. They are known as maximum, intermediate and minimum stresses, σ_{max} , σ_0 and σ_{min} (Equation 2.53).

$$\sigma_D = \frac{\sqrt{(\sigma_{max} - \sigma_{min})^2 + (\sigma_{max} - \sigma_0)^2 + (\sigma_0 - \sigma_{min})^2}}{\sqrt{6}} \quad \text{Equation 2.53}$$

Where

σ_D =	Deviatoric stress	(N/m ²) or (Pa)
σ_{max} =	Maximum principal stress	(N/m ²) or (Pa)
σ_0 =	Intermediate principal stress	(N/m ²) or (Pa)
σ_{min} =	Minimum principal stress	(N/m ²) or (Pa)

The above Equation 2.53 have been also used by (C. Hare et al., 2015; C. Hare & Ghadiri, 2017) to calculate the deviatoric stress. Moreover, (Goh et al., 2017) have used Equation 2.54 to evaluate the stresses of an agitated particle bed using DEM.

$$\sigma_D = \frac{\sqrt{(\sigma_1 - \sigma_2)^2 + (\sigma_1 - \sigma_3)^2 + (\sigma_2 - \sigma_3)^2}}{\sqrt{6}} \quad \text{Equation 2.54}$$

Where

σ_D =	Deviatoric stress	(N/m ²) or (Pa)
σ_1 =	Major principal stress	(N/m ²) or (Pa)
σ_2 =	Intermediate principal stress	(N/m ²) or (Pa)
σ_3 =	Minor principal stress	(N/m ²) or (Pa)

In addition, (C. Hare et al., 2011a; C. L. Hare & Ghadiri, 2013; Colin Hare & Ghadiri, 2013) have calculated the deviatoric stress using the three components of stress tensor, e.g. normal stresses (Equation 2.55).

$$\sigma_D = \frac{\sqrt{(\sigma_{xx} - \sigma_{yy})^2 + (\sigma_{xx} - \sigma_{zz})^2 + (\sigma_{yy} - \sigma_{zz})^2}}{\sqrt{6}} \quad \text{Equation 2.55}$$

Where

$\sigma_D =$	Deviatoric stress	(N/m ²) or (Pa)
$\sigma_{xx}, \sigma_{yy}, \sigma_{zz}$	Normal stresses from stress tensor	(N/m ²) or (Pa)

2.6 Failure criterion theory

In previous studies, a single granule or a compact of granules which initially formed in a granulation process were characterized for their strength by subjecting to mechanical testing e.g. compression and impact tests. They have assumed the stress that granules experienced for breakage during the granulation process can be comparable to the granule strength (obtained by the mechanical testing) (Antonyuk et al., 2006; Moreno et al., 2003; Z. Ning et al., 1997; Seyedi Hosseininia & Mirghasemi, 2006, 2007) Most of the mechanical testing, e.g. compression and impact tests, were conducted in one direction (uniaxial). However, bulk processing equipment such as granulators and shear cell testers involve a complex stress and powder bed experiencing multi stresses from all directions. In addition, the measurement of the stress of granules or compact of granules through the mechanical testing would be problematic due to the smaller size and fragile properties of the granules or compact of granules. Therefore, the accuracy of the measured stress can be questioned.

For this purpose, failure criterion theory was considered which can give a good prediction the breakage of the granules. A previous study by (Davis, 2016) has applied a suitable failure criterion theory for the purpose to link the stresses experienced by the granules in granulation to the granule strength. The values of stresses can be obtained through numerical simulations, and by applying this failure criterion theory, they are transformed into a single value. Consequently, this single value can be compared to the granule strength from the mechanical testing.

The failure of a material can be described when the material exceeds the elastic limit, as a result of the loss of elasticity. It indicates the material has changed to permanent deformation. For this purpose, a hypothesis defining the limit of elasticity in the material and the onset of plastic deformation under any combination of stresses need to be determined.

Failure criteria are designed to predict the conditions under which a material fails by means of the external loads. The criteria determine the safe condition of a material when it is subjected to stresses due to external loads from various directions. They are correlated to the yield of the material by computing its yield stress. Yield stress is the value of stress at which a material begins to deform

plastically. It can be determined from experiments, e.g. the material is subjected to the simple stress conditions. The commonly used tests are the simple tensile test or compression test by which the value of stress at yield or fracture can be easily determined.

Two of the most popular failure criteria used for material yields both in ductile and brittle are von Mises yield and Tresca yield criteria. For this study, the von Mises yield criterion was chosen due to its close relationship with the deforming microstructure of the material in this study. The description of the von Mises yield criterion is given in the following section.

2.6.1 von Mises yield criterion

This criterion has been implemented to develop a yield criterion for ductile materials when subjected to any complex 3D loading condition, regardless of the mix of normal and shear stresses. The von Mises yield criterion predicts the onset of yield and plastic deformation of a material by means of changing the complex stress state into a single scalar number, known as von Mises stress or equivalent tensile stress, σ_v . Further, the value of von Mises stress or equivalent tensile stress, σ_v , is compared to the yield stress of the material in simple tension, σ_{y_t} . Although this theory is an empirical process (observation and experimental), which incurs error and deviations it has generally been found to work well and remains the method of choice.

The previous deviatoric stress, σ_D is expressed by correlating the yield stress of the material in pure shear, k with the second deviator stress tensor J_2 (Section 2.5.2). For the von Mises yield criterion, the value of k is made to be $\frac{1}{\sqrt{3}}$ of tensile yield stress in simple tension, σ_{y_t} at the onset of yielding (Equations 2.56 and 2.57).

$$k = \sqrt{J_2} \quad \text{Equation 2.56}$$

$$k = \frac{\sigma_{y_t}}{\sqrt{3}} \quad \text{Equation 2.57}$$

By combining both equations, the value of k can be expressed in Equations 2.58 and 2.59.

$$\sqrt{J_2} = \frac{\sigma_{y_t}}{\sqrt{3}} \quad \text{Equation 2.58}$$

$$\sigma_{y_t} = \sqrt{3J_2} \quad \text{Equation 2.59}$$

Where

σ_{y_t} =	Tensile yield stress in simple tension	(Pa)
J_2 =	Second deviator stress tensor	(Pa)

The von Mises yield criterion is accomplished by comparing the calculated von Mises stress or equivalent tensile stress, σ_v to the tensile yield stress of the material in simple tension, σ_{y_t} . The von Mises stress or equivalent tensile stress, σ_v is calculated based on the second deviator stress tensor J_2 . The yielding of a material occurs when the calculated von Mises stress or equivalent tensile stress, σ_v reaches or exceeds the tensile yield stress of the material in simple tension, σ_{y_t} (Equation 2.60).

As shown in Equation 2.60, the compression yield stress of the material, σ_{y_c} is used to replace the tensile yield stress of the pellets in simple tension, σ_{y_t} for this current work. This is due to the difficulty of conducting the tensile test on the pellets and obtaining the tensile yield stress of the pellets in simple tension.

$$\sigma_{y_c} = \sigma_v = \sqrt{3J_2} \quad \text{Equation 2.60}$$

Where

σ_{y_c} =	Compression yield stress of the material	(Pa)
σ_v =	von Mises stress or equivalent tensile stress	(Pa)
J_2 =	Second deviator stress tensor	(Pa)

By substituting the value of J_2 (Section 2.5.2.1), the von Mises yield criterion can be expressed in terms of the following forms:

- a) components of stress tensor, σ_{ij} (Equations 2.61 and 2.62)

$$\sigma_v = \sqrt{3J_2} \quad \text{Equation 2.61}$$

$$\sigma_v = \sqrt{\frac{1}{2} [(\sigma_{xx} + \sigma_{yy})^2 + (\sigma_{yy} + \sigma_{zz})^2 + (\sigma_{zz} + \sigma_{xx})^2] + 3(\sigma_{xy}\sigma_{yx} + \sigma_{yz}\sigma_{zy} + \sigma_{zx}\sigma_{xz})} \quad \text{Equation 2.62}$$

b) principal stresses of stress tensor, σ_1 , σ_2 and σ_3 (Equations 2.63 and 2.64)

$$\sigma_v = \sqrt{3}J_2 \quad \text{Equation 2.63}$$

$$\sigma_v = \sqrt{\frac{1}{2}[(\sigma_1 + \sigma_2)^2 + (\sigma_2 + \sigma_3)^2 + (\sigma_3 + \sigma_1)^2]} \quad \text{Equation 2.64}$$

2.7 Numerical simulation of granular materials

In the past, experimental techniques have been used for studying the behaviour of granular particles. Recently, advancements of computer processing speeds have made simulations an effective alternative tool to study and understand the behaviour of granular flow. The use of numerical simulations provides a cost-effective method compared to experiments as no physical material or process equipment is required. Moreover, the simulation results can be predicted and validated. Numerical simulation can be divided into two categories; continuum approach and discrete approach.

The first approach, continuum, treats the particles as a continuous medium where all the quantities are assumed to be smooth and the individual particles as functions of position and time are neglected. It takes into account the conservation of mass, momentum and energy of material. It needs constitutive models that define a particular substance. Due this reason, methods such as finite differences, finite volumes and Finite Elements Method (FEM) are applied to resolve the resulting equation numerically. This type of simulation is suited to investigate large scale systems, e.g. at the unit operation scale (Vedachalam, 2011).

The second approach, the discrete approach, requires a time-discretized in form of equations of motion which governs the particle displacements and rotations. It requires a force law or force-displacement relationship as a means to describe the interactions of particles (Vedachalam, 2011). Development of the discrete approach for particle scale numerical modelling of granular materials has become a powerful and reliable tool. It is considered as an alternative to the continuum approach. The discrete approach requires less computational cost than the continuum approach as the number of elements is reduced to the number of particles studied (Padrós, 2014). Discrete Element Method (DEM) simulations is an example of the discrete approach (Vedachalam, 2011). As this current study

involves a granular system composed of individual particles and each of them moves independently of each other, it is difficult to predict the behaviour of the granular system using continuous models because they exhibit different behaviour. Due to this reason, the discrete approach using Discrete Element Method (DEM) simulations was applied for simulating the pellet deformation in the annular shear cell.

2.7.1 Discrete Element Method (DEM) simulations

Discrete Element Method (DEM) was originally developed by (Cundall & Strack, 1979) to model soil mechanics. DEM has the ability to capture the mechanical interaction between different discrete bodies that cannot be solved by continuum-based techniques (Das, 2007).

DEM is a numerical technique used to model materials that undergo discontinuous deformations because of their contact with other particles in the system which involve breakage of the contact bonds and iteration compaction of the broken fragments (Das, 2007; Vedachalam, 2011). The function of DEM is to model the actions that happen at a microscopic level and study how these actions affect the evolution of the motion of a whole media at a macroscopic level (Padrós, 2014). This method needs mainly particle contact detection and a time-discretized equation of motion that controls the action or behaviour of the particle displacements (Padrós, 2014; Rathbone et al., 2015). In addition, it requires an interaction of contact laws which describes the information related to the impact between two bodies.

According to (Cleary, 2010; Marigo, 2012), the advantages of DEM are 1) It is able to develop the academic DEM models; 2) It is available as new user-friendly commercial software; 3) It can be used for the simulation of complex systems especially for the evaluation of machinery prototypes; 4) It can consider large numbers of particles; 5) It is able to develop from 2D simulations to 3D simulations; 6) It has given the capability for studying the complexity of the systems; 7) It can enhance the fundamental understanding of granular motion and 8) It can help in the improvement of design or operation of systems especially involving particulate material.

2.7.2 Principle of DEM simulations

The principle of DEM simulations is to simulate the movement of particles and their interactions, e.g. particle-particle, particle-wall/boundary and particle-moving objects through collisions. The behaviours of granular systems can be numerically simulated by tracking the movement of all the individual particles, including their interactions with other particles and with their surroundings.

DEM simulations were based on simulating the individual dynamics of every particle in the system by numerically integrating their accelerations resulting from all forces, including contact force and gravity force. A flow diagram of the DEM simulations is shown in Figure 2.12. At the beginning of every time step, the particle positions are recorded, and the particle interactions can then be evaluated. All the forces acting on each particle in the system are first calculated. By considering the mass and the forces acting on each particle, Newton's second law is employed to determine the accelerations. Subsequently, they are integrated with time to find the velocity and position of each particle in the new state. The above steps are repeated for every particle in the system for each time step until the simulation ends.

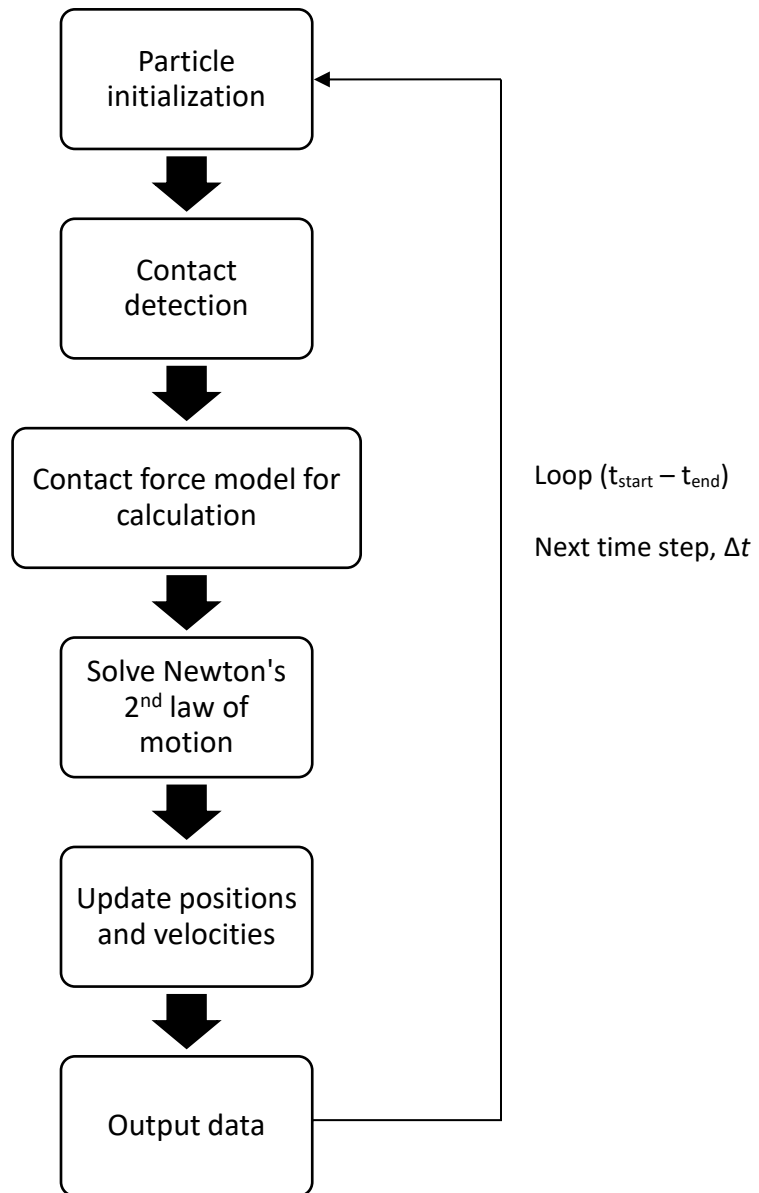


Figure 2.12 Typical flow in DEM simulations (Vedachalam, 2011)

2.7.3 Contact force models

In reality, the particles have contact (acting in compression) and deform at the contact points, and the energy can be dissipated in terms of sound, deformation, vibration and heat. However, in DEM, the particles are modelled based on the rigid body and it is difficult to quantify the deformation between the two rigid bodies in DEM. Due to this reason, they are assumed to have deformed when they have made contact with each other. It means that DEM models each particle as a single rigid element. The particles can “deform” during a physical contact between them by allowing a small amount of overlap

at the contact points. As the result of the contact between particles, forces are generated at the inter-particle contacts.

The contact forces are the result of elastic, viscous and frictional resistance between the moving particles. The particle collisions with each other/ with other parts of the system can be modelled like springs, dashpots, sliders which are generally addressed in the normal and tangential direction (Figure 2.13). The spring represents the particle stiffness and the elastic repulsion force in the system. Dashpot damping represents the dissipation of energy in the system. The shear sliders can be in both normal and tangential directions. In the normal direction, it is used to prevent or limit tensile forces developing between the particles. In tangential direction, shear slider with Coulomb friction represents a frictional resistance between the moving particles. It allows the particles to move relative to each other when the contact frictional strength is exceeded (calculated using Coulomb friction).

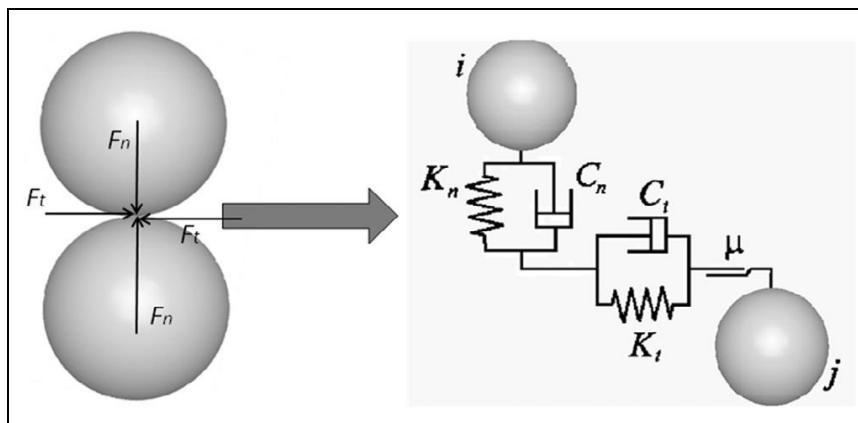


Figure 2.13 Contact force model in normal and tangential directions
(Weerasekara et al., 2016)

The contact forces can be calculated using an equation, known as constitutive contact law or contact force model. It is used to define the contact force - deformation relationship. The contact force - deformation behaviour depends on the material properties of the particles, e.g. the sizes and shape of the two particles in contact, surface conditions and mechanical properties of the contacting bodies (Flores, 2011; Colin Thornton, 2015).

Several contact force models have been published in the literature to calculate the contact forces (Flores, 2011; MacHado et al., 2012) and many contact force models have been developed and reviewed for normal and tangential directions. For the current study, the explanations for the contact force models in the normal direction and tangential direction have been limited to several contact models. The selection of the contact model for this current study is described at the end of this section.

2.7.3.1 Contact force models in normal direction: Linear spring model

The simplest contact force model in normal direction is the linear spring model, also known as Hooke's law. It involves two elastic spherical particles that act in the normal direction and interaction with each other can produce repulsive forces. The spring is used to provide the repulsion force which represents the elastic interaction. Moreover, the spring stiffness of this model is constant and is linearly proportional to the deformation (Figure 2.14).

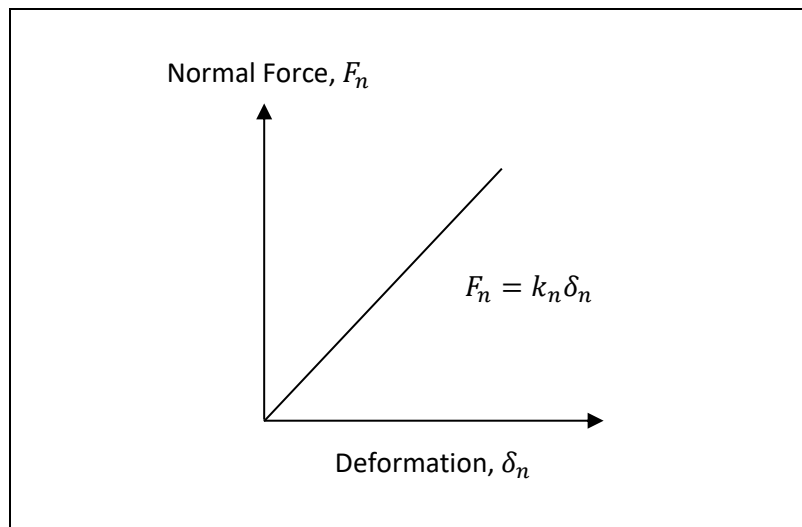


Figure 2.14 Normal force - deformation relationship in linear spring model

The dashpot damping represents the dissipation of energy in the system (Mishra, 2003). The contact force is affected by the shape, surface conditions and mechanical properties of the contacting bodies (Flores, 2011). The linear contact model is not accurate as the overall nonlinear nature during the impact process is not considered (Hu & Guo, 2015). However, it can be used as a good starting point for simulating granular materials. The values of the input parameters for the spring linear model can be calculated using Equation 2.65.

$$F_n = k_n \delta_n + C_n v_n \quad \text{Equation 2.65}$$

where

$F_n =$	Contact force for normal direction	(kN)
$k_n =$	Spring stiffness for normal contact (constant value)	(N/m)
$\delta_n =$	Deformation/ overlap for normal contact	(m)
$C_n =$	Dashpot damping coefficient	(-)
$v_n =$	Relative velocity for 2 particles for normal contact	(m/s)

2.7.3.2 Contact force models in normal direction: Non-linear Hertz contact model

The non-linear Hertz contact model is an improvement of the linear spring model for the purpose of computing the normal force deformation related to the impact between two elastic bodies. The model has been extended to the case where the colliding bodies tend to deform. The particles are allowed to overlap to some extent determined by the value of spring stiffness, k_n . It is proportional to the power of 3/2 of the deformation, $\delta_n^{3/2}$ (Figure 2.15).

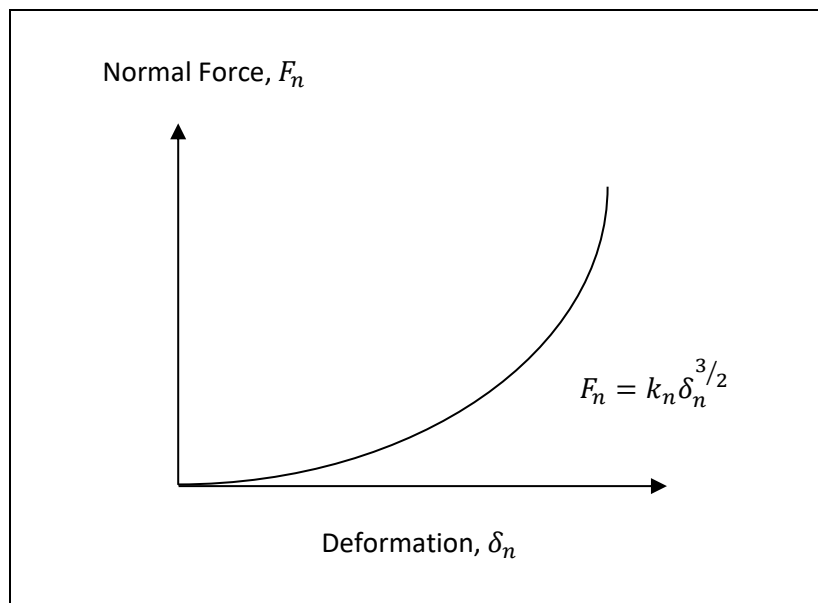


Figure 2.15 Normal force – deformation relationship in non-linear Hertz contact model

The spring stiffness, k_n depends on the radius of particles and, therefore, the amount of overlap between the two particles varies (Padrós, 2014). However, in this model, the overlap can never be larger than the radius of the particles. Due to this reason, a very small amount of overlap is assumed to evaluate the stiffness and this value is used as a constant in DEM models. The model considers the dashpot damping to reflect the dissipation in the contact area (Mishra, 2003). Moreover, the model is applicable when the velocity is relatively small and it is usually applied in static cases (Padrós, 2014).

The values of the parameters for the non-linear Hertz contact model can be calculated using Equations 2.66 to 2.70 (Mishra, 2003; Weerasekara et al., 2016). The effective particle radii and effective Young's modulus (elastic moduli) are applied if $R_1 \neq R_2$ and when dealing with two non-identical particles. Unlike the linear spring model, the spring stiffness in this model relates to the particles' material properties.

$$F_n = k_n \delta_n^{3/2} + C_n v_n \quad \text{Equation 2.66}$$

$$k_n = \frac{4}{3} E^* \sqrt{R^*} \quad \text{Equation 2.67}$$

$$\delta_n = R_1 + R_2 - d \quad \text{Equation 2.68}$$

$$\frac{1}{R^*} = \frac{1}{R_1} + \frac{1}{R_2} \quad \text{Equation 2.69}$$

$$\frac{1}{E^*} = \frac{1 - \nu_1^2}{E_1} + \frac{1 - \nu_2^2}{E_2} \quad \text{Equation 2.70}$$

where

$F_n =$	Non-linear Hertz contact force for normal direction	(kN)
$k_n =$	Spring stiffness for normal contact	(N/m)
$\delta_n =$	Deformation/ overlap in normal direction	(m)
$\nu =$	Poisson's ratio for particle 1 and 2	(-)
$d =$	Distance between the centres of the two particles	m
$R^* =$	Effective of the particles radii	m
$E^* =$	Effective Young's modulus (elastic moduli)	N/m ²
$R_1, R_2 =$	Radii for particle 1 and 2	m
$E_1, E_2 =$	Young's modulus (elastic moduli) for particle 1 and 2	N/m ²
$C_n =$	Dashpot damping coefficient	(-)
$v_n =$	Relative velocity for 2 particles for normal contact	(m/s)
$\alpha =$	Empirical constant (relationship between α and e (Tsuji et al. 1992))	

This model involves the interaction between two elastic bodies in the normal direction, to represent the elastic deformation. In reality, it is unnecessary to model the interaction between materials by considering them to be fully elastic. Due to this reason, this model cannot be chosen to represent the actual contact deformation of a material.

2.7.3.3 Contact force models in tangential direction

For contact force models in the tangential direction, general explanations are given and they are limited to the linear spring slider contact model; Mindlin & Deresiewicz with slip contact model and Mindlin's with no slip model. Direct contact between two particles produces frictional forces that resist the sliding motion of particles in the tangential direction (shear). The frictional forces, known as Coulomb friction can be computed based on the linear spring slider model. The linear spring slider model considers the spring stiffness as a constant value and is limited by the friction coefficient μ (Weerasekara et al., 2016). The value of μ depends on whether the flow is static or sliding (Padrós, 2014).

Slip occurs when the computed friction force is larger than the maximum frictional resistance (Mishra, 2003). The slip consists of the tangential elastic deformation of the contacting surfaces and tangential plastic deformation of the contact. The stored energy from the spring represents the tangential elastic deformation of the contacting surfaces. On the other hand, the tangential permanent deformation of the plastic part is a result of the dissipation energy of dashpot from the tangential motion (Weerasekara et al., 2016). According to (Weerasekara et al., 2016), the values of the parameters for the linear spring slider model can be calculated using Equation 2.71.

$$F_t = \min\{\mu k_t \delta_t + C_t v_t\} \quad \text{Equation 2.71}$$

where

$F_t =$	Contact force in tangential direction	(kN)
$\mu =$	Friction coefficient	(-)
$k_t =$	Spring stiffness in tangential direction (constant value)	(N/m)
$\delta_t =$	Deformation/ overlap in tangential direction	(m)
$C_t =$	Dashpot damping coefficient in tangential direction	(-)
$v_t =$	Relative velocity in tangential direction	(m/s)

The Mindlin & Deresiewicz with slip contact force model is an improvement to the linear spring slider model. This model was developed for elastic frictional contact between two identical spheres in the tangential direction. There is a tangential slip at the contact. The tangential force-displacement relationship depends on the loading history and the rate of change of normal and tangential forces. The Mindlin's no slip tangential contact model is considered for elastic contacts and neglects the effect

of microslip. In this case, the loading and unloading of the tangential forces are the same (Ali Hassanpour, 2015).

2.7.3.4 Simplified Pasha's linear elastic-plastic contact with adhesive contact model

Various contact models have been developed in the literature for elastic-plastic and adhesive contacts; however, they involve complex mathematical equations, which increase the processing time for contact force calculation and the simulation time. A simplified linear elastic-plastic contact with adhesive contact model has been developed by (Massih Pasha et al., 2014a) for the contact between two elastic-plastic spherical particles with adhesion. A general explanation for the simplified Pasha's linear elastic-plastic contact with adhesive contact model is given in this section due to its importance as the reference contact model for the current study. Further details of explanation of the simplified Pasha's linear elastic-plastic contact with adhesive contact model can be found elsewhere (Massih Pasha et al., 2013, 2014a).

The simplified Pasha's linear elastic-plastic contact with adhesive contact model provides the linear profiles for loading and unloading, represented by the plastic and elastic deformation of contacts, and is accompanied by adhesion. As shown in Figure 2.16, there are four different paths which can be characterized in the normal force – overlap relationship and each of the paths is explained here: 1) plastic loading path (line AB); 2) elastic unloading/reloading path (line BC or line CB); 3) adhesive elastic unloading/reloading path (line CD or line DC) and 4) contact detachment (Line $D\alpha_{fp}$ and Line $\alpha_{fp}O$).

When two spheres come into contact at $\alpha = 0$, the contact force drops to a certain negative value, f_0 at point A. The contact is assumed to be elastically deforming for $\alpha < \alpha_0$. For $\alpha \geq \alpha_0$, the contact deformation is elastic-plastic until point B. On compressive loading beyond α_0 , the contact reaches the yield stress and plastic deformation takes place, which is governed by the plastic stiffness, k_p (line α_0B). The contact force increases linearly with the overlap, α until a maximum overlap, α_{max} is reached. Once the contact is unloaded from point B, the path lies on line from B to α_p with elastic stiffness, k_e . The unloading path continues until a maximum tensile force, f_{cp} , known as the pull-off force, is reached (point C). For unloading beyond the pull-off force (line CD), a negative elastic stiffness, $-k_e$, is considered.

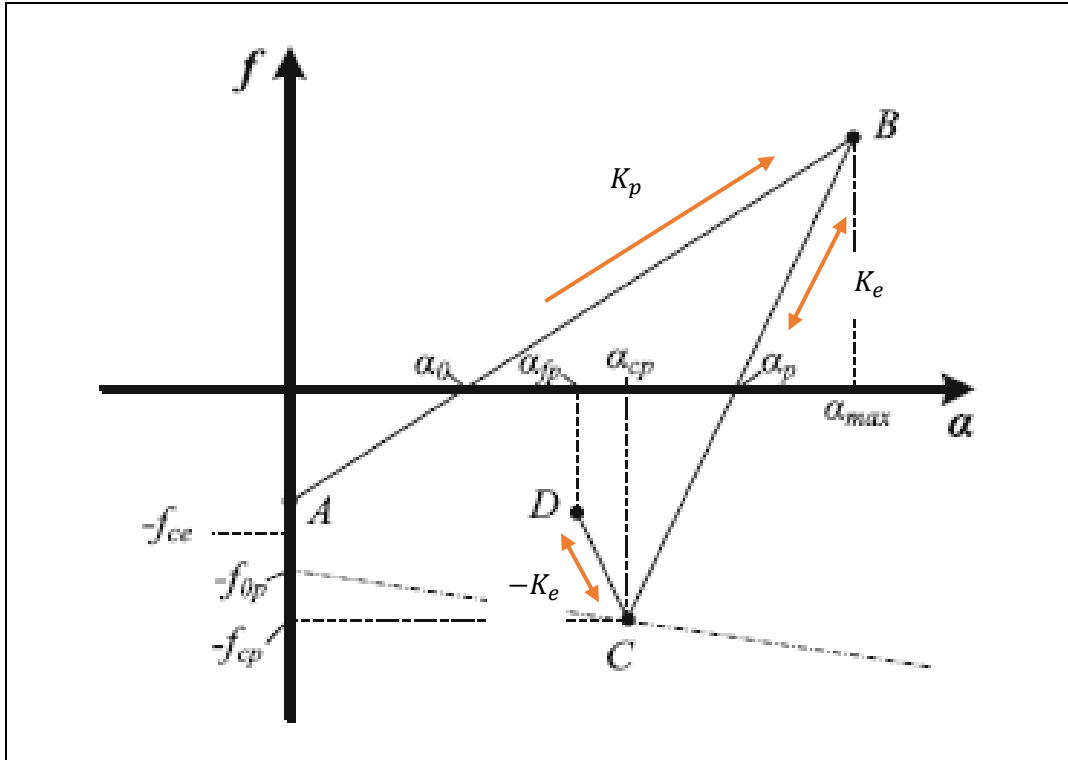


Figure 2.16 Normal force – overlap relationship in the simplified Pasha's linear elastic-plastic with adhesive contact model (Massih Pasha et al., 2014a)

Based on (Massih Pasha et al., 2014a), the four different paths in the normal force – overlap relationship can be represented by the following equations (Equations 2.72 to 2.75).

Plastic loading path (line AB) $f = K_p \alpha + f_0$ **Equation 2.72**

Elastic unloading/reloading path (line BC or line CB) $f = K_e (\alpha - \alpha_p)$ **Equation 2.73**

Adhesive elastic unloading/reloading path (line CD or line DC) $f = -K_e (\alpha - 2\alpha_{cp} + \alpha_p)$ **Equation 2.74**

Contact detachment (Line $D\alpha_{fp}$ and Line $\alpha_{fp}O$) $f = 0$ **Equation 2.75**

where

f_0 =	Tensile force at zero contact force	(N)
K_e =	Plastic stiffness	(N/m)
K_p =	Elastic stiffness	(N/m)
α =	Overlap	(m)
α_p =	Overlap at which the unloading force becomes zero	(m)
α_{cp} =	Overlap at which the pull-off force is achieved	(m)

For the tangential direction, the sliding criteria was modified for the purpose to account the “peeling effect” of adhesive contacts, based on previous studies by (C. Thornton & Yin, 1991). Moreover, in the simplified Pasha’s model, two materials which are particle and geometry are considered. Several input properties for the two materials need to be identified and an example is given in Table 2.6.

Table 2.6. Example of input properties in the simplified Pasha’s model

Material	Property	Unit
Particle	Particle plastic stiffness, k_p	N/m
	Particle elastic stiffness, k_e	N/m
	Particle plastic-adhesive stiffness, k_{cp}	N/m
	Particle tangential stiffness, k_t	N/m
	Particle initial adhesive force, f_0	N
	Particle initial adhesive plastic force, f_{02}	N
Geometry (wall)	Wall plastic stiffness, k_{wp}	N/m
	Wall elastic stiffness, k_{we}	N/m
	Wall plastic-adhesive stiffness, k_{wcp}	N/m
	Wall tangential stiffness, k_{wt}	N/m
	Wall initial adhesive force, k_{w0}	N
	Wall initial adhesive plastic force, k_{w02}	N

The simplified Pasha's model linear elastic-plastic contact force model has several advantages which can be considered as the reference contact force model for this current study: 1) The input properties of the materials such as plastic and elastic stiffness can be obtained experimentally, thus represent the actual elastic-plastic deformation of the materials 2) The model has a built-in stress analysis which is useful to provide the input nine stresses experienced by the pellet. As the aim of this work is to predict the pellet deformation in DEM simulations, therefore, these stresses are important for the deviatoric stress (stress responsible for deformation) measurements; and 3) The model can be easily modified to follow the requirement of current study by adjusting the values of input properties or omitting any irrelevant of the input properties.

2.7.4 Time-step, Δt

The time-step is the time increment chosen for the calculation of the particle motion, e.g. the incremental forces and displacements of the contacting particles, by which it determines the overall simulation time. The validity of a time-step is questionable as it is impossible to illustrate or model the wave pattern of particles in DEM simulations. Due to this reason, it was assumed the surface of the unique particles does not exist and the wave pattern of the particles is often made based on the Rayleigh surface wave. It represents the propagation time of Rayleigh surface wave around a particle (Bednarek et al., 2017).

Previous studies have stated that the time-step used for the simulations is related to the speed of Rayleigh surface wave propagation (Mishra, 2003; Zemin Ning & Ghadiri, 2006). It was suggested the time-step used in the simulations is a fraction of the Rayleigh time-step or critical time-step, Δt_{cr} . The Rayleigh based time-step is often used when dense regimes are made in DEM simulations (Bednarek et al., 2017). Moreover, the speed of the Rayleigh surface wave is based on the physical properties of the discrete medium such as shear modulus and density; indicating that the time-step varies with different particle materials (Ali Hassanpour, 2015; Zemin Ning & Ghadiri, 2006).

The critical time-step was estimated based on the Rayleigh wave speed of the smallest sphere. For a discrete medium consisting of different material types of particles, the critical time-step, Δt_{cr} should be measured based on the smallest particle among them. In addition, the time-step should be smaller than the Rayleigh time-step to prevent excessive overlap with the neighbouring particles (Ali Hassanpour, 2015). The disturbance waves, as a result of motion of the particle, need to propagate

only to the nearest neighbours. This is to prevent numerical instability in the system (Ali Hassanpour, 2015) due to the high energy overlaps leading to simulation failure (Vedachalam, 2011).

According to (Zemin Ning & Ghadiri, 2006), a single particle that is surrounded by a number of neighbouring particles in a packed assembly may collide with neighbouring particles or walls during movement. The particle movement may also affect by particles far beyond its local neighbourhood through propagation of disturbance waves. Under a certain condition, there is a time by which the acting force is transmitted from one contact to another point along this particle surface. On the other hand, the use of a smaller time-step causes the trajectory to cover only a limited proportion in the simulation space.

Therefore, the time-step chosen should be less than or equal to 20 % of the Rayleigh time-step. The time-step used in the simulations and critical time-step for this study can be calculated using Equations 2.77 to 2.78.

$$\Delta t = 0.2\Delta t_{cr} \quad \text{Equation 2.76}$$

$$\Delta t_{cr} = \frac{\pi R \sqrt{\rho/G}}{0.0163\nu + 0.8766} \quad \text{Equation 2.77}$$

where

$\Delta t =$	Time-step	(s)
$\Delta t_{cr} =$	Critical time-step	(s)
$R =$	Radius of the smallest particle in the system	(m)
$\rho =$	Particle density of the smallest particle in the system	(kg/m ³)
$G =$	Shear modulus of the smallest particle in the system	(Pa)
$\nu =$	Poisson's Ratio of the smallest particle in the system	(-)

2.7.5 DEM simulations for shear flow and breakage studies

To date, many studies of DEM simulations have been extensively published in the literatures for shear flow and breakage of granular materials in various processes. The application of DEM simulations in selected types of equipment/techniques are listed in Table 2.7 due to their importance in current study. Due to the limitations of the computer power for handling a large number of particles and speeds (A. Hassanpour et al., 2004; Zemin Ning & Ghadiri, 2006), most studies of DEM simulations have been performed by considering a small section of the equipment with periodic boundaries as the measurement cells (Goh et al., 2017; C. Hare et al., 2015; C. L. Hare & Ghadiri, 2013) or a unit cell of interest to be focused. It is used to improve the computational efficiency and increase the speed for calculating the DEM contact forces.

For the case of a unit cell, it has boundary particles for two planes on the top and the bottom (Davis, 2016; Zemin Ning & Ghadiri, 2006; X. Wang et al., 2012a). It was reported the two boundary planes on the side walls, that are perpendicular to the direction of shear flow are periodic, e.g. once a group of particles are out of the cell in one plane, they will immediately join in the opposite plane. Whereas, the other two boundary planes on the outer and inner walls, e.g. parallel to the direction of shear flow were made stationary (A. Hassanpour et al., 2004; Zemin Ning & Ghadiri, 2006; X. Wang et al., 2012a). However, the periodic boundary conditions have been also considered for the side, outer and inner walls (Davis, 2016). Moreover, an assembly of spherical particles (C. Hare et al., 2015; A. Hassanpour et al., 2004; Zemin Ning & Ghadiri, 2006; C. Thornton & Antony, 2000; X. Wang et al., 2012b), agglomerate of spherical particles (Ali Hassanpour et al., 2007) and a single large spherical particle (Antony & Ghadiri, 2001; Davis, 2016) were considered as the model of tested material (s). The agglomerate of spherical particles and a single large spherical particle were surrounding by primary spherical particles as a medium of shearing.

According to (C. Hare et al., 2015), DEM simulations enable the measurements of the internal bed stresses and velocities. For granule breakage study, the interest has been given in obtaining the values of stresses from the DEM simulations. These stresses were further used as the input parameters for calculating deviatoric stresses (refer to Section 2.5.3), von Mises yield criterion (refer to Section 2.6.1) (Davis, 2016; Goh et al., 2017; C. Hare et al., 2015; C. L. Hare & Ghadiri, 2013).

Table 2.7 DEM simulations for shear flow and breakage studies in selected types of equipment/techniques

No	Types of equipment/Techniques	References
1	Rheometer shear cell	(Bharadwaj et al., 2010) (MacHado et al., 2012) (C. Hare et al., 2015) (Bednarek et al., 2017) (Schwarze et al., 2013) (C. Hare & Ghadiri, 2017)
2	Annular shear cell	(Ji et al., 2009) (Zemin Ning & Ghadiri, 2006) (A. Hassanpour et al., 2004) (Midi, 2004) (Baran & Kondic, 2006) (X. Wang et al., 2012b) (X. Wang et al., 2012a) (McCarthy et al., 2010) (Orlando & Shen, 2013) (Alenzi et al., 2013)
3	Jenike shear cell	(Kheiripour Langroudi et al., 2010)
4	Couette shear device	(Vidyapati et al., 2012)
5	Direct shear box test	(Ali Hassanpour et al., 2008)
6	Split-bottom ring shear cell	(Luding, 2008)
7	Granulator	(Bagherzadeh et al., 2011) (Gantt & Gatzke, 2005) (A. Hassanpour et al., 2009) (Nakamura et al., 2009) (Colin Hare & Ghadiri, 2013) (Zhou et al., 2004)
8	Bladed Mixer	(Halidan et al., 2014) (Zhou et al., 2004)
9	Paddle blade mixer	(Pantaleev et al., 2017)
10	Small-scale dryer	(C. Hare et al., 2011a)
11	Small-scale agitated vessel	(Colin Hare & Ghadiri, 2013)
12	3D cuboidal periodic shear cell	(Antony & Ghadiri, 2001)
13	Agitated powder beds	(Goh et al., 2017)

2.8 Summary

A literature review relating to the current study has been discussed in depth in this chapter.

Of the three rate processes involved in the granulation process, attrition and breakage have been identified as the focus of this work. Granules in the form of granular pellets were considered. A review on shear cell testers was made as it enables elimination of the other two mechanisms that usually occur in the high shear granulation; nucleation, consolidation and growth. A custom-made annular shear cell, by which takes the concept of a rheometer shear cell, is chosen for this study. Some of granulation parameters which related to current study were presented. Primary particle size and shape of powder, binder viscosity and rotational speed, are chosen as the material properties and operating parameters for the shear deformation study in the annular shear cell. The material properties of powder and liquid binder can be used to formulate different types of pellets. Operating parameters based on rotational speed can differently shear deformation behaviour in the annular shear cell.

Several analyses of breakage in granulation are described, such as visualization of the change in pellet morphology, breakage fraction, F_B , degree of elongation and Stokes deformation number, St_{def} . The predictive model using Stokes deformation number, St_{def} has been applied in the case of a high shear mixer and it was believed that no study has been reported on the annular shear cell. For this reason, these analyses were chosen to determine the extent of deformation/breakage and predict the pellet deformation in the annular shear cell. Two types of deformation; plastic and brittle deformation were characterised and described from the compression test. It shows that the deformation of the material is influenced by the operating conditions and types of materials for the formulations. The annular shear cell can be performed in quasi-static, intermediate or high/rapid shear flow behaviour. For this reason, there could be different types of deformation, e.g. plastic deformation, brittle deformation or in between plastic and brittle deformation. DEM simulations were used as a tool to model and simulate the shear flow of the pellet. The mechanism of DEM simulations using a 'soft-particle' model was explained. Several contact models were presented for calculating the contact forces in DEM simulations. It is proposed that pellet deformation can predicted by using DEM simulations to assess the deviatoric stress σ_D on pellets, measuring individual pellet mechanical properties, and correlating with suitable failure criterion theory.

A schematic diagram summarising the research presented in this thesis is given in Figure 2.18. It shows a work flow for both experiments and simulation work. This study begins with compression tests to determine the mechanical properties of pellets, for use in DEM simulations and comparison in the failure theory, described in Chapter 4. The experiments in an annular shear cell are presented in Chapter 5. The information from the experiments such as material properties and set-up conditions were gathered for designing and building the DEM unit shear cell as described in Chapter 6. DEM simulations were implemented as a tool to model and simulate the shear flow behaviour based on the experiments. The stresses of the granular pellets were obtained numerically to predict the shear deformation of the pellets. Further, they were used for defining the “failure” or yielding of the granular pellets using von Mises failure theory. The relation between the experimental results and the predicted pellet deformation results from DEM simulations is described in Chapter 7.

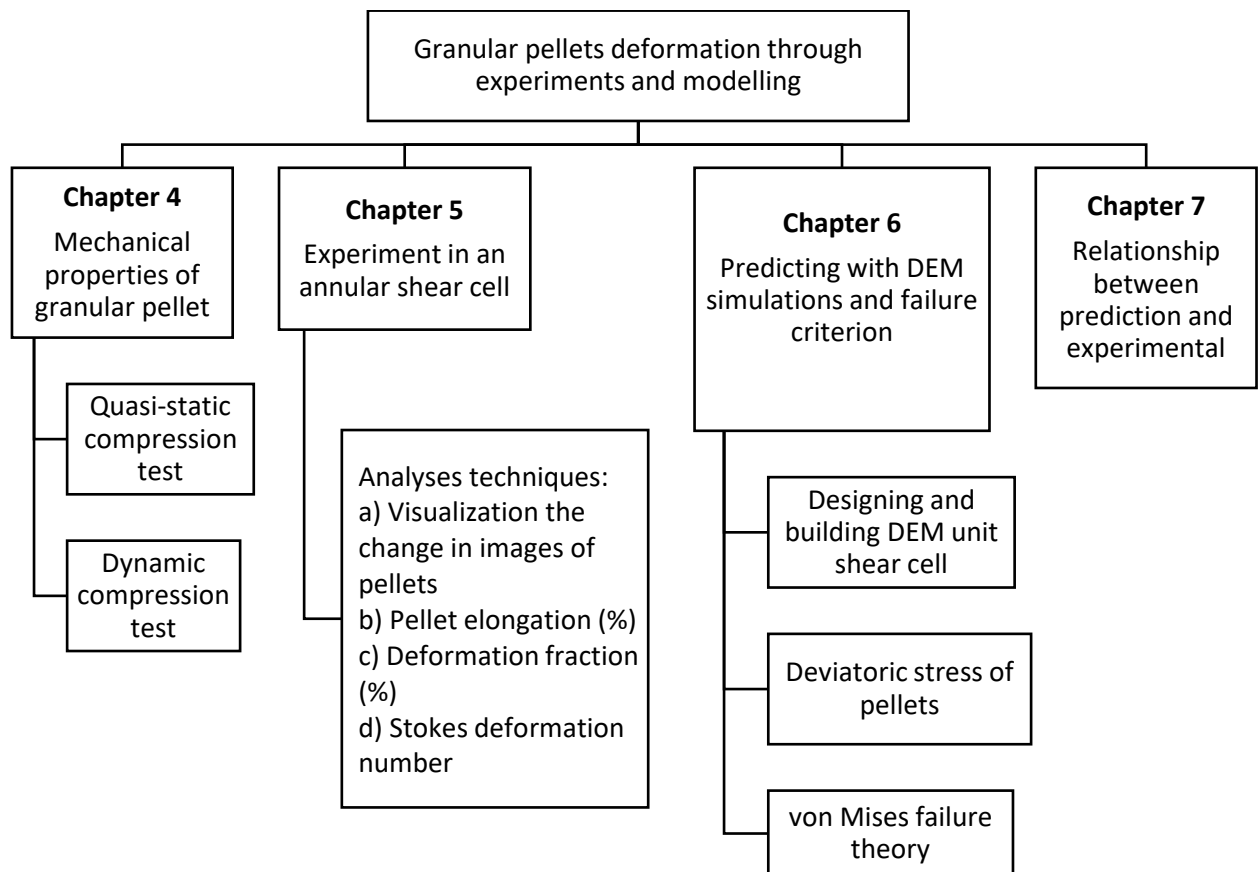


Figure 2.17 Process work flow

3 Experimental: Materials and methods

3.1 Introduction

This chapter presents the information on materials and experimental methods. Details of the materials including methods for their characterisation and properties are given. The results of certain characterisation experiments for powders and liquid binder (e.g. powder morphology, particle size, density and viscosity) are presented. The formulations for paste, methods for paste and pellet preparation are also included in this chapter. It should be noted that the methodology (and results) for mechanical property testing of the pellets is presented separately in Chapter 4.

3.2 Selection of materials and methods

The preparation of the materials and pellets and their properties are described in this section. A series of materials, equipment, and simulation methods have been identified as outlined in Table 3.1, and will be detailed in this section.

Table 3.1 List of materials and methods

	Description
Materials	<ul style="list-style-type: none">• Soda-lime glass beads; 1 - 1.4 mm• Soda-lime glass beads; 2 mm• 63-90 μm ballotini glass beads• 200 Mesh lactose monohydrate (lactose)• Microcrystalline cellulose (MCC)• Solvent blue 59 powder• Silicone oil (0.01 Pa.s, 0.05 Pa.s, 0.1 Pa.s and 1 Pa.s)
Equipment	<ul style="list-style-type: none">• Custom-made annular shear cell
Modelling and simulation	<ul style="list-style-type: none">• DEM simulations using EDEM 2017 software

All experiments and DEM simulations are based on the deformation of granular pellets surrounded by a medium of background beads. The experimental model pellets were made from three different types of powders, and different viscosities of silicone oils. The powders were ballotini glass beads of 63-90 μm , 200 Mesh lactose monohydrate (lactose) and microcrystalline cellulose (MCC). The ballotini glass beads powders were purchased from MO-SCI Corporation, United States. They were translucent, pale grey in colour and spherical in shape. Lactose powders were purchased from DFE Pharma, Germany. MCC powders were purchased from Acros Organic, UK. Information on the properties of the powders is given in Section 3.3.

Silicone oil was chosen as the model binder liquid, due to the ability to purchase different viscosities, and as it does not dry over time. The selection of the different viscosities of silicone oils was based on the expected different deformation behaviour of the pellets. Plastic pellets deform as plastic flow, i.e. squeeze, necking or elongation, indicating the plastic deformation. In contrast, the brittle pellets deform as they break, split into two, crack or fragment. The silicone oil binder was dyed with solvent blue 59 powder to form a blue liquid binder. The solvent blue 59 powder was used as a tracer dye to colour the paste pellets. Both silicone oil and solvent blue 59 powders were purchased from Sigma-Aldrich, UK. Information on the properties of the liquid binders is given in Section 3.4. Further, details of formulating the paste and pellet formation are given in Sections 3.5 and 3.6. The material for the background medium was soda-lime glass beads purchased from VWR International Ltd., UK. Two different sizes of background beads, 1 – 1.4 mm and 2 mm, were chosen. The purpose of the background beads is to facilitate shearing and transmit stresses to the pellets without participating in the shearing process (R M Smith, 2007). Their relatively large size prevents them from being granulated together with the pellets. The background beads are non-porous, have smooth surfaces and are spherical in shape; images of the beads are shown in Figures 3.1 and 3.2. The shear deformation experiments for pellet deformation were performed in a lab scale custom-made annular shear cell. The modelling and simulations were performed by DEM simulations using commercial software EDEM 2017.

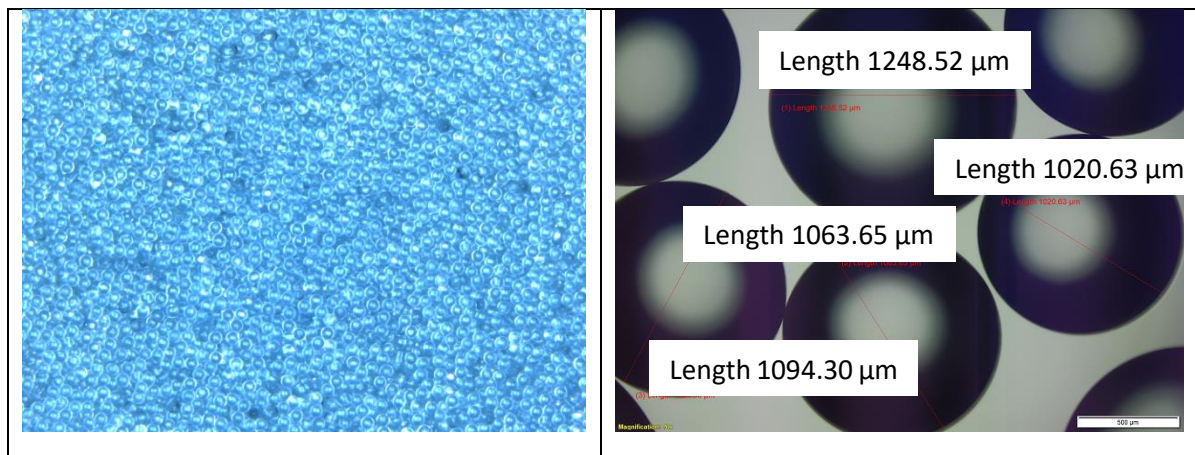


Figure 3.1 Images of 1 – 1.4 mm background beads

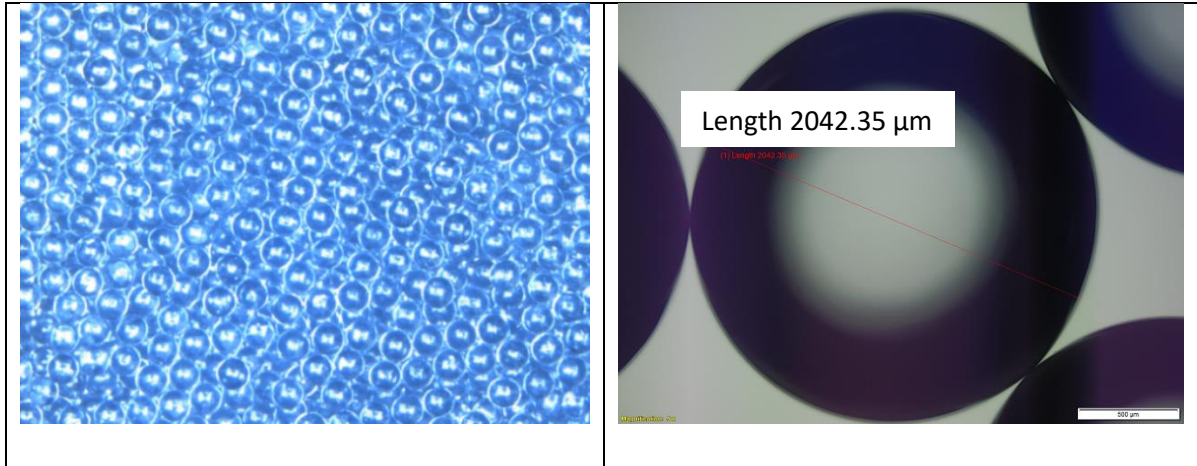


Figure 3.2 Images of 2 mm background beads

3.3 Properties of powders and background beads

In this section, the methods for determining the properties of powder and background beads are given. The material properties measured were the morphology, particle size distribution and densities.

3.3.1 Morphology of powders

Figures 3.3 to 3.5 show the morphologies for three different powders used in this study; ballotini glass beads, MCC and lactose. The images of the powders at 20x magnification were captured using a microscope. The model of the microscope was Olympus BX51 (Olympus Corporation, Japan). The software used was Olympus cellSens Entry version 1.17 (Olympus Corporation, Japan). The ballotini glass bead particles present themselves as smooth, regular (spherical or spheroidal) in shape (Figure 3.3). MCC particles have elongated and well formed shape (Figure 3.4) while well-formed crystal faces and geometric shape were observed for lactose particles (Figure 3.5).

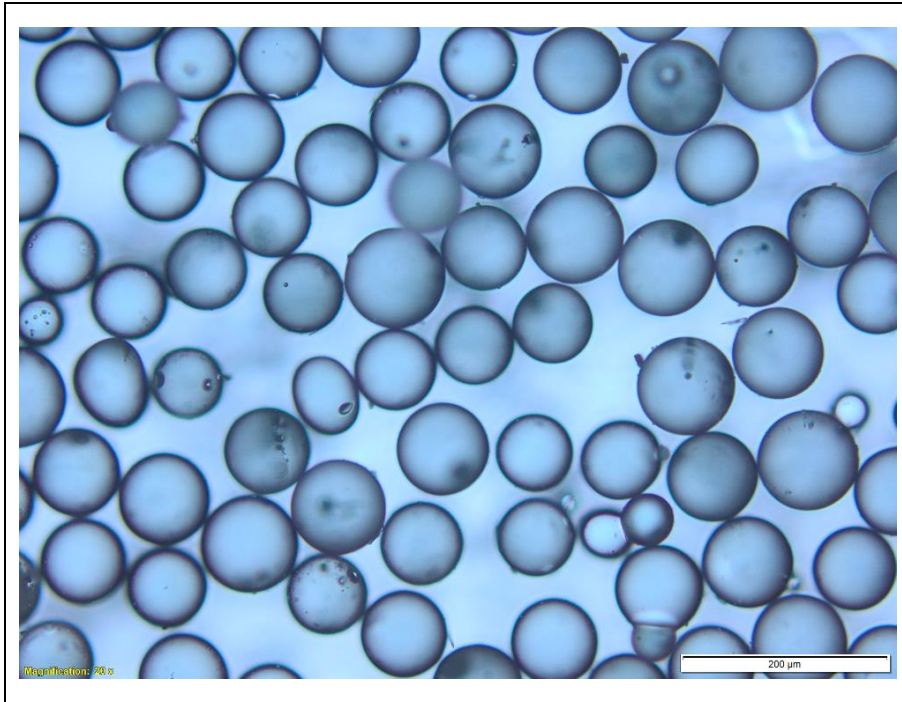


Figure 3.3 Image of ballotini glass beads

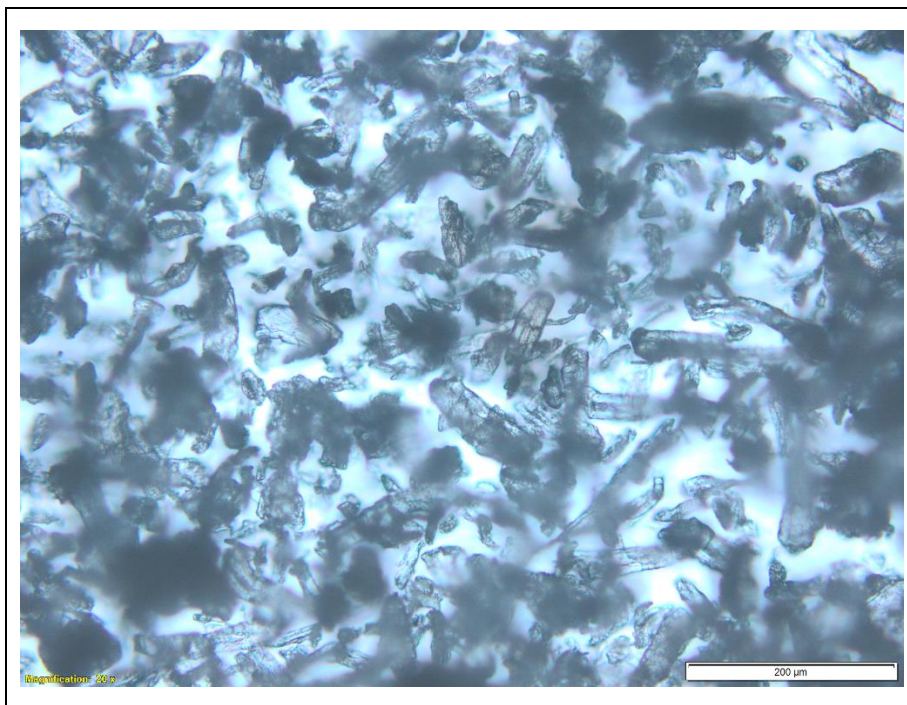


Figure 3.4 Image of MCC

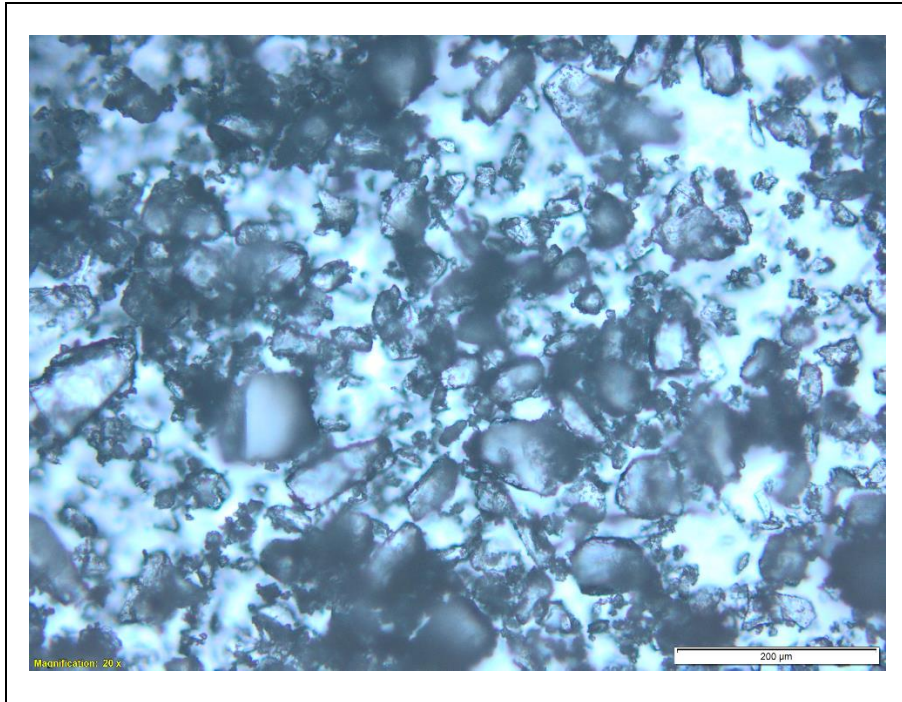


Figure 3.5 Image of lactose

3.3.2 Particle size distributions

Most of the powders contain particles with a range of different equivalent diameters, i.e. they are polydisperse. In order to define the size distribution of the polydisperse powder samples, the size distribution can be split into different size ranges. It can be represented in the form of a curve as a means to compare the characteristics of two or more polydisperse powder samples. The particle size distributions for the powders and background beads were measured by means of a dry sieve method and a static light scattering technique (dry laser diffraction). The sieve method only was performed for background beads due to their relatively large sizes. For each size of these beads, an amount of the sample was sieved in a semi-auto stack at amplitude of 1 mm/g for 1 min. The selections of the mesh sieve size were between 1.7 and 0.85 mm for 1 – 1.4 mm background beads; while a mesh size range between 2.8 mm and 1.18 mm was used for 2 mm background beads. At least three measurements were carried out for each type of beads.

The frequency distribution curve was used for characterizing the size distribution of the background beads. A frequency distribution was measured by dividing the mass fraction of particles (by weight) in each size range by the breadth of the sieve size ranges and multiplied by 100, to find % frequency. When the mass (by percentage) of the background beads lying within a certain size range is plotted against a mean of size range, a frequency distribution curve is obtained. The plot gives a visual

representation of the distribution. Table 3.2 shows the sieve analysis for these two sizes of beads. These size distributions of background beads will be used as the input parameters in DEM simulations in Chapter 6. Figures 3.6 and 3.7 give the frequency distribution by mass versus the mean of size range for both types of background beads using the sieving method. They show narrow unimodal distributions with a size range of approximately from 1.0 to 1.18 mm for 1-1.4 mm background beads and from 1.7 to 2.0 mm for 2 mm background beads. The particle sizes with the highest frequency (mode size) for 1-1.4 mm background beads and 2 mm background beads are 1.18 mm and 2 mm, respectively.

Table 3.2 Particle size distribution for background beads using the sieve method

Properties	1 – 1.4 mm background beads	2 mm background beads
Range of size distribution (mm)	1.0 – 1.4	1.7 – 2
Mode size (mm)	1.18	2.0

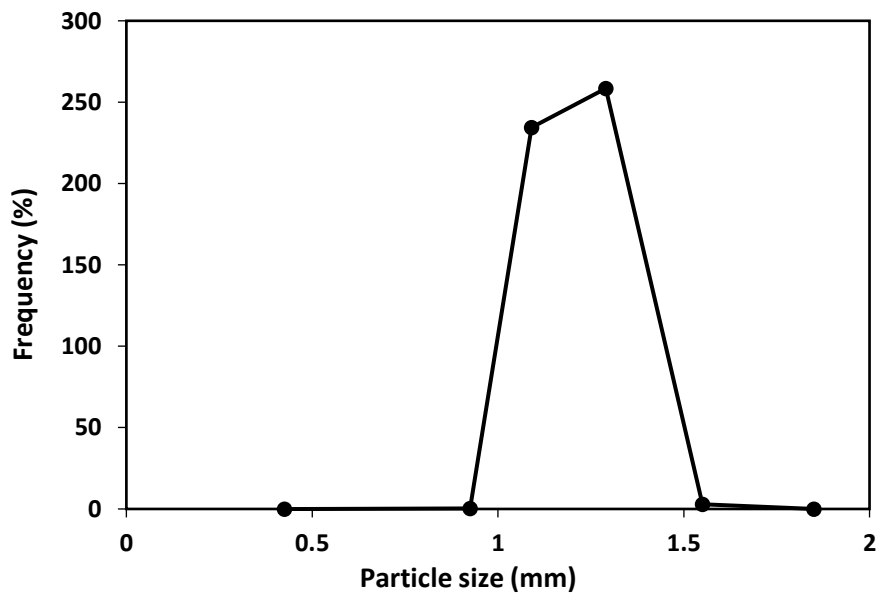


Figure 3.6 Frequency distribution curve for 1 – 1.4 mm background beads

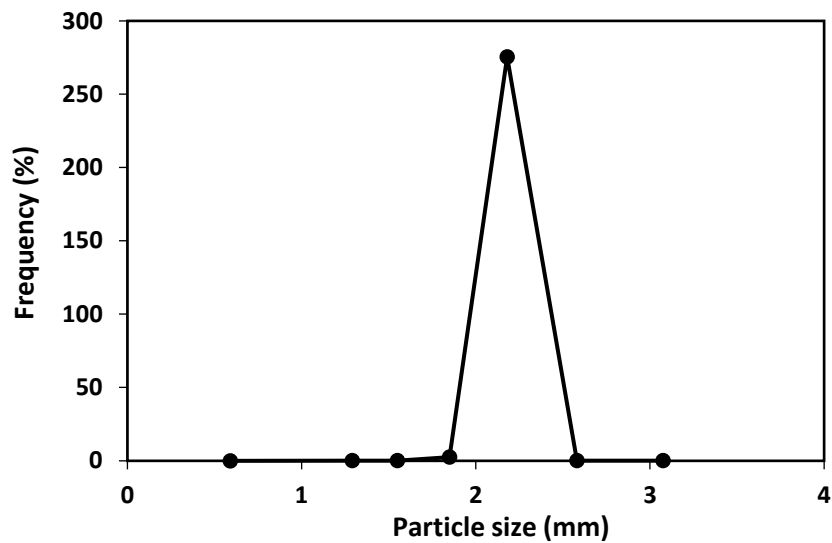


Figure 3.7 Frequency distribution curve for 2 mm background beads

The laser diffraction method using a Malvern Mastersizer 3000 Particle Size Analyzer (Malvern Instrument Ltd., UK) was carried out for ballotini glass beads, MCC and lactose. The principle of laser diffraction particle size analysis is as follows; 1) measuring the light scattering angle and intensity and 2) entering the data obtained into an algorithm that uses the Mie scattering theory to yield information about the particle size. Large particles scatter light at small angles, while small particles scatter light at large angles. The larger particles result in the smaller angle and higher intensity of scattering. On the other hand, the smaller particles scatter light at lower intensities and wider angles compared to larger particles. The type of distribution measured is the volume equivalent of the sample. It gives a volume-weighted distribution which relates to the volume of that particle. The equipment was connected to a dry feeder, and once the measurement was completed, it automatically outputted a list of size distribution properties of the sample. The software used for recording the data results was Malvern v3.40. The particle size distributions were obtained over 4 measurements and expressed in % volume density.

The two most commonly used expressions to define the mean value for describing particle sizing using laser diffraction are $d[4,3]$ and $d[3,2]$. The $d[4,3]$ is the volume mean diameter, based on volume distribution, and is often simply referred to as the mean. On the other hand, $d[3,2]$ or surface mean gives the mean value from the surface area distribution. It is important for measuring specific surface area and, therefore, is important for bioavailability, reactivity, dissolution etc. Among these two mean

based distributions, d[4,3] is preferred for describing the diameter size of the powders in this current study.

Other commonly used expressions to describe the particle size distributions are d-values, (d_{10} , d_{50} and d_{90}) which are the intercepts for 10 %, 50 % and 90 % sample masses of the cumulative size distributions. The d_{10} is the diameter at which 10 % of the sample's mass is comprised of particles with a diameter less than this value. The d_{50} is the diameter of the particle that 50 % of a sample's mass is smaller than and 50 % of a sample's mass is larger than this value. d_{90} is the diameter at which 90 % of the sample's mass is less than this value. The values between d_{10} and d_{90} are considered as well to describe the ranges of the size distribution of the powders. The span of the distribution is the difference between the d_{90} and d_{10} sizes, then divided by the d_{50} size. It gives the indication of the breadth of the size distribution. It can be calculated using Equation 3.1. The size properties from laser diffraction and the span for glass beads, MCC and lactose are listed in Table 3.3.

$$Span = \frac{d_{90} - d_{10}}{d_{50}} \quad \text{Equation 3.1}$$

Where:

- d_{90} = 90% passing size of the distribution (μm)
 d_{10} = 10% passing size of the distribution (μm)
 d_{50} = Median size of the distribution (μm)

Table 3.3 Particle size properties of powders using laser diffraction

Properties	Ballotini glass beads	MCC	Lactose
d[3,2] (μm)	73 (0.025)	35 (0.1453)	6 (0.0410)
d[4,3] (μm)	74 (0.0408)	69 (0.3383)	53 (0.5044)
d_{10} (μm)	62 (0.0408)	17 (0.0577)	5 (0.06)
d_{50} (μm)	73 (0.0408)	56 (0.2963)	41 (0.4163)
d_{90} (μm)	86 (0.1031)	143 (0.5774)	119 (0.8819)
Span	0.33	2.25	2.78

*Parentheses give the standard error values of a minimum of 3 measurements

3.3.3 Density

For a given mass and difference reference of volume used, one can define three densities of powders; bulk, apparent and true density. Bulk density considers volume occupied by a bulk solid including all void space. Apparent density considers the volume occupied by a single particle including internal porosity. Here, an imaginary envelope around the particle defines the volume of the particle. True density considers only the true solid volume of the particle. Knowledge of both the bulk and true densities are useful for DEM simulations and the annular shear cell experiments. The bulk density was used for calculating the mass of background beads required for filling both the DEM unit shear cell and the trough of the annular shear cell. The true density was used for calculating the contact forces and time-step estimation in DEM simulations. The bulk densities of the background beads were determined using a measuring cylinder method. An empty 25 ml measuring cylinder was weighed and the mass was recorded. The background beads were filled into the measuring cylinder to desired volume level. The mass of the background beads in the measuring cylinder was recorded. The density of the background beads can be calculated using Equations 3.2 and 3.3.

$$\rho_p = \frac{m_2 - m_1}{V_p} \quad \text{Equation 3.2}$$

$$\rho_p = \frac{m_p}{V_p} \quad \text{Equation 3.3}$$

Where:

ρ_p =	Density of background particles	(kg/m ³)
m_1 =	Mass of empty measuring cylinder	(kg)
m_2 =	Mass of liquid + measuring cylinder	(kg)
m_p =	Mass of background particles	(kg)
V_p =	Volume of background particles	(m ³)

The true density for the powders and background beads was determined using an AccuPyc 1340 Automatic Gas Pycnometer (Micromeritics, Norcross, USA). The software used was FoamPyc V 1.05. The apparatus uses helium gas as a displacement medium for measuring the true solid density. Three measurements were taken for each of the samples. The bulk and true densities for the powders and background beads are listed in Table 3.4 and Table 3.5.

Table 3.4 Density of powders

Material	True density (g/cm ³)
Ballotini glass beads	2.472 (0.002)
MCC	1.564 (0.001)
Lactose	1.544 (0.001)

*Parentheses give the standard error values of a minimum of 2 measurements

Table 3.5 Densities of background beads

Material	True density (g/cm ³)	Bulk density (g/cm ³)
1 – 1.4 mm background beads	2.5234 (0.00113)	1.494 (0.0058)
2 mm background beads	2.5572 (0.00025)	1.5190 (0.0072)

*Parentheses give the standard error values of a minimum of 4 measurements

3.4 Properties of liquid binder

This section describes the methods for preparation the blue dyed silicone oil binders and their properties; density and viscosity.

3.4.1 Preparation of blue dyed silicone oil

Four different viscosities of silicone oils (0.01 Pa.s, 0.05 Pa.s, 0.1 Pa.s and 1 Pa.s) were used as the liquid binder for pellet formation. 0.05 g of blue dye powder (0.05% wt/wt) and 99.95 g of silicone oil were mixed and continuously shaken until they became homogenous (visual observation). The dye was used as a tracer to colour the pellets for visualization purposes.

3.4.2 Measuring the density of liquid binder

The density of the liquid binder was measured using a measuring cylinder method. An empty 10 ml cylinder measuring flask was weighed and the mass was recorded. The liquid binder was filled into the cylinder measuring flask to desired volume level. The mass of the liquid binder in the cylinder measuring flask was recorded. The density of liquid binder was calculated using Equations 3.4 and 3.5. The densities of the liquid binder are listed in Table 3.6. Three measurements of the density of the liquid binder were taken.

$$\rho_l = \frac{m_2 - m_1}{V_l} \quad \text{Equation 3.4}$$

$$\rho_l = \frac{m_l}{V_l} \quad \text{Equation 3.5}$$

Where:

ρ_l =	Density of liquid	(kg/m ³)
m_1 =	Mass of empty cylinder measuring flask	(kg)
m_2 =	Mass of liquid + cylinder measuring flask	(kg)
m_l =	Mass of liquid	(kg)
V_l =	Volume of liquid	(m ³)

Table 3.6 Densities of liquid binder

Liquid binder	Density value (g/ml)
Blue dyed 0.01 Pa.s silicone oil (0.05% wt/wt)	0.9336 (0.0007)
Blue dyed 0.05 Pa.s silicone oil (0.05% wt/wt)	0.9599 (0.0011)
Blue dyed 0.1 Pa.s silicone oil (0.05% wt/wt)	0.9630 (0.0018)
Blue dyed 1 Pa.s silicone oil (0.05% wt/wt)	0.9743 (0.0044)

*Parentheses give the standard error values of 3 measurements

3.4.3 Measuring the viscosity of liquid binder

The viscosity of 0.05% wt/wt blue dyed silicone oils was determined using a rheometer (Figure 3.8). The model of the rheometer was a Modular Compact Rheometer MCR 502 (Anton Paar, Austria). The software used was Anton Paar RheoCompass s1.14, version 1.14.494.0 (Anton Paar, GmbH). This apparatus uses a cone type of plate with angle 2° and the diameter of the plate is 50 mm. The wide plate diameter was chosen to ensure it could be fully covered by the liquid binder for adequate measurement of the viscosity. At least two measurements of viscosity were taken for each sample and averaged.

Figure 3.9 shows the logarithmic plot of viscosities of the dyed silicone oil solutions as a function of shear rate at a constant temperature of 25°C. For the silicone oil liquids, there is no observable dependence of viscosity on shear rate in the ranges studied, indicating a Newtonian fluid behaviour.



Figure 3.8 Modular Compact Rheometer MCR 502

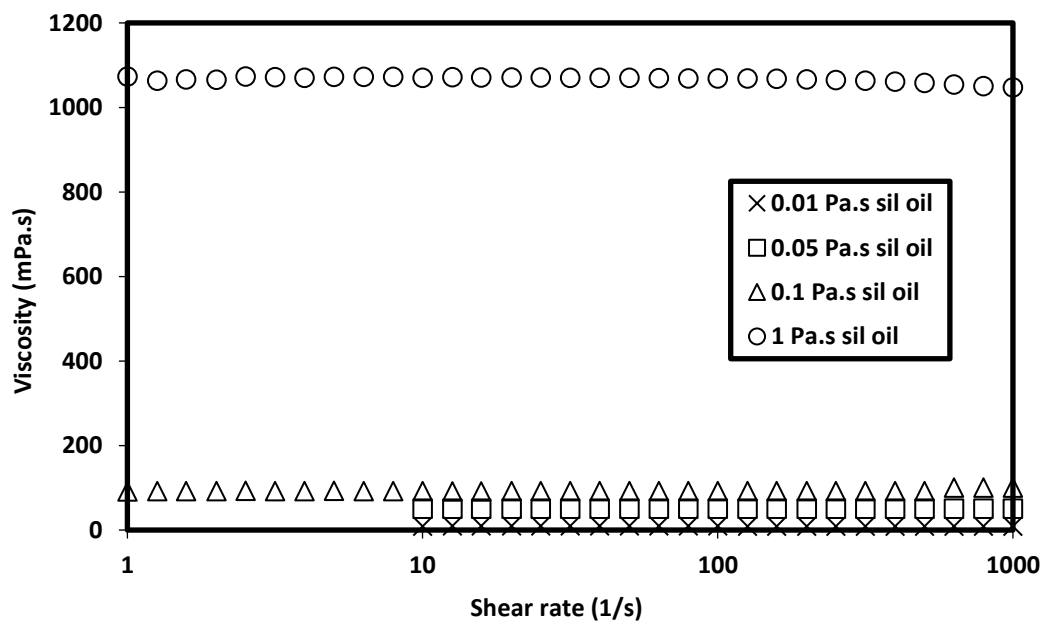


Figure 3.9 The logarithmic plot of viscosity of blue dyed silicone oil solutions as a function of shear rate, at a constant temperature of 25°C

Table 3.7 lists the viscosity of the liquid binders. The measured viscosity values were compared to the standard values for the silicone oils. It can be seen that the measured values were very similar to the standard values. The addition of 0.05% wt/wt blue dye did not make any significant difference to the viscosity of the liquid binders.

Table 3.7 Viscosity of liquid binder

Liquid binder	Standard value (Pa.s)	Measured value (Pa.s)
Blue dyed 0.01 Pa.s silicone oil (0.05% wt/wt)	0.01	0.0086 (0.0004)
Blue dyed 0.05 Pa.s silicone oil (0.05% wt/wt)	0.05	0.0504 (0.0002)
Blue dyed 0.1 Pa.s silicone oil (0.05% wt/wt)	0.1	0.0989 (0.001)
Blue dyed 1 Pa.s silicone oil (0.05% wt/wt)	1	1.0662 (0.0137)

*Parentheses give the standard error values of a minimum of 2 measurements

3.5 Formulation of different paste materials

This section describes the methods used to make the pastes of different formulations. These pastes will subsequently be used for forming the pellets.

3.5.1 Measuring volume of solid and density of solid

The desired mass of the powders, m_s , were weighed out. The density of powders, ρ_s , was determined based on the method described in Section 3.3.3. The volume of solid, V_s , can be calculated using Equation 3.6.

$$V_s = \frac{m_s}{\rho_s} \quad \text{Equation 3.6}$$

Where:

V_s =	Volume of solid	(m ³)
m_s =	Mass of solid	(kg)
ρ_s =	Density of powder	(kg/ m ³)

3.5.2 Calculating the void volume in the paste

The known total volume of a pellet can be calculated from known values of height and diameter of the die, which is the size of the die. Therefore, the total volume of the paste is equal to the volume of the pellet. The total volume of the paste, V_T , comprises the solid volume, V_s , and the void volume, V_v . The void volume, V_v , is also equivalent to the mixture of the air volume, V_a , and the liquid volume, V_l as shown in Equations 3.7 and 3.8.

$$V_T = V_s + V_v \quad \text{Equation 3.7}$$

$$V_T = V_s + (V_a + V_l) \quad \text{Equation 3.8}$$

Therefore, the void volume, V_v , can be calculated using Equation 3.9:

$$V_v = V_T - V_s \quad \text{Equation 3.9}$$

Where:

V_T =	Total volume	(m ³)
V_s =	Solid volume	(m ³)
V_v =	Void volume	(m ³)
V_a =	Air volume	(m ³)
V_l =	Liquid volume	(m ³)

3.5.3 Calculating liquid volume and air volume in the paste

The pore saturation influences the properties of the paste. For these experiments, the ideal saturation, s , gives a paste texture which is neither crumbly nor wet and sticky. The liquid volume, V_l , can be calculated using the desired saturation value (Equations 3.10 to 3.12).

$$s = \frac{V_l}{V_v} \quad \text{Equation 3.10}$$

$$s = \frac{V_l}{V_a + V_l} \quad \text{Equation 3.11}$$

$$V_l = s * V_v \quad \text{Equation 3.12}$$

Based on liquid volume and void volume, air volume can be calculated using Equations 3.13 and 3.14.

$$V_v = V_a + V_l \quad \text{Equation 3.13}$$

$$V_a = V_v - V_l \quad \text{Equation 3.14}$$

Where:

$s =$	Saturation	(g/ml)
$V_v =$	Volume of void	(ml)
$V_a =$	Volume of air	(ml)
$V_l =$	Volume of liquid	(ml)

3.5.4 Calculating the mass of the paste

The mass of paste was determined from the mixture of mass of powders and liquid binder. The solid/liquid binder ratio in the pellet, R can be calculated using Equation 3.15:

$$R = \frac{m_s}{m_l} \quad \text{Equation 3.15}$$

Where:

$R =$	Ratio	
$m_s =$	Mass of solid	(g)
$m_l =$	Mass of liquid	(g)
$\rho_s =$	Density of solid	(g/ml)
$\rho_l =$	Density of liquid	(g/ml)
$V_s =$	Volume of solid	(ml)
$V_l =$	Volume of liquid	(ml)

3.5.5 Methods for making the paste

Two methods to form the paste have been identified. The first method is kneading by hand the mixture of liquid binder and powders in a plastic bag (Figure 3.10 (left)). As shown in Figure 3.10 (right), the distribution of the liquid binder with the powders was visibly inhomogeneous, with liquid binder localized at certain parts of the powders. The second method is pre-mixing the mixture in a beaker (Figure 3.11 (left)). This was chosen over the first method due to a more uniform distribution of the liquid binder and powders as observed visually (Figure 3.11 (right)).



Figure 3.10 Hand-kneading the mixture in a plastic bag (left) and localization of liquid binder within powders (right)

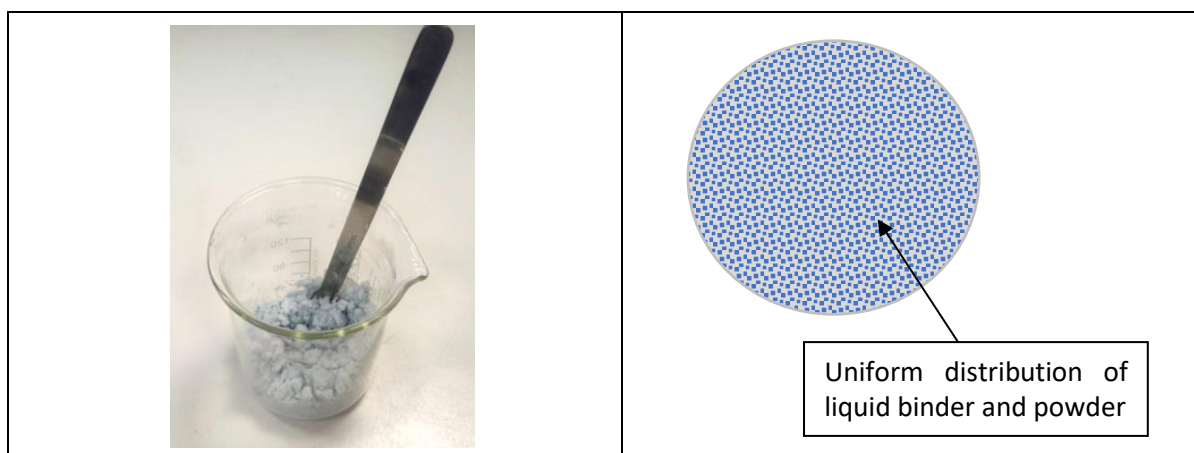


Figure 3.11 Pre-mixing the mixture in a beaker (left) and uniform distribution of the liquid binder and powder (right)

Based on the calculated ratio and known mass, the powders and liquid binder were mixed in a beaker until a homogenous mixture was formed. A trial-and-error experiment was performed to ensure the texture of the paste was neither sticky nor crumbly, and could be easily shaped into the die. A list of formulations for the ballotini glass beads, lactose and MCC paste is given in Tables 3.8 to 3.10. An indication given by a “tick” was chosen as the best paste formulation for each combination of powder and liquid binder. Whereas, paste formulation between wet and crumble was given by a “cross” indication.

Table 3.8 Ballotini glass beads paste formulations

Powder	Liquid binder	S=0.50	S=0.53	S=0.55
Ballotini glass beads	Blue dyed 0.01 Pa.s silicone oil (0.05% wt/wt)	R=6.7392	R=6.3578	R=6.1266
		mL=10 g	mL=10 g	mL=10 g
		mS=67.392 g	mS=63.578 g	mS=61.266 g
		Crumbly	Bit crumbly	✓
Powder				
Powder	Liquid binder	S=0.50	S=0.53	
Ballotini glass beads	Blue dyed 0.05 Pa.s silicone oil (0.05% wt/wt)	R=6.5546	R=6.1836	
		mL=10 g	mL=10 g	
		mS=65.546 g	mS=61.836 g	
		✗	✓	
Powder				
Powder	Liquid binder	S=0.50	S=0.53	
Ballotini glass beads	Blue dyed 0.1 Pa.s silicone oil (0.05% wt/wt)	R=6.5335	R=6.1637	
		mL=10 g	mL=10 g	
		mS=65.335 g	mS=61.637 g	
		✗	✓	
Powder				
Powder	Liquid binder	S=0.50	S=0.53	
Ballotini glass beads	Blue dyed 1 Pa.s silicone oil (0.05% wt/wt)	R=6.4577	R=6.0922	
		mL=10 g	mL=10 g	
		mS=64.577 g	mS=60.922 g	
		Crumbly		✓

Where:

S = Saturation (-)
 R= Ratio (-)
 mL= Mass of liquid (g)
 mS = Mass of solid (g)

Table 3.9 Lactose paste formulations

Powder	Liquid binder	S=0.40	S=0.5	S=0.33	S=0.30
Lactose	Blue dyed 0.01 Pa.s silicone oil (0.05% wt/wt)	R=2.0531	R=1.64245	R=2.4886	R=2.7374
		mL=10 g	mL=10 g	mL=10 g	mL=10 g
		mS=20.531 g	mS=16.4245 g	mS=24.886 g	mS=27.374 g
		Sticky	Sticky	Bit Sticky	✓
Powder	Liquid binder	S=0.50	S=0.40	S=0.35	S=0.30
Lactose	Blue dyed 1 Pa.s silicone oil (0.05% wt/wt)	R=1.5738	R=1.9673	R=2.2483	R=2.6231
		mL=10 g	mL=10 g	mL=10 g	mL=10 g
		mS=15.738 g	mS=19.673 g	mS=22.483 g	mS=26.231 g
		Too sticky, wet	Sticky	Bit sticky	✓

Table 3.10 MCC paste formulations

Powder	Liquid binder	S=0.50	S=0.45	S=0.4	S=0.55	S=0.53
MCC	Blue dyed 0.01 Pa.s silicone oil (0.05% wt/wt)	R=0.9804	R=1.0894	R=1.2255	R=0.8913	R=0.9249
		mL=10 g	mL=10 g	mL=10 g	mL=10 g	mL=10 g
		mS=9.804 g	mS=10.894 g	mS=12.255 g	mS=8.913 g	mS=9.249 g
		Crumbly	✗	✗	✓	Bit crumbly
Powder	Liquid binder	S=0.50	S=0.55	S=0.53	S=0.54	
MCC	Blue dyed 1 Pa.s silicone oil (0.05% wt/wt)	R=0.9395	R=0.8541	R=0.8863	R=0.8699	
		mL=10 g	mL=10 g	mL=10 g	mL=10 g	
		mS=9.395 g	mS=8.541 g	mS=8.863 g	mS=8.699 g	
		Crumbly	Too sticky	Bit crumbly	✓	

Where:

S =	Saturation	(-)
R=	Ratio	(-)
mL=	Mass of liquid	(g)
mS =	Mass of solid	(g)

Tables 3.11 describes the selected paste formulations for the combinations of powder and liquid binder. The desired saturation, s , and ratio of solid to liquid binder mass, R , were used to formulate the different pastes. Different viscosities of liquid binders caused the liquid saturation to be 0.3 to 0.55. The ratio of solid to liquid binder mass for glass beads formulations was in the order of 6 across the different formulations.

Table 3.11 Selected formulations of the different pastes

Powders	Liquid binders	Saturation, s	Ratio, R (solid/liquid)
Ballotini glass beads	Blue dyed $0.01 Pa.s$ silicone oil (0.05% wt/wt)	0.55	6.1266
	Blue dyed $0.05 Pa.s$ silicone oil (0.05% wt/wt)	0.53	6.1836
	Blue dyed $0.1 Pa.s$ silicone oil (0.05% wt/wt)	0.53	6.1637
	Blue dyed $1 Pa.s$ silicone oil (0.05% wt/wt)	0.53	6.0922
Lactose	Blue dyed $0.01 Pa.s$ silicone oil (0.05% wt/wt)	0.3	2.7374
	Blue dyed $1 Pa.s$ silicone oil (0.05% wt/wt)	0.3	2.6231
MCC	Blue dyed $0.01 Pa.s$ silicone oil (0.05% wt/wt)	0.55	0.8913
	Blue dyed $1 Pa.s$ silicone oil (0.05% wt/wt)	0.54	0.8699

3.6 Formation of pellets

Eight types of pellets with a size of 20 mm were prepared from different paste formulations as summarized in Figure 3.12. The nomenclature listed on the left hand side of the figure will be used throughout this thesis.

Ballotini 10 cSt pellet	<ul style="list-style-type: none">•Ballotini glass beads powders•Blue dyed 0.01 Pa.s silicone oil (0.05% wt/wt)
Ballotini 50 cSt pellet	<ul style="list-style-type: none">•Ballotini glass beads powders•Blue dyed 0.05 Pa.s silicone oil (0.05% wt/wt)
Ballotini 100 cSt pellet	<ul style="list-style-type: none">•Ballotini glass beads powders•Blue dyed 0.1 Pa.s silicone oil (0.05% wt/wt)
Ballotini 1000 cSt pellet	<ul style="list-style-type: none">•Ballotini glass beads powders•Blue dyed 1 Pa.s silicone oil (0.05% wt/wt)
Lactose 10 cSt pellet	<ul style="list-style-type: none">•Lactose powders•Blue dyed 0.01 Pa.s silicone oil (0.05% wt/wt)
Lactose 1000 cSt pellet	<ul style="list-style-type: none">•Lactose powders•Blue dyed 1 Pa.s silicone oil (0.05% wt/wt)
MCC 10 cSt pellet	<ul style="list-style-type: none">•MCC powders•Blue dyed 0.01 Pa.s silicone oil (0.05% wt/wt)
MCC 1000 cSt pellet	<ul style="list-style-type: none">•MCC powders•Blue dyed 1 Pa.s silicone oil (0.05% wt/wt)

Figure 3.12 Types of pellets

3.6.1 Properties of the pellets

Table 3.12 lists the properties of the pellets. The shape for all pellets was cylindrical with an aspect ratio of 1. The volume of pellets can be calculated from known values of height and diameter of the pellets. As a result of the pellet voidage, the porosity of pellets allows for volume reduction upon compression. The mass of the paste to make the pellet was determined based on the pre-determined porosity in the pellet and ratio of solid to liquid binder mass, R . The mass of paste was equivalent to the mass of pellet. Furthermore, the density of pellets was determined from the volume and mass of the pellet.

Table 3.12 List of properties of the pellets

	Diameter (m)	Height (m)	Volume of pellet ($\times 10^{-6} \text{ m}^3$)	Pellet porosity (%)	Mass of paste/ pellet (g)	Density of pellet (kg/m^3)
Ballotini 10 cSt pellets	0.02	0.02	6.2832	0.38	11.20	1783
Ballotini 50 cSt pellets	0.02	0.02	6.2832	0.38	11.19	1780
Ballotini 100 cSt pellets	0.02	0.02	6.2832	0.38	11.19	1781
Ballotini 1000 cSt pellets	0.02	0.02	6.2832	0.38	11.21	1784
MCC 10 cSt pellets	0.02	0.02	6.2832	0.6882	6.50	1035
MCC 1000 cSt pellets	0.02	0.02	6.2832	0.6496	7.40	1178
Lactose 10 cSt pellets	0.02	0.02	6.2832	0.3581	8.50	1353
Lactose 1000 cSt pellets	0.02	0.02	6.2832	0.3581	8.60	1369

3.6.2 Methods for making the pellets

A manual hand pressed method was chosen to obtain the desired porosity (refer to Table 3.12) in the pellet and avoid over-deforming the paste. The following steps for producing the pellet were carried out. The desired mass of paste (refer to Table 3.12) was placed in a set of custom-made die, with an internal diameter of 20 mm. It consisted of a cylindrical die, bottom base, head puncher and a spacer (Figure 3.13).

The paste was placed in the cylindrical die with the bottom base. The spacer was positioned in between the die and the head puncher. The paste was manually pressed by hand until the final height; 20 mm was obtained. The spacer was used to ensure the final height of pellet would be 20 mm. The bottom base was pulled out to eject the pellet. Then, the head puncher was pressed down to eject the pellet from bottom. The pellet was removed carefully or shaved off with a small piece of cardboard paper. Care was taken to ensure a smooth surface was produced. Any excess paste on surface of the head puncher and bottom base was cleaned off with a wet paper/tissue. Pressing on both sides of the pellet is necessary to produce smooth surfaces at both the top and bottom of the pellet. This can be done by exchanging the position of the bottom base and the head puncher, and hand pressed for a second time. If the shape of the pellet is not well-shaped during the pressing, the paste can be reshaped and reused again for making a new pellet.

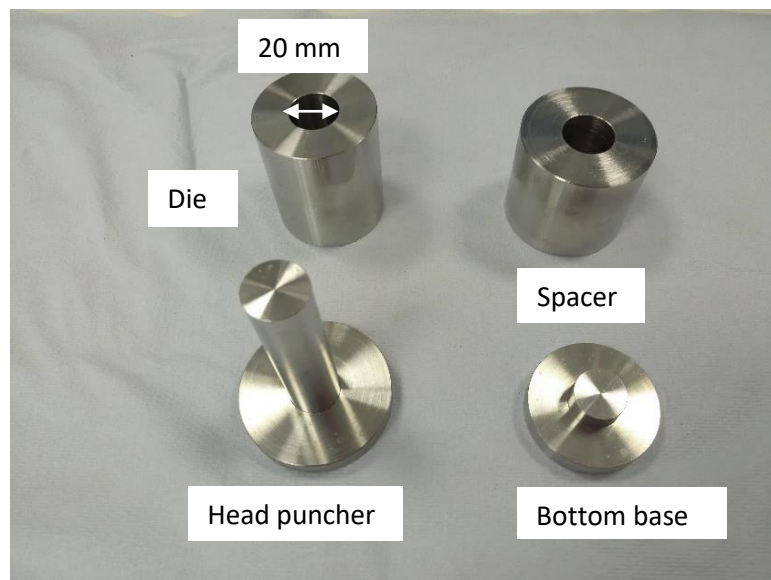


Figure 3.13 Custom-made die, bottom base, head puncher and spacer

3.7 Summary

This chapter has described the materials used in this research and the methodology and results for material property characterisation. The preparation of paste formulations and production of pellets was also given. The next chapter gives the methodology and results for the mechanical properties of pellets obtained from quasi-static and dynamic compression test.

4 Mechanical properties of granular pellets

4.1 Introduction

In this chapter, mechanical properties such as Young's modulus, plastic and elastic stiffness and yield stresses of granular pellets were experimentally measured from two different types of compression tests, namely quasi-static and dynamic compression tests. The methods for performing the compression testing of the pellets are described in this chapter, and the results are discussed. The quasi-static compression properties such as Young's modulus, plastic and elastic stiffness were measured and used as the input materials in the DEM simulations. Yield stresses of pellets were measured from the dynamic compression test and further used as the input parameter for comparison in the failure theory. Eight types of pellets, as described in Table 3.12, Chapter 3, were tested using the quasi-static compression test. Five types of pellets (ballotini 10cSt, ballotini 50cSt, ballotini 100cSt, ballotini 1000cSt and lactose 10cSt) were chosen for the dynamic compression test.

4.2 Experimental methodology

4.2.1 Quasi-static compression test

Quasi-static compression tests were conducted to obtain the properties of the pellets (e.g. Young's modulus, plastic and elastic stiffness) for further use in DEM simulations. The tests were performed using an Instron 5500R/1175 Universal Testing Machine (Instron Ltd, UK) with a load cell at the bottom adjustable crosshead (Figure 4.1).

The speed was set for 0.02 mm/s during the compression (loading part), and zero during releasing (unloading part). The loading and unloading parts in one cycle were obtained before the pellet yielding point occurred. This relatively slow speed was able to capture the linear portion of the force-displacement loading curve during the compression test. A single pellet was compressed between a lower steel plate and an upper steel plate in the axial direction (Figure 4.2). The pellets were relatively soft and fragile; therefore, the axial direction for quasi-static compression test could avoid the initial crack /splitting of the pellet at the early stage of compression testing.

and load cells of 10 N (for all types of ballotini pellets and MCC pellets) and 100 N (for all types of lactose pellets). Instron Bluehill software was used to record the measured compression force-displacement data for both loading and unloading stages at the end of the testing.



Figure 4.1 Instron 5500R/1175 Universal Testing Machine

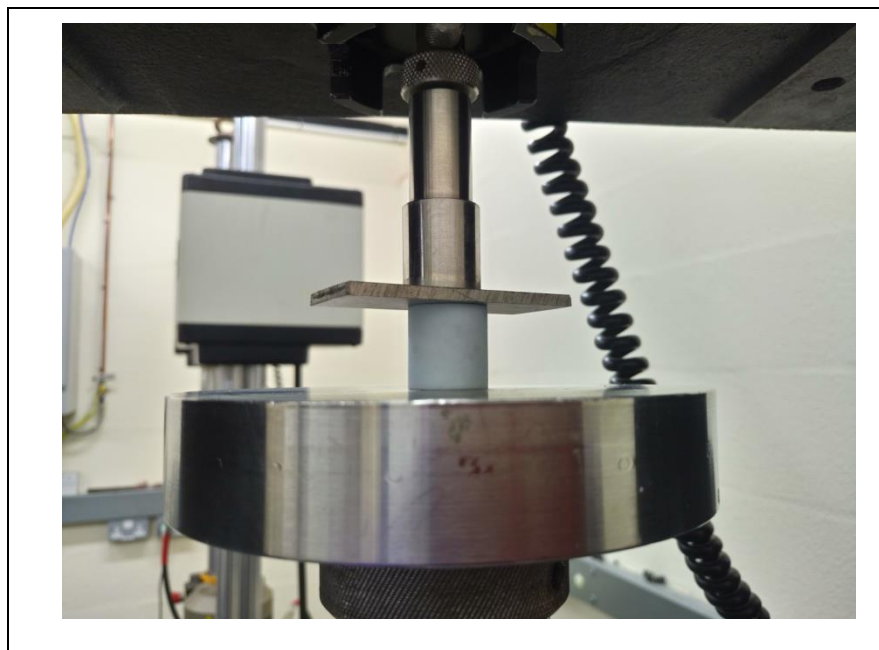


Figure 4.2 Image of pre-test pellet

4.2.2 Dynamic compression test

A dynamic compression test for determining the dynamic yield stress of pellets was performed using an Instron Electropuls E1000 testing machine (Instron Ltd, High Wycombe, UK) with a load cell at the bottom adjustable crosshead (Figure 4.3). Five types of pellets (ballotini 10cSt, ballotini 50cSt, ballotini 100cSt, ballotini 1000cSt and lactose 10cSt) were compressed at four different speeds between 1 and 125.7 mm/s. In the dynamic compression test, data for the loading part until the pellet yielding point occurred were considered. The highest compression speed of 125.7 mm/s was equivalent to the lowest rotational speed in the annular shear cell; 15 rpm. However, the shear rate as experienced by the pellets in the annular shear cell are expected to be lower than the shear rate of top lid of the annular shear cell, as shear bands form within the shearing medium. Two different load cells, 50 and 100 N, were used during the compression test. The load cell of 100 N was only used for lactose 10cSt pellets compressed at the highest compression speed 125.7 mm/s. The pellet was compressed until reaching 60% of axial strain. The set-up conditions for the test are given in Table 4.1.



Figure 4.3 Instron Electropuls E1000 testing machine

Table 4.1 Set-up conditions for the dynamic compression test

Condition	Value
Load cell nominal force (N)	50 and 100
Compression velocity (mm/s)	1, 10, 50 and 125.7
The diameter of the pellet (mm)	20
The initial height of pellet (mm)	20
The final height of pellet after compression (mm)	8
Axial strain (%)	60
Distance travelled during compression (mm)	22
Gap between top platen and pellet (mm)	10
Initial platens height apart before compression (mm)	30

The dynamic compression test method is explained as follows. The first step was to create the test file on the computer, i.e., the compression speed, the location to save the data results and the end point of the test. The pellet was positioned axially between the two parallel platens, the same as in the quasi-static compression test (see Figure 4.2). According to previous study by (R M Smith, 2007), the axial position of the pellet could provide a clear noticeable point; a yielding point for the pellet. In Figure 4.4, both top and bottom platens were set 30 mm apart. The top platen was placed 10 mm apart from the top of the pellet allowing enough space for rapid compression speed. The bottom platen was in the stationary condition. The pellet was subjected to a prescribed load until reaching 60% of axial strain. The final height of the pellet was 8 mm. The force data obtained from the load cell and increasing displacements were recorded using Instron Bluehill software.

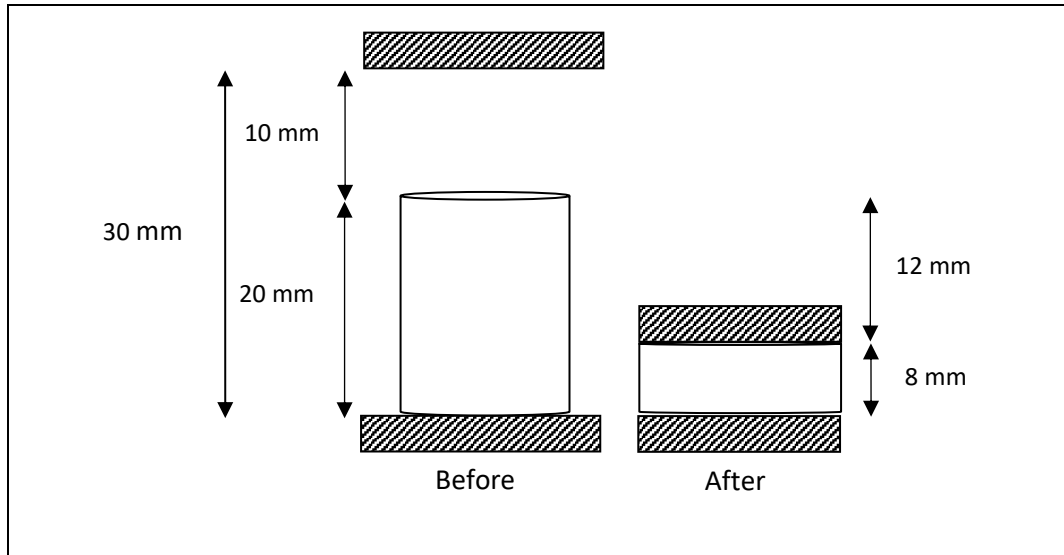


Figure 4.4 Initial position of the pellet before and after the dynamic compression test

4.3 Methods of analysis

4.3.1 Analysis of raw data from the compression test

During compression tests, the pellet's height/length and cross-sectional area change over the time. As a result, the volume of the pellet is changed over the time. A true stress-strain curve is preferable for accurate measurement of the behaviour of pellets, as it considers the actual (instantaneous) dimensions of the deformed pellets. The force-displacement raw data obtained from both quasi-static and dynamic compression tests can be converted to a true stress-strain curve according to the following steps: 1) determining the zeroed force-displacement point; 2) determining instantaneous height of the pellet at each data point (any time); 3) determining instantaneous cross-sectional area of the pellet for each data point (any time) and 4) Solving the equations for true stress and true strain.

The moment when the platen first comes in contact with the pellet was identified by noting where the force starts to increase. Some small variations at the early stages of compression were neglected and these variations were different for types of pellets and compression speeds. The zeroed force and displacement values were obtained once the pellet and platen were in contact. This can be done by subtracting the initial height from each of the platen position values; resulting in a start position of 0 mm. The same step was applied for zeroing the forces, by which the force values prior to the pellet-platen contact were subtracted from each of the force values, giving a starting force of zero. The

instantaneous height of the pellet at each moment of time, H_i , can be obtained by subtracting the platen position (after pellet and platen in contact) from the initial pellet height of 20 mm, H_o .

The instantaneous cross-sectional area of the pellet for each data point (any time), A_i , can be calculated using Equation 4.1:

$$A_i = \frac{A_o H_o}{H_i} \quad \text{Equation 4.1}$$

The instantaneous volume of the pellet for each data point (any time), V_i can be solved using Equation 4.2:

$$V_i = A_i H_i \quad \text{Equation 4.2}$$

where:

A_o =	Initial cross-sectional area of pellet	(m ²)
A_i =	Instantaneous cross-sectional area (at any time)	(m ²)
H_o =	Initial height of pellet	(m)
H_i =	Instantaneous height of the pellet (at any time)	(m)
V_i =	Instantaneous volume of the pellet (at any time)	(m ³)

In Equation 4.3, true stress, σ_t , is the load force, F , divided by the actual (instantaneous) cross sectional area, A_i , over which deformation is occurring. It can be calculated by substituting A_i (from Equation 4.1) into the true stress equation, σ_t (Equations 4.4 and 4.5)

$$\sigma_t = \frac{F}{A_i} \quad \text{Equation 4.3}$$

$$\sigma_t = \frac{F}{\frac{A_o H_o}{H_i}} \quad \text{Equation 4.4}$$

$$\sigma_t = \frac{F \cdot H_i}{A_o H_o} \quad \text{Equation 4.5}$$

where:

σ_t =	True stress	(Pa)
F =	Applied force	(N)
A_i =	Instantaneous cross-sectional area (at any time)	(m ²)

The true strain, ε , is the rate instantaneous increase in the pellet height which can be determined using Equations 4.6 and 4.7.

$$\varepsilon = \int_{H_o}^{H_i} \frac{dH}{H} \quad \text{Equation 4.6}$$

$$\varepsilon = \ln(H_i - H_o) \quad \text{Equation 4.7}$$

The final definition of the true strain (positive value) is shown in Equation 4.8. The displacement was converted into the true strain (not engineering strain) by taking the negative logarithm of the pellet height divided by the initial height of the pellet.

$$\varepsilon = -\ln \frac{H_i}{H_o} \quad \text{Equation 4.8}$$

where:

ε =	True strain	(mm/mm)
H_o =	Initial height of pellet	(mm)
H_i =	Instantaneous height of the pellet (at any time)	(mm)

4.3.2 Characterising the regions of the force-displacement curve from the quasi-static compression test

Based on previous works by (Mattucci & Cronin, 2015), four regions were obtained from the non-linear pattern of force-displacement curve; 1) Toe region (Point OA), 2) Linear region (Point AB), 3) Traumatic region (Point BC) and 4) Post failure (after Point C) (Figure 4.5). It can be seen that the curve was non-linear in fashion and similar in shape to the force-displacement curves generated in this work under the quasi-static compression test, as shown in Figure 4.6.

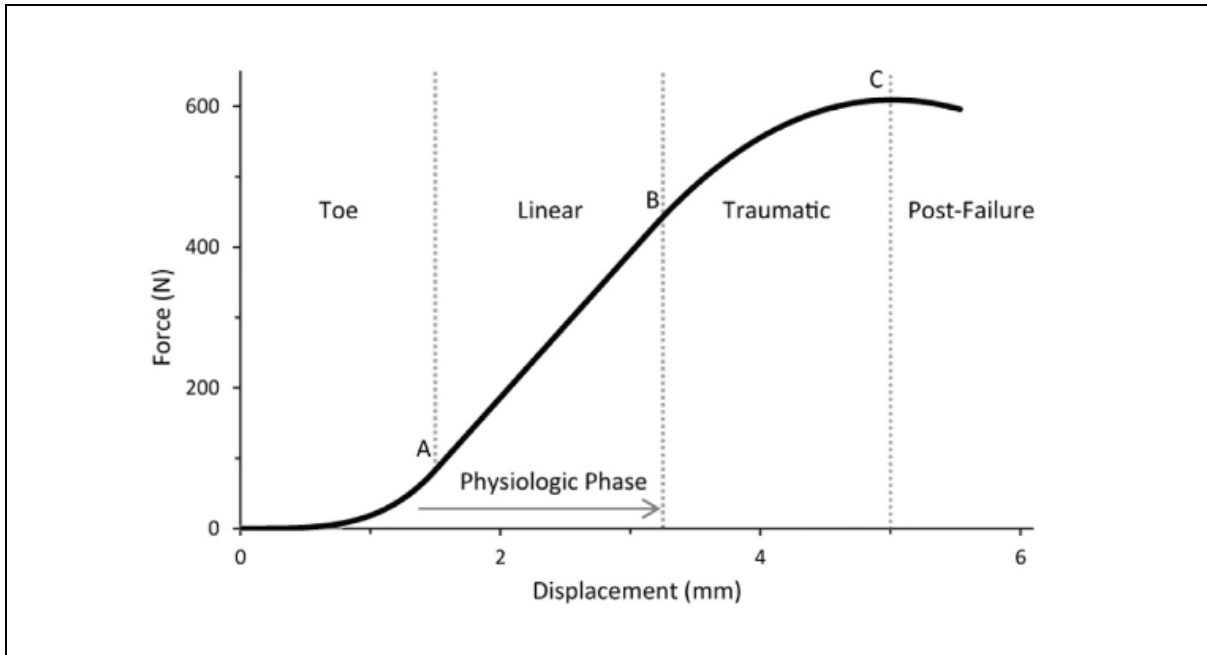


Figure 4.5 Regions from the non-linear force-displacement curve based on (MattuCCI & Cronin, 2015) works

As seen in Figure 4.6, a non-linear curve of force and displacement relationship was presented for compression of a ballotini 10cSt pellet compressed with 10 N and compression speed of 0.02 mm/s. The force-displacement curve before the pellet failure/breakage was used for measuring the plastic and elastic stiffness. Under compressive loading, the pellet was assumed to deform plastically with a slope. The slope of the loading part (linear region, line AB) is used for measuring the plastic stiffness, K_1 . The plastic stiffness was characterized from the individual region from the loading part of the force-displacement curve. The compressive unloading followed the line with slope until the unloading path reached the maximum displacement and zero force. The contact was assumed to be elastically deforming. The slope of the initial unloading path was used for measuring the elastic stiffness, K_2 . Three regions can be characterized which are the toe region, linear region and plastic region. The failure region was not considered for the current study as it was not possible to measure the compressive unloading path. The toe region (Point OA) is the initial segment where the displacement does not linearly increase with the applied force. In the linear region (Point AB), the pellet is compressed, but if the force is released, the pellet could return to its original height. This region is also known as the elastic region due to its reversible characteristic. The pellet is assumed to start deforming at the plastic region (Point BC) and finally the pellet breaks if Point C is exceeded.

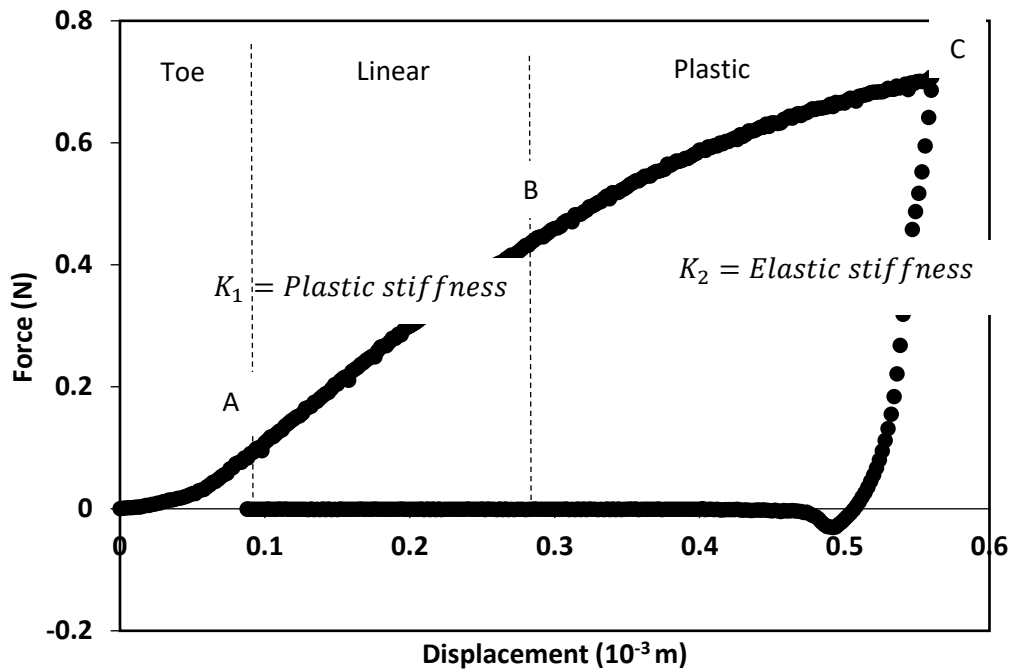


Figure 4.6 Example of a non-linear force-displacement curve obtained from a ballotini 10cSt pellet with 10 N and compression speed of 0.02 mm/s

Previous studies by (Chandrashekar et al., 2008; Lynch, 2003; Mattucci & Cronin, 2015; Quapp & Weiss, 1998) have proposed two methods, namely bi-linear model and multi-curves fit model. The bi-linear model was performed by splitting the non-linear force-displacement curve into two linear models between the toe and linear regions. Previous works by (Chandrashekar et al., 2008) have applied a curve fitting method to identify the approximate points; Point A (the transitions between the toe-linear region) and Point B at the linear region on a stress-strain curve (Figure 4.7). The portion of the stress-strain curve was fitted to the bi-linear model given in Equations 4.9 and 4.10 using a least squares method (Elliott & Setton, 2001; Lynch, 2003).

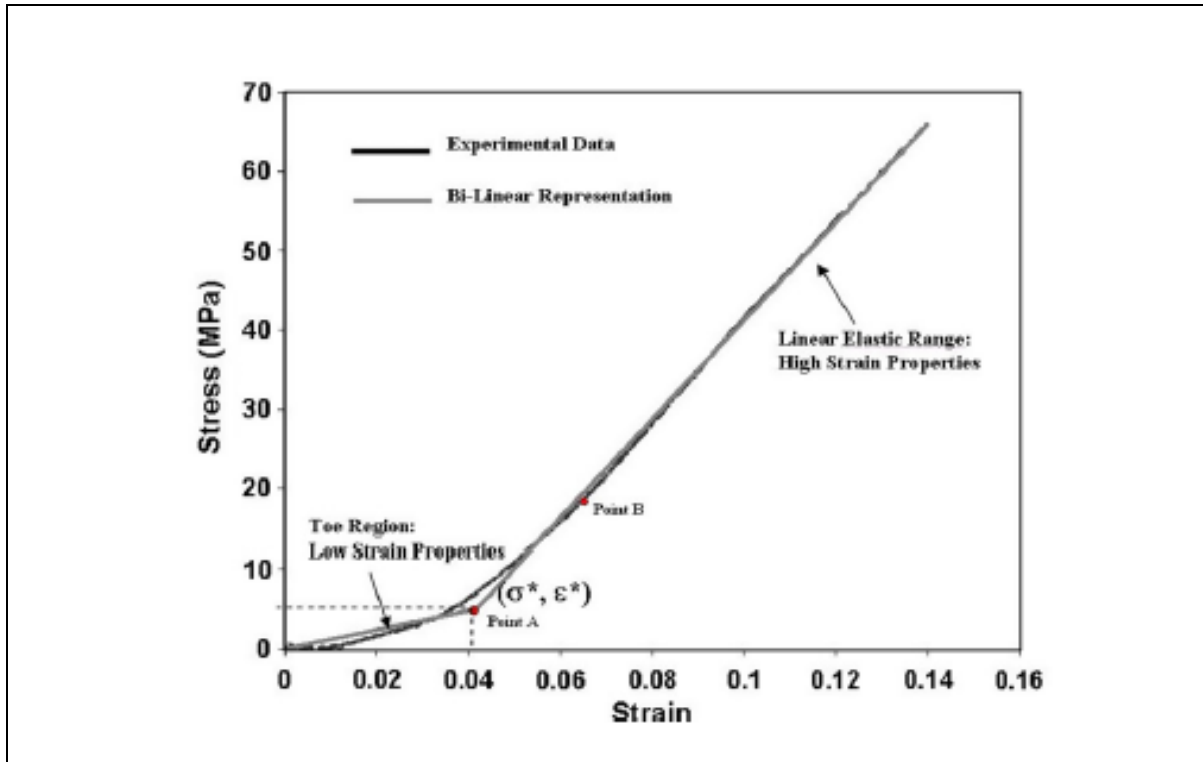


Figure 4.7 Bi-linear model from (Chandrashekar et al., 2008) works

For the toe region, the condition must be $\varepsilon \leq \varepsilon^*$

$$\sigma = E_0 \varepsilon \quad \text{Equation 4.9}$$

For the linear region, the condition must be $\varepsilon > \varepsilon^*$

$$\sigma = E(\varepsilon - \varepsilon^*) + E_0 \varepsilon^* \quad \text{Equation 4.10}$$

where

$\sigma =$	Engineering stress	(MPa)
$\varepsilon =$	Engineering strain	(-)
$\varepsilon^* =$	Strain at the transition point between toe region and the linear region (transition strain)	(-)
$E_0 =$	Modulus of elasticity of the toe region	(MPa)
$E =$	Modulus of elasticity of the linear region	(MPa)

In this study, the bi-linear model could also be considered on the force-displacement curve using Equations 4.11 to 4.13. A combination of two linear models (linear model 1 and linear model 2) represents the bi-linear model. The two linear models; Linear model 1 and Linear model 2 were fitted to the experimental data in toe and linear regions, respectively.

For the toe region, the condition must be $d \leq d^*$

$$F = C_0d \quad \text{Equation 4.11}$$

For the linear region, the condition must be $d > d^*$

$$F = C_1(d - d^*) + C_0d^* \quad \text{Equation 4.12}$$

$$F = C_1d - C_1d^* + C_0d^* \quad \text{Equation 4.13}$$

where

$F =$	Force	(N)
$d =$	Displacement	(m)
$C_0 =$	Slope or stiffness of the toe region	(N/m)
$C_1 =$	Slope or stiffness of the linear region	(N/m)
$d^* =$	Displacement at the transition point from toe to linear region	(-)

The second method, the multi-curves fit model, was based on characterizing the individual regions from the force-displacement curve. Each region from the force-displacement curve was fitted to the exponential curve model (toe region), linear curve model (linear region) and 3rd order polynomial model (traumatic region) using a (GRG) nonlinear optimization solver (Mattucci & Cronin, 2015; Quapp & Weiss, 1998). Referring to Figure 4.8, the transition points between the toe and linear region and between the linear and traumatic region can be determined by fitting the experimental data into an exponential curve, linear curve and 3rd order polynomial models, according to (Quapp & Weiss, 1998) works.

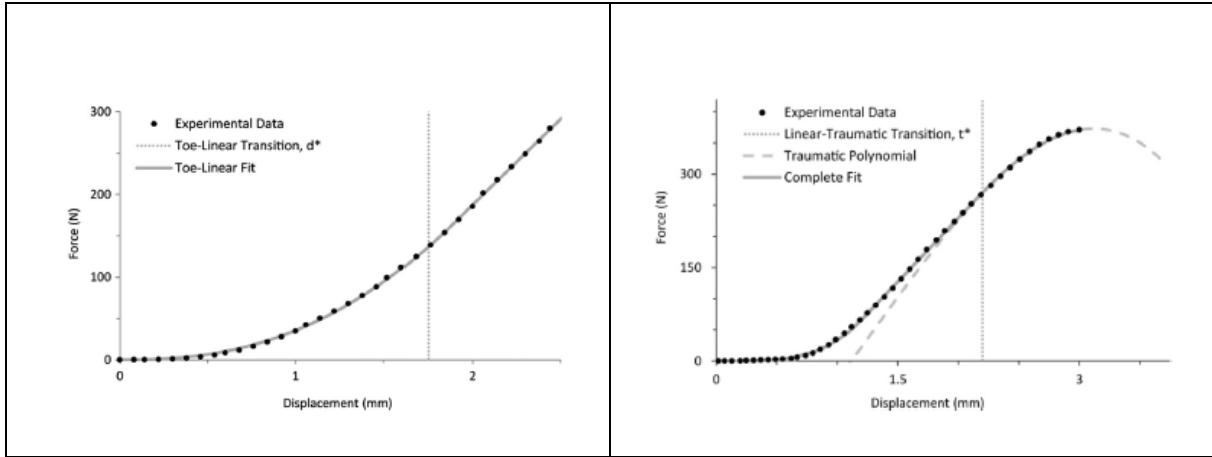


Figure 4.8 Example of multi-curves fit model: toe to linear regions (left) and linear to traumatic regions (right) based on (MattuCCI & Cronin, 2015) works

In this study, the multi-curves model could be applied and a combination of three models were involved: a) an exponential curve model was fitted to the toe region (Equations 4.15 and 4.16); b) a linear curve model was fitted to the linear region (Equations 4.17 and 4.18) and c) a polynomial curve model was fitted to the plastic region (Equation 4.19).

The toe region can be calculated using Equations 4.14 and 4.15:

$$F = C_3(\exp(C_4 \cdot d) - 1)d^{m^*}, \quad d < d^* \quad \text{Equation 4.14}$$

$$F = C_3d^{m^*} \exp(C_4d) - C_3d^{m^*}, \quad d < d^* \quad \text{Equation 4.15}$$

The linear region can be calculated using Equations 4.16 and 4.17:

$$F = F_{d^*} + (d - d^*)C_5, \quad d > d^* \quad \text{Equation 4.16}$$

$$F = F_{d^*} + C_5d - C_5d^*, \quad d > d^* \quad \text{Equation 4.17}$$

The plastic region can be calculated using Equation 4.18:

$$F = Ad^3 + Bd^2 + Cd + D, \quad d > t^* \quad \text{Equation 4.18}$$

where

$F =$	Force	(N)
C_3, C_4, m^*	Toe region constants	(-)
$d =$	Displacement	(m)
$d^* =$	Displacement at the transition point from toe to the linear region	(-)
$F_{d^*} =$	Force at the transition point from toe to the linear region	(N)
$C_5 =$	Slope or stiffness of the linear region	(N/m)
$A, B, C \text{ and } D =$	Constants for the polynomial	
$t^* =$	Displacement at the transition point from linear region to the plastic region	(m)

The transition displacement, d^* , identified at the end of the toe region, was determined using the best fit approach. The slope and forces of the toe and linear regions were equal at d^* . Constraints were applied to limit $m^* \geq 1$ to preserve the characteristic shape. In addition, the slope and force at d^* were set to be equal in both exponential and linear curves. For the curve fits to the plastic region, a 3rd order polynomial model was fit to the plastic region. Constraints were applied to ensure the slope was equal to the linear region at t^* , and the force of the linear and plastic regions were equal at t^* . In addition, the slope and force at t^* were constrained as well to be continuous with the toe or linear region fit.

The curves were fit to maximise the R^2 value by adjusting the variables, $C_3, C_4, m^*, F_{d^*}, C_5, d^*, A, B, C, D$ and t^* using a commercial nonlinear optimization solver (Generalized Reduced Gradient (GRG) Nonlinear Optimization Solver, Excel 2013, Microsoft) to minimize least squares fit. C_5 was identified as the slope of a least squares fit to the linear portion of the curve.

According to (Mattucci & Cronin, 2015), this method could identify the shape of the curve, i.e. toe, linear and plastic regions. They found that the individual coefficients of determination ($R^2 - R$ -square) were 0.989 to 1.000, indicating an excellent fit. In addition, it is a promising and novel method by which a set of scatter experimental data could be fitted using a curve approach to the toe, linear and plastic regions. This method could provide an accurate representation of the test data and the expected material property effects corresponding to varying the deformation rates.

4.3.3 Measuring plastic and elastic stiffness of pellets from quasi-static compression test

The regions of the force-displacement curve from quasi-static compression tests were characterized to determine the values of plastic and elastic stiffness. Both plastic and elastic stiffness were used as the input material properties in DEM simulations in Chapter 6. For this purpose, work by (Mattucci & Cronin, 2015) in Section 4.3.2 was used as the reference to characterise the regions of the non-linear force-displacement curve from the quasi-static compression test in Figure 4.6. Two methods, bi-linear and multi-curves fit models that have been described previously, were tested and the best model that fitted well with the experimental data was then chosen. Further to this, the approximate Points A and B were determined for measuring the slope of the straight line.

The first method, the bi-linear model, was applied to the loading part of the force-displacement curve (Figure 4.9). A combination of two linear models (linear model 1 and linear model 2) represents the bi-linear model. The first linear curve model (linear model 1) was fitted to the toe-linear region, followed by the second linear curve model (linear model 2) to the linear region. The approximate Point A was determined based on the following steps: 1) the square residuals between the fitted data of two linear models were obtained; 2) the minimum value of square residuals between these fitted data of two linear models was identified. The value indicates the intersect for these two linear models has reached as close as possible and 3) the experimental data point at this minimum value of square residuals was the intersect data point and therefore was chosen as the approximate Point A. The approximate Point B could be determined by finding the experimental data point at the minimum value of square residuals between the experimental data in linear region and Linear model 2.

In Figure 4.9, both linear model 1 and linear model 2 have an excellent coefficient of determination, $R^2 = 1$. The approximate Point B could easily be determined from the straight-line portion of linear region but this was not in the case for approximate Point A. It showed that the asymmetric sigmoidal shape profile at the initial force-displacement curve had vanished. The approximate intersection point from the toe region to the linear region, therefore, was difficult to identify. Although this first method is simply a straight forward model by using the combination of two linear models, it is very difficult to interpret the results. It can be seen that the approximate intersection point did not fit well to the experimental data of transition toe-linear region (Figure 4.9). Moreover, the fitting curves for both linear model 1 and linear model 2 deviate from the exponential function data at the transition toe-linear region.

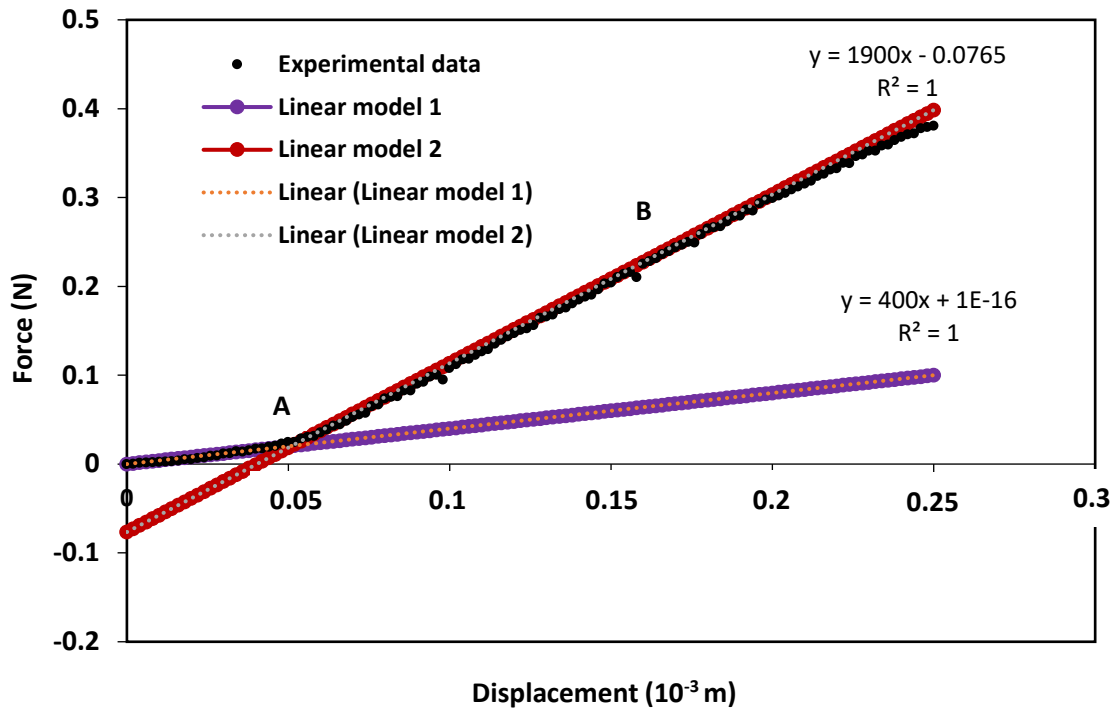


Figure 4.9 Bi-linear model on the loading force-displacement curve for a ballotini 10cSt pellet compressed with 10 N and compression speed of 0.02 mm/s

The asymmetric sigmoidal shape profile at the initial force-displacement curve must be preserved in order to obtain the correct value of Point A. Due to this reason, the second method using the multi-curves fit model was chosen as the method of analysis (Figure 4.10). In this method, both points A and B were determined to identify the linear region. A combination of three curve fitting models was used for this method; exponential curve model, linear curve model and 3rd polynomial model. The intersection between the toe-linear regions and the linear-plastic region was used to determine the approximate Points A and B, respectively. The approximate Point A was determined based on the following steps: 1) the fitted data of exponential curve and linear curve models were obtained; 2) the minimum value of square residuals between these fitted data of two models was identified and 3) The experimental data point at this minimum value of square residuals was chosen as the approximate Point A. Similar steps were applied for approximate Point B. The minimum value of square residuals between linear curve and 3rd polynomial models was obtained. The experimental data point at the minimum value of square residuals was identified and chosen as approximate Point B.

In Figure 4.10, the intersection points can clearly be seen by the combination of these three curve fitting models. Different colours were used to differentiate the three different curve fitting models; 1) purple line for toe region, 2) red line for linear region and 3) green line for plastic region. The second method fitted well to the experimental data and was chosen to determine the most linear region. The portion of the most linear region connecting Points A and B was obtained from Figure 4.10, and was then plotted (Figure 4.11). It was fitted to the linear regression in order to estimate the value of coefficient of determination, R^2 . The coefficient of determination, R^2 , must always be more than 0.99. The slope from this portion of the linear region was the plastic stiffness value.

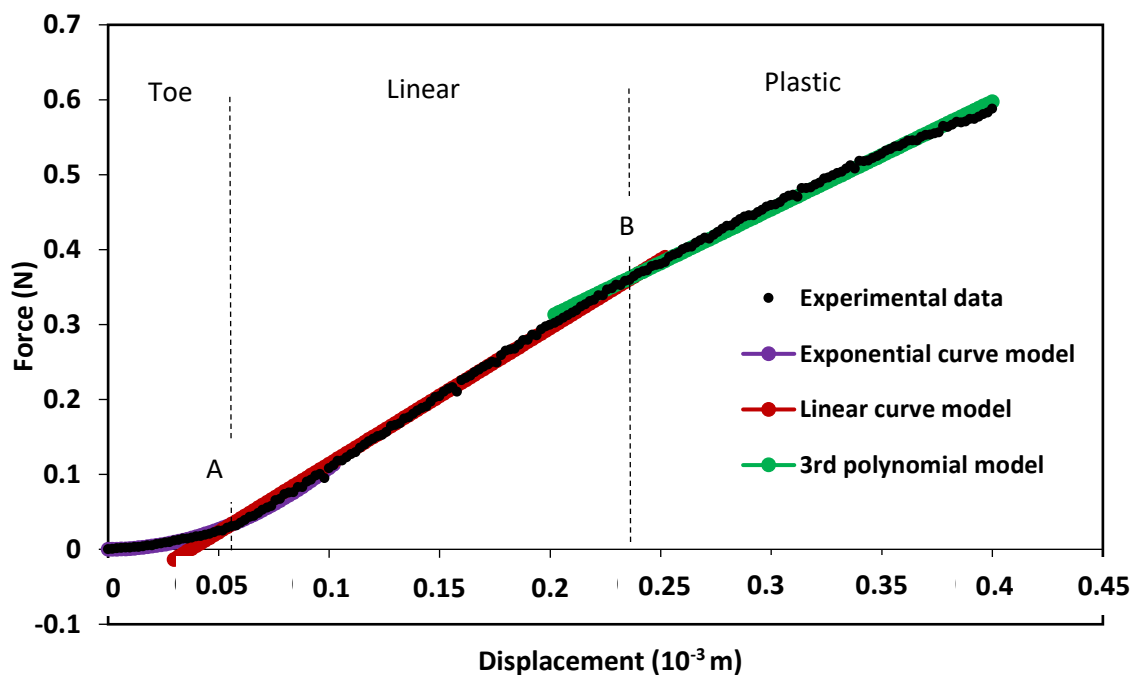


Figure 4.10 Multi-curves fit model on the loading force-displacement curve for a ballotini 10cSt pellet compressed with 10 N and compression speed of 0.02 mm/s

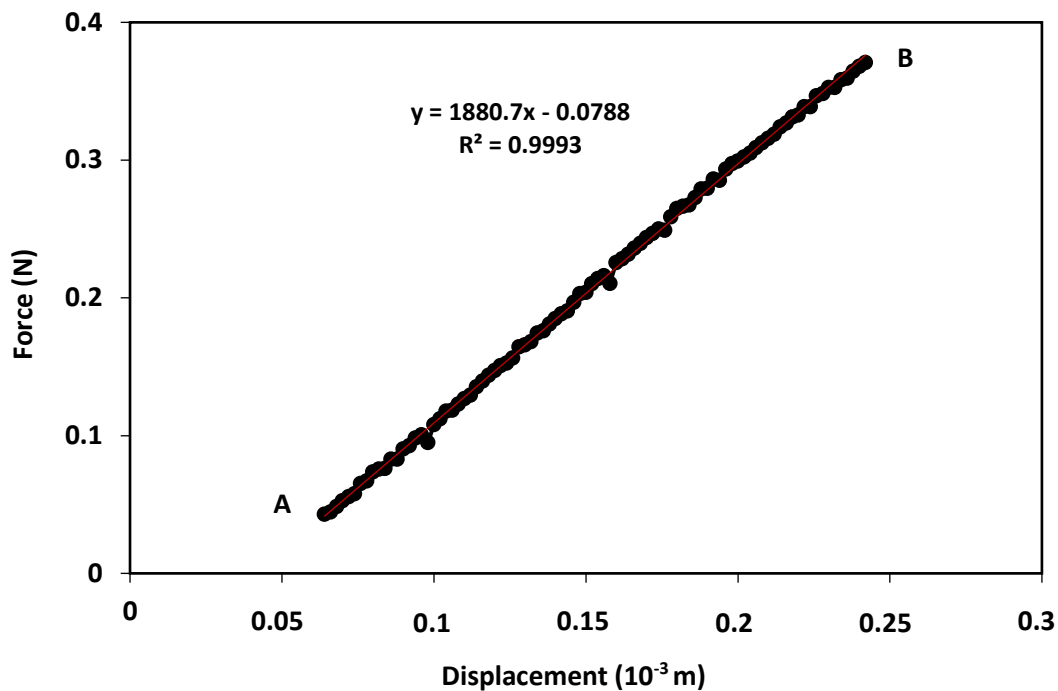


Figure 4.11 Linear regression fitted to the portion of the linear region of the loading force-displacement curve for a ballotini 10cSt pellet compressed with 10 N and compression speed of 0.02 mm/s

The elastic stiffness is defined as the slope of the force-displacement at the initial unloading process (J. Y. Wang et al., 2011). The unloading part of force-displacement curve on Point C in Figure 4.6 was plotted with an additional Point D (Figure 4.12) for measuring the elastic stiffness. Based on Figure 4.12, the approximate Points C and D were determined using the multi-curves fit model to obtain the linear portion from the unloading part. The approximate Point C was determined based on the following steps: 1) the minimum value of square residuals between the experimental data in linear region of the unloading part and fitted data of linear curve model were obtained and 2) the experimental data point at square residuals between the experimental data in linear region and linear curve model was determined. The approximate Point D was determined based on the following steps: 1) the square residuals between the fitted data of exponential and linear curve models were obtained; 2) the minimum value of square residuals between these fitted data of models was identified and 3) the experimental data point at this minimum value of square residuals was the intersect data point and chosen as the approximate Point D. Then, a linear regression was fitted to the linear portion to obtain the slope, which represents the elastic stiffness value (Figure 4.13). At least two replications were taken during the measurements.

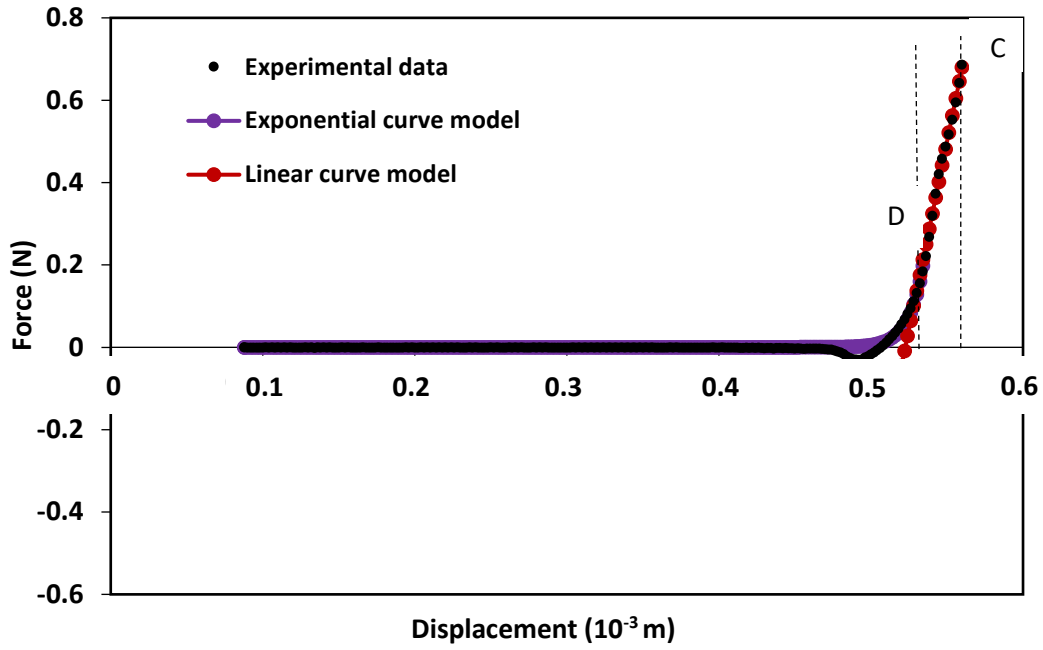


Figure 4.12 Multi-curves fit model on the unloading force-displacement curve for a ballotini 10cSt pellet compressed with 10 N and compression speed of 0.02 mm/s

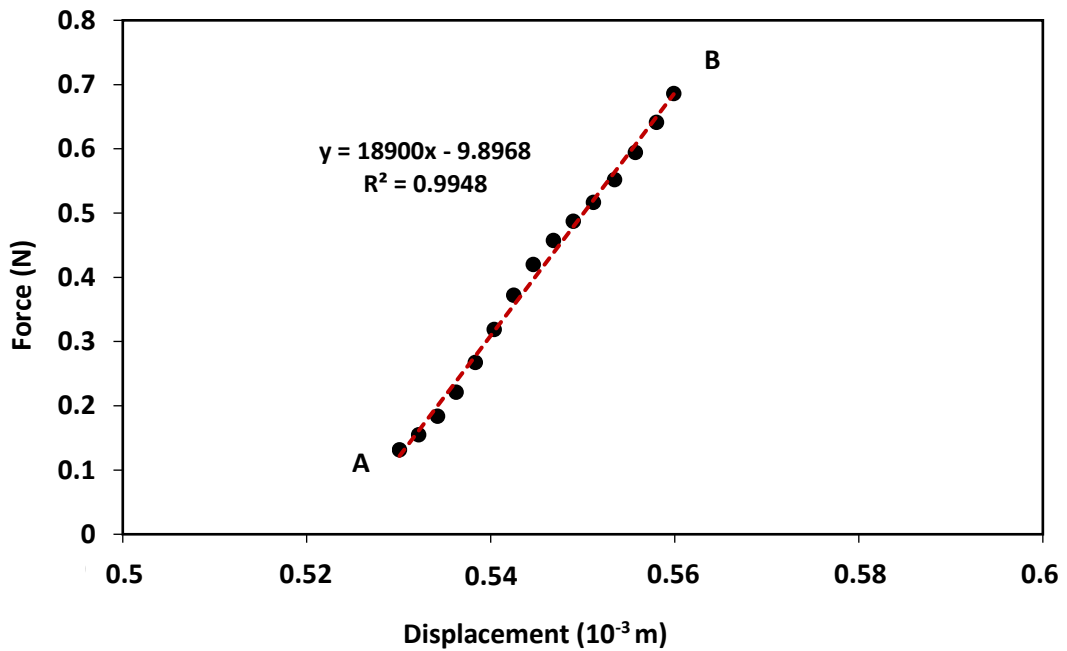


Figure 4.13 Linear regression fitted to the portion of linear region of the unloading force-displacement curve for a ballotini 10cSt pellet compressed with 10 N and compression speed of 0.02 mm/s

4.3.4 Measuring Young's modulus of pellets from the quasi-static compression test

Young's modulus of the pellets, E , is defined as the slope of the linear region from the stress (Pa) versus strain (mm/mm) curve. It is a material property that provides some basic parameters for modelling processes used in computer simulations involving pellets (Šibanc et al., 2013). In this work, it was used to give a better understanding of the elastic properties of the pellets. The values were further used as an input parameter for the DEM simulations. By converting the force-displacement curve (e.g., Figure 4.6) to a stress – strain curve, the Young's modulus of the pellets, E , can be determined.

Figure 4.14 shows an example stress – strain curve for the case of ballotini 10cSt pellets compressed with 10 N and 0.02 mm/s. In Figure 4.15, the linear region connecting approximate Points A to B was determined using the multi-curves fit model. The approximate Point A was determined based on the following steps: 1) the fitted data of exponential curve and linear curve models were obtained; 2) the minimum value of square residuals between these fitted data of two models was identified and 3) the experimental data point at this minimum value of square residuals was chosen as the approximate Point A. The approximate Point B could be determined by finding the experimental data point at the minimum value of square residuals between the experimental data in linear region and linear curve model. The 3rd polynomial model was not in the linear region, therefore, was not considered for determining the approximate Point B. The slope of the straight-line portion was fitted to the linear regression using Equation 4.19. The slope of the linear regression equation represents the Young's modulus, E (Figure 4.16). The minimum coefficient of determination R^2 value must be more than 0.99.

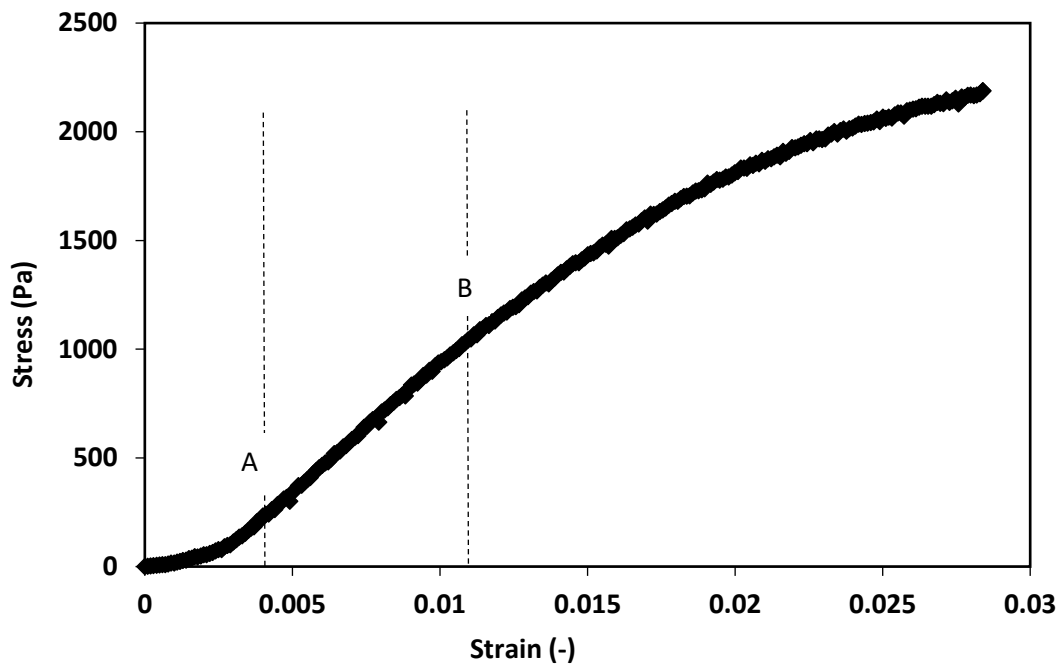


Figure 4.14 Stress (Pa) versus strain (mm/mm) curve for a ballotini 10cSt pellet compressed with 10 N and compression speed of 0.02 mm/s

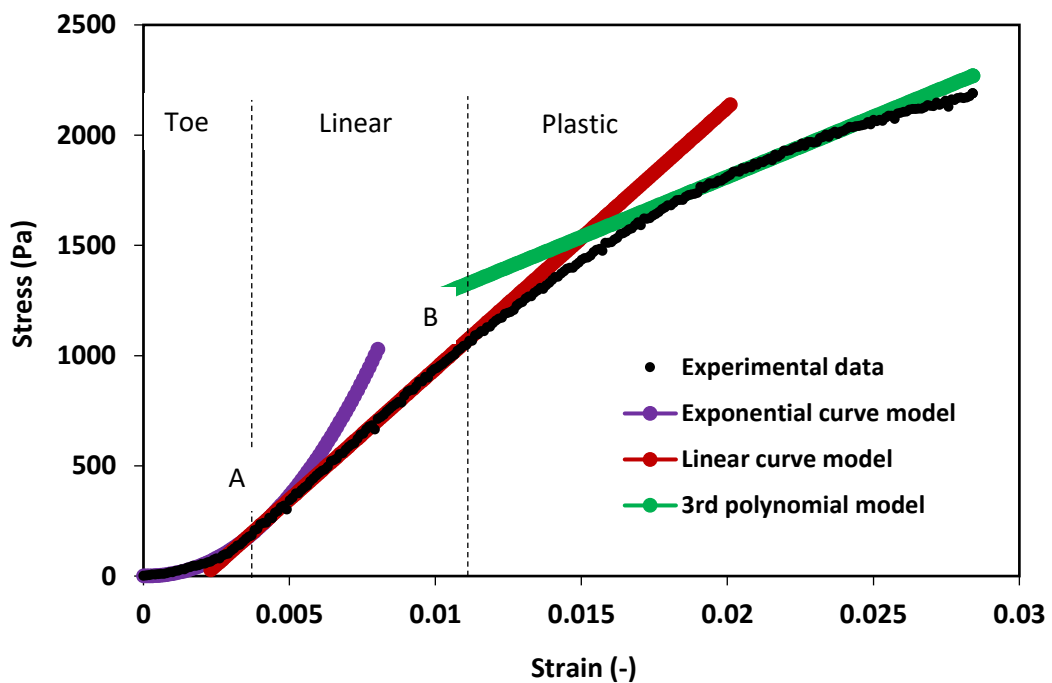


Figure 4.15 The linear region of the stress- strain curve using the multi-curves fit model for a ballotini 10cSt pellet compressed with 10 N and compression speed of 0.02 mm/s

$$\sigma = E\varepsilon + a$$

Equation 4.19

where:

σ =	True stress	(MPa)
E =	Slope (Young's modulus)	(MPa)
ε =	True strain	(mm/mm)
a =	Regression coefficient	(MPa)

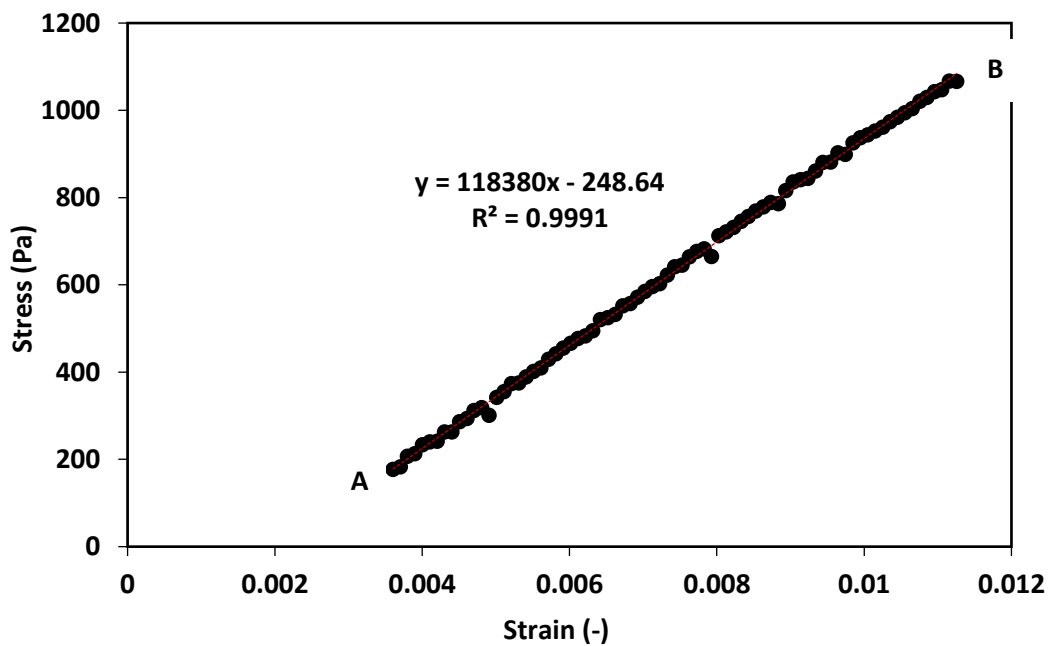


Figure 4.16 Linear regression fitted to the portion of the linear region of the stress – strain curve for a ballotini 10cSt pellet compressed with 10 N and compression speed of 0.02 mm/s

4.3.5 Measuring the yield stress of pellets from the dynamic compression test

The yield stresses of the pellets were determined from the dynamic compression test, which was previously explained in Section 4.2.2. Five types of pellets (ballotini 10cSt, ballotini 50cSt, ballotini 100cSt, ballotini 1000cSt and lactose 10cSt) were tested. The pellets were compressed at prescribed compression speeds and loads of 50 N and 100 N (if applicable). OriginPro 2019 software was utilised for accurate measurement of the yield stress from the stress-strain curve. The peak stress value by which the plastic deformation begins, or where phenomenon of yielding occurs is chosen as the yield stress value. At least two replicates were taken during the measurements.

4.4 Results and discussion

4.4.1 Plastic and elastic stiffness of pellets from the quasi-static compression test

Figure 4.17 and Table 4.2 show the average values for the plastic and elastic stiffness of the pellets. All the measurements were repeated at least 3 times. In general, the ballotini pellets have the lowest plastic stiffness followed by MCC pellets and lactose pellets (the highest plastic stiffness). It was observed that the use of three different powders, ballotini glass beads 63-90 μm , MCC and lactose, have contributed to the variations in values of plastic and elastic stiffness. This could be due to the different physical properties, shapes and structures of the powders (refer to Figures 3.4 to 3.6). In Figure 4.18, increasing the viscosity of silicone oils from 0.01 Pa.s to 1 Pa.s has decreased both the plastic and elastic stiffness of the ballotini pellets.

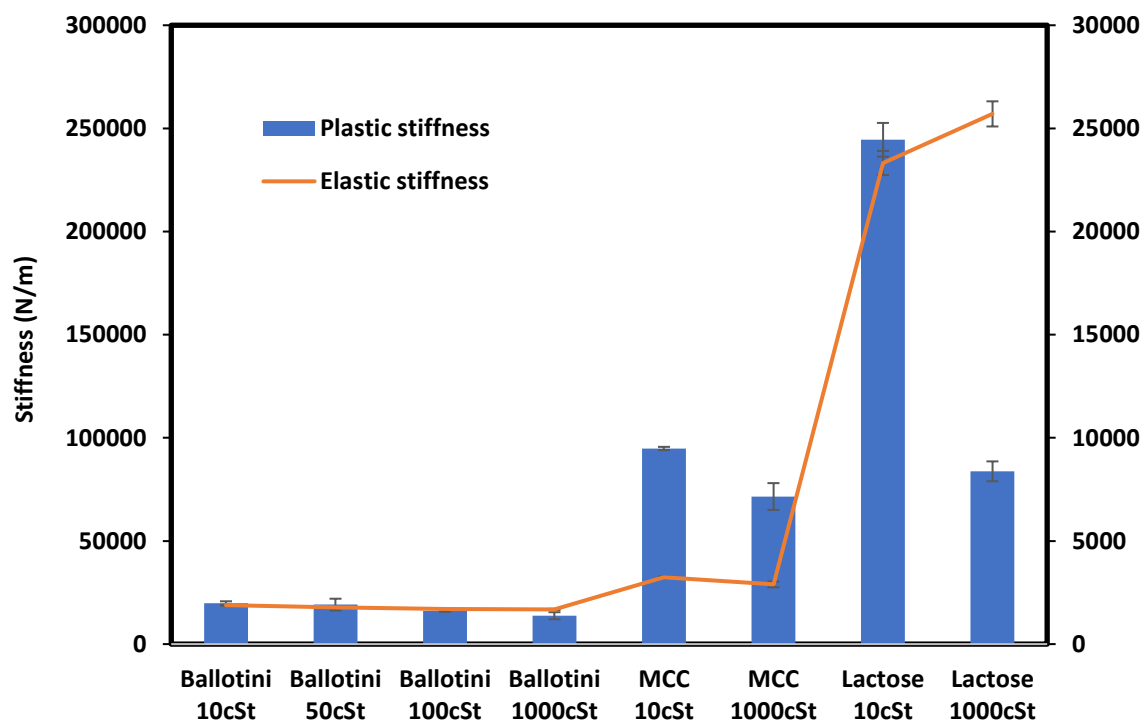


Figure 4.17 Plastic and elastic stiffness of different types of pellets. Error bars represent the standard error values of a minimum of 3 measurements

Table 4.2 Plastic and elastic stiffness of pellets using the quasi-static compression test

Types of pellets	Number of sample, n	Plastic stiffness, k_p (N/m)	Elastic stiffness, k_e (N/m)
Ballotini 10 cSt pellets	3	1983 (92)	18871 (177)
Ballotini 50 cSt pellets	5	1914 (287)	17863 (256)
Ballotini 100 cSt pellets	4	1613 (42)	16971 (184)
Ballotini 1000 cSt pellets	3	1379 (168)	16816 (301)
MCC 10cSt pellets	3	9483 (79)	32406 (381)
MCC 1000cSt pellets	5	7155 (649)	28943 (1397)
Lactose 10cSt pellets	5	24447 (819)	233233 (5846)
Lactose 1000cSt pellets	3	8377 (482)	257036 (6098)

*Parentheses give the standard error values of a minimum of 3 measurements

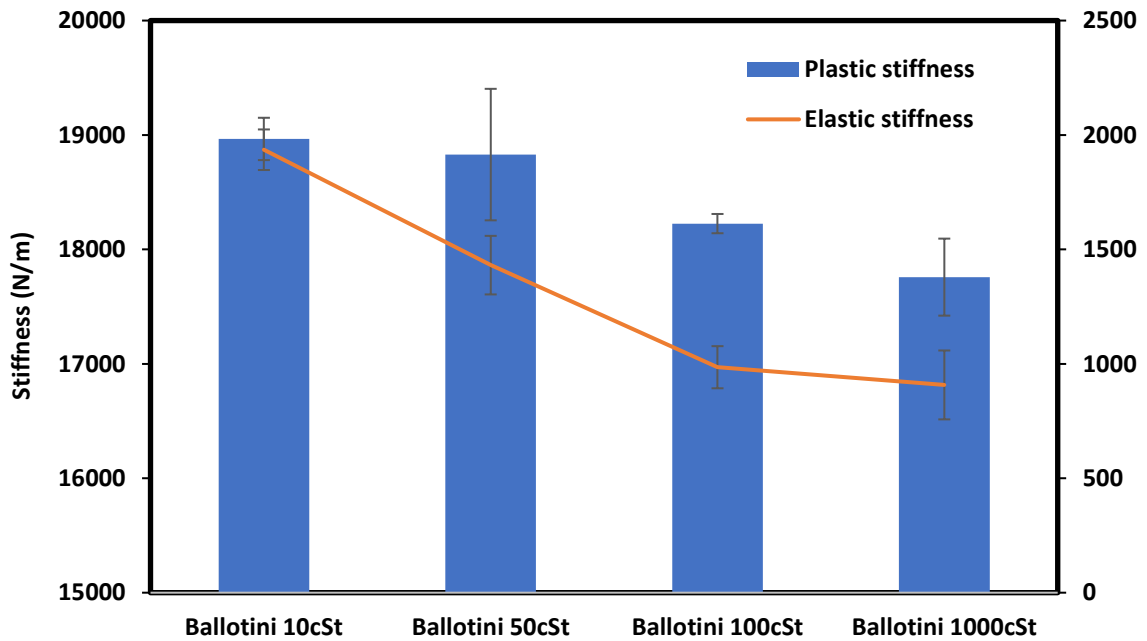


Figure 4.18 Plastic and elastic stiffness for ballotini pellets with different viscosity of silicone oils. Error bars represent the standard error values of a minimum of 3 measurements

4.4.2 Young's modulus of pellets from the quasi-static compression test

Figure 4.19 and Table 4.3 show the average values for Young's modulus for different types of pellets. According to (L. G. Wang, 2016) , a specimen with a high value of Young's modulus has a high resistance to breakage. Consequently, the specimen is not broken easily. Based on Table 4.3, the decrease in values of Young's modulus of the pellets can be arranged as follows: ballotini 1000cSt pellets < ballotini 100 cSt pellets < ballotini 50cSt pellets < ballotini 10cst pellets < lactose 1000cst pellets < MCC 1000cst pellets < MCC 10cst pellets < lactose 10cst pellets. A large differences in the value of Young's modulus can be found for lactose 10cst pellets and lactose 1000cst pellets. It can be due to the binder viscosity used is predominant within the lactose pellets. The used of the highest viscosity of 1 Pa.s has greatly increased the 'plastic flow' effect within the lactose pellets and lowered the value of Young's modulus of lactose pellets, indicates by lactose 1000cst pellets.

It shows that lactose 10cst pellets can be considered as very stiff pellets and ballotini 1000 cSt pellets are the softest pellets. MCC pellets can be categorized as moderate stiffness due to their moderate Young's modulus values. In Figure 4.20, the effect of the viscosity of silicone oils on the Young's modulus of the ballotini pellets is observed. The comparison among the ballotini pellets indicates that increasing the viscosity has lowered the Young's modulus values. This means that increasing the viscosity of silicone oils produces easily deformed pellets (soft pellets).

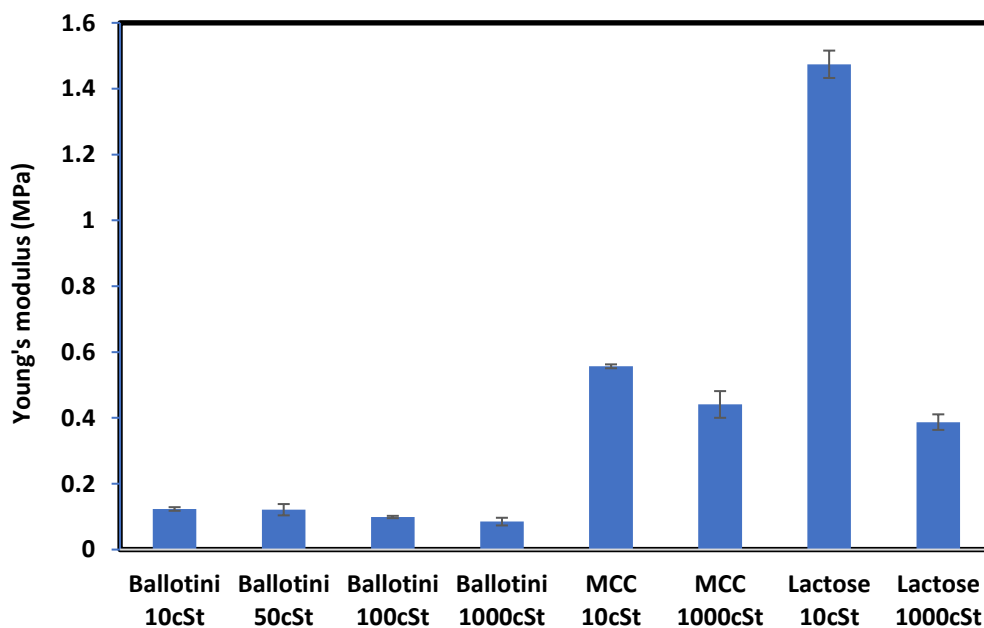


Figure 4.19 Young's modulus of different types of pellets. Error bars represent the standard error values of a minimum of 3 measurements

Table 4.3 Young's modulus of pellets using the quasi-static compression test

Types of pellets	Number of sample, n	Young's modulus (MPa)
Ballotini 10 cSt pellets	3	0.123 (0.006)
Ballotini 50 cSt pellets	5	0.121 (0.017)
Ballotini 100 cSt pellets	4	0.099 (0.004)
Ballotini 1000 cSt pellets	3	0.085 (0.012)
MCC 10cSt pellets	3	0.557 (0.006)
MCC 1000cSt pellets	5	0.441 (0.041)
Lactose 10cSt pellets	5	1.474 (0.042)
Lactose 1000cSt pellets	3	0.387 (0.024)

*Parentheses give the standard error values of a minimum of 3 measurements

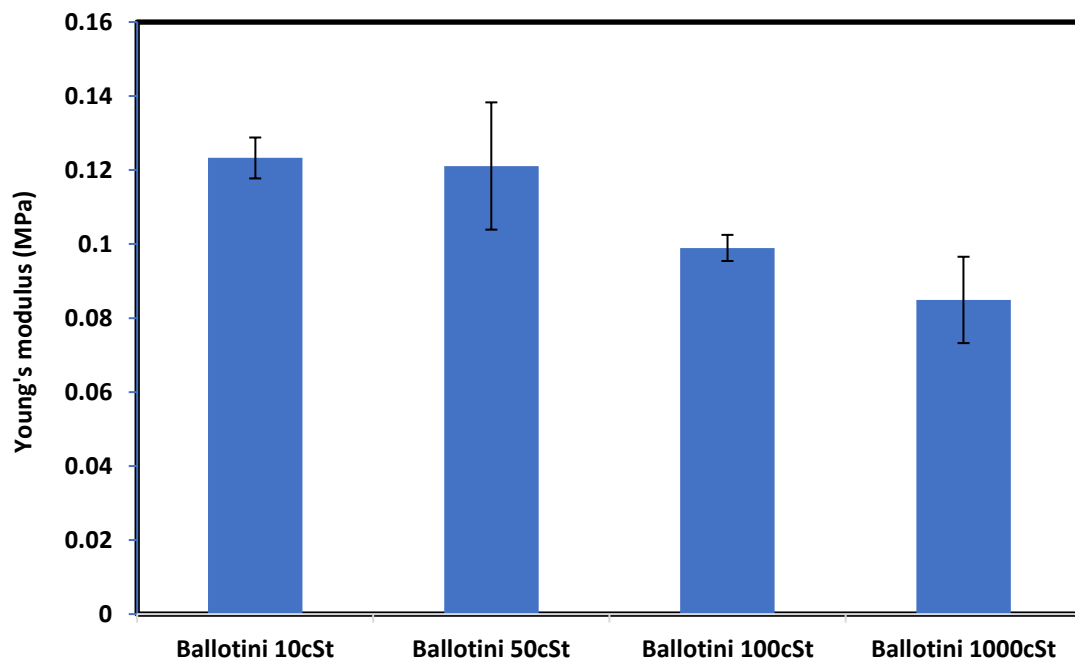


Figure 4.20 Young's modulus for ballotini pellets with different viscosity of silicone oils. Error bars represent the standard error values of a minimum of 3 measurements

4.4.3 Yield stress of pellets from the dynamic compression test

Figures 4.21 to 4.27 show the stress-strain curves for each type of pellet. The stress increased with increasing strain until it reached a peak. The material begins to yield (permanent deformation/plastic deformation) whenever it exceeds the elastic limit. This can be indicated by a noticeable point; a yielding point beyond which elasticity is lost. Generally, increasing the compression speed increases the yield stress for all types of pellets. Figures 4.21 to 4.24 show the effect of viscosity of silicone oils on the stress-strain for the ballotini pellets. Fluctuations in the profiles of the stress-strain curves were observed for ballotini pellets with lower viscosity of silicone oils (0.01 Pa.s, 0.05 Pa.s and 0.1 Pa.s), as shown in Figures 4.21 to 4.23). It shows that fragments and brittle behaviour of the ballotini powder are predominant within the pellets rather than the binder viscosity used. However, this fluctuation of the profiles of the stress-strain curves decreased significantly when increasing the viscosity of silicone oils from 0.01 Pa.s to 0.1 Pa.s. Smooth profiles of the stress-strain curves were observed for ballotini pellets with the highest viscosity of 1 Pa.s (Figure 4.24). The noticeable point (yielding point), which represents the peak stress value can be clearly identified and distinguished between the compression speeds used. This indicates that increasing the binder viscosity to 1 Pa.s has greatly increased the 'plastic flow' effect within the ballotini pellets.

Despite ballotini and lactose powders both being brittle materials, the differences of profile of stress-strain curves between them could clearly be observed. In Figures 4.21 and 4.25, a smooth profile of stress-strain curves can be seen for pellets made from lactose powder in comparison to ballotini powder. The possible reasons may be due to the different physical properties, shapes and structures of the powders (refer to Figures 3.4 and 3.6). Moreover, the comparison of using two different load cells on yield stresses of lactose 10cSt pellets has been made, as shown in Figure 4.26. The lactose 10cSt pellets were compressed at the highest speed using both 50 N and 100 N loads. The use of the 100 N load has decreased the yield stresses of the lactose 10cSt pellets compared to the 50 N load. This could be due to the higher stress experienced by the lactose pellet using 100 N.

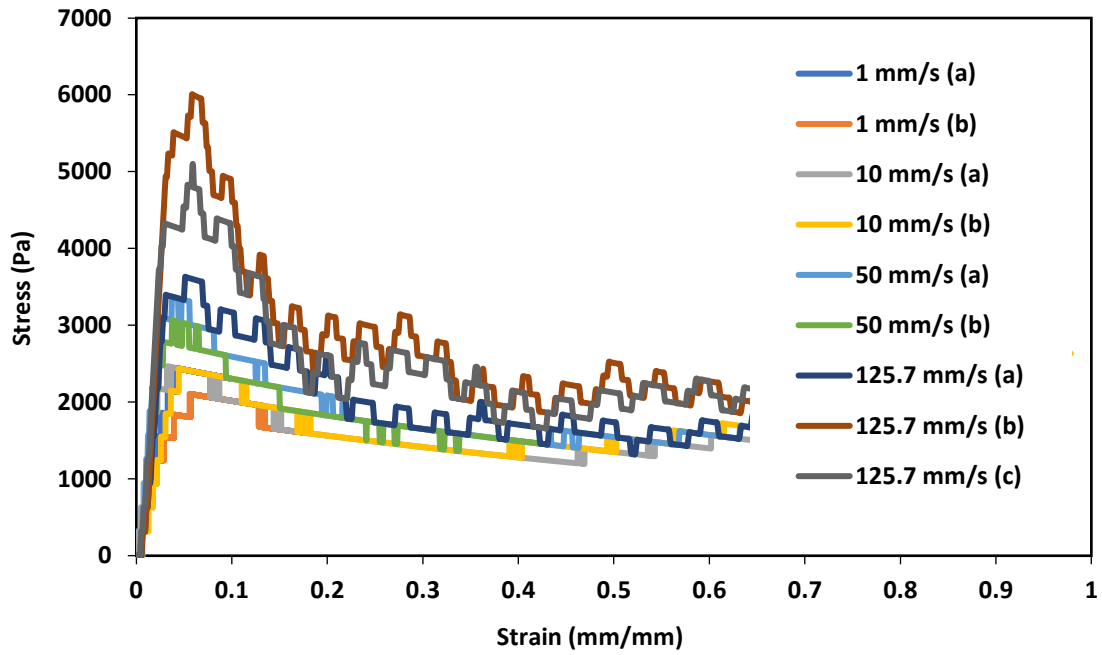


Figure 4.21 Stress (Pa) versus strain (mm/mm) curve for ballotini 10cSt pellets. Load cell of 50 N and compression speeds from 1 to 125.7 mm/s

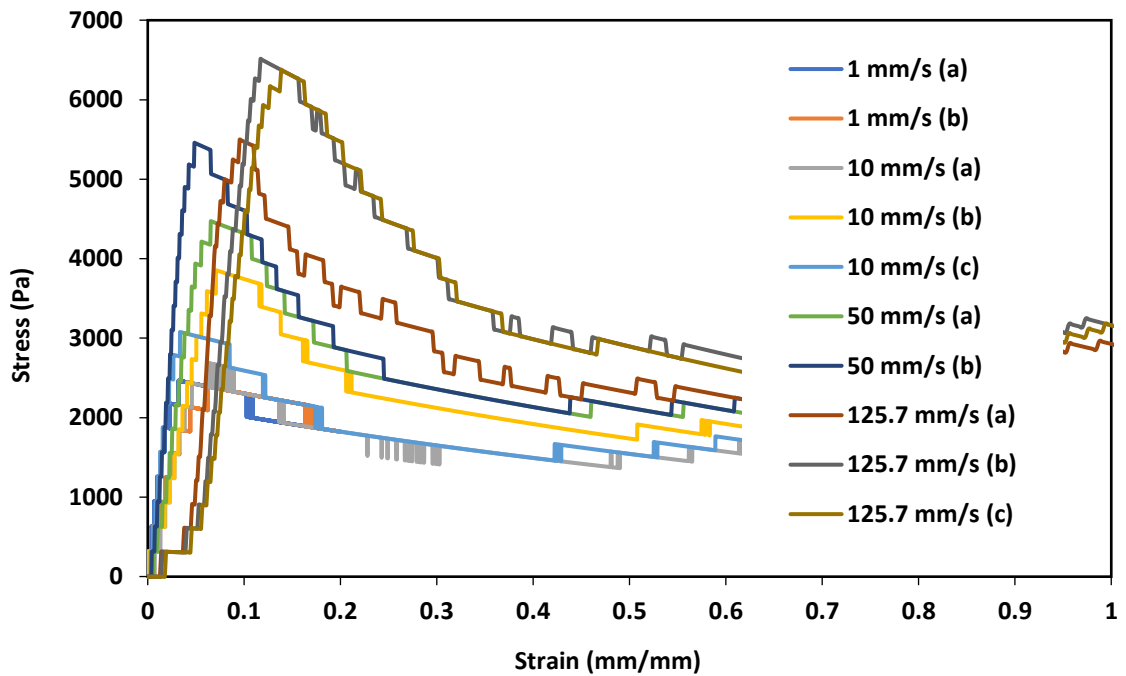


Figure 4.22 Stress (Pa) versus strain (mm/mm) curve for ballotini 50cSt pellets. Load cell of 50 N and compression speeds from 1 to 125.7 mm/s

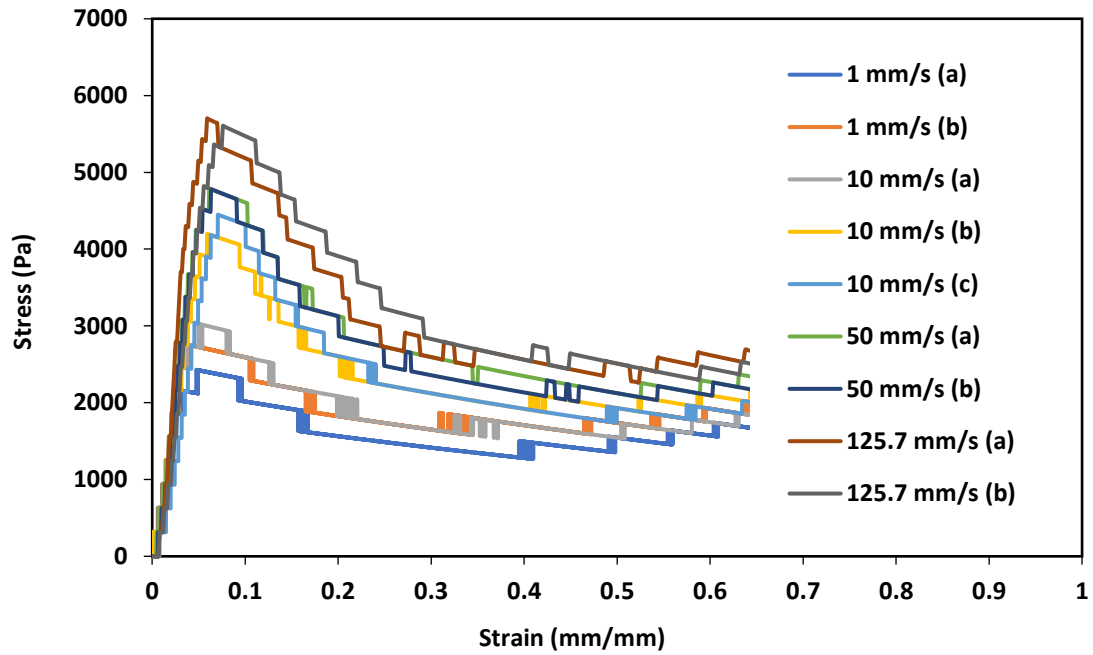


Figure 4.23 Stress (Pa) versus strain (mm/mm) curve for ballotini 100cSt pellets. Load cell of 50 N and compression speeds from 1 to 125.7 mm/s

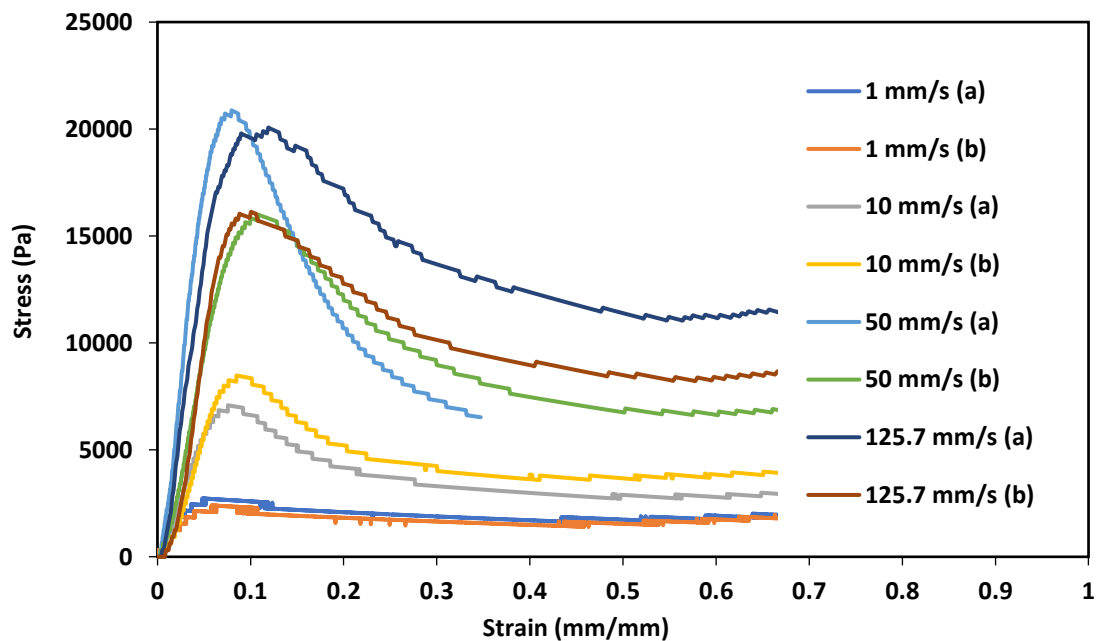


Figure 4.24 Stress (Pa) versus strain (mm/mm) curve for ballotini 1000cSt pellets. Load cell of 50 N and compression speeds from 1 to 125.7 mm/s

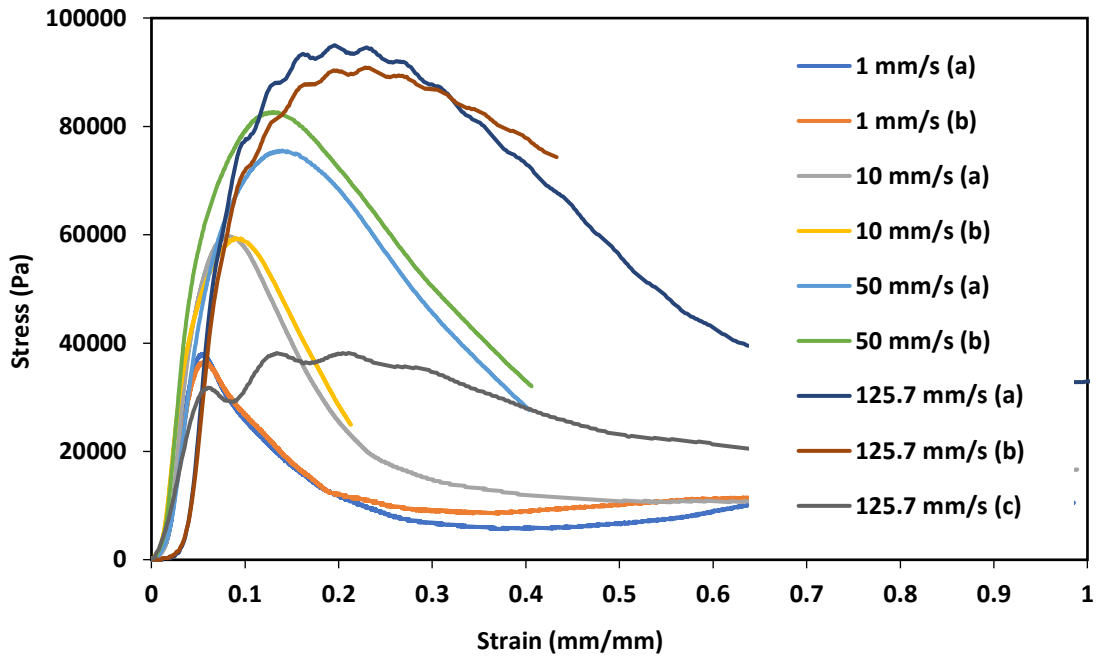


Figure 4.25 Stress (Pa) versus strain (mm/mm) curve for lactose 10cSt pellets. Load cell of 50 N and compression speeds from 1 to 125.7 mm/s

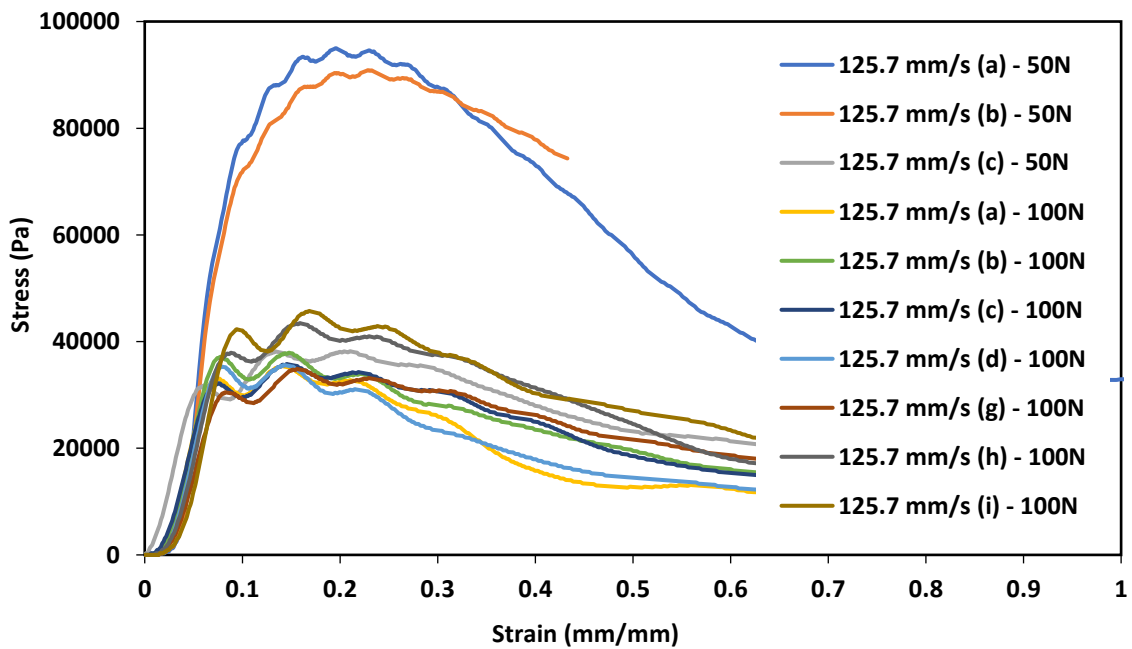


Figure 4.26 Stress (Pa) versus strain (mm/mm) curve for lactose 10cSt pellets. Load cells of 50 N and 100 N and compression speed of 125.7 mm/s

Based on the stress – strain curves, the peak stress values indicating the yield stresses for different compression speeds, were determined using OriginPro 2019 software, as previously described in Section 4.3.5. Table 4.4 shows the average values for the yield stresses of the pellets compressed at different compression speeds and loads. All the measurements were repeated at least 2 times. Of all the pellets tested, ballotini 10cSt pellets and lactose 10cSt pellets were the weakest and strongest pellets, respectively, regardless of the compression speed.

Table 4.4 Yield stress of pellets using the dynamic compression test

Types of pellets	Speed of top platen (mm/s)	Yield stress (Pa)
Ballotini 10 cSt pellets	1	2274 (167)
	10	2451 (15)
	50	3220 (154)
	125.7	4490 (549)
Ballotini 50 cSt pellets	1	2432 (35)
	10	3208 (343)
	50	4965 (493)
	125.7	6128 (318)
Ballotini 100 cSt pellets	1	2591 (163)
	10	3893 (438)
	50	4785 (5)
	125.7	5653 (48)
Ballotini 1000 cSt pellets	1	2566 (164)
	10	7781 (699)
	50	18433 (2438)
	125.7	17909 (1877)
Lactose 10cSt pellets	1	37244 (772)
	10	59654 (247)
	50	79131 (3554)
	125.7	71846 (20058)
	125.7**	35491 (1516)

*Parentheses give the standard error values of a minimum of 2 measurements

** Using 100 N load cell

4.5 Summary

In this chapter, quasi-static and dynamic compression tests were performed on the pellets of different formulations. The quasi-static compression properties such as Young's modulus, plastic and elastic stiffness were measured as the input materials for the DEM simulations. The yield stresses of pellets were measured from the dynamic compression tests and further used as the input parameter for comparison in the failure theory. Based on quasi-static compression test, lactose 10cSt and ballotini 1000cSt pellets have been identified as very stiff and softest pellets, respectively. From dynamic compression test, increasing the compression speeds increases the yield stresses of the pellets. Lactose 10cSt pellets ballotini 10cSt pellets had the highest and lowest yield stresses, respectively, regardless of the compression speed.

5 Granular pellet deformation in an annular shear cell

5.1 Introduction

This chapter presents the development of a custom-made annular shear cell to produce a simple shear flow to investigate granule breakage. The deformation behaviour of pellets using this shear cell are presented and discussed.

The custom-made annular shear cell was designed to: 1) mimic some of the flow conditions in a granulator; 2) require a small amount of powder for testing in comparison to the granulator; 3) focus on the breakage mechanism, and exclude nucleation and growth and consolidation; 4) establish quasi-static, intermediate or high/rapid shear flow behaviour; 5) have a moving and rotating top lid which can confine and grip the bed powder and a stationary bottom plate; 6) enable varying loads to be placed on the top lid.

5.2 Materials and methods

The parameters and experiments for pellet deformation in the annular shear cell are explained in this section. A flow diagram for the experiments is shown in Figure 5.1. The paste formulation, paste and pellets preparation, and the properties of pellets and background materials are given in Chapter 3. Two types of pellets; ballotini 10cSt and lactose 10cSt pellets were chosen for testing in the annular shear cell experiments. They represented the weakest and strongest pellets respectively. Amongst the weak and soft pellets, ballotini 1000cSt pellets were identified as the weakest pellets (refer to Table 4.3, Section 4.4.2, Chapter 4). However, they were too soft and difficult to handle during the loading and unloading stages. For this reason, the ballotini 10cSt pellets were selected instead of ballotini 1000cSt pellets. Glass ballotini 63-90 μm and 200 Mesh lactose powders were used with 0.01 Pa.s silicone oil. As described in Sections 3.5.5 and 3.6.2, Chapter 3, the pellets were produced by pre-mixing and were then formed in a die. Pellets were relatively low in strength.

The shear rates of 5.03/s and 40.21/s were chosen. Deformation prior to shearing (i.e. 0 s) was considered for the effect of any compression from the top lid. The applied pressure was varied between 383 and 2000 Pa. The time of shearing was between 0 s and 100 s. The sizes of the background beads were 1-1.4 mm and 2 mm.

The images of deformed pellets were visualized and three different analyses were performed to characterize the deformation of the pellets:

- determining the degree of deformation by means of pellet elongation, E_p
- determining the deformation fraction, F_D
- relating with a predictive model; the Stokes deformation number, St_{def}

Pellet elongation, E_p , was based on pellet length of longest diagonal while deformation fraction, F_D , was based on mass changes on the 4 mm sieve. The predictive model; Stokes deformation number, St_{def} , was implemented to support the experimental results. The Stokes deformation number, St_{def} , is defined in Section 2.2.1.4, Chapter 2.

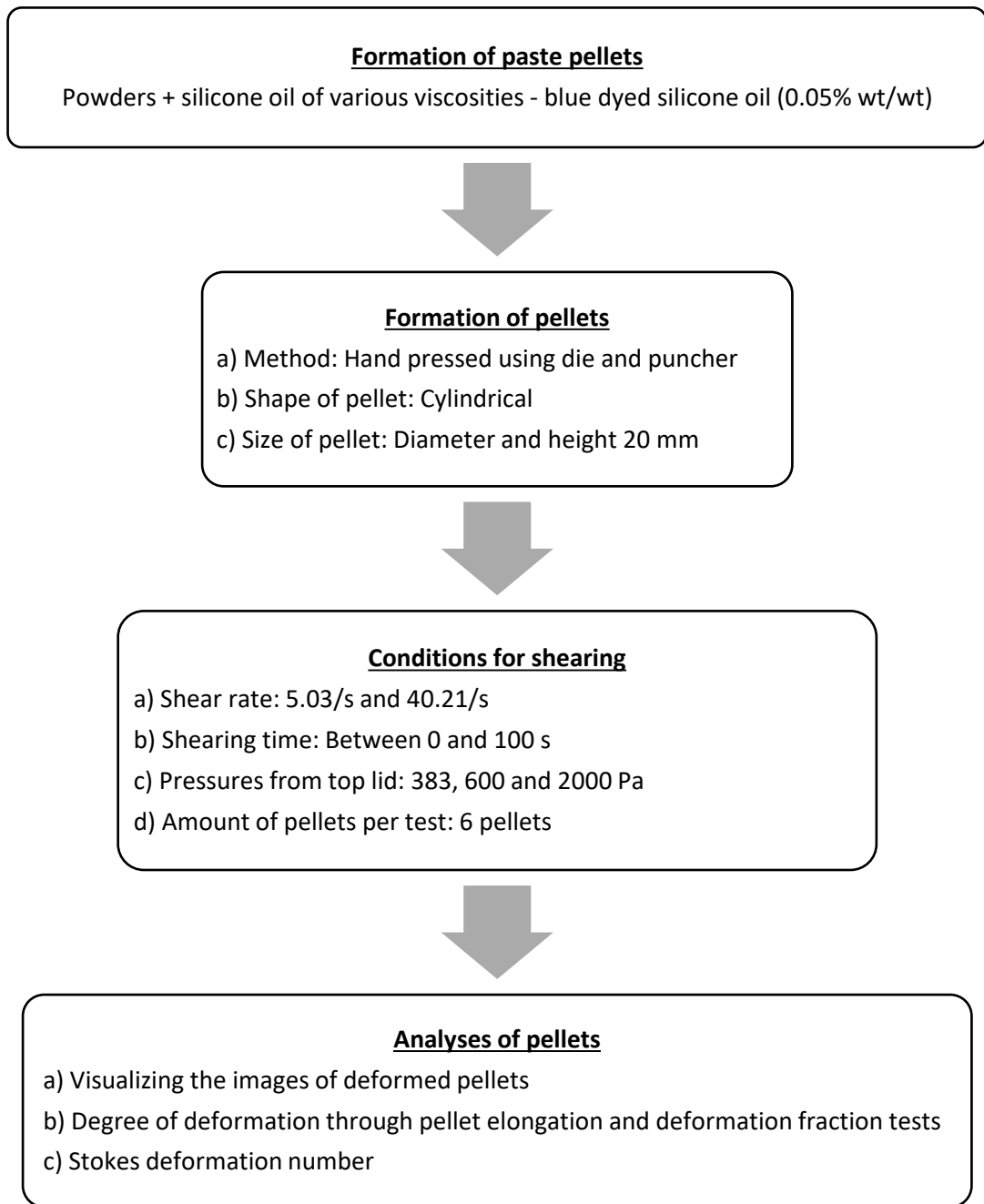


Figure 5.1 Flow diagram of experimental work

5.2.1 Properties of the annular shear cell

The shear deformation of the pellets was performed in a custom-made annular shear cell, designed and constructed as part of this PhD research. The annular shear cell was designed to allow the movement and rotation of the top lid while the bottom base was fixed. It was manufactured at The University of Sheffield. It contains an interlock door, a fan, a bottom base, a moving and rotational top lid, a shear cell controller box with an installed software, a power system and a motor at the base. An additional load can be added on the top lid for applying additional force. The top lid can move axially and rotate for the purpose to confine, grip and shear the bed particles (pellets and background beads). The motor and power system was connected to the shear cell controller box for setting the time and rotational speed of the top lid. The general specifications of the annular shear cell are given in Table 5.1 and Figures 5.2 to 5.4.

Table 5.1 Specifications of the annular shear cell

Specifications	Description
Inner diameter (mm)	110
Outer diameter (mm)	210
The width of the trough bowl (mm)	50
The depth of trough bowl (mm)	50
Default time (s)	10 (minimum) and 300 (maximum)
Default motor speed (rpm)	15 (minimum) and 120 (maximum)

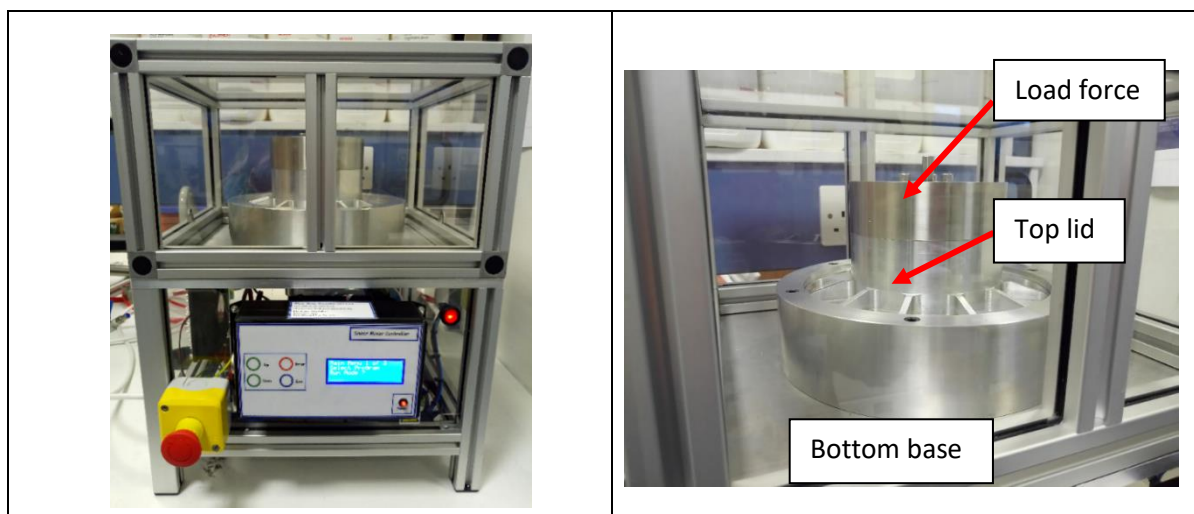


Figure 5.2 Load force, top lid and bottom base of the annular shear cell

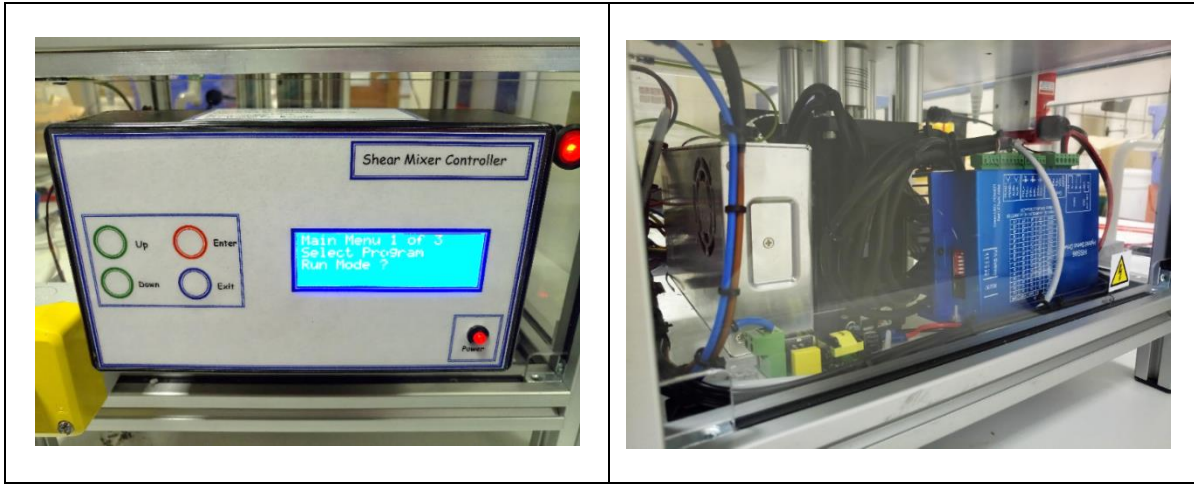


Figure 5.3 Shear cell controller box (left) and motor and power system (right)

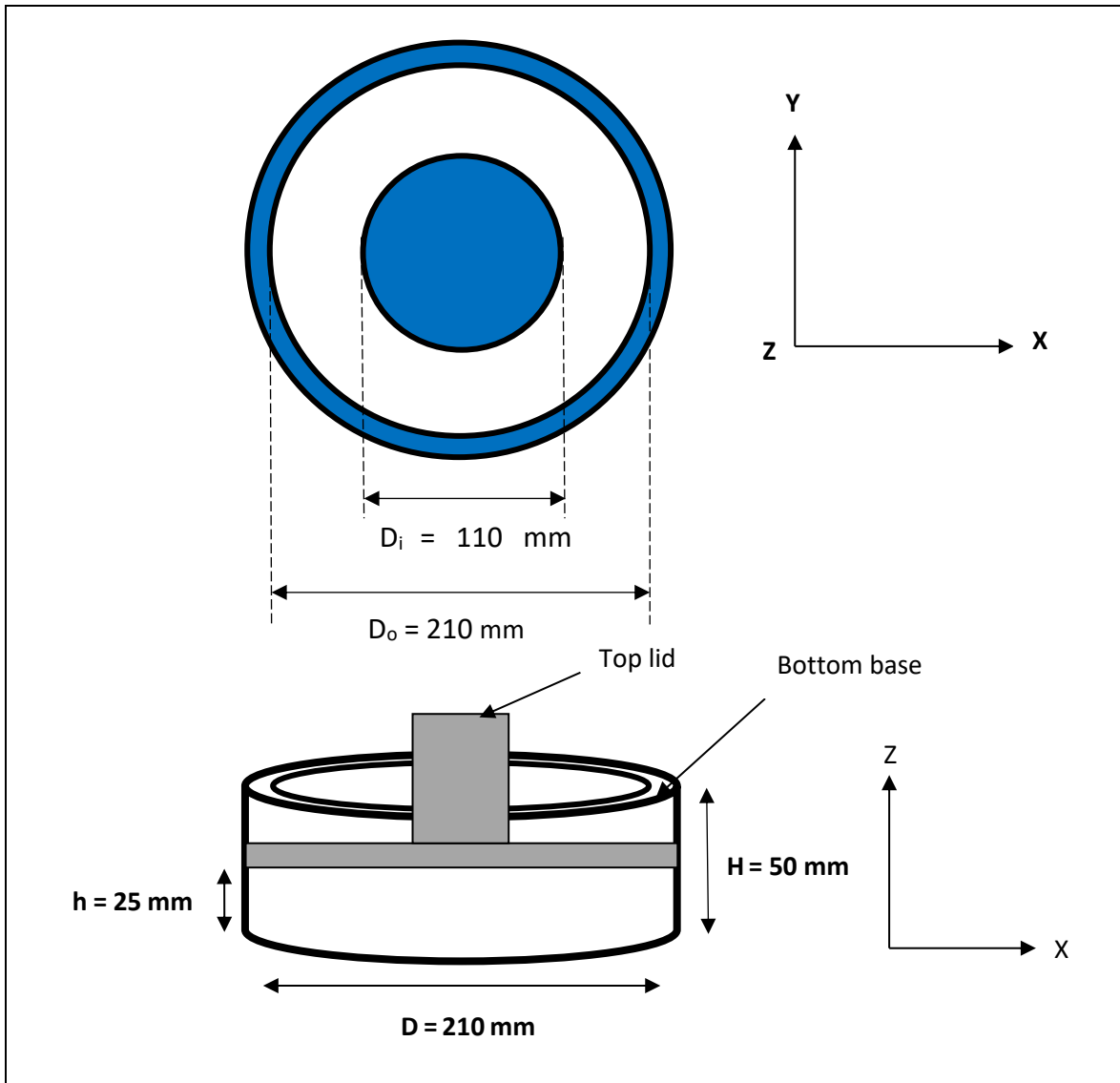


Figure 5.4 Schematic diagram of the annular shear cell: Top view of the bottom base (Top) and side view with top lid and bottom base (Bottom)

The surfaces of the top lid and bottom base that had direct contact with the bed particles were created to be rough by adhering 60 grit sandpaper to these surfaces (Figure 5.5). According to (Khan & Tardos, 1997) uniform shear flow of granular materials could be obtained by roughening the walls of the device that are in contact with the materials with sandpaper of appropriate coarseness. The thickness of sample (pellets and background beads) was kept constant for all experiments.

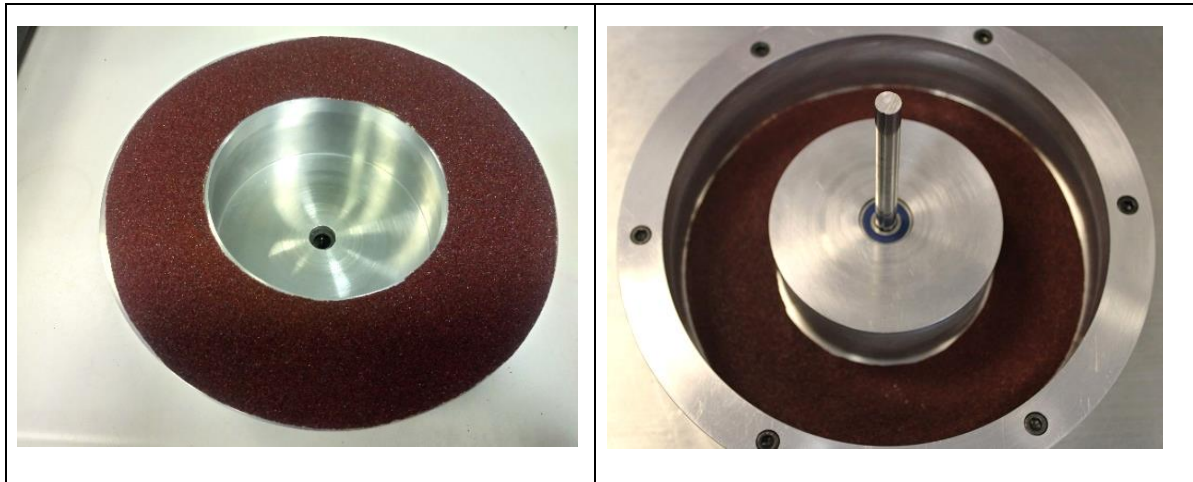


Figure 5.5 The surfaces of the top lid (left) and bottom base (right) with 60 grit sandpaper

5.2.2 Parameters for the experiments

Two types of pellets were chosen for the experiments in the annular shear cell. They were subjected to different operating parameters such as shear rate of the top lid, applied pressure of the top lid and size of the background beads (Table 5.2).

Table 5.2 Variable parameters for annular shear cell experiments

Parameters	Description
Types of pellets	Ballotini 10cSt and lactose 10cSt
Shear rate (1/s)	5.03 and 40.21
Time of shearing (s)	Between 0 and 100
Applied pressure of the top lid (Pa)	383, 600 and 2000
Size of background beads (mm)	1.0-1.4 and 2.0

5.2.2.1 Varying the shear rate of the top lid

As described in Table 5.1, 15 and 120 rpm are the default rotational speeds of the annular shear cell. The speed of 120 rpm is the highest speed that annular shear cell can achieve. The speed of 15 rpm was based on previous work by (C. Liao et al., 2017b; Paramanathan & Bridgwater, 1983b, 1983a). In Figure 5.6, the pellet was placed at the centre in the trough of the annular shear cell, which was equivalent to the radius of the annular shear cell, r^* , with a value of 0.08 m. With known values of rotational speed and this specific radius of the annular shear cell, r^* , the linear speeds of top lid were 1.0053 and 0.1257 m/s for 120 and 15 rpm, respectively. The pellets were placed in between the bed of background beads to reach a bed height of 25 mm in the annular shear cell. By considering a sample thickness of 25 mm and these linear speeds, the shear rates from top lid were equivalent to 40.21/s and 5.03/s, respectively. These shear rates of the top lid; 5.03/s and 40.21/s were tested for the strongest and weakest pellets; lactose 10cSt and ballotini 10cSt pellets. The conditions for the base case are shown in Table 5.3. The other operating parameters were kept constant.

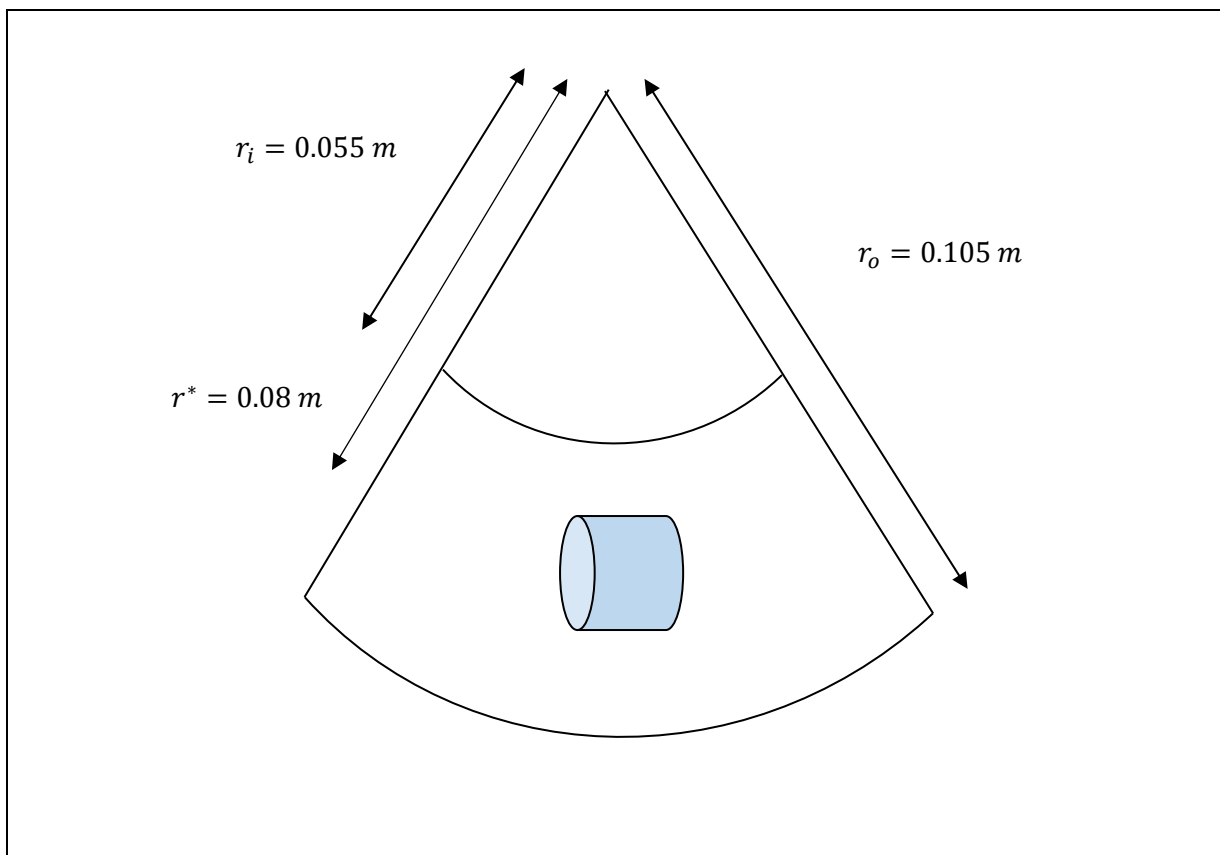


Figure 5.6 Position of the pellet at the centre in the trough of the annular shear cell and the specific radius of the annular shear cell, r^* (r_i =Inner radius and r_o = outer radius)

Table 5.3 Variation of the shear rate of the top lid

Operating parameters	Lactose 10cSt pellets	Ballotini 10cSt pellets
Size of background beads (mm)	1-1.4	1-1.4
	2	-
Pressure of the top lid (Pa)	2000	2000
Shear rate (1/s)	5.03	5.03
	40.21	40.21

5.2.2.2 Varying the pressure of the top lid

Weights were applied to the top lid of the shear cell to apply a uniform downward pressure. The axial motion of the top lid was allowed to confine and grip the bed particles and maintain the given pressure level. The pressure of the top lid was the load force divided by the area of the top lid.

The mass of the top lid provided a pressure of 383 Pa and was used as the default pressure. The mass of the top lid is 981 g. The area of the top lid is 0.0251 m^2 . The other pressures investigated were 600 and 2000 Pa. They were chosen based on a previous study by (Ji et al., 2009) who used ranges between 0.6 to 20 kPa. Therefore, additional weights of 554.69 g and 4.138 kg were added to the default mass of the top lid to apply 600 and 2000 Pa, respectively. The conditions for the base case is shown in Table 5.4. The other operating parameters were kept constant.

Table 5.4 Variation of the pressure of the top lid

Operating Parameters	Lactose 10cSt pellets	Ballotini 10cSt pellets
Size of background beads (mm)	1-1.4	1-1.4
Shear rate (1/s)	40.21	40.21
Pressure of the top lid (Pa)	383	383
	600	600
	2000	2000

5.2.2.3 Varying the size of the background beads

Two sizes of background beads, 1-1.4 mm and 2 mm, were used as the medium of shearing. In order to maintain consistency of the size and shape of the background beads, they were replaced for each experiment and sieved to the chosen selected sizes. The required mass of the background beads for each experiment is listed in Table 5.5. The different sizes give different voidages, hence the difference in mass. The bed height of 25 mm was set constant and the total mass of background beads (excluding the pellets) was measured.

Table 5.5 Mass of background beads for the experiments

Properties	Glass beads 1-1.4 mm	Glass beads 2 mm
Total mass (g)	882.65	897.14
Mass for bottom base (g)	93.90	95.44

5.2.3 Performing shearing in the annular shear cell

Several steps were performed for the shearing in the annular shear cell. The selected types of pellets were dyed blue to mark the location of the pellets in the bottom base. The first step was to load a specified amount of the background beads into the bottom base (refer to Table 5.5) and these were spread evenly over the base. Then, 6 pellets were placed at the centre of different parts in the annular shear cell (Figure 5.7 (left)). The centre of the trough of annular shear cell, which has a potential for the failure zone (pellet to be deformed) was chosen as the area of interest. The spacing between the pellets ensured that the pellets would not be sheared among themselves. The pellets were relatively soft and fragile. For this reason, the side position of the pellets in the annular shear cell could minimize the initial crack /splitting of the pellets prior to the start of shearing in the annular shear cell. The remaining amount of the background beads was evenly scattered on top of the pellets (Figure 5.7 (right)). The top lid was placed on the bed particles with a defined normal load. The shearing was performed for a period of time between 0 and 100 s. Once the shearing process ended, pellets were scooped out using a ladle. The experiments were repeated with fresh background beads for different types of pellets and different operating parameters. The sandpaper attached to the top lid and bottom base were used for a maximum of two runs.

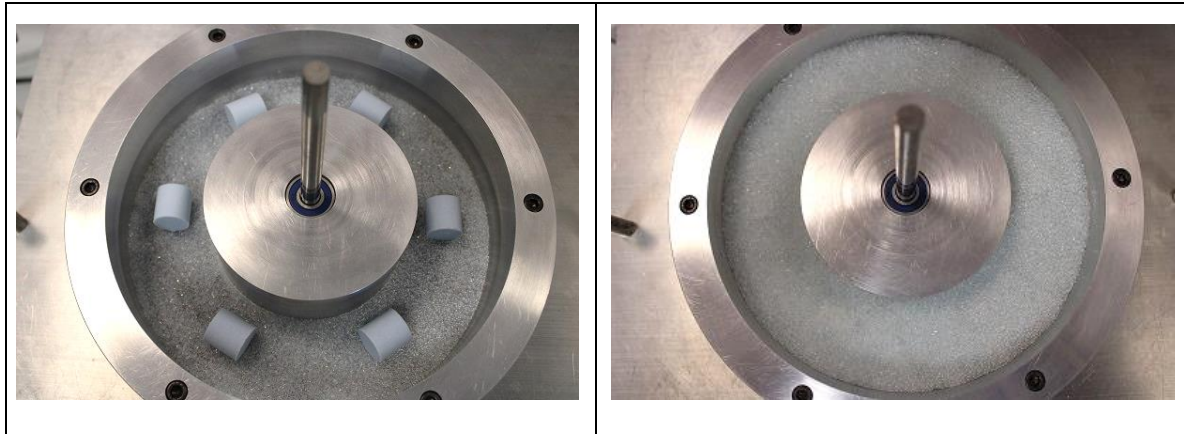


Figure 5.7 Position of pellets and proportion of background beads in the bottom base (left) and after addition of the remaining background beads (right)

5.2.4 Analyses of the pellets

The bulk mass after the shearing process was hand sieved using a sieve stack of 4 mm, 2.80 mm and bottom base sieves to separate the pellets from the background beads and any fragments. The pellets retained on the 4 mm sieve at 0 s and each interval of shearing time were visualized for any changes and further analysed for deformation fraction, F_D , degree of deformation through pellet elongation, E_p and Stokes deformation number, St_{def} .

5.2.4.1 Visualization of deformed pellets

Images of the pellets on the 4 mm sieve were captured using a digital camera, Canon EOS 2000D DSLR Camera (Canon Inc., Taiwan), in side views and different angles to distinguish clearly the un-deformed and deformed pellets. The pellets were considered deformed when the shape had changed from the original due to the shearing. In Figure 5.8, different deformation behaviours were observed for the weakest and strongest pellets, although both were made of brittle powders. The soft structure of the weakest pellets, ballotini 10cSt pellets had flattened and segregated, which resulted in some fragments. However, the strongest pellets, lactose 10cSt pellets, were observed to elongate during shearing.



Figure 5.8 Ballotini 10cSt pellets flattened/fragmented (left) and lactose 10cSt pellets elongated (right)

The soft structure of the weakest pellets resulted in inaccurate measurement the elongation of the deformed pellets. For this purpose, the deformation fraction, F_D , test was chosen for the weakest pellets. On the other hand, degree of deformation were measured based on pellet elongation, E_p . The test was carried out for the strongest pellets as the background beads had a tendency to attach themselves to the surfaces of the pellets after the shearing. As a result, there would be error in weighing the mass of the deformed pellets. Details of the tests are explained in Section 5.2.4.2.

5.2.4.2 Deformation fraction, F_D

The deformation fraction, F_D , was determined by weighing the mass of the pellets retained on the 4 mm sieve at 0 s and each interval of shearing time. The mass of pellets at 0 sec was set as the initial mass. For example, Figures 5.9 shows the ballotini 10cSt pellets retained on the 4 mm sieve at 0 and 100 s. Deformation fraction, F_D , can be calculated using Equation 5.1.

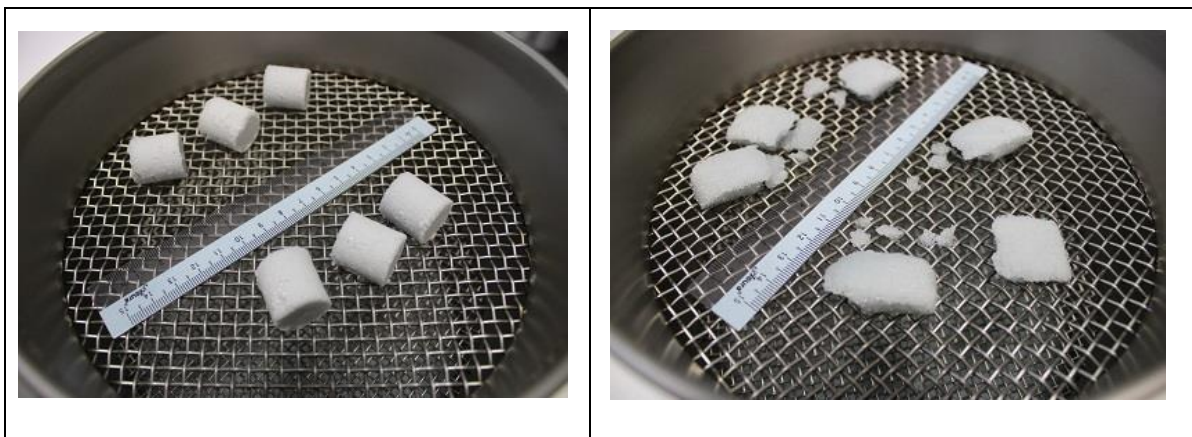


Figure 5.9 Ballotini 10cSt pellets retained on the 4 mm sieve at 0 sec (left) and 100 sec (right)

$$F_D = \frac{M_0 - M_{t_i}}{M_0} \times 100 \quad \text{Equation 5.1}$$

where:

F_D	Deformation fraction	(%)
M_0	Mass of pellets retained on the 4 mm sieve at 0 sec	(g)
M_{t_i}	Mass of pellets retained on the 4 mm sieve at interval shearing time	(g)

5.2.4.3 Degree of deformation through pellet elongation, E_p

Degree of deformation through pellet elongation, E_p , was determined by measuring the length of the longest diagonal of the pellets at 0 s and each interval of shearing time using an image analysis program, Image Processing and Analysis in Java (ImageJ), version 1.52a (National Institutes of Health, USA). For example, Figure 5.10 shows the lactose 10cSt pellets retained on the 4 mm sieve at 0 and 100 s. Figure 5.11 shows the measurement setup in ImageJ for length of the longest diagonal of the pellets at 0 s and 100 s. The pellet elongation, E_p , can be calculated by using Equation 5.2. The length of the longest diagonal of the pellets at 0 s was set as the original length.

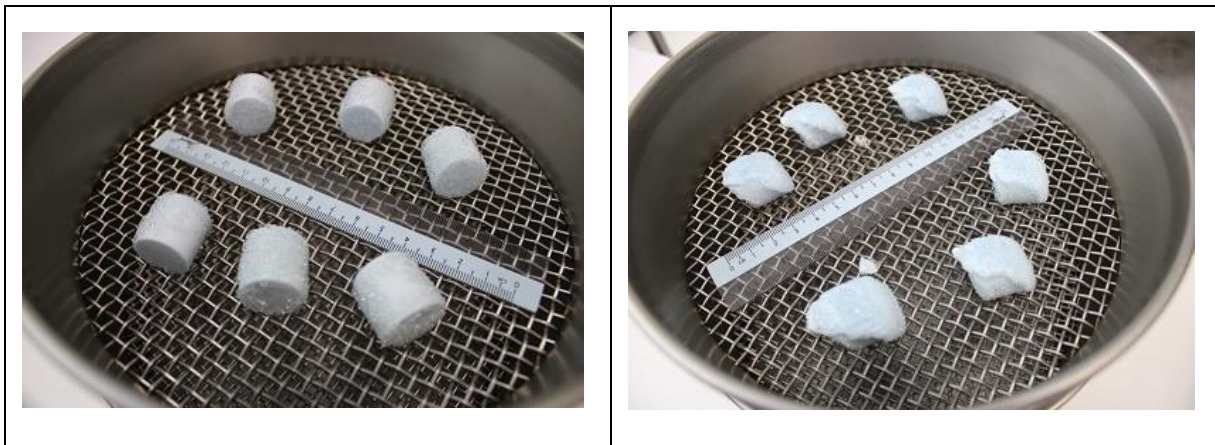


Figure 5.10 Lactose 10cSt pellets retained on the 4 mm sieve at 0 sec (left) and 100 sec (right)

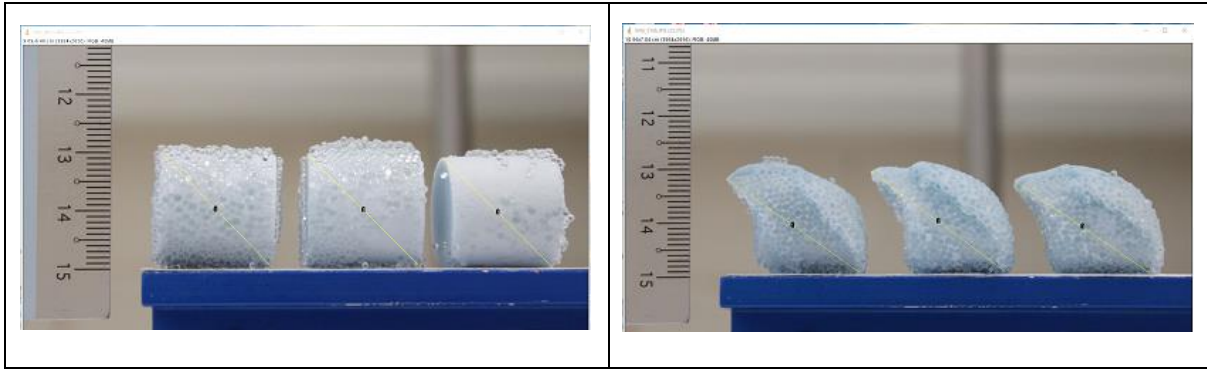


Figure 5.11 Measurement setup in ImageJ for length of the longest diagonal for lactose 10cSt pellets at 0 sec (left) and 100 sec (right)

$$E_p = \frac{L_{t_i} - L_{t_0}}{L_{t_0}} \times 100 \quad \text{Equation 5.2}$$

where:

E_p	Pellet elongation	(%)
L_{t_0}	Length of the longest diagonal of the pellets at 0 s	(cm)
L_{t_i}	Length of the longest diagonal of the pellets at each interval shearing time	(cm)

5.2.4.4 Stokes deformation number, St_{def}

The Stokes deformation number, St_{def} , was explained briefly in Section 2.2.1.4, Chapter 2. For this study, the Stokes deformation number was investigated for its suitability to describe or predict pellet deformation in the annular shear cell. Previous studies have implemented the Stokes deformation number for the cases of a high shear mixer and a fluidized bed (Section 2.2.1.4, Chapter 2). The annular shear cell involves the shear mechanism similar to these shear devices. The factors of material properties or equipment conditions are considered for calculating the Stokes deformation number, and the critical Stokes deformation number, St_{def}^* , can be determined. Below the critical Stokes number, minimal deformation can be expected. Above the critical Stokes deformation number, the pellet can be expected to deform. The Stokes deformation number, based on (Bouwman et al., 2006b; Kayrak-Talay et al., 2013; Knight et al., 2001; L. X. Liu et al., 2009) was chosen for this study and is shown in Equation 5.3:

$$St_{def} = \frac{\rho_g v_c^2}{2Y_g} \quad \text{Equation 5.3}$$

where:

ρ_g =	Density of pellet	(kg/m ³)
v_c =	Representative collision velocity in the annular shear cell and represents the process intensity	(m/s)
Y_g =	Dynamic yield stress of pellet	(Pa) or (kg.m.m ⁻² .s ⁻²)

In literature studies, the representative collision velocity, v_c , was assumed to be 15 - 20 % of the impeller tip speed and was used as a fixed value in the calculation of the Stokes deformation number (Kayrak-Talay et al., 2013; Knight et al., 2001; L. X. Liu et al., 2009). For this current study in the annular shear cell, the representative collision velocity in the annular shear cell, v_c , was assumed to be 15 % of the linear speed of the top lid. As described in Section 5.2.2.1, the linear speeds were 1.0053 m/s and 0.1257 m/s for the rotational speeds of 120 rpm and 15 rpm, respectively. Furthermore, the values of 0.1508 and 0.0189 m/s were used for the corresponding representative collision velocity in the annular shear cell. The annular shear cell can be operated under dynamic conditions, e.g. high shear velocity, which resulted in different deformation behavior of the pellets. One of the input parameters in the Stokes deformation number, the dynamic yield stress of pellets, Y_g , needs to be determined. In this study, the dynamic yield stress of the pellets was obtained experimentally from different compression speeds (see Section 4.4.3, Chapter 4).

5.3 Results and Discussion

5.3.1 Deformation behavior of strongest pellets (lactose 10cSt pellets)

This section describes the results and discussion for the strongest pellets; lactose 10cSt pellets. The applied compression pressure from the top lid, shear rates, normal pressures and size of background beads were tested for their effect on the deformation of the pellets.

5.3.1.1 Effect of any compression from the top lid

Figure 5.12 shows the images of lactose pellets before loading the top lid onto the annular shear cell. In Figures 5.13 and 5.14, the images of the lactose pellets after removing the top lid were observed from the side angle and top view for 1-1.4 mm and 2 mm background beads, respectively. Here, the lactose pellets were loaded into the annular shear cell without turning on the annular the shear cell, corresponding to 0 s shear time. The loading of the top lid did not appear to change the shape of the lactose pellets. However, some of the background beads were stuck to the surfaces of the lactose pellets.

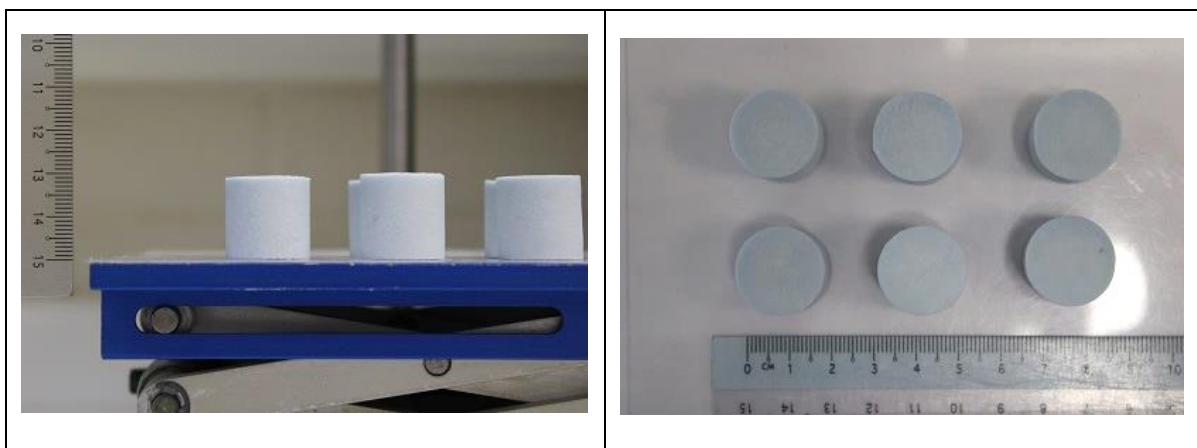


Figure 5.12 Shape of lactose 10cSt pellets beads before loading the top lid

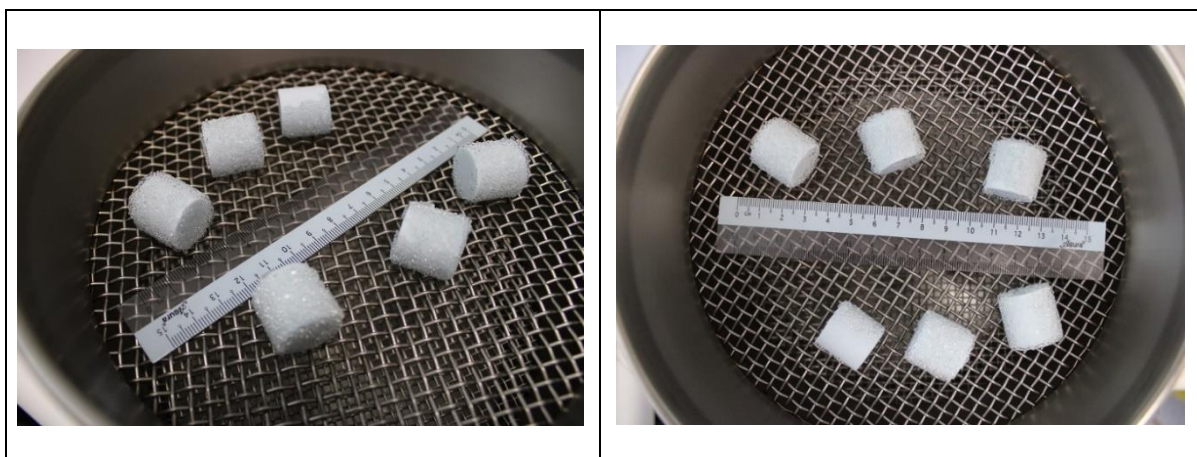


Figure 5.13 Shape of lactose 10cSt pellets with 1-1.4 mm beads after uplifting the top lid

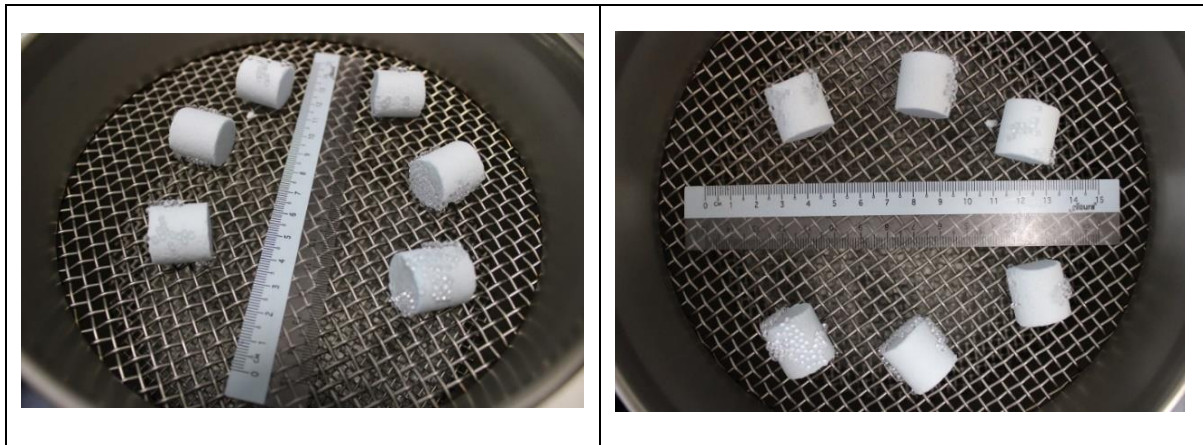


Figure 5.14 Shape of lactose 10cSt pellets with 2 mm beads after uplifting top lid

5.3.1.2 Effect of shear rates (5.03/s and 40.21/s) with conditions: 2000 Pa and 1-1.4 mm beads

Figure 5.15 shows the degree of deformation through elongation of lactose 10cSt pellets for 2000 Pa, 1-1.4 mm background beads and two different shear rates; 40.21/s and 5.03/s. They represented the higher and lower shear rate used in this study, respectively. During the shearing, the top surfaces of pellets which are near to the top lid are likely to experience the highest shear due to the movement and rotation of the top lid. As a result, the length of the longest diagonal of pellets would be greater. Analysis of pellet elongation, E_p was carried out for the lactose 10cSt pellets, which was based on the difference of length of the longest diagonal of pellet. It was noted that fresh lactose pellets were used for every interval shearing time to observe any deformation of the pellets. The pellet elongation results were the average of pellet elongation data at different shearing times between 30 and 100 s. Overall, two different shear rates showed very different levels of pellet elongation. A small elongation, an elongation of 2 % was recorded for pellets sheared at 5.03/s. The lower degree of deformation, was probably due to the stagnant/little movement of the pellets during the shearing. It is likely a slip existed between the pellets and the background beads as increasing the shearing time from 30 s to 100 s. Lactose pellets at shear rate of 40.21/s showed elongation of 11.79 %, a higher degree of deformation.

In Figure 5.16, the images of the lactose 10cSt pellets for two different shear rates were observed to support the results in Figure 5.15. A significant shear deformation on top surfaces of pellets took place for pellets shearing with the higher shear rate; 40.21/s. However, this is not for the case of pellets sheared with lower shear rate; 5.03/s, by which only slight shear deformation can be seen on top surfaces of the pellets. These findings show that the use of two different shear rates with the conditions of 2000 Pa and 1-1.4 mm beads produces a significant difference in the deformation

behaviour of the pellets. Due to the small values, the elongation may not be significant for the 5.03/s case.

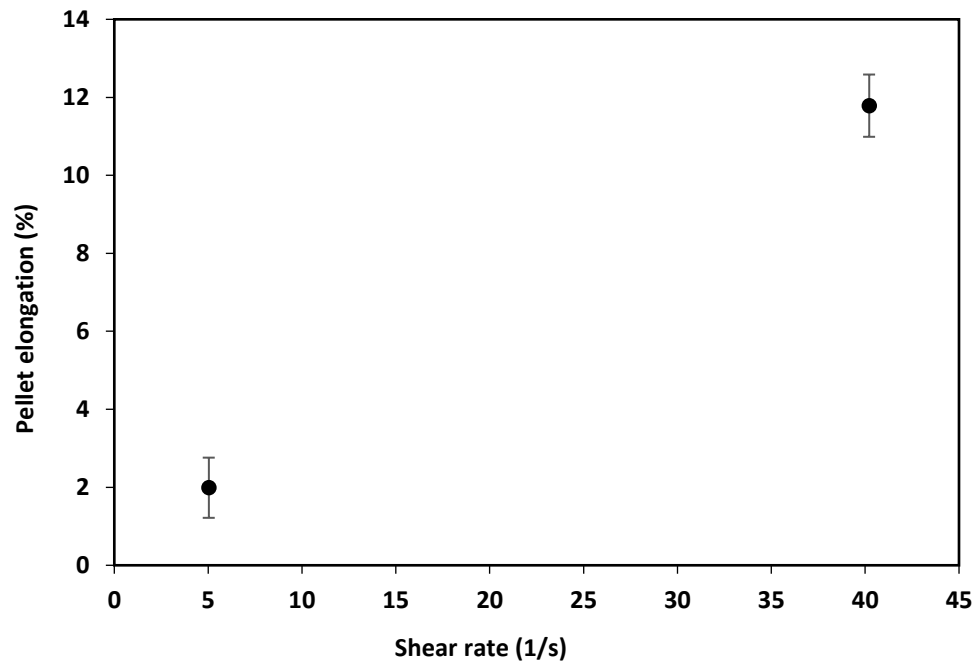


Figure 5.15 Pellet elongation, E_p , versus shear rate for lactose 10cSt pellets with a top lid pressure of 2000 Pa and 1-1.4 mm background beads. Error bars represent the standard error of 4 measurements

Increasing the shearing time (s)

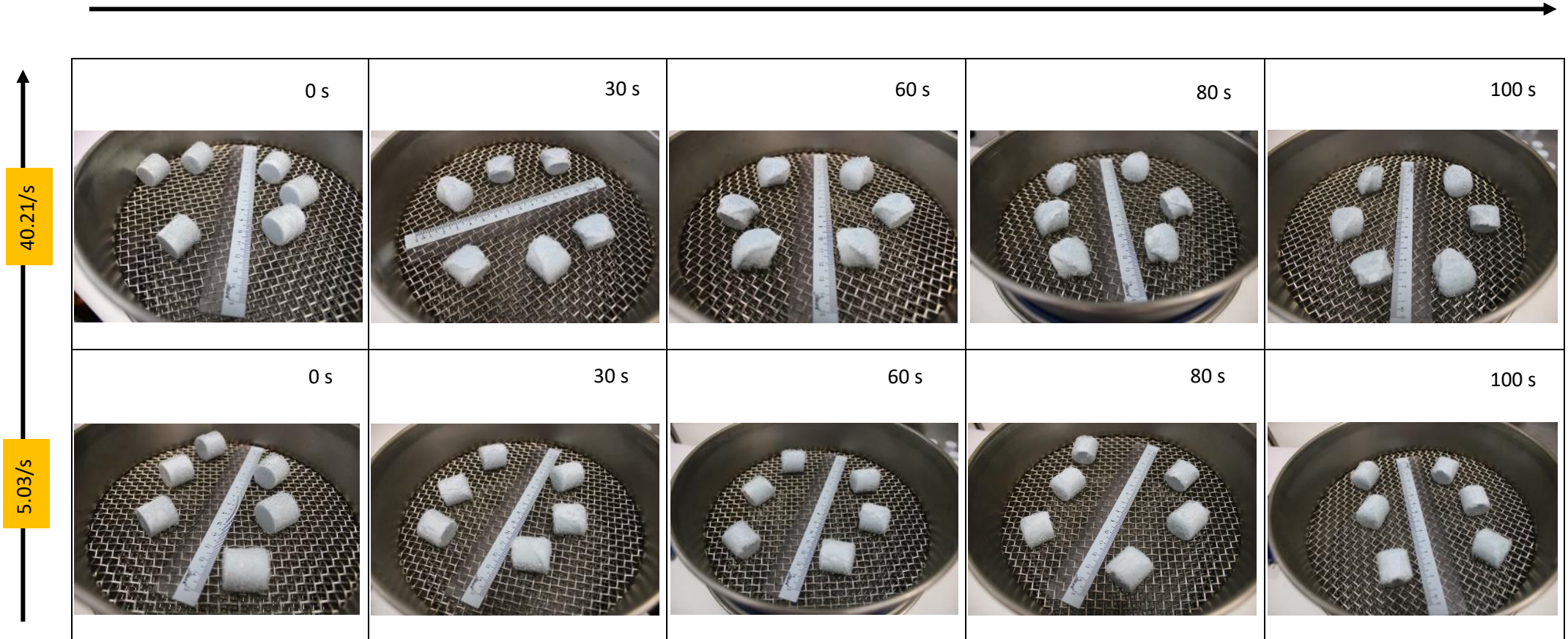


Figure 5.16 Images of lactose 10cSt pellets with shearing time with a top lid pressure of 2000 Pa and 1-1.4 mm background beads for conditions: 5.03/s (bottom) and 40.21/s (top)

5.3.1.3 Effect of shear rates (5.03/s and 40.21/s) with conditions: 2000 Pa and 2 mm beads

In Figure 5.17, the results of degree of deformation through elongation as a function of different shear rates for lactose 10cSt pellets sheared at 2000 Pa and the larger 2 mm background beads were plotted. The pellet elongation results were the average of pellet elongation data at different shearing times between 30 and 100 s. The results showed that pellets at shear rate of 5.03/s resulting the lower values of elongation of the pellets (about 25 %). The pellets at the higher shear rate of 40.21/s had achieved 100 % elongation. It should be noted that in cases where there was substantial pellet breakup and elongation it was not possible to measure these pellets and the pellet elongation was given a value of 100%. Similar to the previous results in Section 5.3.1.2 for lactose pellets sheared at different shear rates with conditions of 2000 Pa and 1-1.4 mm beads, the lower shear rate of 5.03/s resulting the lower values of elongation in comparison to the higher shear rate of 40.21/s.

Images of the pellets are shown in Figure 5.18. An elongation due to shear deformation was observed for the pellets sheared with the lower shear rate, 5.03/s, especially at the top surfaces and after 30 s of shearing. It can be seen that the pellets sheared at the higher shear rate, 40.21/s, had completely deformed (flattened) after 30 s of shearing. For this purpose, the elongation of the pellet could not be measured, and it was assumed that 100 % elongation had been achieved. These findings show that the use of the higher shear rate, along with 2000 Pa and 2 mm beads, results in large values of deformation.

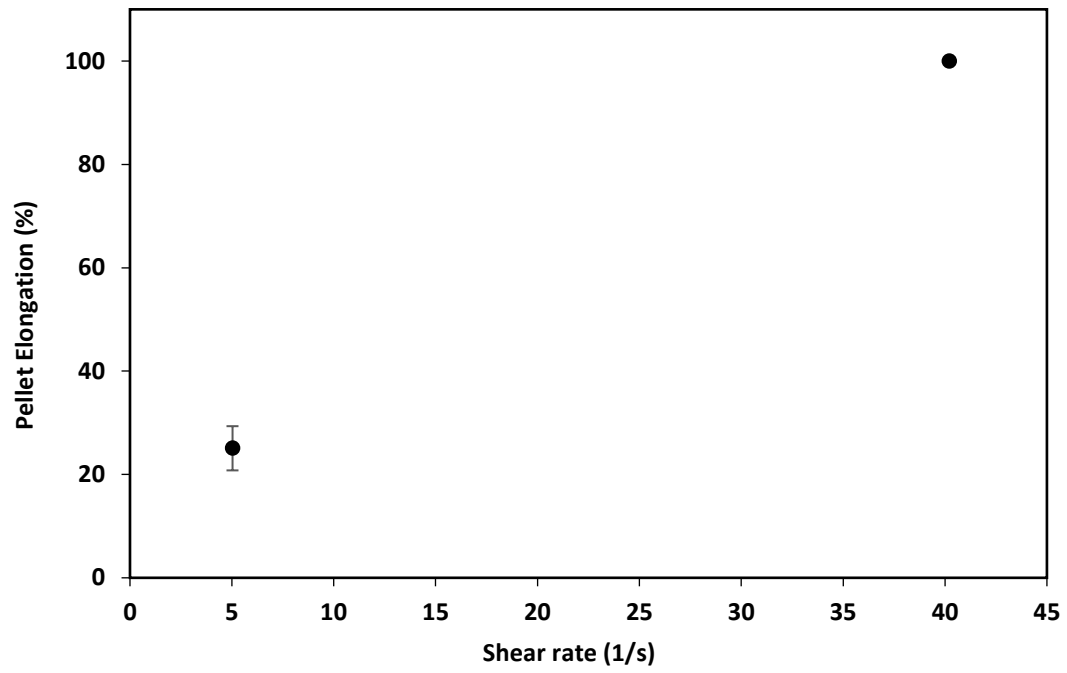


Figure 5.17 Pellet elongation, E_p , versus shear rate for lactose 10cSt pellets with a top lid pressure of 2000 Pa and 2 mm background beads. Error bars represent the standard error of 4 measurements

Increasing the shearing time (s)

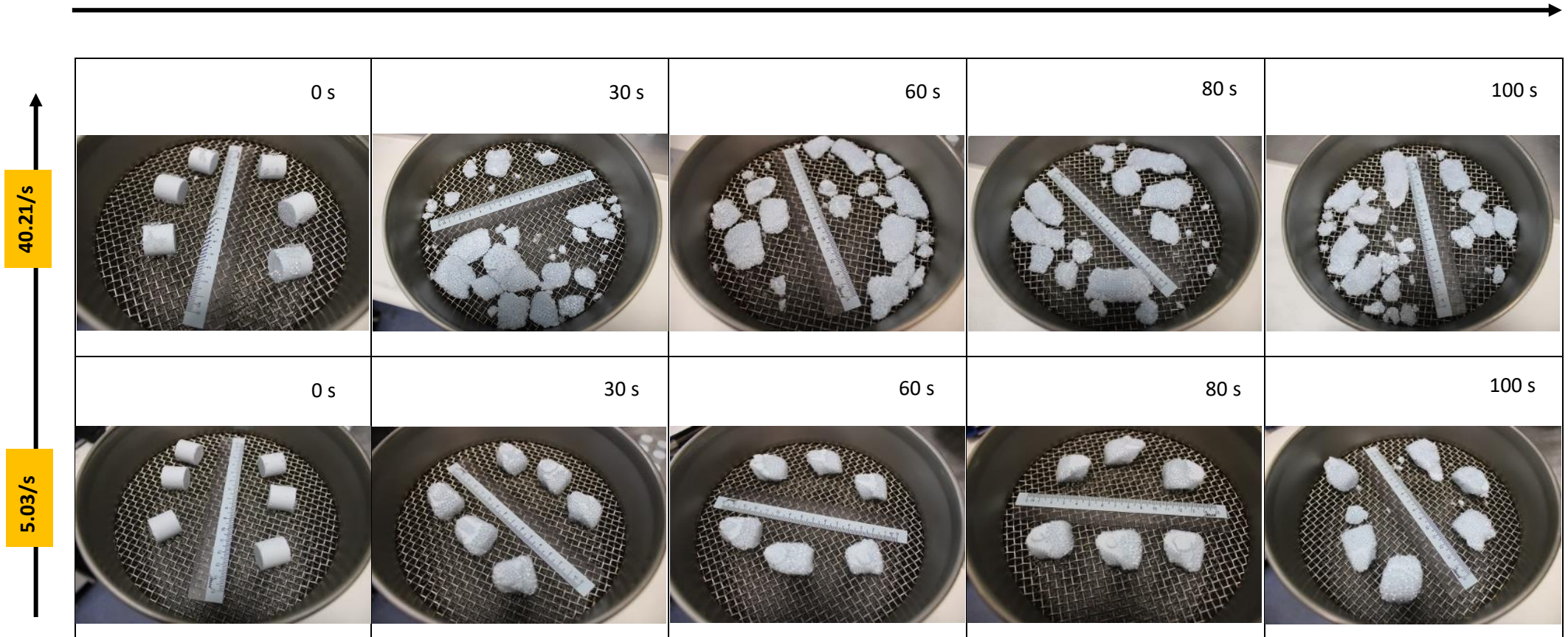


Figure 5.18 Images of lactose 10cSt pellets with shearing time, with a top lid pressure of 2000 Pa and 2 mm background beads for conditions: 5.03/s (bottom) and 40.21/s (top)

5.3.1.4 Effect of normal pressures (383 Pa, 600 Pa and 2000 Pa)

Figure 5.19 shows the effect of normal pressures (383 Pa, 600 Pa and 2000 Pa) on the elongation of lactose 10cSt pellets for conditions of higher shear rate, 40.21/s, and the smaller 1-1.4 mm background beads. The pellet elongation results were obtained by averaging the pellet elongation data at different shearing times between 30 and 100 s. Increasing normal pressure led to increasing elongation (%). Pellets with highest pressure of 2000 Pa show the highest % of elongation (11.79 %) in comparison to the other two pressures 383 and 600 Pa. This is likely due to two effects. As the normal pressure increases, the pellets will experience greater compression forces. Additionally, it is likely that increasing the normal pressure reduced inter-particle slip, potentially providing higher local shear rates. The medium normal pressure of 600 Pa showed only small elongation, 1.66 %. Pellets sheared with the lowest normal pressure of 383 Pa effectively did not show any elongation (0.20 %), which could be due to compression on both sides of the pellets and some elongation may be instantaneously reversible.

Figure 5.20 shows the images of the pellets sheared with different normal pressures between 383 and 2000 Pa for conditions; 40.21/s and 1-1.4 mm beads over the shearing time. Increasing deformation can be observed especially on the top surfaces of the pellets with increasing normal pressure from the top lid. The use of the highest pressure, 2000 Pa, caused greater deformation on the top surfaces of the pellets in comparison to the lowest and medium normal pressures; 383 and 600 Pa. As expected, this observation was in line to the elongation results presented in Figure 5.19. As the shearing time increased up to 100 s, substantial deformation can be observed at the top surfaces of the pellets sheared with a normal pressure of 2000. On the other hand, the shear effect on the top surfaces of pellets sheared with normal pressures of 383 and 600 Pa did not show much difference over the shearing time.

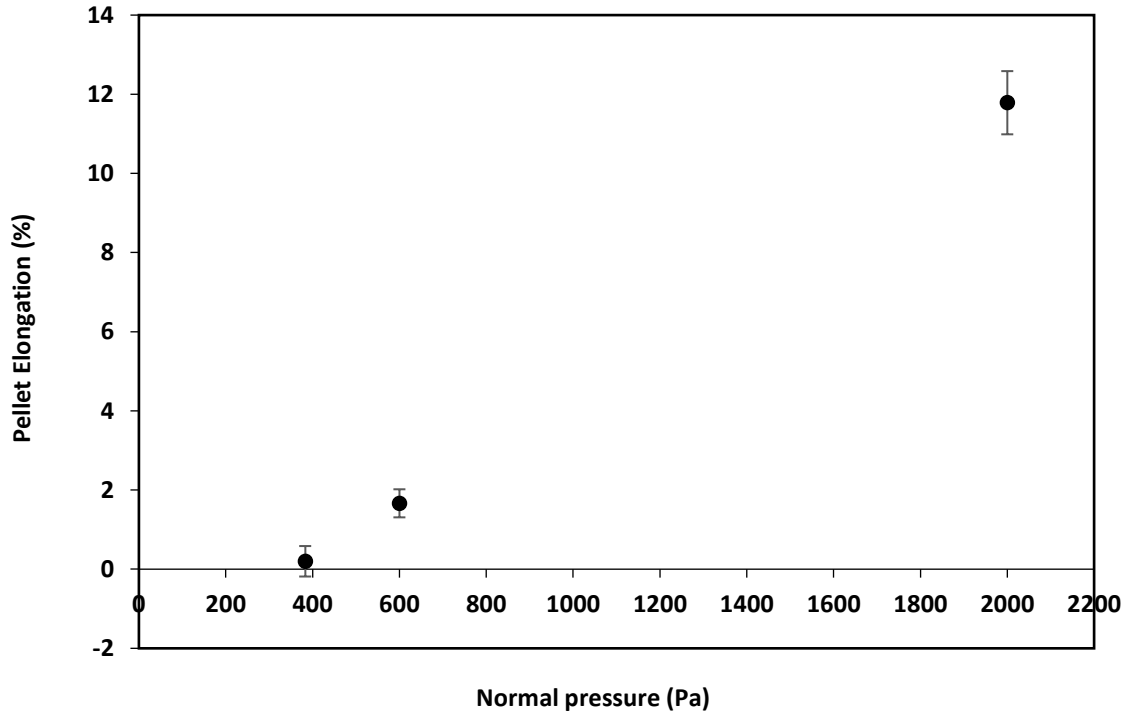


Figure 5.19 Pellet elongation, E_p , versus normal pressure for lactose 10cSt pellets with a shear rate of 40.21/s and 1-1.4 mm background beads. Error bars represent the standard error of 4 measurements

Increasing the shearing time (s)

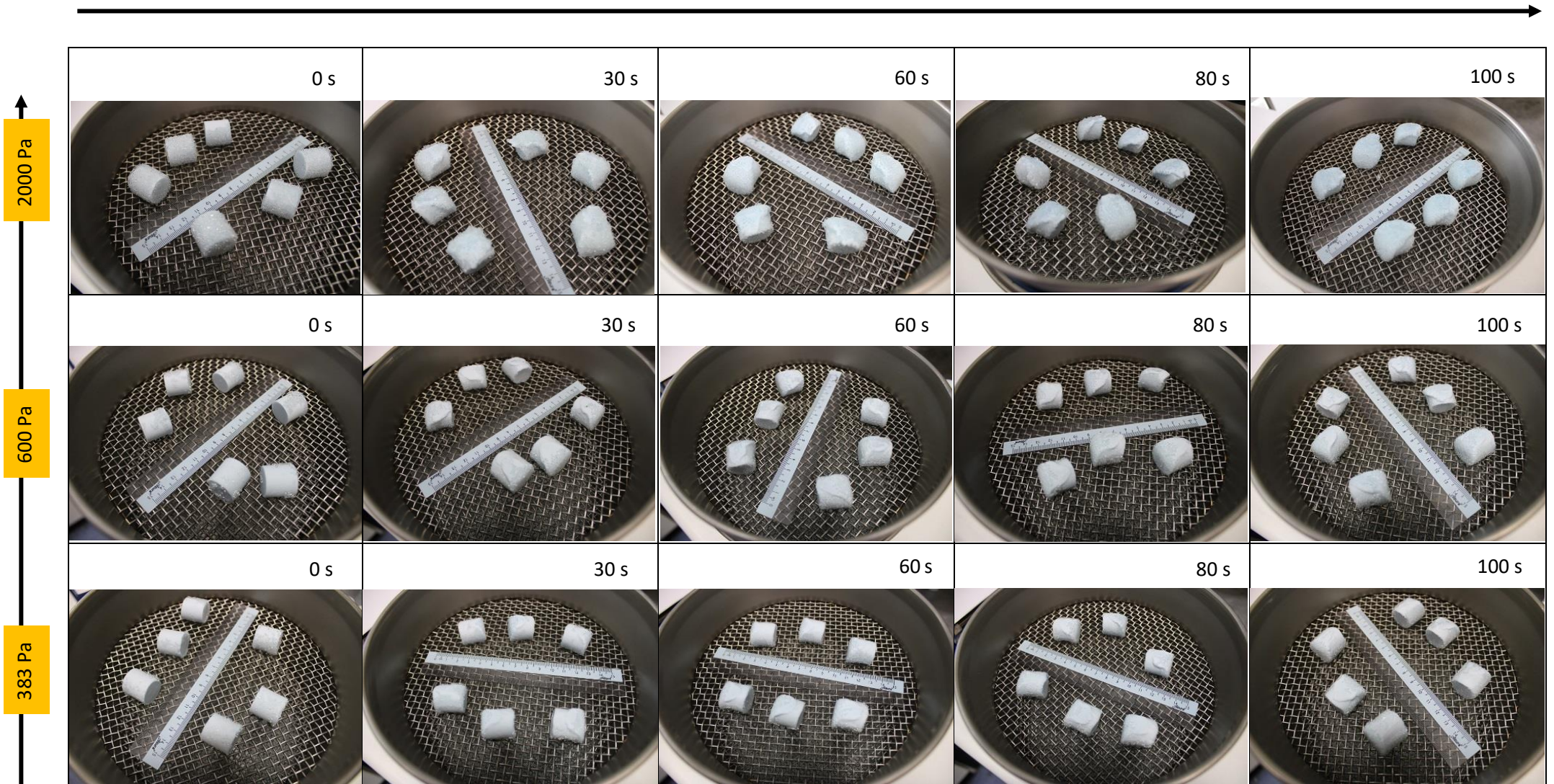


Figure 5.20 Images of lactose 10cSt pellets with shearing time, at a shear rate of 40.21/s and 1-1.4 mm background beads for conditions: 383 Pa (bottom), 600 Pa (middle) and 2000 Pa (top)

5.3.1.5 Effect of size of background beads (1 -1.4 mm and 2 mm)

Figure 5.21 shows the pellet elongation and sizes of background beads relationship for lactose 10cSt pellets with conditions of 40.21/s, 2000 Pa. The pellet elongation results were the average of pellet elongation data at different shearing times between 30 and 100 s. A 100 % elongation was recorded for pellets sheared with larger sized beads in comparison to the smaller sized beads. It is likely that the larger size of beads has transmitted greater stresses to the pellets causing the pellets to deform completely. An elongation of 11.79 % were observed for pellets sheared with smaller beads.

These findings were supported by the images of the pellets (Figure 5.22). It can be seen that the pellets sheared with 2 mm beads were flattened after 30 s of shearing, indicating 100 % elongation has been achieved. For this purpose, the pellets were deformed completely. Further prolonging the shearing for 100 s resulted in 100 % elongation for pellets sheared with 2 mm beads. For pellets sheared with 1-1.4 mm beads, the top surfaces of the pellets showed large deformation. Prolonging the shearing time up to 100 s did not result in any significant difference to the shape of the pellets.

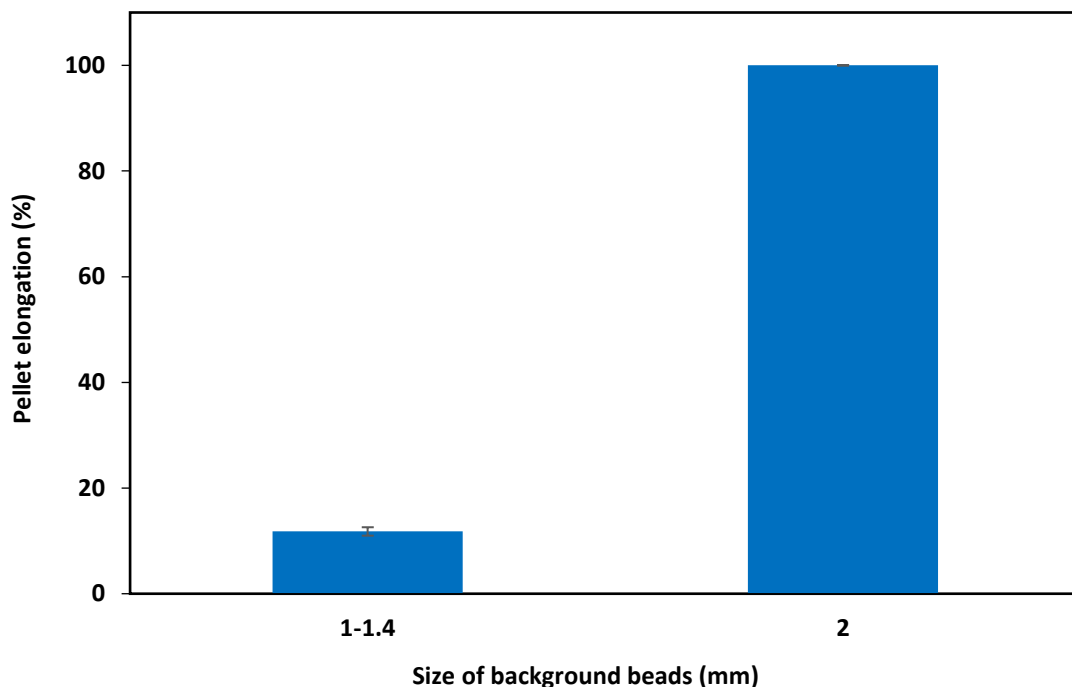


Figure 5.21 Pellet elongation, E_p , versus size of background beads for lactose 10cSt pellets with a shear rate of 40.21/s and a top lid pressure of 2000 Pa. Error bars represent the standard error of 4 measurements

Increasing the shearing time (s)

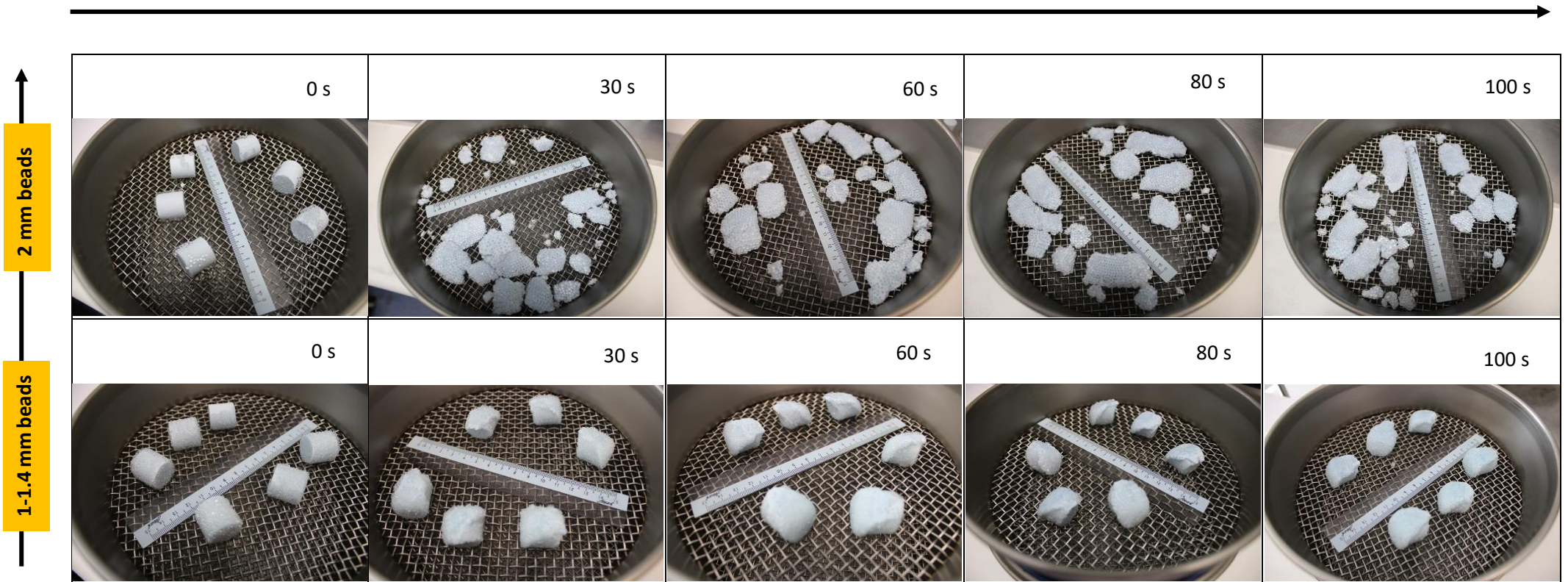


Figure 5.22 Images of lactose 10cSt pellets with shearing time, using a shear rate of 40.21/s and a top lid pressure of 2000 Pa for conditions: 1-1.4 mm beads (bottom) and 2 mm beads (top)

5.3.2 Deformation behavior of the weakest pellets (ballotini 10cSt pellets)

The following section provides the results and discussion for the weakest pellets; ballotini 10cSt pellets. The effect of several parameters such as compression from the top lid, shear rates and normal pressures on pellet deformation were considered.

5.3.2.1 Effect of any compression from the top lid

Pressure as a result of loading and uplifting the top lid on the bed particles might cause some deformation of the ballotini pellets. Therefore, the shape of the ballotini pellets before loading and after lifting the top lid was observed by capturing the images of the pellets at 0 s, i.e., without turning on the annular shear cell. A comparison has been made for ballotini pellets (normal pressure of 2000 Pa and a background bead size of 1-1.14 mm) before loading the top lid (Figure 5.23) and after lifting the top lid (Figure 5.24). As shown in Figure 5.24, some of the pellets had minor chipping, or were fragmented due to the process of scooping them out from the annular shear cell. However, in general, there was no substantial difference to the shapes of the 6 pellets after lifting the top lid.

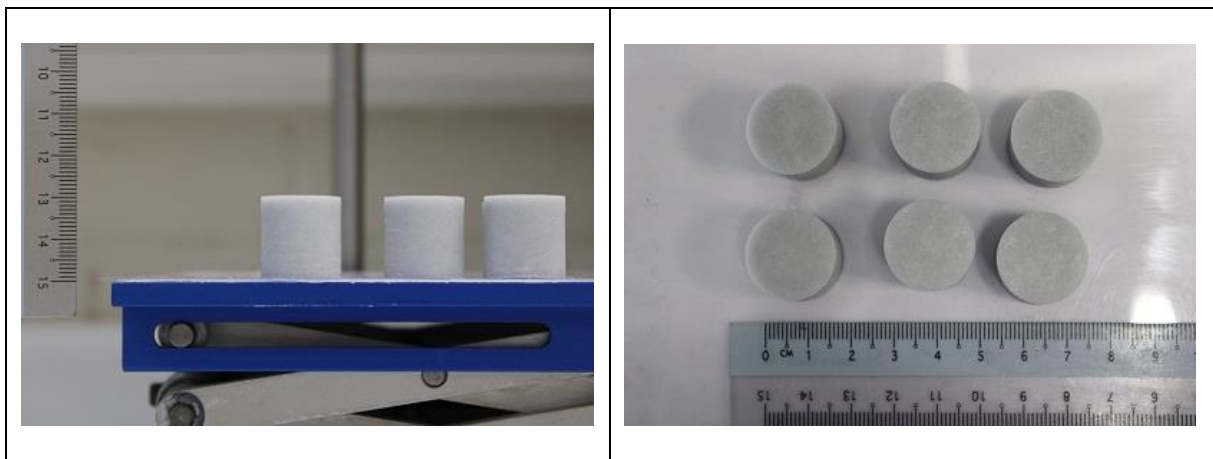


Figure 5.23 Shape of ballotini 10cSt pellets with 1-1.4 mm beads before loading top lid

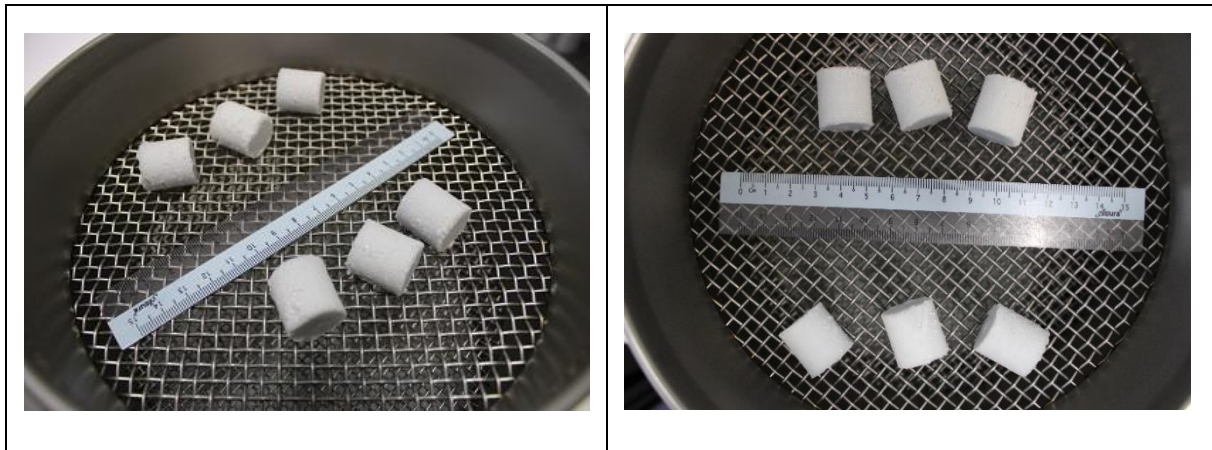


Figure 5.24 Shape of ballotini 10cSt pellets with 1-1.4 mm beads after uplifting the top lid

5.3.2.2 Effect of shear rate (5.03/s and 40.21/s)

Figure 5.25 shows the deformation fraction (%) of ballotini pellets using conditions of 2000 Pa, 1-1.4 mm background beads and two different shear rates; 40.21/s and 5.03/s. The deformation fraction results were the average of deformation fraction data at different shearing times between 30 and 100 s. There was a significant difference between the two shear rates on deformation of the ballotini pellets. Small negative values of deformation fraction were recorded for 5.03/s, which demonstrate minimal deformation, and likely represents the accumulation of some of the beads on the surface of the pellets. Large differences in deformation fraction were observed between these two shear rates. This can be due to the soft and fragile properties of the ballotini pellets, which could not withstand the higher shear rate of 40.21/s and likely to fragments and breakup as compared to the lower shear rate of 5.03/s.

The deformation fraction results are supported by the images of the pellets. Figure 5.26 shows the images of the deformed ballotini pellets at the different shear rates. The effect of compression and shearing can be observed on the top surfaces of pellets with a shear rate of 5.03/s. Significant deformation can be observed for the pellets sheared at 40.21/s, especially on the top surfaces of the pellets. Greater deformation is seen that captured in Figures 5.26. Deformation for ballotini pellets sheared with the higher shear rate, 40.21/s increased as increasing the shearing time from 30 s to 100 s. Some parts of the pellets were broken resulting in small fragments being produced after 30 s of shearing. Increasing the shearing time up to 100 s results in more compression and shearing of the pellets.

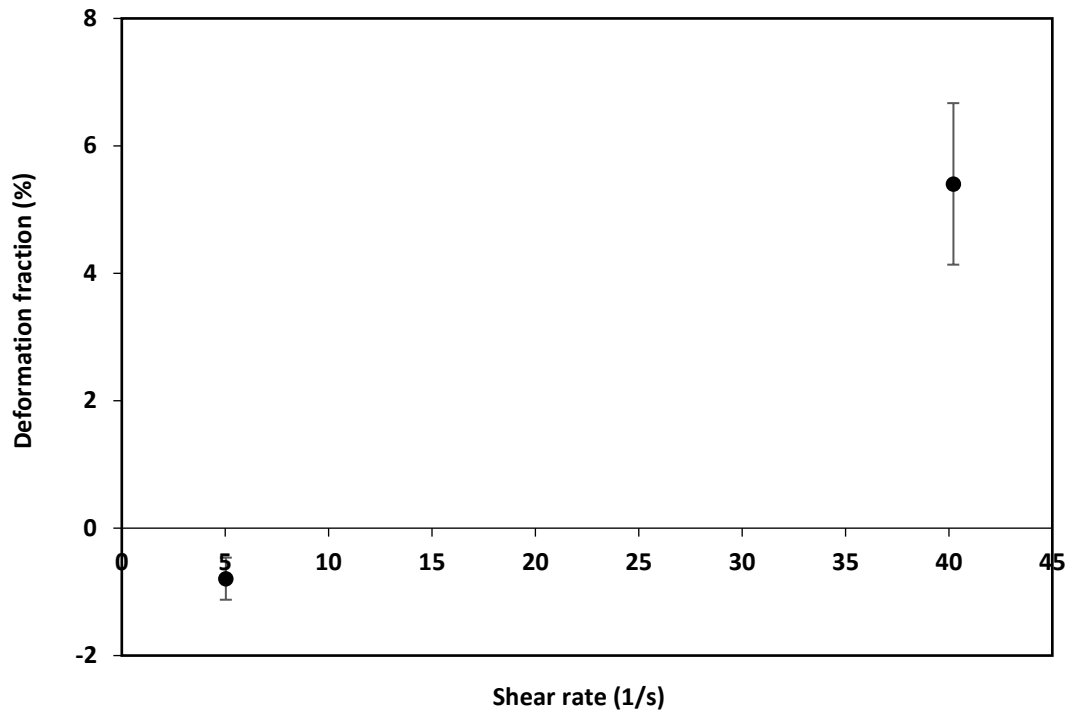


Figure 5.25 Deformation fraction, F_D , versus shear rate for ballotini 10cSt pellets with a top lid pressure of 2000 Pa and 1-1.4 mm background beads. Error bars represent the standard error s of 4 measurements

Increasing the shearing time (s)

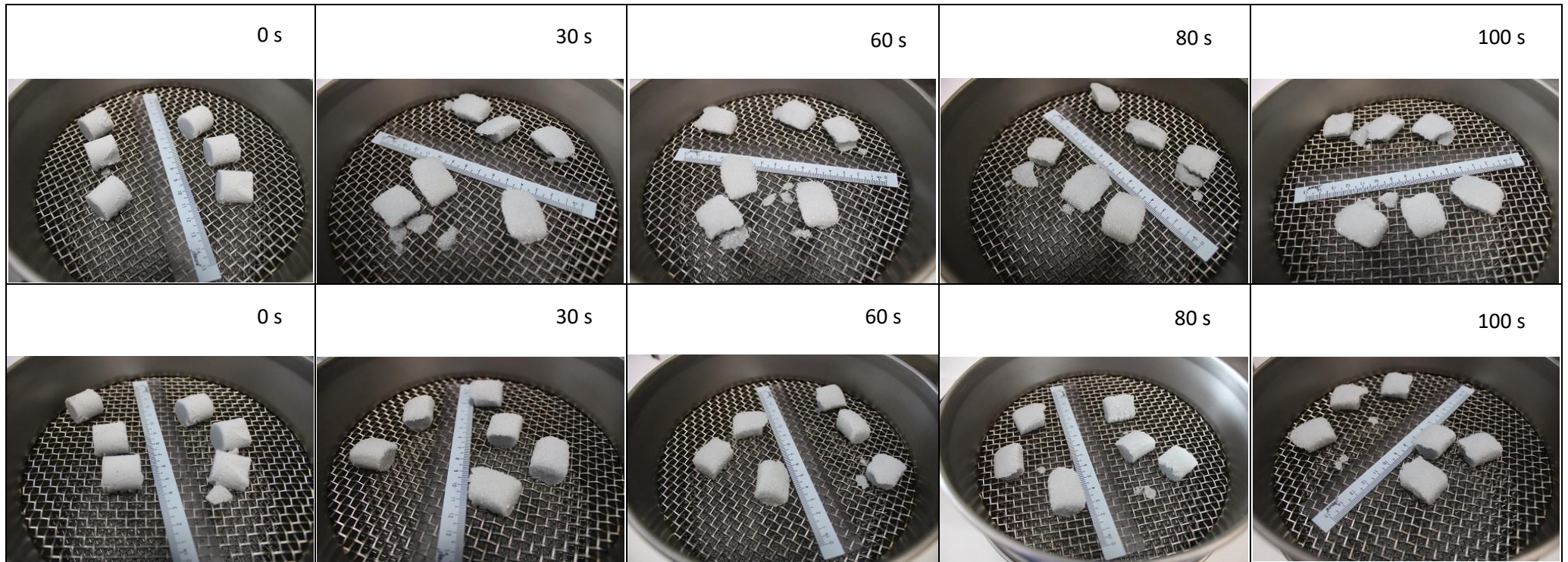


Figure 5.26 Images of ballotini 10cSt pellets with shearing time, with a top lid pressure of 2000 Pa and 1-1.4 mm background beads for conditions: 5.03/s (bottom) and 40.21/s (top)

5.3.2.3 Effect of normal pressures (383 Pa, 600 Pa and 2000 Pa)

Figure 5.27 shows the deformation fraction (%) versus different normal pressures tested for ballotini 10cSt pellets with conditions of the highest shear rate, 40.21/s, and the smaller size of beads; 1-1.4 mm beads. The deformation fraction results were obtained by averaging the deformation fraction data at different shearing times between 30 and 100 s. Higher values of deformation fraction (%) with almost same level of deformation were observed for both pellets sheared with 383 and 2000 Pa. These two different shear rates showed values of deformation fraction; 5.36 % and 5.40 %, respectively. The values of deformation fraction for pellets sheared with the medium normal pressure (600 Pa) were less than 1 % and unexpectedly below those for 383 Pa. While the reason for this is not known, it is possible that this effect is due to experimental error. Possible sources of error are 1) the presence of background beads on the surfaces of the pellets, which contributes to the increasing mass of the pellets during the weighing measurements; 2) error in weighing measurements which were very sensitive and 3) lack of repeats for the 600 Pa case. It is also possible that the deformation fraction is not fully capturing the deformation behaviour.

In Figure 5.28, the effect of different normal pressures (2000 Pa, 600 Pa and 383 Pa) with conditions of 40.21/s and 1-1.4 mm beads on the ballotini pellets were supported by the images of the pellets. As the shearing time increased to 100 s, pellets sheared with the highest normal pressure of 2000 Pa exhibited a significant deformation on top surfaces of pellets with some fragments observed throughout the 100 s of shearing time. These observations were in line to the increasing of deformation fraction (%) results in Figure 5.27. On the other hand, pellets sheared with lowest and medium normal pressures; 383 and 600 Pa showed only minor deformation on the top surfaces This deformation as a result of shearing did not change much over the period of 100 s. Unlike the quantitative results in Figure 5.27, the significant difference in deformation behaviour between highest pressure, 2000 Pa and the lower pressures, 383 and 600 Pa, could be observed qualitatively. It is possible that in the case where there is not large pellet breakup, the deformation fraction measure is not able to capture the deformation.

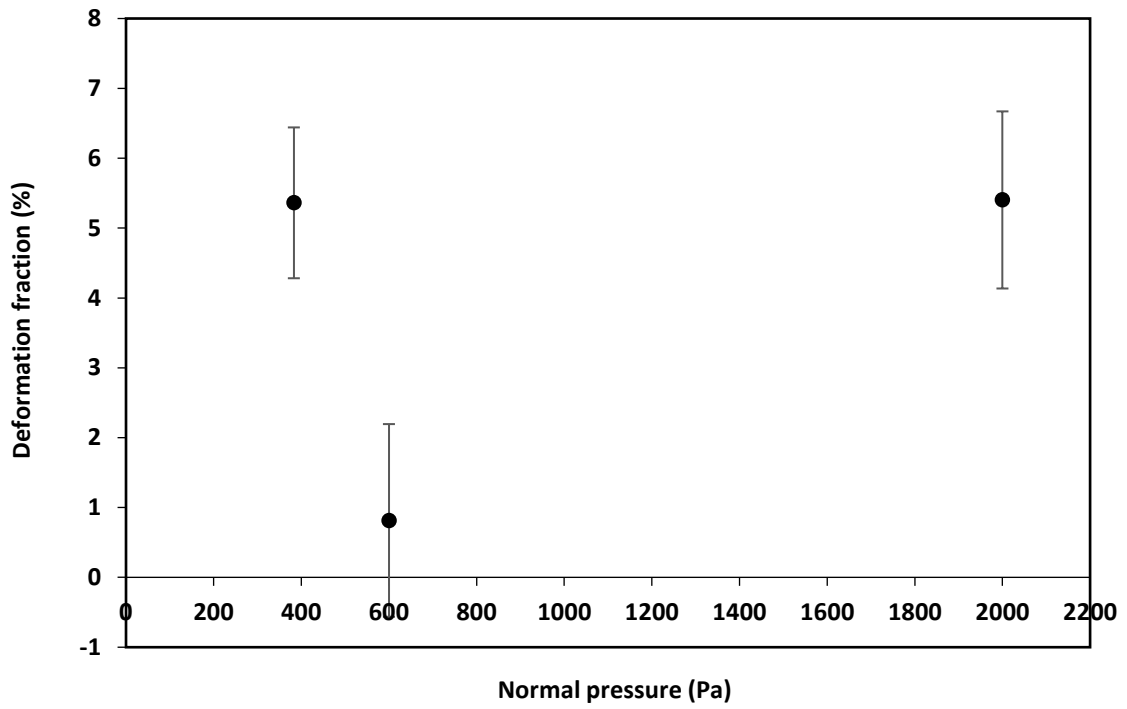


Figure 5.27 Deformation fraction, F_D , versus normal pressure for ballotini 10cSt pellets with a shear rate of 40.21/s and 1-1.4 mm background beads. Error bars represent the standard error of 4 measurements

Increasing the shearing time (s)

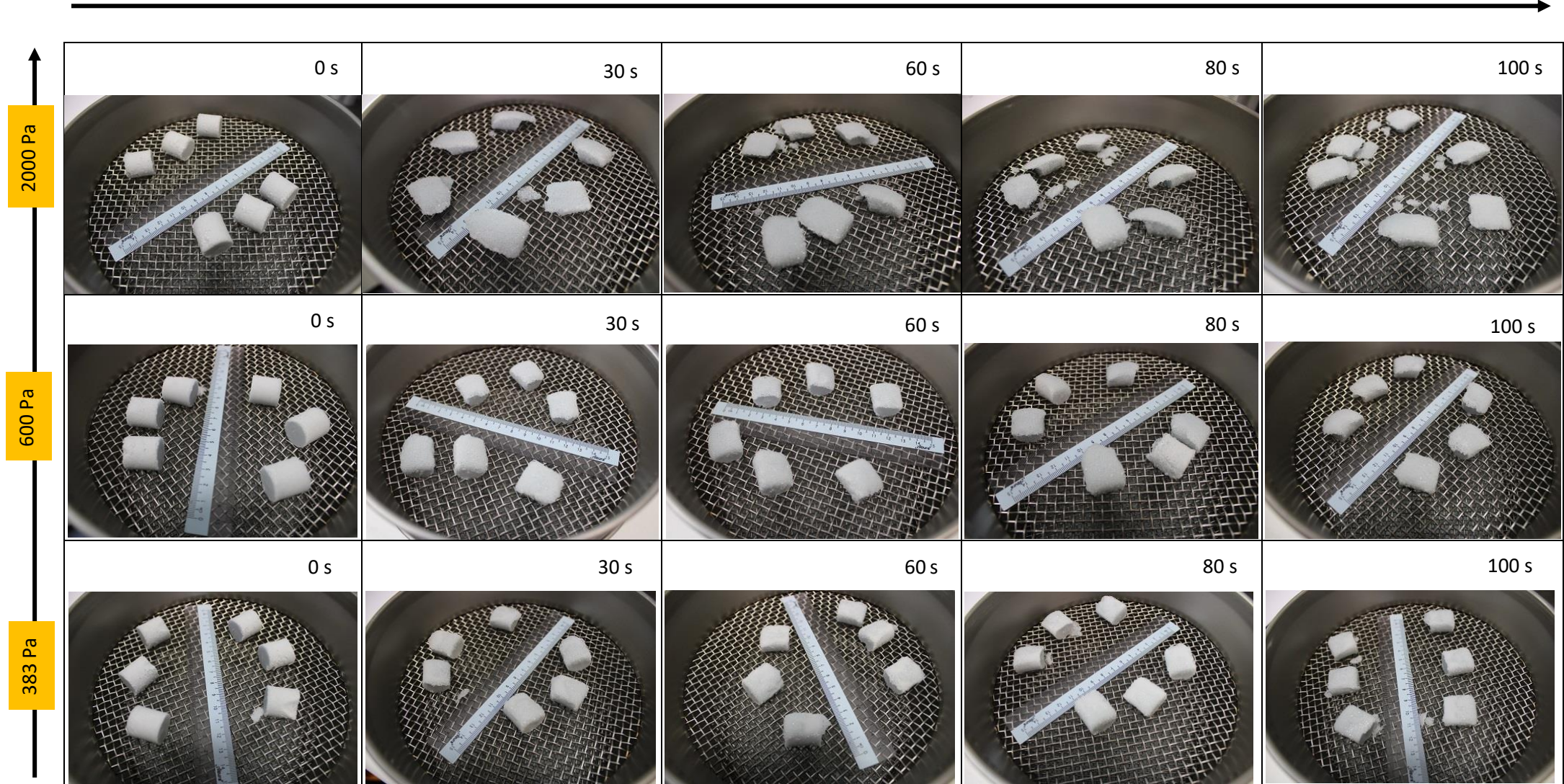


Figure 5.28 Images of ballotini 10cSt pellets with shearing time, with a shear rate of 40.21/s and 1-1.4 mm background beads for conditions: 383 Pa (bottom), 600 Pa (middle) and 2000 Pa (top)

5.3.3 Pellet deformation and the Stokes deformation number, St_{def} relationship

This section describes the results and discussion for the relationship between the experimental pellet deformation and the Stokes deformation number, St_{def} . The experimental results of pellet elongation and deformation fraction were obtained from Sections 5.3.1 and 5.3.2. Stokes deformation number, St_{def} was chosen as one of the analyses for describing or predicting the pellet deformation in the annular shear cell, i.e., small and large deformation. Moreover, the range values of critical Stokes deformation numbers, St_{def}^* , are defined from the same figure of St_{def} to predict the safe condition for the pellets shearing in the annular shear cell. These values are between small and large deformation. Stokes deformation number, St_{def} can be calculated using Equation 5.3 in Section 5.2.4.4. One of the parameters of Stokes deformation number, St_{def} , the representative collision velocity in the annular shear cell, v_c , is an approximation based on the rotation rate of the lid; assumed to be 15 % of the rate of the lid. For this reason, the change of the shear rate is selected and used in the calculation of Stokes deformation number, St_{def}

5.3.3.1 Lactose 10cSt pellets with conditions: 2000 Pa and 1-1.4 mm beads

Figure 5.29 shows the pellet elongation for lactose pellets sheared with two different shear rates, 2000 Pa and 1-1.4 mm beads plotted against the Stokes deformation number, St_{def} . The pellet elongation results were the average of pellet elongation data, taken at different shearing times between 30 and 100 s in the previous Section 5.3.1.2. The values of St_{def} shown in Figure 5.29 include several different measurements for the dynamic yield stress, taken at different crosshead speeds (See Section 4.4.3, Chapter 4). The two different shear rates showed very different levels of deformation, the areas of small and large deformation in the St_{def} plot. Pellets sheared with higher shear rate of 40.21/s and elongation values greater than 10 % are given St_{def} higher than 1.9×10^{-4} , indicating large deformation. The pellets sheared with the lower shear rate of 5.03/s and the elongation values was less than 4 % are given St_{def} lower than 6.8×10^{-6} , which represents small deformation. These findings were similar to the previous elongation results plotted in Figure 5.15, by which the higher shear rate resulting in higher values of elongation in comparison to the lower shear rate.

The value of St_{def} is dependent on the value of the yield stress, and for these granular pellets the yield stress is a dynamic property. From this graph, increasing the yield stresses of pellets by compressing the pellets from 1 to 50 mm/s resulting in lower values of St_{def} . These range values of yield stresses could lower the probability of deformation of the pellets. Whereas, pellets compressed

with highest speed of 125.7 mm/s are given a high value of St_{def} , indicating a high probability of deformation. The reason is that the highest compression speed of 125.7 mm/s leads to the lowest yield stress, as obtained from the dynamic compression test. Based on these range values of yield stresses of pellets obtained from different compression speeds, the range values of the critical Stokes deformation number, St_{def}^* , are between 6.8×10^{-6} and 1.9×10^{-4} .

As the highest compression speed, 125.7 mm/s, is roughly equivalent to the lowest annular shear cell rate of 5.03/s, the St_{def} , calculated at a compression speed of 125.7 mm/s would be considered. It would appear the values of the critical Stokes deformation number, St_{def}^* are between 6.8×10^{-6} and 1.9×10^{-4} , which predicted the safe condition of shearing in the annular shear cell for lactose pellets sheared with two different shear rates, 2000 Pa and 1-1.4 mm beads. While a coarse correlation between pellet elongation St_{def} is apparent, in this instance St_{def} could able to predict the probability of deformation, i.e., small and large deformation and range values of the critical Stokes deformation number, St_{def}^* for lactose pellets sheared with two shear rates, 2000 Pa and 1-1.4 mm beads.

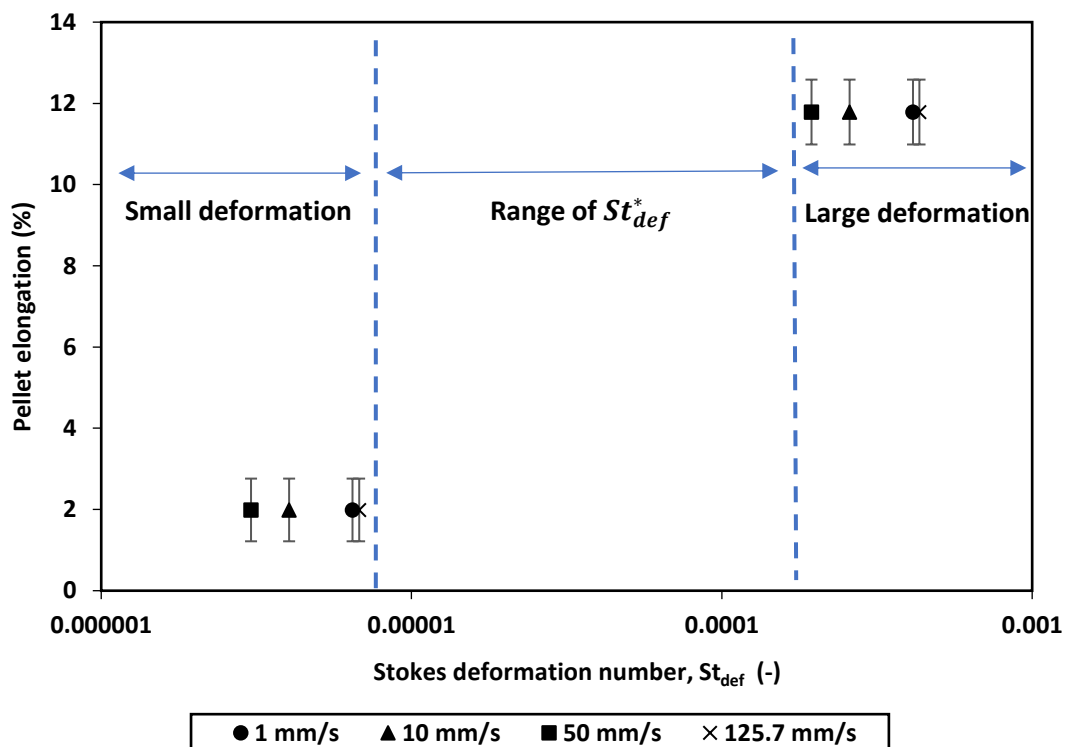


Figure 5.29 Pellet elongation, E_p , and Stokes deformation number, St_{def} , relationship for lactose 10cSt pellets at shear rates of 5.03/s and 40.21/s, a top lid pressure of 2000 Pa, 1-1.4 mm background beads and uniaxial compression speeds between 1 mm/s and 125.7 mm/s. Error bars represent the standard error of 4 measurements

5.3.3.2 Lactose 10cSt pellets with conditions: 2000 Pa and 2 mm beads

In Figure 5.30, the pellet elongation results were plotted against the Stokes deformation number, St_{def} , for the effect of different shear rates with condition of 2000 Pa and 2 mm beads. The pellet elongation results were average of pellet elongation data at different shearing times between 30 and 100 s in the previous Section 5.3.1.3. The values of St_{def} were calculated based on the yield stresses of lactose pellets compressed at compression speeds between 1 mm/s and 125.7 mm/s. The different shear rates have created the areas of small and large deformation in the St_{def} plot. A St_{def} higher than 1.9×10^{-4} showed large deformation, represented by pellets sheared with higher shear rate, 40.21/s and 100 % elongation. Pellets sheared at the lower shear rate, 5.03/s and about 25 % elongation showed small deformation with St_{def} lower than 6.8×10^{-6} . These findings were in line with the elongation results shown in Figure 5.17. The higher shear rate resulted in 100 % elongation, indicating 100 % deformation of the pellets in comparison to the lower shear rate.

It can be seen that increasing the yield stresses of pellets by compressing the pellets from 1 to 50 mm/s resulted in lower values of the St_{def} . The high values of yield stresses could lower the probability of deformation of the pellets, whereas, pellets compressed with highest speed of 125.7 mm/s had a high value of the St_{def} . The high probability of deformation was due to the lower value of yield stress, similar to the previous results obtained using the smaller background beads (Section 5.3.3.1). The critical Stokes deformation number, St_{def}^* , appears to be between 6.8×10^{-6} and 1.9×10^{-4} , for St_{def} calculated from several yield stresses of lactose pellets compressed at different compression speeds.

By considering the pellets with lower shear rate of 5.03/s and the values of St_{def} calculated from the yield stresses of lactose pellets compressed at the highest compression speed of 125.7 mm/s, both are equivalent to the lowest rotational speed of the annular shear cell; 15 rpm. The range values of the critical Stokes deformation number, St_{def}^* , are between 6.8×10^{-6} and 4.3×10^{-4} . These range values of St_{def}^* indicate the safe condition of shearing in the annular shear cell for lactose pellets with two different shear rates, 2000 Pa and 2 mm beads. These findings were similar to the previous results using the smaller sized background beads (Section 5.3.3.1). It shows that predicting the deformation of the lactose pellets for different shear rates, 2000 Pa and 2 mm beads using St_{def} could be made.

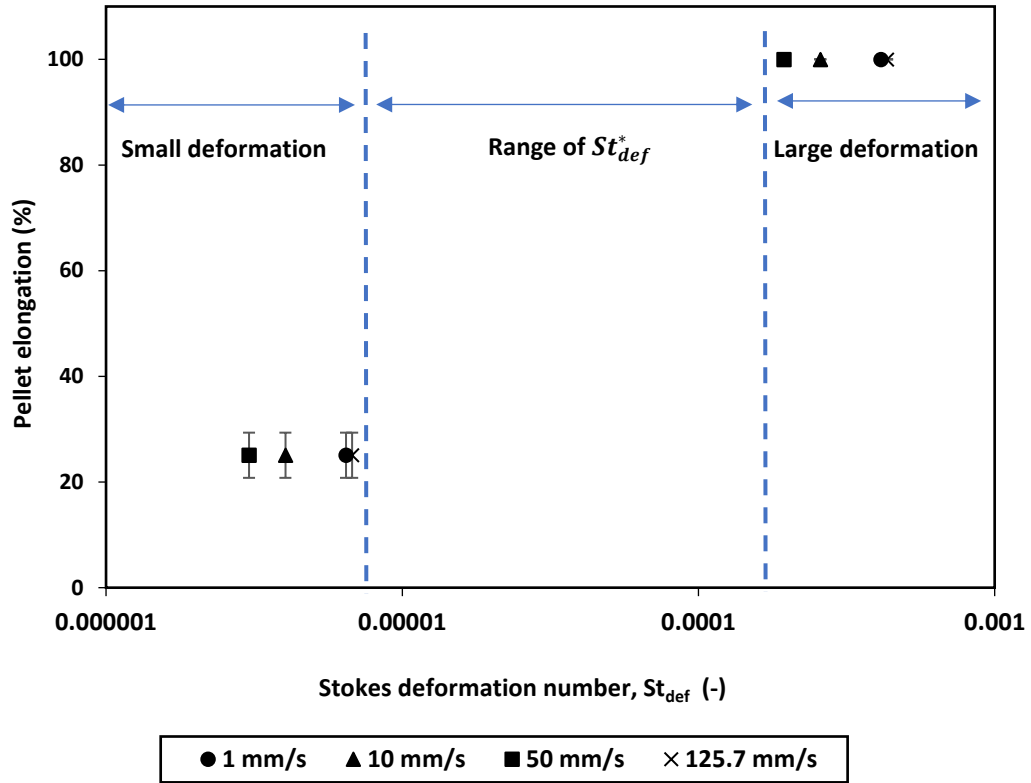


Figure 5.30 Pellet elongation, E_p , and Stokes deformation number, St_{def} , relationship for lactose 10cSt pellets at shear rates of 5.03/s and 40.21/s, a top lid pressure of 2000 Pa, 2 mm background beads and uniaxial compression speeds between 1 mm/s and 125.7 mm/s. Error bars represent the standard error of 4 measurements

5.3.3.3 Ballotini 10cSt pellets

In Figure 5.31, the deformation fraction for ballotini pellets sheared at the two different shear rates, 2000 Pa and 1-1.4 mm beads are plotted against the Stokes deformation number, St_{def} . The deformation fraction results were average of deformation fraction data, taken at different shearing times between 30 and 100 s in the previous Section 5.3.2.2. The values of St_{def} were calculated based on the values of yield stresses at compression speed of between 1 and 125.7 mm/s. A St_{def} above a value of 4.5×10^{-3} , represents the area of large deformation was dominated by pellets sheared with the higher shear rate, 40.21/s, and a deformation fraction above zero. Below the St_{def} value of 1.4×10^{-4} , showed small deformation for pellets sheared with lower shear rate, 5.03/s, and a deformation fraction below zero. The results were similar to the deformation fraction results in Figure 5.25, by which the higher shear rate resulted in high % values of deformation fraction in comparison to the lower shear rate.

Moreover, increasing the compression speeds from 1 to 125.7 mm/s increased the yield stress of the ballotini 10cSt pellets (refer to Table 4.4, Section 4.4.3, Chapter 4). As expected, increasing yield stresses of ballotini 10cSt pellets resulted in lower values of the St_{def} . These results were found for both shear rates. The range values for the critical Stokes deformation number, St_{def}^* are between 1.4×10^{-4} and 4.5×10^{-3} , by which the values of St_{def} calculated from several yield stresses at different compression speeds.

The safe condition of shearing in the annular shear cell for the ballotini pellets was predicted based on the values of the St_{def} , calculated from yield stresses at a compression speed of 125.7 mm/s, which is roughly equivalent to the lowest annular shear cell rate of 5.03/s. Therefore, it would appear the values of the critical Stokes deformation number, St_{def}^* are between 7.1×10^{-5} and 4.5×10^{-3} . In this analysis, the Stokes deformation number as calculated here is able to predict pellet deformation behaviour and the safe condition for ballotini pellets sheared with two different shear rates, 2000 Pa and 1-1.4 mm beads in the annular shear cell.

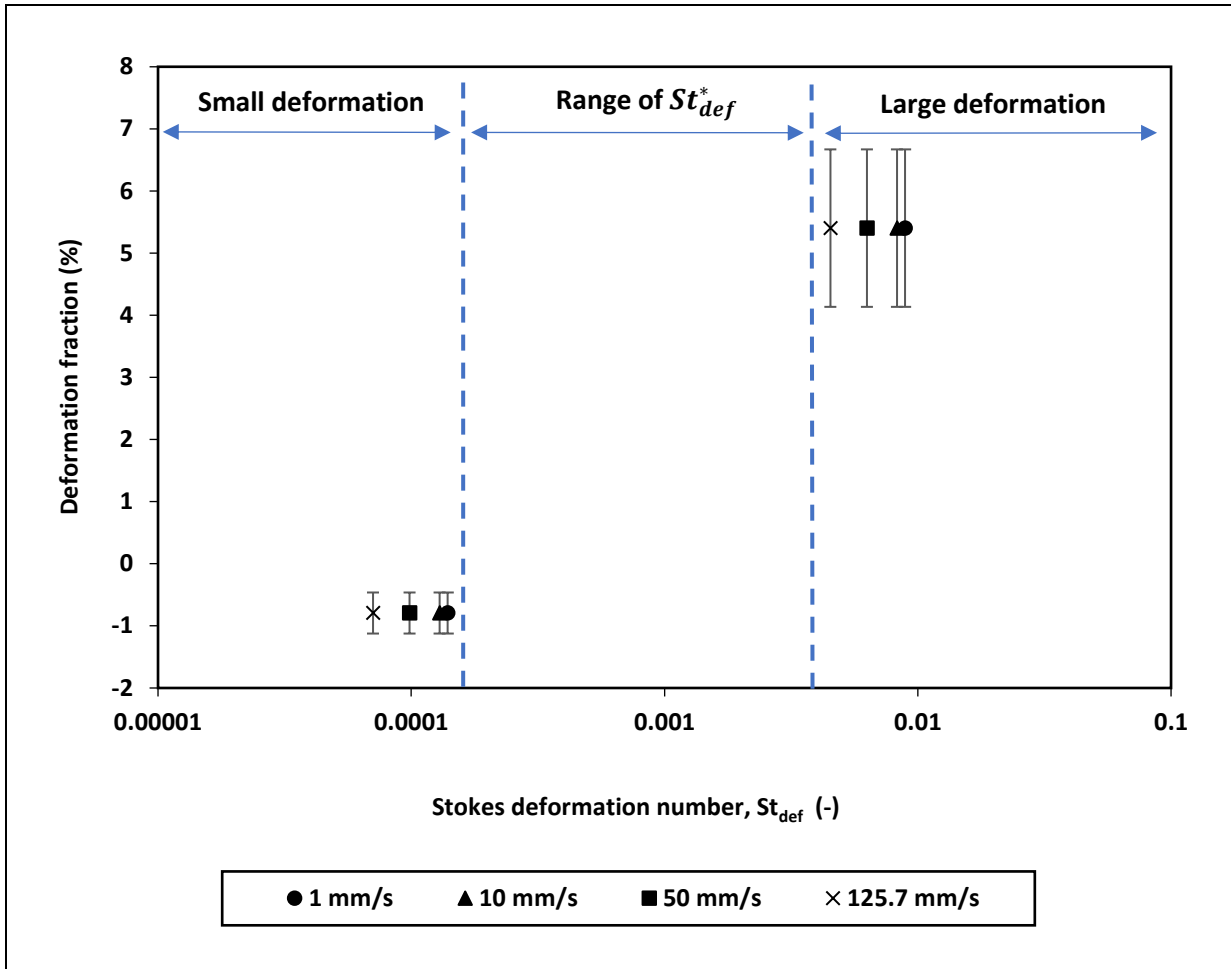


Figure 5.31 Deformation fraction, F_D , and Stokes deformation number, St_{def} , relationship for ballotini 10cSt pellets at shear rates of 5.03/s and 40.21/s, a top lid pressure of 2000 Pa, 1-1.4 mm background beads and uniaxial compression speeds between 1 mm/s and 125.7 mm/s. Error bars represent the standard error of 4 measurements

5.4 Summary

In this chapter, the results from deformation experiments on selected granular pellets; (lactose 10cSt and ballotini 10cSt) pellets in an annular shear cell have been presented. Several operating parameters such as compression from the top lid, shear rates, normal pressures, size of background beads and shearing time were considered. Types of deformation, degree of deformation through pellet elongation (%) and deformation fraction (%) have been evaluated by varying these operating parameters. In general, pellet deformation was promoted by increasing normal pressure, high shear rates, larger background beads and longer shearing times.

The experiments have been shown to be capable of providing both good qualitative and quantitative results of the deformation of pellets under different operating parameters in the annular shear cell. In particular, the elongation % is promising as a method to capture the deformation behaviours. However, the deformation fraction may not be able to capture deformation behaviour in the case where there is not significant fragmentation.

The experimental results were compared with the Stokes deformation number, St_{def} . The input parameters for the Stokes deformation number, St_{def} , were obtained experimentally based on the material properties or equipment conditions. The range of values of critical Stokes deformation number, St_{def}^* , were proposed from the plotted Stokes deformation number, St_{def} .

The Stokes deformation number, St_{def} , may be able to be used as a predictive tool for predicting the deformation of pellets for changing shear rate. Several values of critical Stokes deformation number, St_{def}^* , were obtained by considering shear rates and the values of dynamic yield stresses measured at different compression speeds as the input parameters of the Stokes deformation number. The safe condition of shearing in the annular shear cell for both lactose and ballotini pellets with certain conditions could be predicted by using two different shear rates and the values of the St_{def} , calculated from yield stresses at a compression speed of 125.7 mm/s.

In the next chapter, simulations and prediction of granular pellet deformation will be based on the experiments described in this chapter. The pellet deformation is predicted by means of both DEM simulations and von Mises failure theory.

6 Predicting granular pellet deformation through DEM simulations and failure theory

6.1 Introduction

The experimental measurement of internal stresses in granular flows is a well-known problem, without current practical solutions. It has been suggested that the most appropriate approach for this purpose is the use of DEM simulations (Massih Pasha et al., 2013). Development of a DEM unit shear cell is described in this chapter, including the conditions for designing and building the DEM unit shear cell, creating the DEM cylindrical pellets, the contact force model for interaction of the materials and the setup for DEM simulations. The setup for pressure from the top plate, lists of material properties for DEM simulations, interaction properties for all materials, parameters, processing and post-processing for DEM simulations are also explained. The DEM simulations are used to assess the stresses experienced by a granular pellet in the DEM unit shear cell. Further, the pellet deformation is predicted by means of both DEM simulations and von Mises failure theory.

6.2 Designing and building the DEM unit shear cell

A DEM unit shear cell was developed in DEM simulations based on the experimental annular shear cell. As shown in Figure 6.1, the annular shear cell has inner diameter, D_i , of 110 mm and outer diameter, D_o , of 210 mm. The cell was divided into 6 sections based on the arrangement of the pellets. This corresponds to a 60° wedge, from the centre of the annular shear cell in the y-x plane. From the 60° wedge, a section of the annular shear cell represented by a rectangular unit shear cell was chosen as a “DEM unit shear cell” model. This section describes several factors for designing and building the DEM unit shear cell such as periodic boundaries, length, width and height of the DEM unit shear cell.

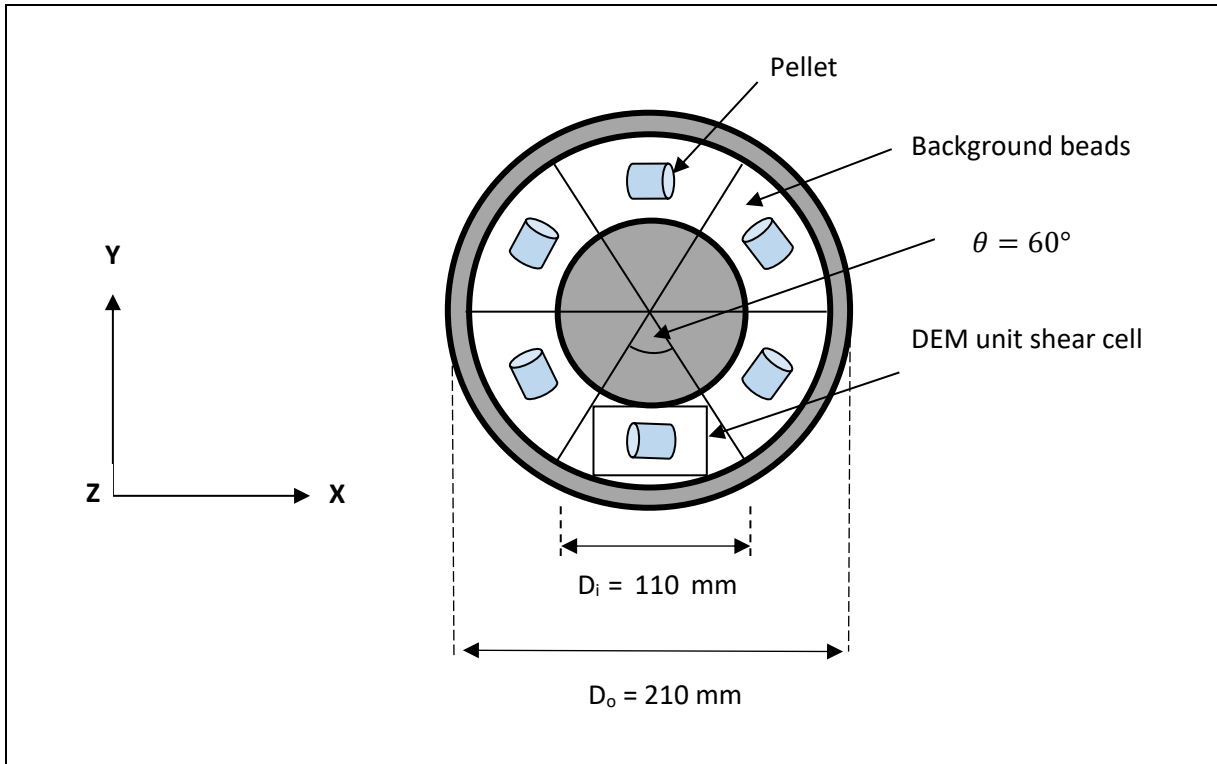


Figure 6.1 Sections of the annular shear cell and the DEM unit shear cell

6.2.1 Periodic boundaries

The DEM unit shear cell was given periodic boundaries in the x and y directions to represent the symmetrical geometry of the whole annular shear cell. The periodic boundaries of the DEM unit shear cell were designed to improve the computational efficiency of the DEM simulations. The effect of circumferential curvature from the annular shear cell was ignored in this study. However, the other key operational features of the annular shear cell were still maintained.

6.2.2 Length and width of the DEM unit shear cell

Both the lengths of the DEM unit shear cell, s_1 and s_2 , were set to be same for simplicity of the measurement. The length in the x-direction of the DEM unit shear cell was computed by using the arc length formulation and the centre angle in degrees (Equations 6.1 to 6.3). The width in the y-direction of the DEM unit shear cell is the difference between the two specified radii, $r_2 - r_1$. Therefore, the length in the x-direction and the width in the y-direction of the DEM unit shear cell are 0.06283 m and 0.03 m, respectively (Figure 6.2).

$$\text{Length } s_1 = \frac{\theta}{360^\circ} \times 2\pi \times r_1 \quad \text{Equation 6.1}$$

$$s_1 = 0.06283 \text{ m} \quad \text{Equation 6.2}$$

$$s_1 = s_2 = 0.06283 \text{ m} \quad \text{Equation 6.3}$$

where

$\theta =$	Angle of the section	(°)
s_1 and s_2	Lengths of the DEM unit shear cell	(m)
r_1 and r_2	Two specified radii of the annular unit shear cell	(m)
$r_i =$	Inner radius of the annular unit shear cell	(m)
$r_o =$	Outer radius of the annular shear cell	(m)

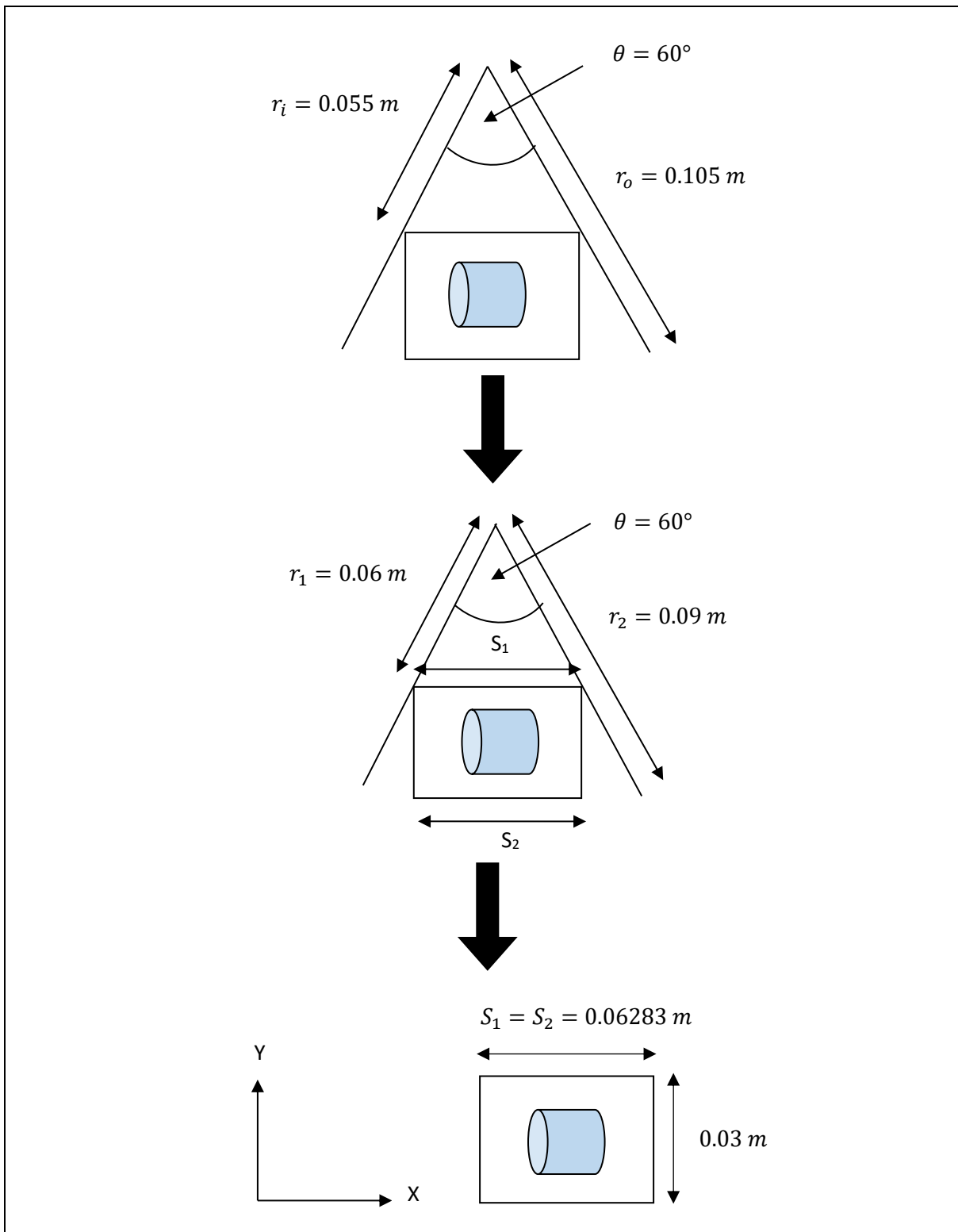


Figure 6.2 Length in the x-direction and width in the y-direction for the DEM unit shear cell

6.2.3 Height of the DEM unit shear cell and simulation domain

For this study, the height of DEM unit shear cell was equal to the depth of bed particles (pellet and background beads) which filled the trough of the annular shear cell (refer to Section 5.2, Chapter 5). In previous studies, the 'sample thickness' term was often used to refer to the depth of bed particles (granular particles) filling the trough in the annular shear cell. Additionally, the number of particle diameters of granular particles was often used as an indicator to measure the depth of bed particles filling the trough.

According to (Paramanathan & Bridgwater, 1983a), the sample thickness is a very critical parameter in the shear cell. They found that part of the granular particles could not be sheared if the sample thickness was too large. (Paramanathan & Bridgwater, 1983b, 1983a) used sample thicknesses of 10, 12 and 20 mm. Meanwhile, the study by (C. Liao et al., 2017b) used 33.35 mm as the sample thickness.

(Ghadiri et al., 2000b) chose a sample thickness of 13.38 mm and an average particle size of 2.23 mm (in diameter) to ensure that all the granular particles were subjected to a shear strain. Therefore, the sample thickness was equivalent to 6 granular particles. Moreover, they found that beyond this sample thickness, a stagnant block of granular particles would be developed at the bottom of the shear cell. The granular particles would become jammed /stuck and unable to move during the shearing. From their study, it showed that the full shear cell would only remain in the failure zone if the sample thickness was less than 5 - 6 spherical granular particles. (Paramanathan & Bridgwater, 1983a) used a particle size between 200 and 2000 μm (in diameter). The shear cell was built to allow a maximum sample thickness of 20 mm to form a complete failure zone. Thus, an amount of 10 granular particles (for particle size of 2000 μm) was assumed to be within the failure zone.

For this current study, the pellet thickness was 20 mm and the background beads had mean diameters of 1.18 mm and 2 mm. A maximum sample thickness of 25 mm was chosen to ensure the pellet was fully covered by the background beads. The sample thickness would be equivalent to approximately 21 particles of 1.18 mm beads and 13 particles of 2 mm beads, respectively. As these amounts of beads were higher than the previous studies, it was expected that some of the shearing medium would be in the failure zone.

Figure 6.3 shows the height in the z-direction for the DEM unit shear cell. The height of the DEM unit shear cell was 25 mm, which was equivalent to the sample thickness. The height of the simulation domain was made to be double this value; 50 mm. This height of the simulation domain was chosen to ensure the required number of beads could be fully generated within the DEM unit shear cell.

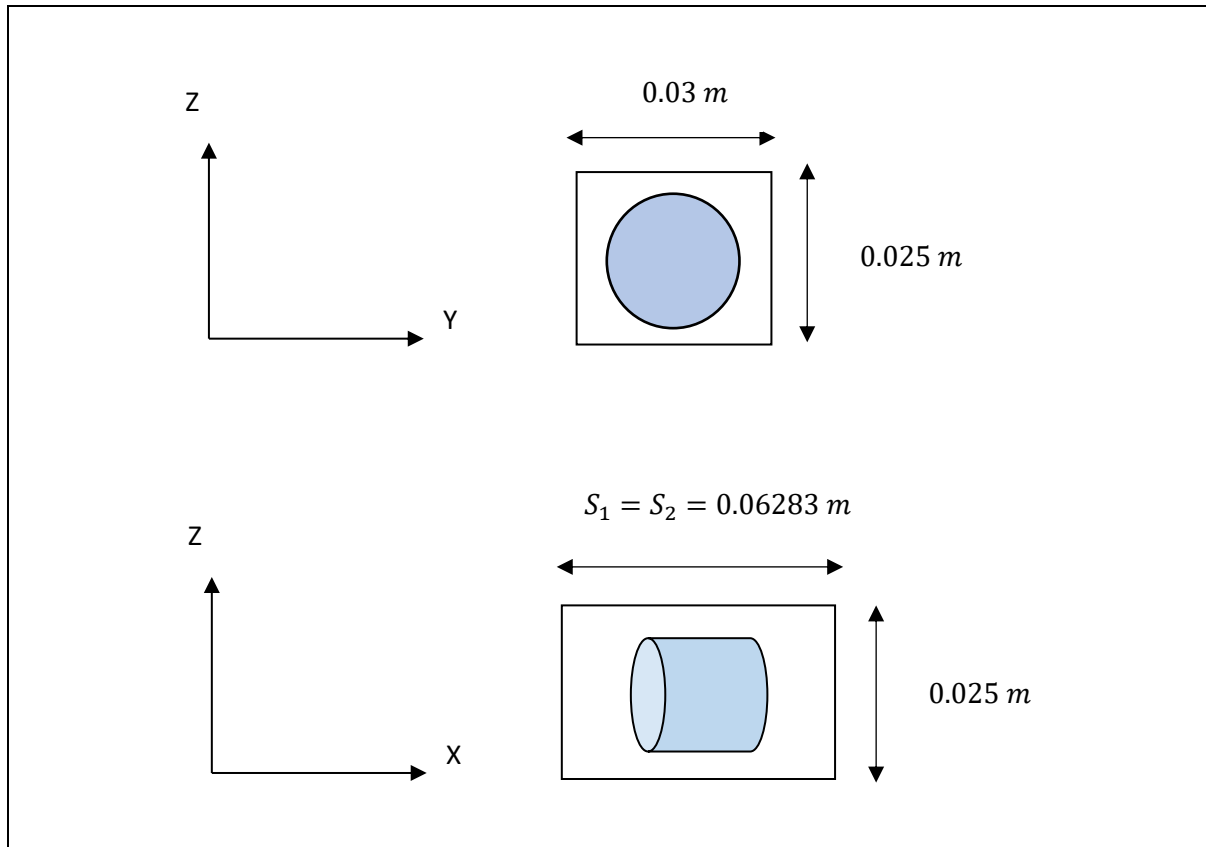


Figure 6.3 Height in the z-direction for the DEM unit shear cell

6.3 Creating a DEM cylindrical pellet

Figure 6.4 describes the steps for creating the pellet in DEM simulations. The model material of the DEM cylindrical pellet consists of an agglomeration of multi-sphere particles. The diameter and length of the pellets were 20 mm, chosen to enable reliable measurements of unconfined yield strength. First, the pellet was produced based on the experimentally produced pellets (Figure 6.4 (a)). Second, a 3D geometry of the pellet was designed in Autodesk Inventor 2016 software (Figure 6.4 (b)). Then, the 3D geometry was saved and exported into .stp file format and used as the 3D meshes in the DEM simulations (Figure 6.4 (c)). A single DEM cylindrical pellet was constructed using a combination of 142

spherical particles of 2 mm and 44 spherical particles of 3 mm. They were filled at a specific position within the 3D meshes to form the 3D model of the cylindrical pellet (Figure 6.4 (d)).

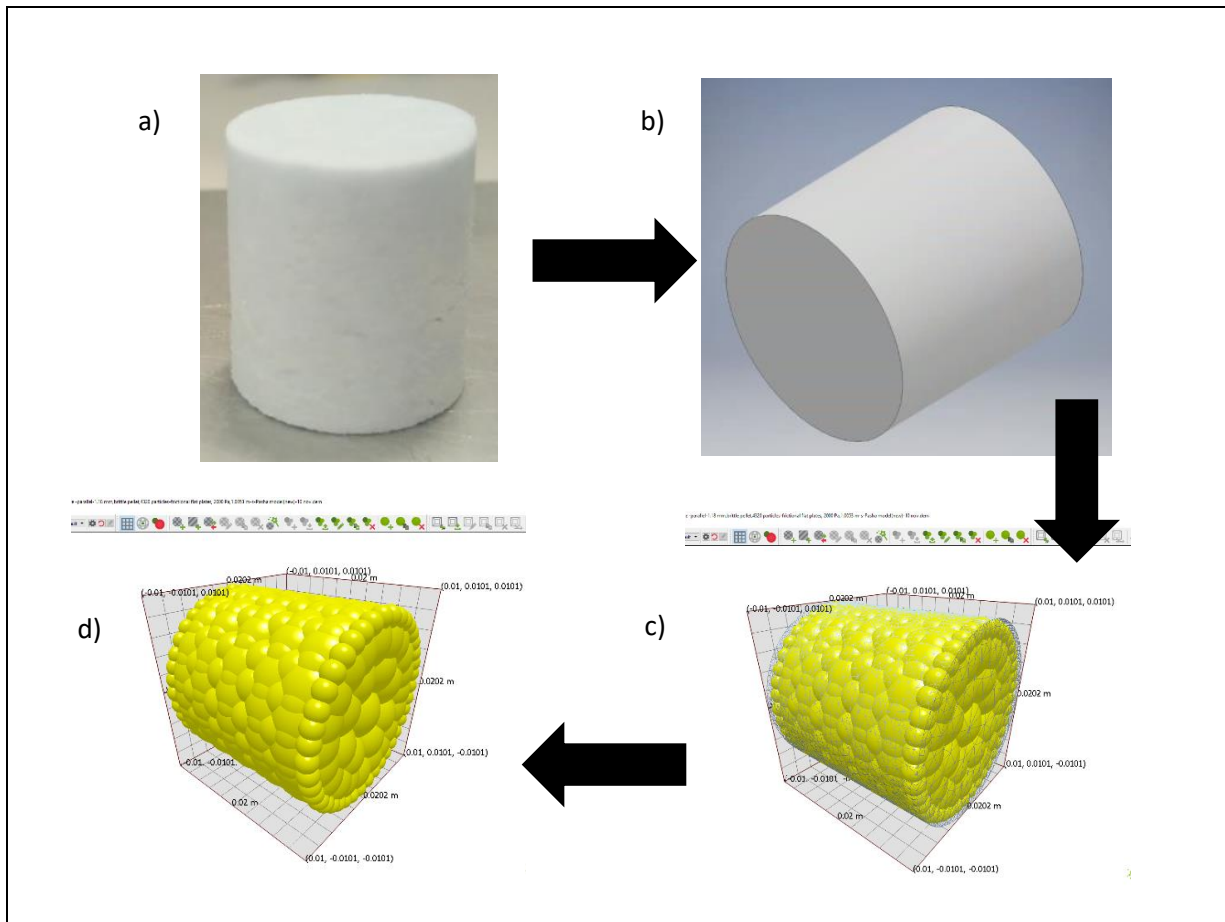


Figure 6.4 (a) Experimentally produced pellet; (b) 3D geometry of the pellet; (c) 3D meshes of the pellet in DEM simulations and (d) 3D model of the pellet in DEM simulations

6.4 Contact force models

For validation purposes, the shearing process in DEM simulations must be able to imitate the shearing process in the annular shear cell experiment. This is to ensure the results from DEM simulations can be compared to the experimental results. Two contact models; a moving plane model and a linear elastic, plastic contact without adhesive contact model, modified version of Simplified Pasha’s model were chosen for this current study. A moving plane model was applied on the active moving plane; in this case, it refers to the top plate. It was built in the EDEM software and added for the geometry – particle interaction.

The modified version of Simplified Pasha's model represents the linear elastic-plastic without adhesive contact model. It was applied as a current contact model by add-on the Simplified Pasha's contact model into the EDEM, consisting of a compile file and an input properties file in .txt of Simplified Pasha's contact model. The input properties file in .txt of Simplified Pasha's contact model requires the values of plastic and elastic stiffness of the materials to be used. However, the Simplified Pasha's model requires only two types of materials, namely particle and geometry, to be defined.

The term 'particle' refers to granular particles and the term 'geometry' refers to the vessel and impeller blade, i.e. stainless steel. The pellet and background beads are chosen as the two materials to be used in this study, and the background beads have direct contact with the pellet during shearing. The pellets which were formulated from different paste materials in the experiments are assumed to behave as elastic-plastic contact with no adhesion. Similarly, the model of background beads behaves as elastic-plastic contact with no adhesion. The values of plastic and elastic stiffness for both pellet and background beads are set in the input properties file in .txt of Simplified Pasha's contact model to represent the current contact model, the modified version of Simplified Pasha's model.

Figure 6.5 shows the normal force – overlap relationship the modified version of Simplified Pasha's contact model. All the adhesive stiffness and adhesive forces are zero. The contact starts from zero, by which the contact force and overlap are zero, $f_0 = 0$ and $\alpha = 0$. Under compressive loading (line OA), the contact is deformed with a line of slope k_p (plastic stiffness) until reaching the maximum overlap, α_{max} (point A). The unloading path (line A α_p) is represented by the line with slope k_e (elastic stiffness) until the unloading force becomes zero at α_p .

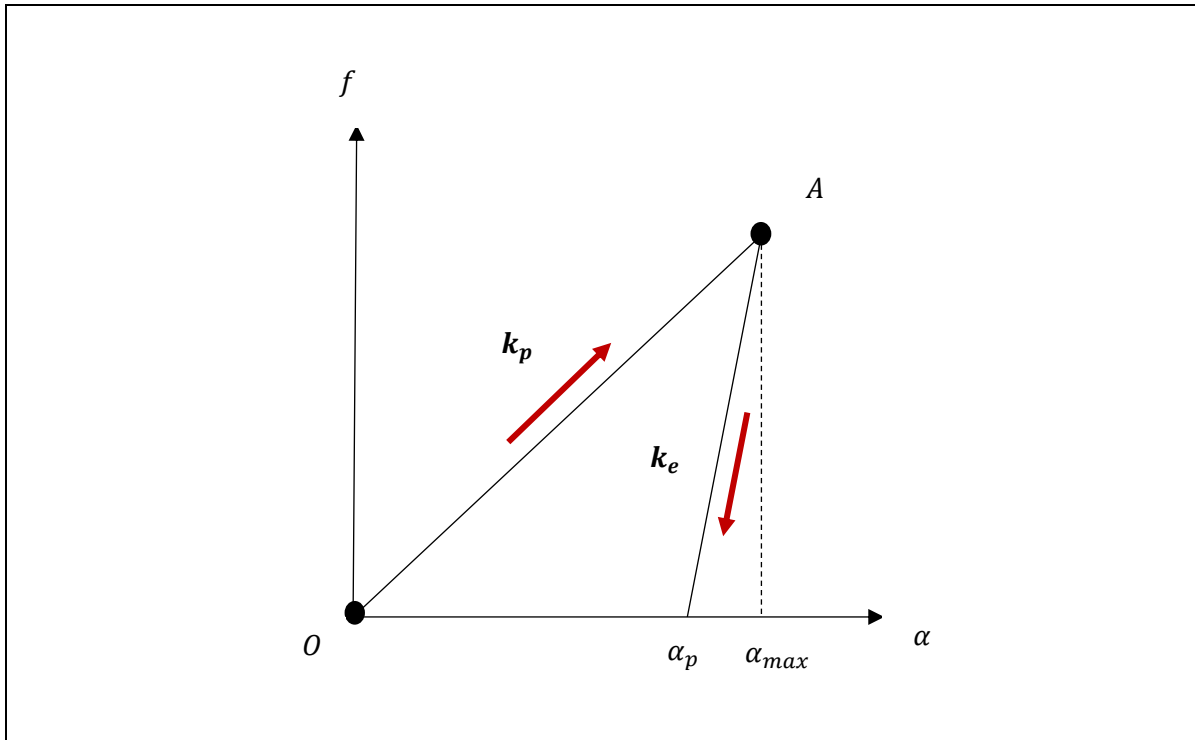


Figure 6.5 Normal force – overlap relationship in the modified version of Simplified Pasha's model: linear elastic-plastic without adhesive contact model

In the modified version of Simplified Pasha's model, the loading (line OA) and unloading (line A α_p) equations are considered (Equations 6.4 and 6.5).

$$f = k_p \alpha \quad \text{Equation 6.4}$$

$$f = k_e(\alpha - \alpha_p) \quad \text{Equation 6.5}$$

where

$f =$	Normal force	(N)
$k_p =$	Plastic stiffness	(N/m)
$k_e =$	Elastic stiffness	(N/m)
$\alpha =$	Overlap	(m)
$\alpha_p =$	Overlap at which the unloading force becomes zero	(m)

6.5 Setup for DEM simulations

The hardware and system requirements for the DEM simulations were identified. The DEM simulations were performed with commercial software, EDEM version 2017, running on a Dell Precision T5610 computer. The computer uses Windows 10 Pro, dual core processors of Intel® Xeon® CPU E5-2637 v2 at 3.50 GHz, 32 GB of installed RAM and a 64-bit operating system. The EDEM software allows the running of DEM simulations with a maximum of 8 cores.

6.6 Pressure from the top plate of the DEM unit shear cell

The pressure from the top plate of the DEM unit shear cell was similar to the pressure applied from the top lid in the annular shear cell experiments. A constant load force was added to the EDEM software to apply the constant pressure from top plate. The EDEM software was coupled with an interface of external code files created in a C++ file and an input file in .txt to execute the constant load force. The top plate information, such as the name of the top plate given in EDEM, mass of the top plate, area of the top plate, pressure of top plate, initial velocity for the top plate to move downward, time for the top plate to start shearing, simulation end time and time step ratio for simulation stability are defined in the input file in .txt. The area of the top plate was equivalent to the area of the DEM unit shear cell; $0.06283 \times 0.03 = 0.0018849 \text{ m}^2$. The mass of the top plate was calculated based on the known values of pressure and area of the top plate, as shown in Table 6.1.

Table 6.1 Pressure, mass and area of the top plate

Pressure from top plate (Pa)	Mass of top plate (kg)	Area of top plate (m²)
383	0.073594	0.0018849
600	0.115324	0.0018849
2000	0.384413	0.0018849

6.7 Material properties for DEM simulations

The material properties for DEM simulations were identified and are explained in this section. They were particle size, mass, stiffness, Young's modulus, shear modulus and density. Some of the properties of background beads such as the particle size distribution, mass and density, properties of pellets such as density, stiffness and Young's modulus were experimentally determined in Chapters 3 and 4.

6.7.1 Particle size distribution and mass of background beads for DEM simulations

In reality, the background beads consisted of a range of different sizes; they were polydisperse. By mimicking the real size distribution of the background beads in the DEM simulations (as opposed to using monodisperse particles), more accurate results of the shearing process can be obtained and compared with the experiment.

Based on the sieve method explained in Section 3.3.2, Chapter 3, the selected ranges of size distribution for the background beads were further sieved to obtain the mass (by percentage). The size distribution for the background beads in DEM requires a scale and mass (by percentage) at that scale. The scale is the ratio of selected sieve size to the particle size with the highest frequency (mode size) (Equation 6.6). The mode sizes for beads of 1-1.4 mm and 2 mm are 1.18 mm and 2 mm, respectively (see Table 3.2).

$$Scale = \frac{\textit{sieve size (mm)}}{\textit{mode size (mm)}} \quad \textbf{Equation 6.6}$$

Tables 6.2 and 6.3 show the selected ranges of sieve size and the pan below the smallest sieve size. The pan must be a numerical value, and it was assumed as 0.85 mm and 1.4 mm for beads of 1-1.4 mm and beads 2 mm, respectively. There was less than 0.2 % of the mass of the beads in the pan for both types of beads, and for ease of computation, these particles were added to the smallest sieve fraction. The chosen mass of beads in the DEM simulations (%) for each of selected ranges of sieve size is shown in the final columns of Tables 6.2 and 6.3.

Table 6.2 Scale and percentage of mass for background beads 1-1.4 mm in DEM simulations

Sieve size (mm)	Scale	Percentage of mass (%)					Chosen mass in DEM (%)
		1	2	3	4	Average	
1.4	1.19	0.71	0.92	0.88	0.92	0.86	0.86
1.18	1	53.73	53.09	54.48	49.56	52.71	52.71
1	0.85	45.42	45.84	44.59	49.37	46.31	46.43
0.85	0.72	0.14	0.14	0.06	0.15	0.12	
Total		100	100	100	100	100	

Table 6.3 Scale and percentage of mass for background beads 2 mm in DEM simulations

Sieve size (mm)	Scale	Percentage of mass (%)					Chosen mass in DEM (%)
		1	2	3	4	Average	
2	1	99.96	99.96	99.96	99.94	99.96	99.96
1.7	0.85	0.03	0.03	0.04	0.03	0.03	0.04
1.4	0.7	0.01	0.01	0	0.03	0.01	
Total		100	100	100	100	100	

6.7.2 Stiffness of pellets and background beads for DEM simulations

The modified version of Simplified Pasha's model requires plastic and elastic stiffness of the pellets and background beads. The plastic and elastic stiffness of different pellets were determined experimentally from the slope of the linear part of loading and unloading of force-displacement curve (see Table 4.2). However, the plastic and elastic stiffness for the background beads were based (M. Pasha et al., 2015) works, which used model of particles that had a density of 2500 kg/m³; a value of density close to the background beads. Therefore, plastic and elastic stiffness of 0.1 M N/m and 1 M N/m were chosen for the background beads. Table 6.4 lists the values of stiffness for the pellets and background beads. The tangential stiffness, k_t was equal to the elastic stiffness, k_e for each type of material, following the works by (Massih Pasha et al., 2013, 2014b).

Table 6.4 Stiffness of pellets and background beads in the DEM simulations

Materials	Plastic stiffness, k_p (N/m)	Elastic stiffness, k_e (N/m)	Tangential stiffness, k_t (N/m)
Background beads ^a	100 000	1000 000	1000 000
Types of pellets			
Ballotini 10cSt	1983 (92)	18871 (177)	18871 (177)
Ballotini 50cSt	1914 (287)	17863 (256)	17863 (256)
Ballotini 100cSt	1613 (42)	16971 (184)	16971 (184)
Ballotini 1000cSt	1379 (168)	16816 (301)	16816 (301)
Lactose 10cSt	24447 (819)	233233 (5846)	233233 (5846)
Lactose 1000cSt	8377 (482)	257036 (6098)	257036 (6098)
MCC 10cSt	9483 (79)	32406 (381)	32406 (381)
MCC 1000cSt	7155 (649)	28943 (1397)	28943 (1397)

^a Literature data from (M. Pasha et al., 2015)

*Parentheses give the standard error values of a minimum of 3 measurements

6.7.3 Young's modulus of materials for DEM simulations

The top and bottom plates were made from stainless steel and their value of Young's modulus was 189.8 GPa (Bharadwaj et al., 2010; Pantaleev et al., 2017). The value of Young's modulus for background beads was 70 GPa. The value was based on ballotini beads with size ranging between 1 and 3 mm, as reported by (Cavarretta et al., 2010). Table 6.5 lists the Young's modulus of the pellets for DEM simulations. They were measured from quasi-static compression tests using 10 N and 0.02 mm/s (see Table 4.3).

Table 6.5 Young's modulus of pellets for DEM simulations

	Ballotini 10cSt pellets	Ballotini 50cSt pellets	Ballotini 100cSt pellets	Ballotini 1000cSt pellets	Lactose 10cSt pellets
Young's modulus (MPa)	0.123	0.121	0.099	0.085	1.474

6.7.4 Shear modulus of materials for DEM simulations

By knowing the values of Young’s modulus and Poisson’s ratio, the values of shear modulus can be calculated using Equation 6.7. It was computed automatically in the DEM simulations. The values of Poisson’s ratio for all type of pellets and background beads were assumed as 0.25. The top and bottom plates were made of stainless steel with a Poisson’s ratio of 0.30 (Bharadwaj et al., 2010; C. Hare et al., 2011b; Pantaleev et al., 2017).

$$G = \frac{E}{2(1 + \nu)} \quad \text{Equation 6.7}$$

Where

- $G =$ Shear modulus (Pa)
- $E =$ Young’s modulus (Pa)
- $\nu =$ Poisson’s ratio (-)

6.7.5 Density of materials for DEM simulations

The value of density for the top and bottom plates was 7800 kg/m³ (Bharadwaj et al., 2010; Pantaleev et al., 2017). Table 6.6 lists the density of the pellets for DEM simulations. The values of the density were measured from the mass and volume of the pellets (see Table 3.14). The true solid and bulk densities of background beads were determined experimentally (see Table 3.5) and are listed in Table 6.7.

Table 6.6 Density of pellets for DEM simulations

	Ballotini 10cSt pellets	Ballotini 50cSt pellets	Ballotini 100cSt pellets	Ballotini 1000cSt pellets	Lactose 10cSt pellets
Density of pellet (kg/m³)	1783	1780	1781	1784	1353

Table 6.7 Densities of background beads for DEM simulations

Properties	1 – 1.4 mm glass beads	2 mm glass beads
True solid density (kg/m ³)	2523	2557
Bulk density (kg/m ³)	1494	1519

6.8 Interaction properties for DEM simulations

The coefficient of restitution (e), coefficient of friction (μ_f) and coefficient of rolling friction (μ_r) are required for the interaction properties in DEM simulations. The interaction properties for all the cases are listed in Table 6.8. For this study, the values of the coefficient of restitution (e), coefficient of friction (μ_f) and coefficient of rolling friction (μ_r) for the interactions were assumed. The coefficient of restitution for the pellet - background beads and pellet – plates were set to be 0.3. The pellet has a tendency to be rebound less after impact. As a result, there will be a low coefficient of restitution for these interactions. The coefficient of restitution for background beads themselves and background beads – plates were set to be 0.5. The background beads have a tendency to be rebound highly after impact. As a result, a high coefficient of restitution will be produced. The coefficient of friction for all contacts was set at a value of 0.4 or 0.5. The coefficient of rolling friction for all contacts was set at a lower value of 0.01.

Table 6.8 Interaction properties for all cases

Interactional property	Background beads - Background beads	Background beads - Pellet	Background beads - Plates	Pellet - Plates
Coefficient of restitution (e)	0.5	0.3	0.5	0.3
Coefficient of friction (μ_f)	0.4	0.5	0.4	0.5
Coefficient of rolling friction (μ_r)	0.01	0.01	0.01	0.01

6.9 Parameters for DEM simulations

Table 6.9 lists the parameters for DEM simulations such as size of the background beads, shear rate and normal pressure from the top plate. The effect of the formulation of the pellets such as viscosity of silicone oil and types of powders are also considered. The descriptions for some of the parameters are given in this section.

Table 6.9 Parameters for DEM simulations

Parameters	Description
Size of background beads	Between 1-1.4 mm and 6 mm
Shear rate from the top plate	Between 5.03/s and 40.21/s
Normal pressure from the top plate	383, 600 and 2000 Pa
Formulation of pellets	<ul style="list-style-type: none"> • Viscosity of silicone oils (0.01 to 1 Pa.s) • Types of powders (ballotini beads and lactose powders)

As the depth of bed particles (pellet covered by background beads) was kept constant at 25 mm, each size of background beads requires a different mass and amount of beads generated in the DEM unit shear cell. The properties for these beads are summarized in Table 6.10. The number of background beads was generated automatically in the DEM simulations based on the known mass.

Table 6.10 Properties of background beads for DEM simulations

Properties	Background beads 1-1.4 mm	Background beads 2 mm	Background beads 4 mm ^a	Background beads 6 mm ^a
Range size distribution of background beads (mm)	1-1.4	1.7-2.36	3.35-4	5.5-6
Mean diameter of background beads (mm)	1.18	2	4	6
Depth of bed particles in DEM unit shear cell (mm)	25	25	25	25
Mass of background beads in DEM unit shear cell (g)	61.03	62.03	62.08	62.16
Amount of beads generated in DEM unit shear cell	36415	5791	723	214

^a Properties for these size of beads were assumed

The position of the pellet in the DEM unit shear cell is similar to its position in the trough of the annular shear cell. The shear velocity from top plate of the DEM unit shear cell in DEM simulations can be calculated using Equation 6.8. The specific radius of the annular shear cell, r^* has been described previously in Section 5.2.2.1.

$$\mathcal{V}_s = N \times \frac{1 \text{ min}}{60 \text{ s}} \times \frac{\pi (2r^*)}{1 \text{ rev}} \quad \text{Equation 6.8}$$

Where

$\mathcal{V}_s =$	Shear velocity from top plate of DEM unit shear cell	(m/s)
$N =$	Rotational speed	(rpm)
$r^* =$	Specific radius of the annular shear cell	(m)

The shear rate from the top plate of the DEM unit shear cell can be calculated based on the shear velocity from the top plate of the DEM unit shear cell and the depth of bed particles, as shown in Equation 6.9. In Table 6.11, the shear rates from the top plate of the DEM unit shear cell were between 5.03 and 40.21/s. According (S. S. Hsiau & Yang, 2002; C. Liao et al., 2017b), to shear rates between 9.292 and 20.692/s indicate the presence of dynamic shear flow of the granular materials. The shear rates in current study were higher than the range of shear rates studied by (S. S. Hsiau & Yang, 2002; C. Liao et al., 2017b) It was believed that certain types of the pellets could be deformed under this higher range of shear rates.

$$\dot{\gamma} = \frac{\mathcal{V}_s}{h} \quad \text{Equation 6.9}$$

where

$\mathcal{V}_s =$	Shear velocity of the top plate	(m/s)
$\dot{\gamma} =$	Shear rates applied from DEM unit shear cell	(1/s)
$h =$	Sample depth of bed particles	(m)

Table 6.11 Shear rates from top plate of the DEM unit shear cell

Rotational speed (rpm)	Specific radius of the annular shear cell, r^* (m)	Shear velocity from the top plate of the DEM unit shear cell (m/s)	Bed depth (m)	Shear rates applied from the top plate of the DEM unit shear cell (1/s)
15	0.08	0.1257	0.025	5.028
27.732	0.08	0.2323	0.025	9.292 ^a
30	0.08	0.2513	0.025	10.052
60	0.08	0.5027	0.025	20.108
61.7422	0.08	0.5173	0.025	20.692 ^a
90	0.08	0.7540	0.025	30.16
120	0.08	1.0053	0.025	40.212

^a From previous studies by (S. S. Hsiau & Yang, 2002; C. Liao et al., 2017b)

6.10 Processing and post processing for DEM simulations

The DEM unit shear cell size was chosen to mimic the real, physical test in the annular shear cell, i.e. the pellet within the DEM unit shear cell is be fully covered and sheared by the surrounding background beads, which was driven by the top plate of the DEM unit shear cell. After considering the conditions in Sections 6.2.1 to 6.2.3, a dimension of 62.83 mm × 30 mm × 25 mm (X × Y × Z) was chosen for the DEM unit shear cell. The dimension for the simulation domain was 62.83 mm × 30 mm × 50 mm (X × Y × Z). The dimension of the DEM unit shear cell was made to equal the dimension of the simulation domain in the x and y-directions. Both the simulation domain and DEM unit shear cell were built at the origin point (0 m x 0 m x 0 m). The periodic boundaries of the side walls were created in the x and y directions. As a result, the movement of bed particles (pellet or a group of background beads) that are out on one side and return into another side can be visualized clearly. A combination of rigid walls and periodic boundaries of side walls were considered to build the DEM unit shear cell. The rigid walls were a moving and shearing top plate, and a stationary bottom plate. They were flat plates with friction and parallel to each other.

Both the pellet and background beads were generated together at once within the DEM unit shear cell. The pellet was positioned initially at the centre and the background beads gradually filled the space inside the DEM unit shear cell and were allowed to fall under gravity. This was to imitate the initial position of the pellet in the annular shear cell experiment. The depth of bed particles in the DEM unit shear cell was 25 mm, similar to the experimental depth of bed particles in the annular shear cell. It was equivalent to approximately 21 particles with a mean diameter of 1.18 mm and 13 particles with a mean diameter of 2 mm.

Using an approach by (A. Hassanpour et al., 2009; Ali Hassanpour et al., 2011), the total mass of the simulated bed was set to be equal to the real bed. This approach is also supported by (C. Hare et al., 2011b), who also agreed that the density of the simulated particles needs to be set similar to the real bed particles. For this study, the bulk density of background beads, which was measured experimentally, was used to calculate the required mass of the background beads to fill the DEM unit shear cell. This was to ensure the simulated bed height was equal to the experimental depth of bed particles in the annular shear cell.

The motion of the top plate in the z-direction was allowed to grip the bed particles (pellet and background beads). The top plate was started to move in the z-direction at 0.01 s to allow for the prescribed mass of background beads to be fully generated in the DEM unit shear cell. It was set to move downward with a constant velocity of 0.3 m/s. Although this relatively low velocity could increase the simulation time, it should, however, avoid any bouncing of the bed particles when touching the top plate. In this case, once the beads had settled down, they were allowed to rest to reach equilibrium in the system.

A constant force was given to the top plate in the z-direction for the purpose of giving and maintaining the pre-defining target pressure. Some properties for the movement, shearing and pressure of the top plate were defined from the add-on constant load force (refer to Section 6.6). A conveyor translation motion was applied to the top plate to shear in the x-direction. Specifications such as start time, end time, initial velocity, acceleration, initial position of the top plate and end position of the top plate were set in the EDEM. The bed particles were sheared at the prescribed shear velocity of the top plate in the x-direction. The shearing start time, total period of shearing and the simulation end time were different, depending on the conditions and operating parameters. Once the DEM simulations were completed, the resulting data generated were exported and saved into csv file format for further post-processing and analysis in MATLAB. Figure 6.6 illustrates the simulation domain, DEM unit shear cell and direction of movement and shearing of the top plate and pressure from the top plate. The position of the cylindrical pellet surrounded by the background beads from side and front views is shown in Figure 6.7.

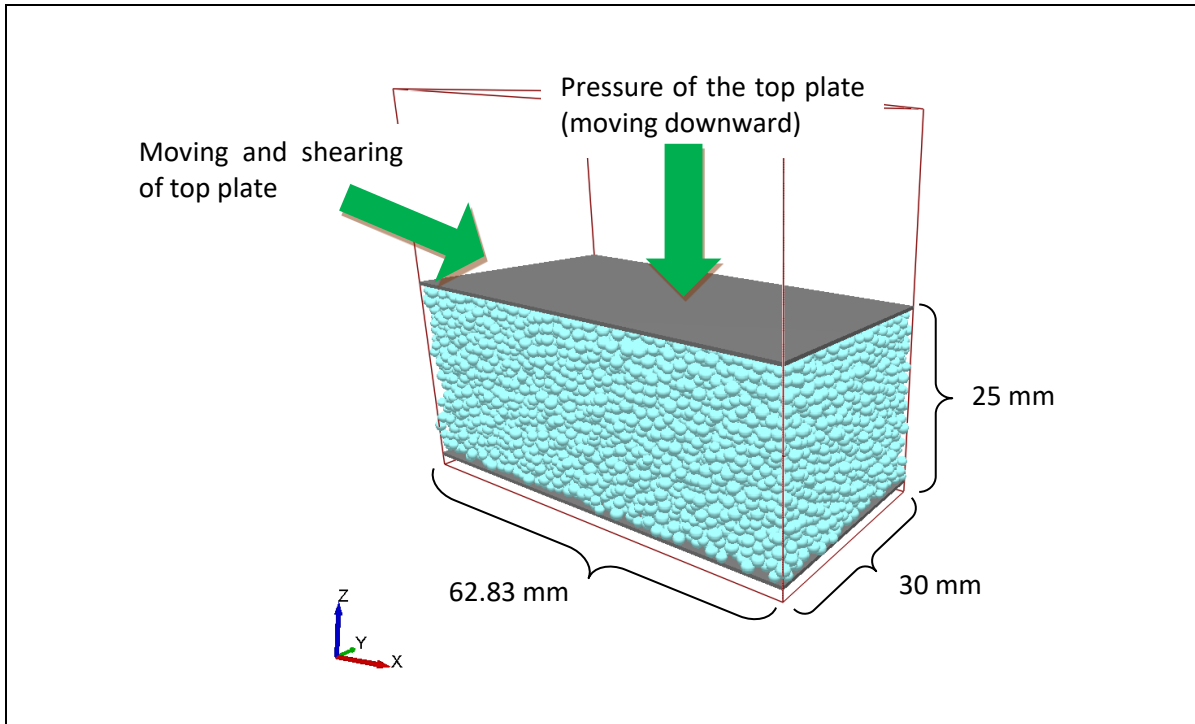


Figure 6.6 The DEM unit shear cell was built within the simulation domain box (red lines). The top plate was able to move and apply pressure in the z-direction and to shear in the x-direction.

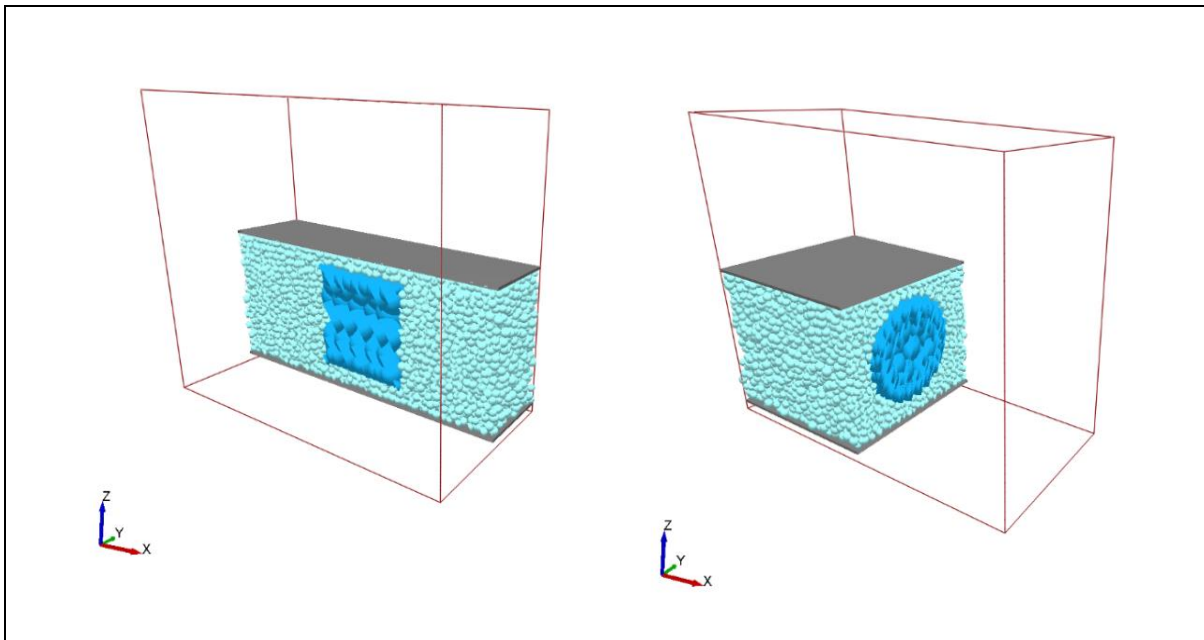


Figure 6.7 Position of the cylindrical pellet surrounded by the background beads from side view (left) and front view (right)

6.11 Stress components from DEM simulations

A combination of applied shear and normal force from the top plate is responsible for the shear flow of bed particles and pellet deformation in the DEM unit shear cell. The stresses exerted on the pellet can be computed from DEM simulations for every time-step. In Figure 6.8, the stress components can be represented by normal and tangential directions. The three mutually orthogonal planes in the normal direction of the pellet are responsible for the three normal stresses: σ_{xx} , σ_{yy} and σ_{zz} . The shear stresses acting in the tangential direction of the pellet are: σ_{xy} , σ_{yx} , σ_{zx} , σ_{xz} , σ_{yz} and σ_{zy} . The shear flow direction for the bed particles (pellet and background beads) is in the x-direction.

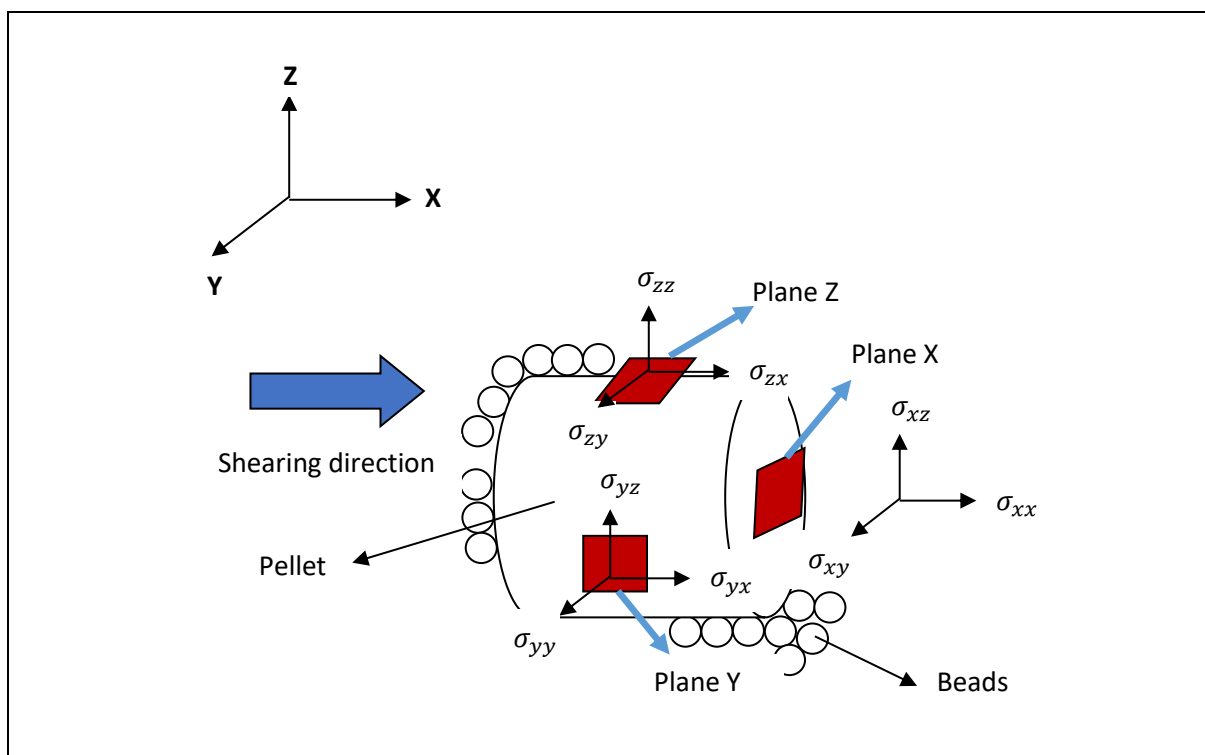


Figure 6.8 Stress components acting on the pellet

The nine stresses can be assembled into a 3×3 matrix known as the Cauchy stress tensor (Equation 6.10).

$$\sigma_{ij} = \begin{bmatrix} \sigma_{xx} & \sigma_{xy} & \sigma_{xz} \\ \sigma_{yx} & \sigma_{yy} & \sigma_{yz} \\ \sigma_{zx} & \sigma_{zy} & \sigma_{zz} \end{bmatrix} \quad \text{Equation 6.10}$$

Table 6.12 shows an example of extracted data of stress components from DEM simulations for lactose 10cSt pellets with shear rate of 40.21/s, top plate pressure of 2000 Pa and 1-1.4 mm background beads. The nine stresses are listed for every time-step accordingly. It can be seen that all the nine stresses give different values over the shearing time. The post-processing of DEM simulations was carried out in Matlab for analysing these stress components.

Table 6.12 Example extracted data of stress components from DEM simulations

TIME:	0.1
stress xx : Particle Particle Stress New 0:	-689.382
stress xy : Particle Particle Stress New 1:	-9.05079
stress xz : Particle Particle Stress New 2:	-15.3352
stress yx : Particle Particle Stress New 3:	-3.18497
stress yy : Particle Particle Stress New 4:	-1503.34
stress yz : Particle Particle Stress New 5:	-10.0648
stress zx : Particle Particle Stress New 6:	-28.5209
stress zy : Particle Particle Stress New 7:	-14.136
stress zz : Particle Particle Stress New 8:	-4704.8
TIME:	0.101
stress xx : Particle Particle Stress New 0:	-716.336
stress xy : Particle Particle Stress New 1:	-9.53368
stress xz : Particle Particle Stress New 2:	-14.3032
stress yx : Particle Particle Stress New 3:	-3.75643
stress yy : Particle Particle Stress New 4:	-1539.41
stress yz : Particle Particle Stress New 5:	-10.4972
stress zx : Particle Particle Stress New 6:	-27.4736
stress zy : Particle Particle Stress New 7:	-14.6212
stress zz : Particle Particle Stress New 8:	-4760.21
TIME:	0.102
stress xx : Particle Particle Stress New 0:	-734.673
stress xy : Particle Particle Stress New 1:	-9.73509
stress xz : Particle Particle Stress New 2:	-12.922
stress yx : Particle Particle Stress New 3:	-4.14358
stress yy : Particle Particle Stress New 4:	-1563.33
stress yz : Particle Particle Stress New 5:	-11.0135
stress zx : Particle Particle Stress New 6:	-25.3404
stress zy : Particle Particle Stress New 7:	-15.5977
stress zz : Particle Particle Stress New 8:	-4789.33

The stresses obtained from DEM simulations were used to calculate the deviatoric stress (a measure of deformation stress of a pellet) and the von Mises stress, which is an input parameter for the von Mises failure theory. The von Mises failure theory is then applied, along with measured peak yield stresses for granular pellets to predict the deformation of these pellets. According to von Mises failure theory, the pellet would deform if the calculated von Mises stress exceeds the measured yield stress of a pellet (refer to Section 2.6.1, Chapter 2).

6.12 Results and discussion

6.12.1 Steady-state condition in the DEM simulations

Several methods were used to investigate the time taken to achieve steady state condition in the DEM simulations. The position of the top plate, the pressure of the top plate in the z-axis and the position of the pellet in the z-axis in the simulation space were all investigated. As the time taken to reach steady state is expected to be insensitive to the properties of the pellet, and due to the very long time taken for a simulation to reach steady (ranging from 3 to 7 days), the steady state condition investigation was limited to one pellet formulation (lactose 10cSt), at a shear rate of 40.21/s, and with 1-1.4 mm and 2 mm background beads.

Figure 6.9 shows the top plate position with shearing time. The size of the background beads influenced the total simulation time for the system to achieve the steady state. The position of the top plate in the z-axis varied with the size of the background beads. For both simulations, the z-position for the top plate increased slightly with time. The equilibrium position of the top plate was slightly higher than 0.025 m for a pellet sheared with 1-1.4 mm beads. The variation in position of the top plate in the z-axis showed minor fluctuations within the range of 0.025 mm with both sizes of background beads. The reason for the slight change of the top plate position in the z-axis is the dilation of the background beads. The background beads need to move over each other throughout the shearing time. The position of the top plate remains constant after approximately 2 s, with a final value of 0.0254 m for the smaller size of 1-1.4 mm beads. The position of the top plate reached a constant value of approximately 0.025 m after 4.5 for the larger size 2 mm beads.

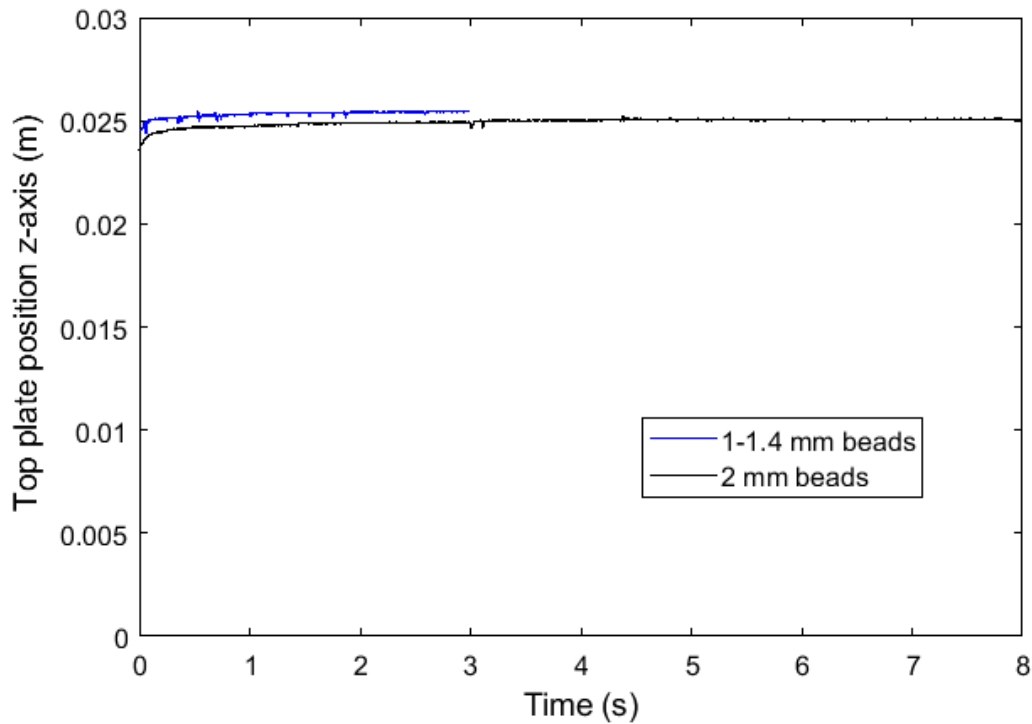


Figure 6.9 Top plate position in the z-axis over shearing time for lactose 10cSt pellets with different size of background beads, shear rate of 40.21/s and top plate pressure of 2000 Pa

Figure 6.10 shows the top plate pressure with time and the pre-set pressure for the top plate is 2000 Pa. As shown in Figure 6.10, higher fluctuations of top plate pressures between 19000 and 100000 Pa were observed for a pellet sheared with 1-1.4 mm beads within 1 s of shearing. After 1 s of shearing, the top plate pressures for pellets sheared with 1-1.4 mm and 2 mm beads both showed lower fluctuation of top plate pressures. These variations are to be expected; as the particles move, there are frequent cases of stick-slip, where movement is restricted, pressure builds, and is released when particles move again.

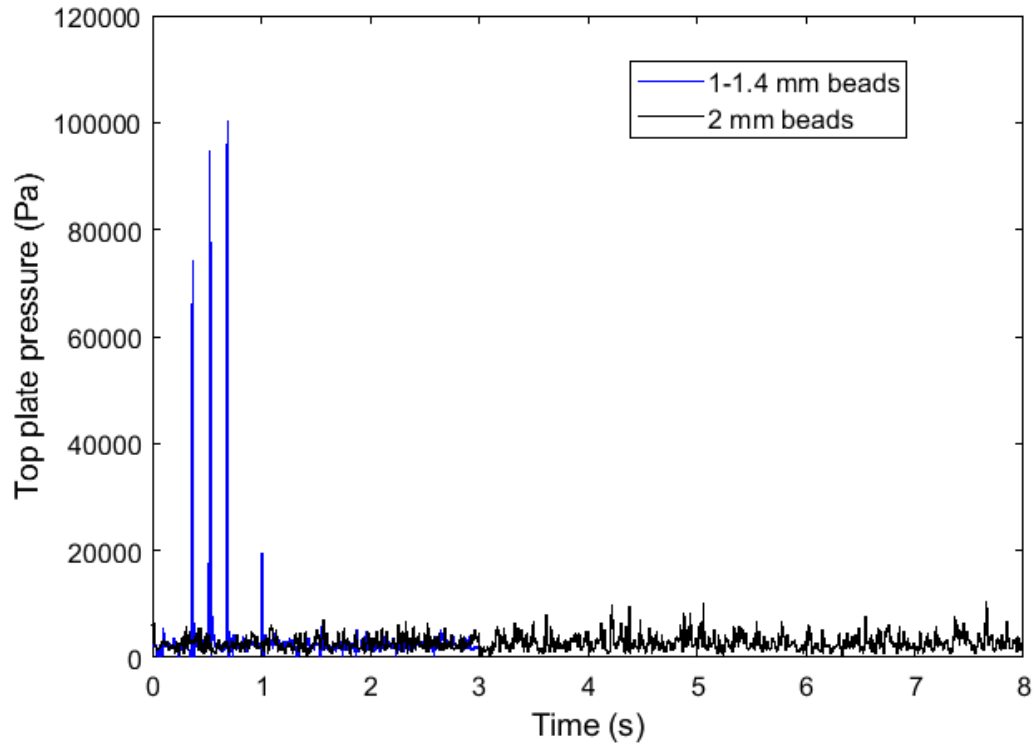


Figure 6.10 Top plate pressure over shearing time for lactose 10cSt pellets with different size of background beads, shear rate of 40.21/s and top plate pressure of 2000 Pa

Figure 6.11 shows the variation of pellet position in the z-axis over the shearing time. The original position of the lactose 10cSt pellet in the z-axis was positioned at the centre of the DEM unit shear cell; 0.0125 m. For 1-1.4 mm beads, the position in the z-axis slightly increased once the shearing began, starting to level off at approximately 1.5 s. The position in the z-axis for a pellet sheared with the larger 2 mm beads was below 0.012 m from the start of shearing. After a period of 4.5 s, the position of pellet became stable, reaching 0.012 m.

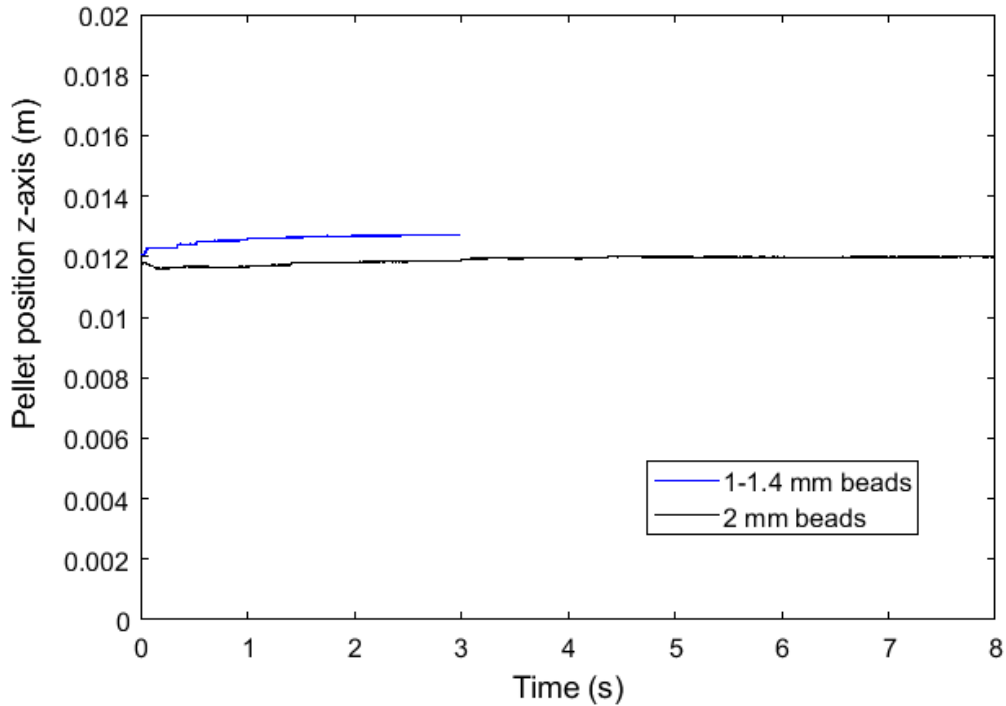


Figure 6.11 Position of lactose 10cSt pellet in the z-axis over the shearing time. Conditions for shear rate of 40.21/s and top plate pressure of 2000 Pa

The steady state of the DEM simulations was evaluated for lactose 10cSt pellets based on three conditions; top plate pressure and position in the z-axis, and the position of the lactose pellet in the z-axis. Roughly, the steady state conditions for top plate pressure and position in z-axis were achieved after approximately 1 s. The position of lactose 10cSt pellet in z-axis sheared with 1-1.4 mm and 2 mm beads achieved the steady state conditions after approximately 1.5 and 4.5 s, respectively.

6.12.2 Deviatoric stress of the pellets

The results of deviatoric stress of lactose 10cSt and ballotini 10cSt pellets are discussed in this section. The influence of several operating parameters such as the size of the background beads, shear rate and normal pressure were investigated. The effect of different formulation of pellets on deviatoric stress was also studied based on: 1) viscosity of silicone oils and 2) types of powders.

6.12.2.1 Effect of size of background beads

In Figure 6.12, the deviatoric stress versus time for lactose pellets sheared at 40.21/s and 2000 Pa was evaluated for different sizes of background beads. The deviatoric stress for all bead sizes increased with increasing shearing time. Higher deviatoric stresses were observed for the lactose pellet sheared with smaller bead sizes (from 1-1.4 mm to 4 mm). The lowest deviatoric stress was observed for lactose pellets sheared with 6 mm beads. The gradient of deviatoric stress is steepest for 1-1.4 mm beads and the gradient decreases with increasing bead size.

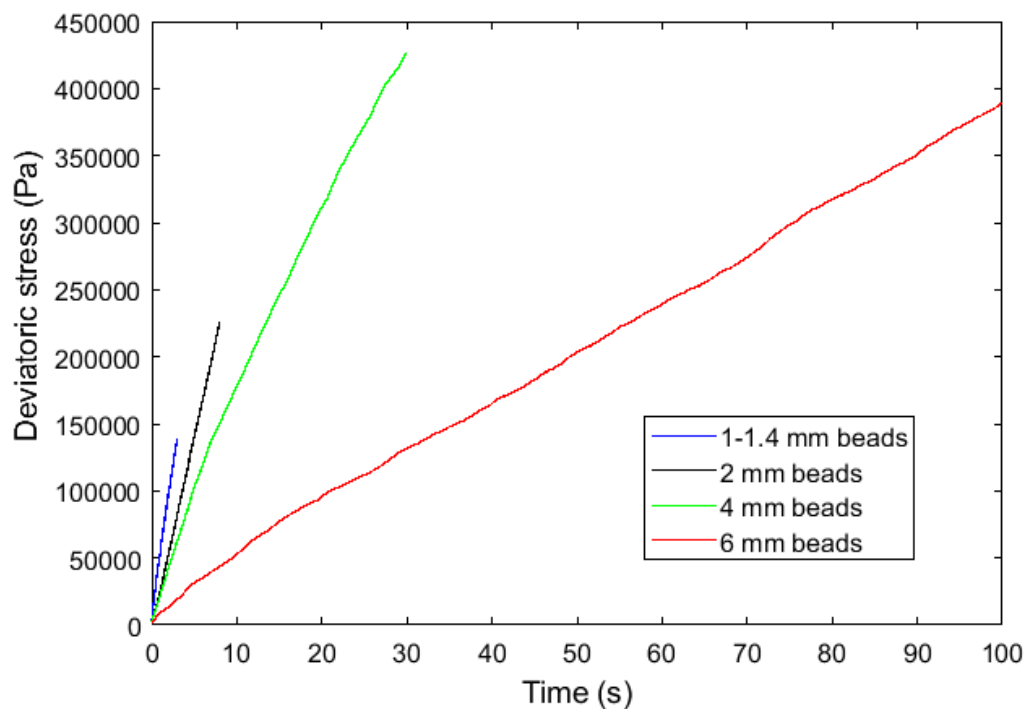


Figure 6.12 Deviatoric stress versus time for lactose 10cSt pellet with different background beads, shear rate of 40.21/s and top plate pressure of 2000 Pa

As the nine stress components acting on the pellet are input parameters for calculating the deviatoric stress of pellets (refer to Table 6.12, Section 6.11), it is necessary to evaluate the nine stress components of the lactose pellet. Figures 6.13 to 6.21 show the nine stress components for lactose 10cSt pellets sheared with a shear rate of 40.21/s, top plate pressure of 2000 Pa and surrounded by four different size of background beads (1-1.4, 2, 4 and 6 mm beads).

In Figure 6.13, a decreasing XX stress of the pellets over time was observed for all the sizes of background beads. The slope of the XX stress graph becomes steeper with decreasing bead size. In Figure 6.14, the change in the XY stress of the pellets over time was minimal for 1-1.4 mm and 2 mm beads. An increase and decrease of XY stresses of the pellets was observed for 4 mm and 6 mm beads, respectively. In Figure 6.15, all the sizes of the background beads showed increasing XZ stress of the pellets over time. The gradient is steepest for 1.4mm beads, and the gradient decreases with increasing background bead size. Figure 6.16 shows almost constant YX stress of the pellets over time for 1-1.4 and 2 mm beads. Decreasing and increasing YX stresses of the pellets over time were observed for 4 mm and 6 mm beads, respectively. In Figure 6.17, YY stress of the pellets decreases time for all sizes of background beads. The steepest slope was observed for 1-1.4 mm beads, and the slope of the graph becomes less steep as the bead size increases.

In Figure 6.18, slight increases in YZ stress of the pellets over time was observed for 1-1.4, 2 and 4 mm beads. However, decreasing YZ stress of the pellet over time could be seen for 6 mm beads. Figure 6.19 shows an increasing ZX stress of the pellets over time for all sizes of background beads. The slope of the graph is steepest for 1-1.4 mm beads. A similar gradient of the graph can be seen for 2 mm and 4 mm beads. The slope of the graph is less steep for 6 mm beads. Figure 6.20 shows a relatively constant ZY stress of the pellet over time for 1-1.4 mm beads. Increasing ZY stress of the pellets over time was observed for both 2 and 4 mm beads and decreasing ZY stress of the pellet over time for 6 mm beads. Figure 6.21 shows decreasing ZZ stress of the pellets over time for all sizes of background beads. A similar gradient was observed for 1-1.4, 2 and 4 mm beads, and the lowest gradient for 6 mm beads. Overall, a variety of trends were observed for different sizes of background beads. These differences for each of the stress components will contribute to the increase of deviatoric stress over time of the lactose pellets with different gradients.

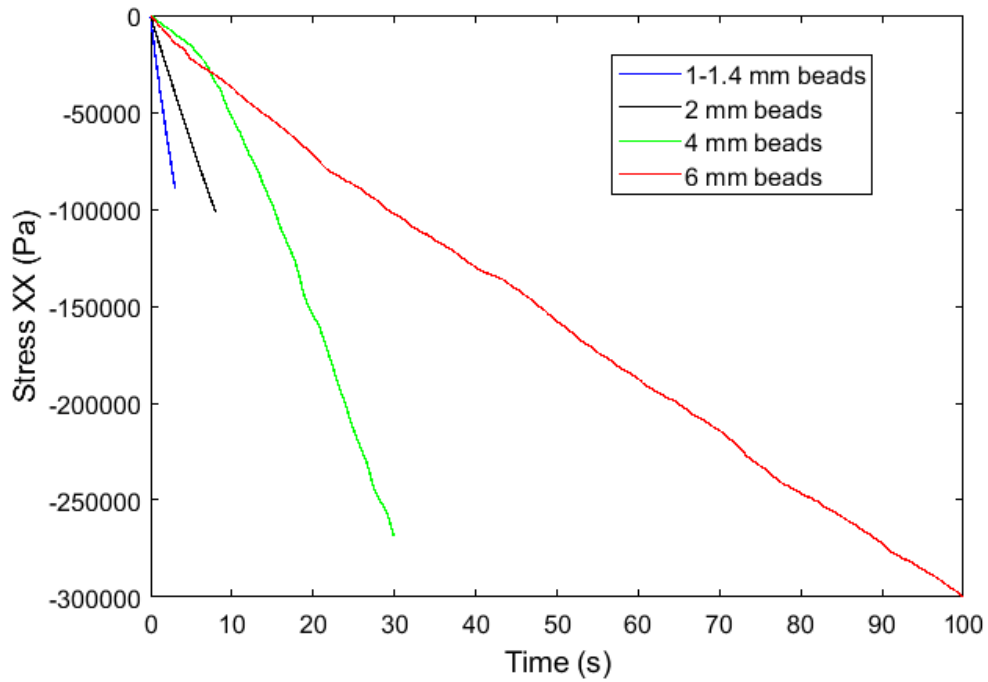


Figure 6.13 Stress σ_{xx} over time for lactose 10cSt pellets with variation of size of background beads, shear rate of 40.21/s and top plate pressure of 2000 Pa

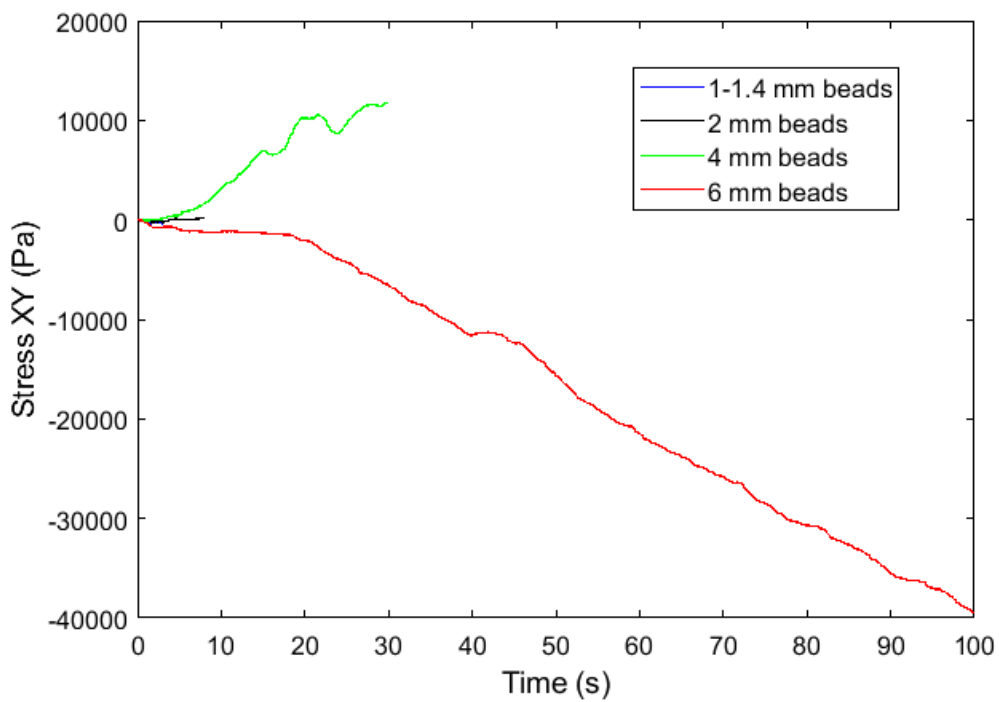


Figure 6.14 Stress σ_{xy} over time for lactose 10cSt pellets with variation of size of background beads, shear rate of 40.21/s and top plate pressure of 2000 Pa

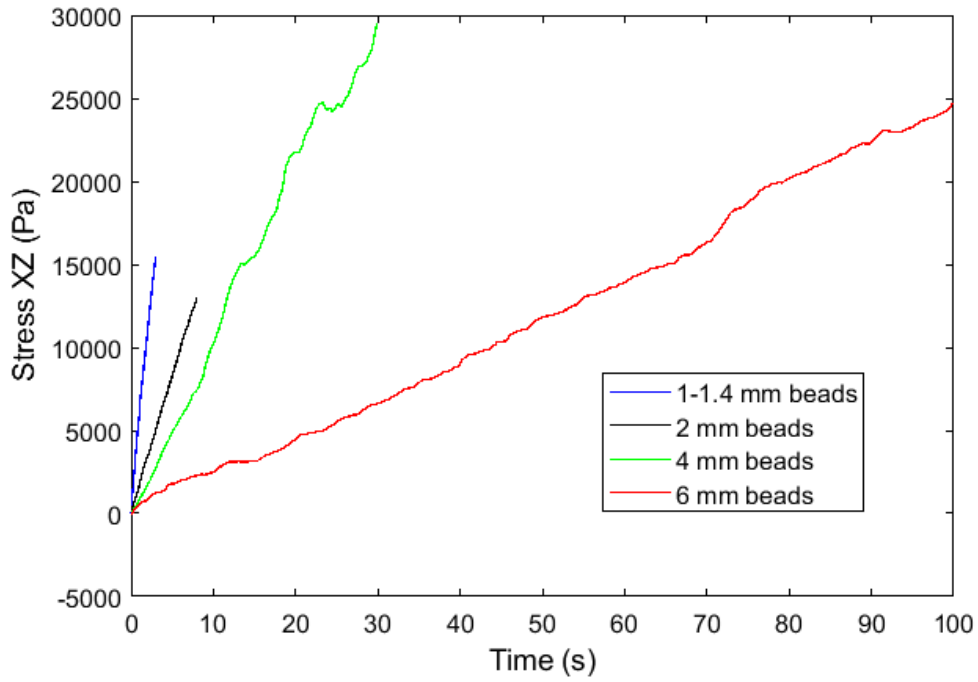


Figure 6.15 Stress σ_{xz} over time for lactose 10cSt pellets with of variation size of background beads, shear rate of 40.21/s and top plate pressure of 2000 Pa

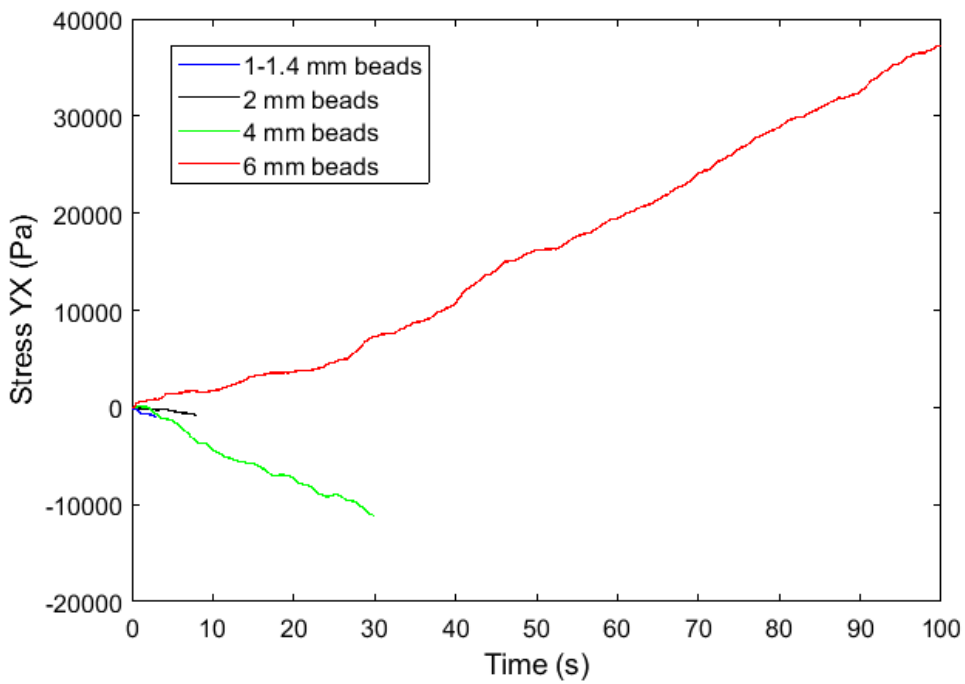


Figure 6.16 Stress σ_{yx} over time for lactose 10cSt pellets with variation of size of background beads, shear rate of 40.21/s and top plate pressure of 2000 Pa

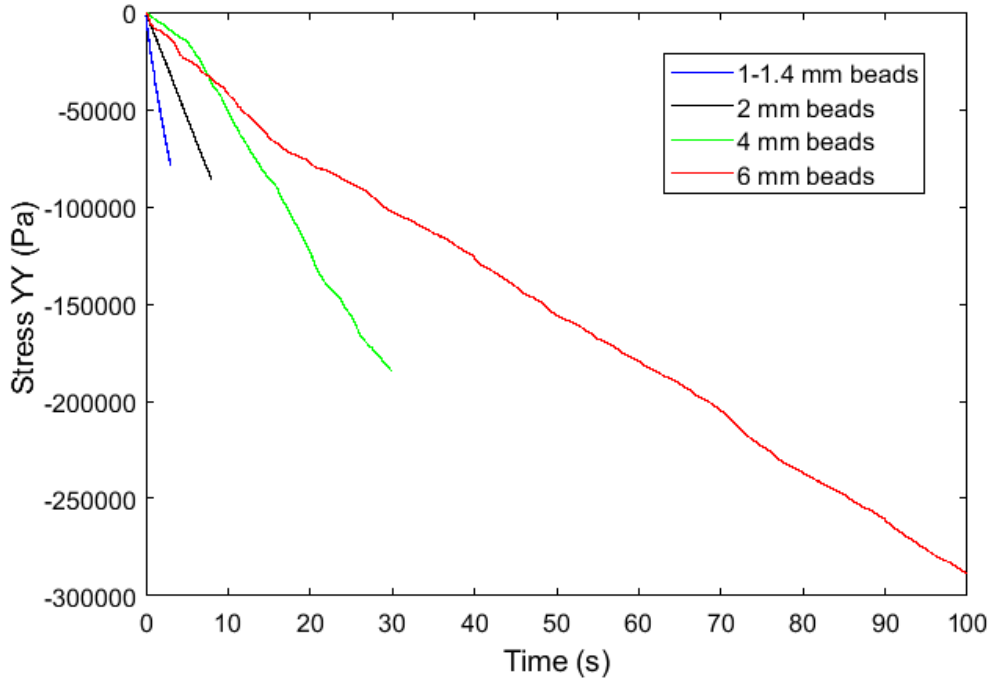


Figure 6.17 Stress σ_{yy} over time for lactose 10cSt pellets with variation of size of background beads, shear rate of 40.21/s and top plate pressure of 2000 Pa

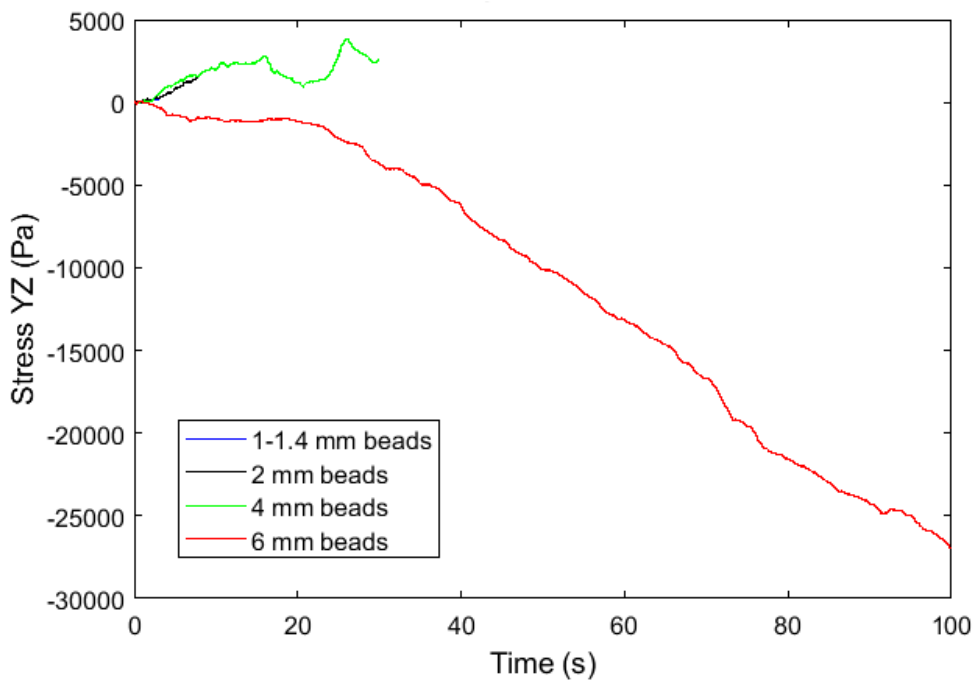


Figure 6.18 Stress σ_{yz} over time for lactose 10cSt pellets with variation of size of background beads, shear rate of 40.21/s and top plate pressure of 2000 Pa

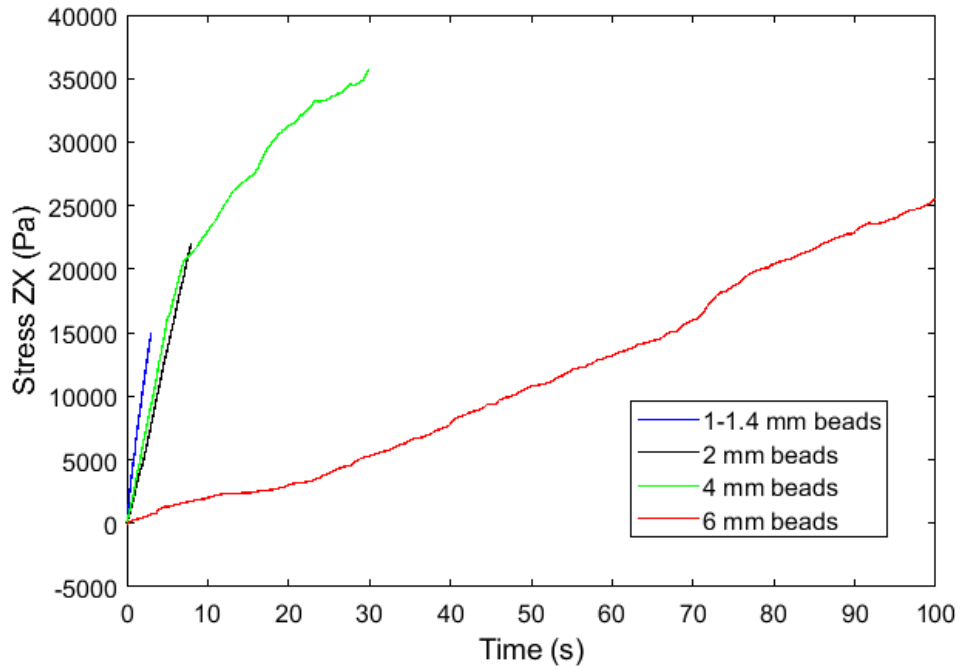


Figure 6.19 Stress σ_{zx} over time for lactose 10cSt pellets with variation of size of background beads, shear rate of 40.21/s and top plate pressure of 2000 Pa

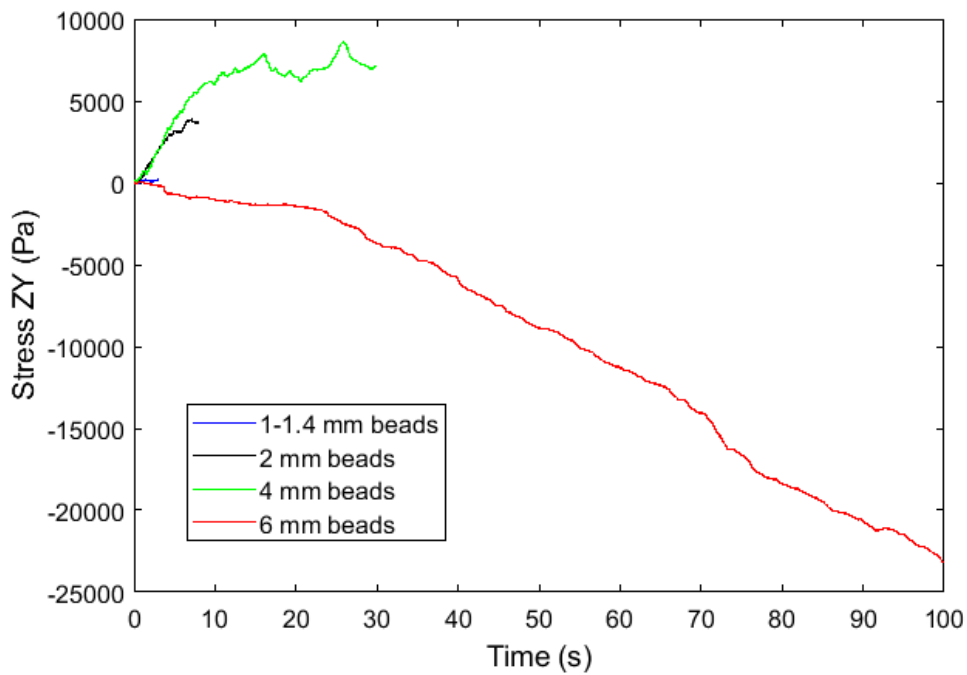


Figure 6.20 Stress σ_{zy} over time for lactose 10cSt pellets with variation of size of background beads, shear rate of 40.21/s and top plate pressure of 2000 Pa

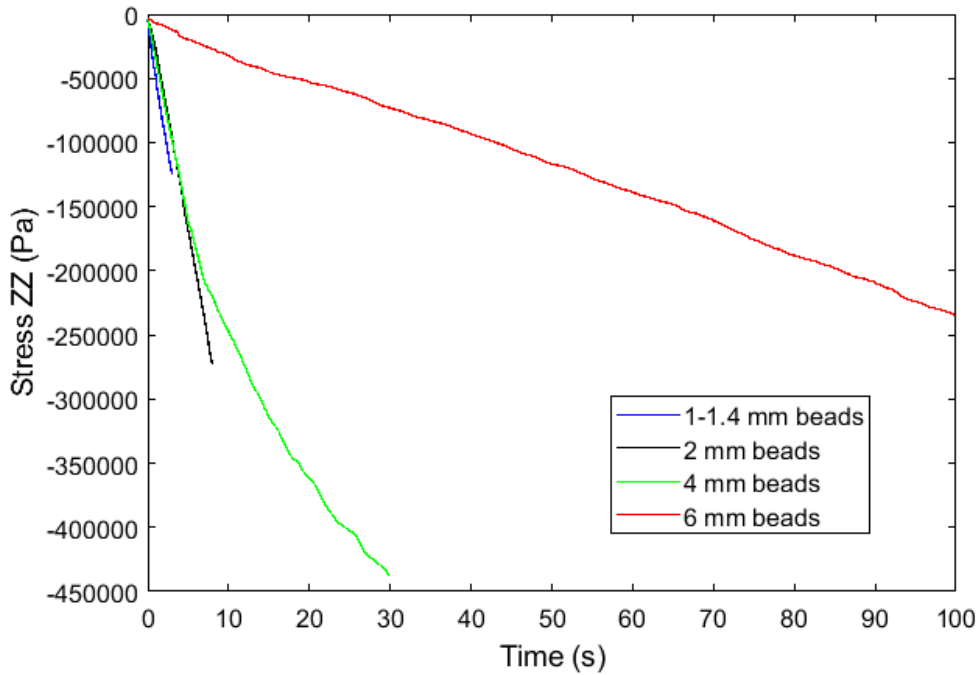


Figure 6.21 Stress σ_{zz} over time for lactose 10cSt pellets with variation of size of background beads, shear rate of 40.21/s and top plate pressure of 2000 Pa

The relationship between the size of beads and the number of beads making up the height of the DEM unit shear cell is shown in Table 6.13. It was found that the height of DEM unit shear cell could be made up of approximately 5 to 6 particles by using 6 mm beads, which is the typical number of particle diameters in a shear zone, as demonstrated by (Ghadiri et al., 2000b). On the other hand, bead sizes between 1-1.4 mm and 4 mm results in the height of the DEM unit shear cell being made up by more than 6 particles.

Table 6.13 Relationship between size of beads and amount of background beads for making up the height of the DEM unit shear cell

Size of background beads (mm)	Number of beads for making up the height of DEM unit shear cell
1-1.4	Approximately 27 particles
2	Approximately 15 particles
4	Approximately 7 particles
6	Approximately 5 to 6 particles

In Table 6.13, the 6 mm beads required the least amount of the particles generated. As previously shown (Ghadiri et al., 2000b), typical shear zone widths are expected to be 5-6 particle diameters in size. Therefore, for the 6 mm bead case, the highest strain rates are expected to be experienced by the pellets, and the highest deviatoric stresses. However, this was not found for the lactose pellet sheared with 6 mm beads. A possible reason could be due to the difference in the pellet position over time during the simulations. It was observed the pellet moved in the x and y planes over time for all bead sizes. However, the x and y velocities of the pellets was highest in the large beads, and decreased with decreasing size of beads. This relative movement will act to reduce the deviatoric stress, and may explain the effect of size of background beads on the magnitude of deviatoric stress in Figure 6.22.

Figure 6.22 shows the deviatoric stress versus time for ballotini pellets sheared with two sizes of background beads, 1-1.4 mm and 2 mm, a shear rate of 40.21/s and top plate pressure of 2000 Pa. An increase of deviatoric stress of the ballotini pellets was observed with time and was higher with the smaller background beads. Moreover, the gradient of the deviatoric stress decreased with increasing size of beads. A 'jamming' phenomenon appears to have occurred for the ballotini pellet sheared with 1-1.4 mm beads at 0.15 s. The continuous shearing and dilation of the surrounding background beads to overcome the 'jamming' results in the ballotini pellet experiencing an increase in deviatoric stress.

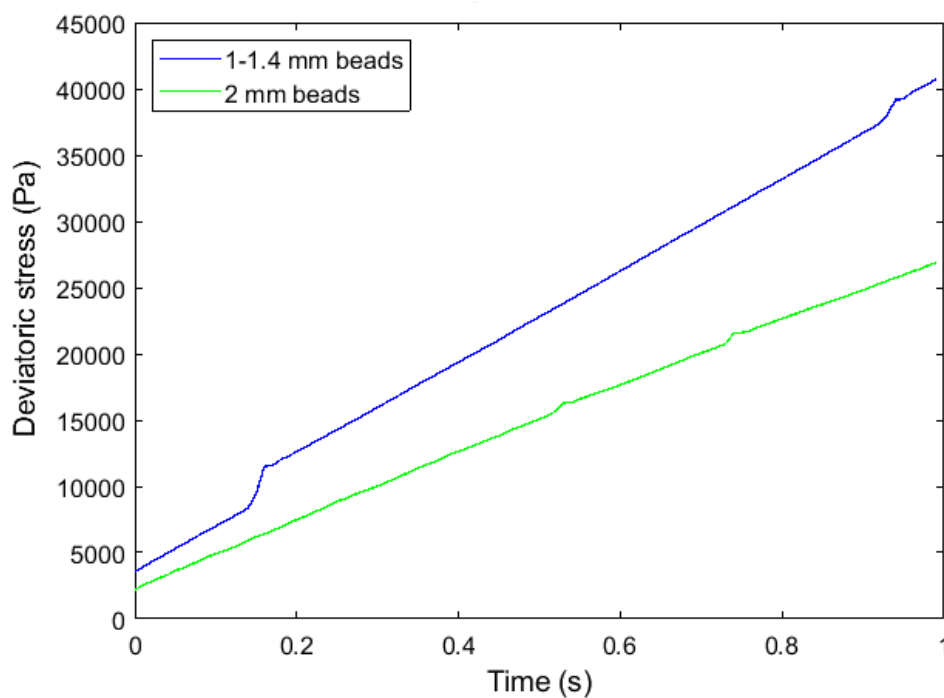


Figure 6.22 Deviatoric stress versus time for ballotini 10cSt pellets with different size of background beads, shear rate of 40.21/s and top plate pressure of 2000 Pa

An increase in the deviatoric stress over the time for ballotini pellets with two size of beads, 1-1.4 and 2 mm, was similar to the results of deviatoric stress for lactose pellets with 1-1.4 and 2 mm beads in Figure 6.12. Again, the deviatoric stress is a calculation from the nine stress components acting on the ballotini pellets. The nine stress components for ballotini 10cSt pellets with two sizes of background beads (1-1.4 and 2 mm beads), shear rate of 40.21/s and top plate pressure of 2000 Pa are shown in Figures 6.23 to 6.31.

In Figure 6.23, a decreasing XX stress over time for the ballotini pellets was observed with the greatest slope for 1-1.4 mm beads. In Figure 6.24, an increasing XY stress over time for the ballotini pellets was observed with highest for smaller beads; 1-1.4 mm. In Figure 6.25, all the size of the background beads shows increasing XZ stress over time for the ballotini pellets. The gradient is steepest for 1.4mm, and the gradient decreases with increasing size of background beads. Figure 6.26 shows increasing and decreasing YX stresses over time for the ballotini pellets with 1-1.4 and 2 mm beads, respectively. In Figure 6.27, both sizes of background beads show decreasing YY stress over time for the ballotini pellets. The steepest of the slope was observed for 1-1.4 mm beads. In Figure 6.28, a combination of decreasing and increasing YZ stress over time was observed for 1-1.4 beads. Increasing and decreasing YZ stress over time could be seen for 2 mm beads. Figure 6.29 shows an increasing ZX stress over time for both sizes of background beads. The slope of the graph is steepest for 1-1.4 mm beads. Figure 6.30 shows a decreasing trend for ZY stress over time for 1-1.4 mm beads. A mixture of increasing and decreasing trends was observed for 2 mm beads. Figure 6.31 shows decreasing ZZ stress over time for both sizes of background beads.

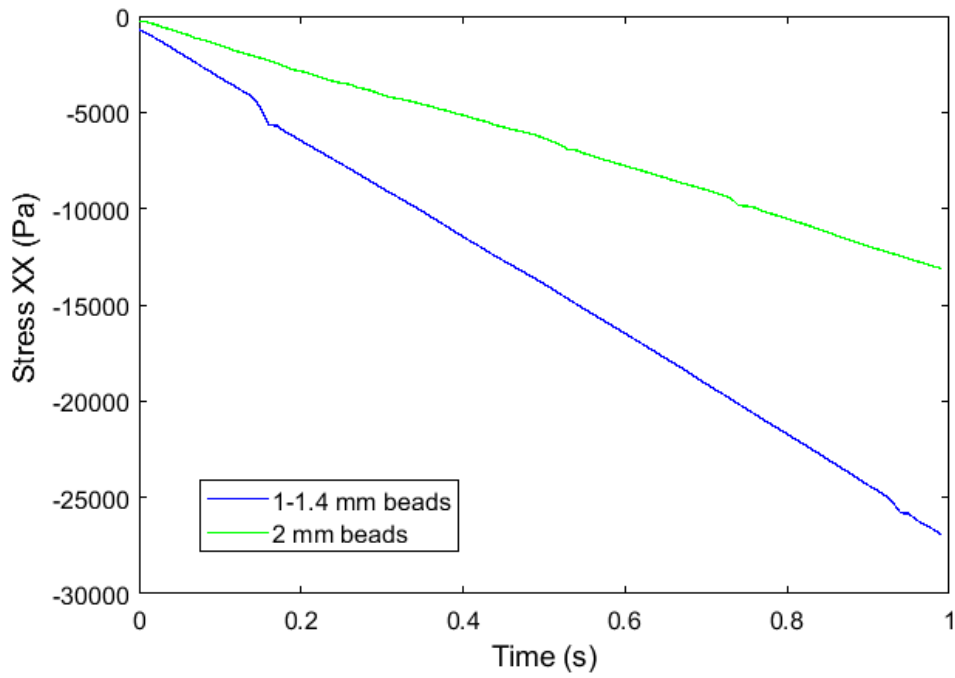


Figure 6.23 Stress σ_{xx} over time for ballotini 10cSt pellets with variation of size of background beads, shear rate of 40.21/s and top plate pressure of 2000 Pa

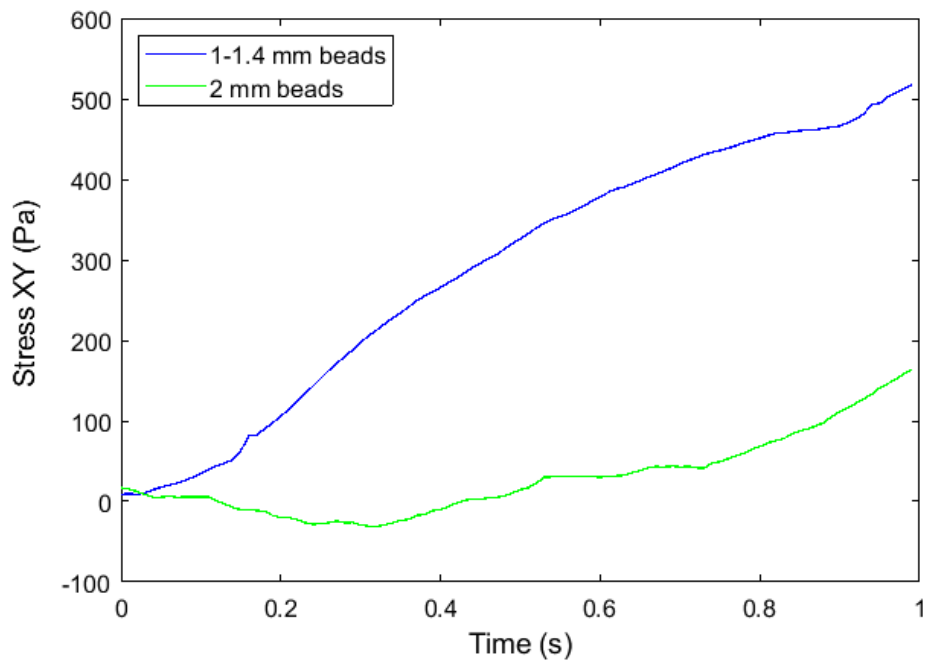


Figure 6.24 Stress σ_{xy} over time for ballotini 10cSt pellets with variation of size of background beads, shear rate of 40.21/s and top plate pressure of 2000 Pa

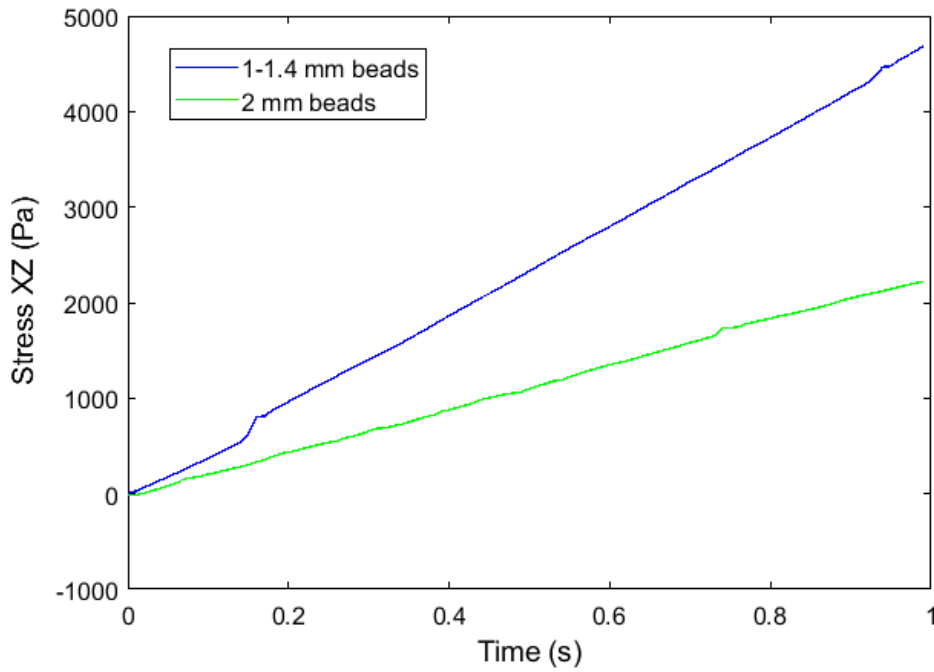


Figure 6.25 Stress σ_{xz} over time for ballotini 10cSt pellets with variation of size of background beads, shear rate of 40.21/s and top plate pressure of 2000 Pa

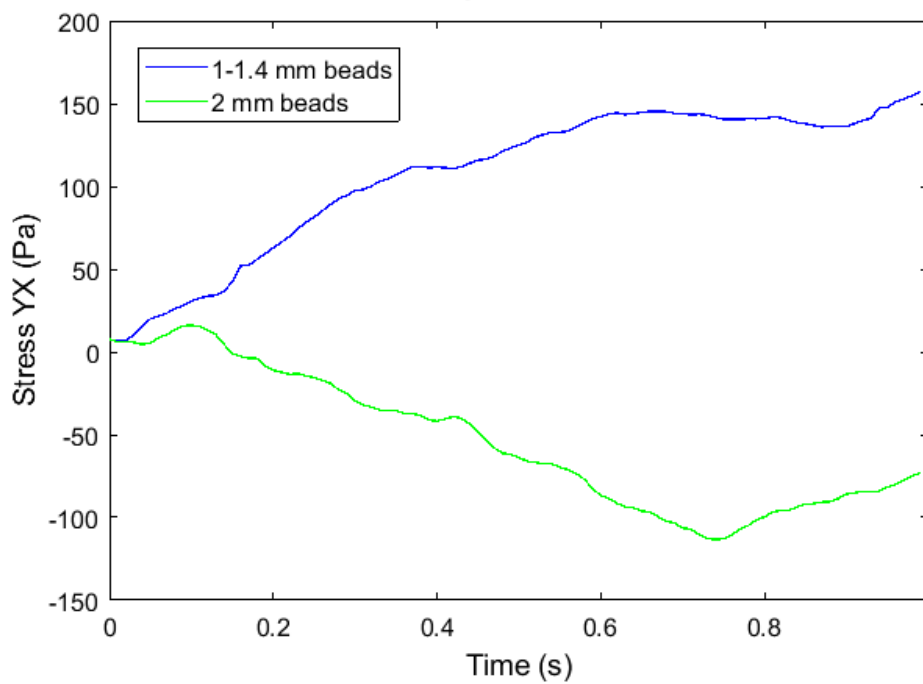


Figure 6.26 Stress σ_{yx} over time for ballotini 10cSt pellets with variation of size of background beads, shear rate of 40.21/s and top plate pressure of 2000 Pa

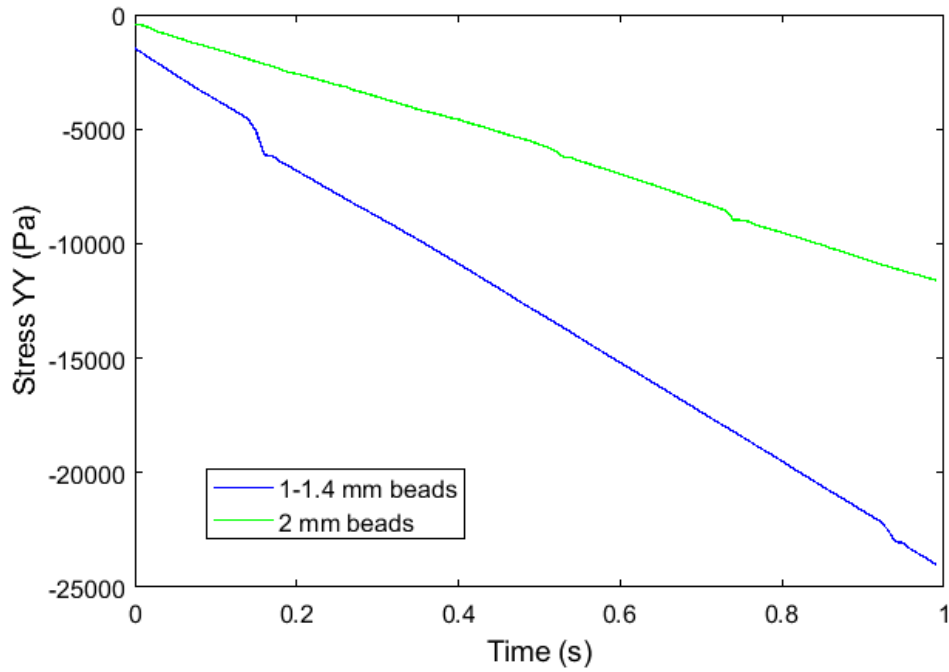


Figure 6.27 Stress σ_{yy} over time for ballotini 10cSt pellets with variation of size of background beads, shear rate of 40.21/s and top plate pressure of 2000 Pa

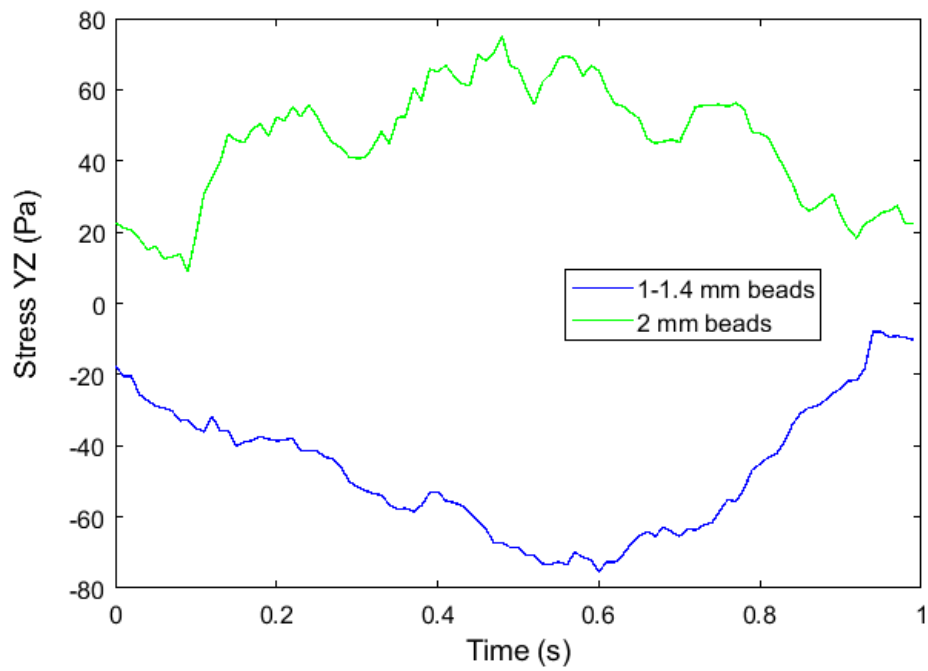


Figure 6.28 Stress σ_{yz} over time for ballotini 10cSt pellets with variation of size of background beads, shear rate of 40.21/s and top plate pressure of 2000 Pa

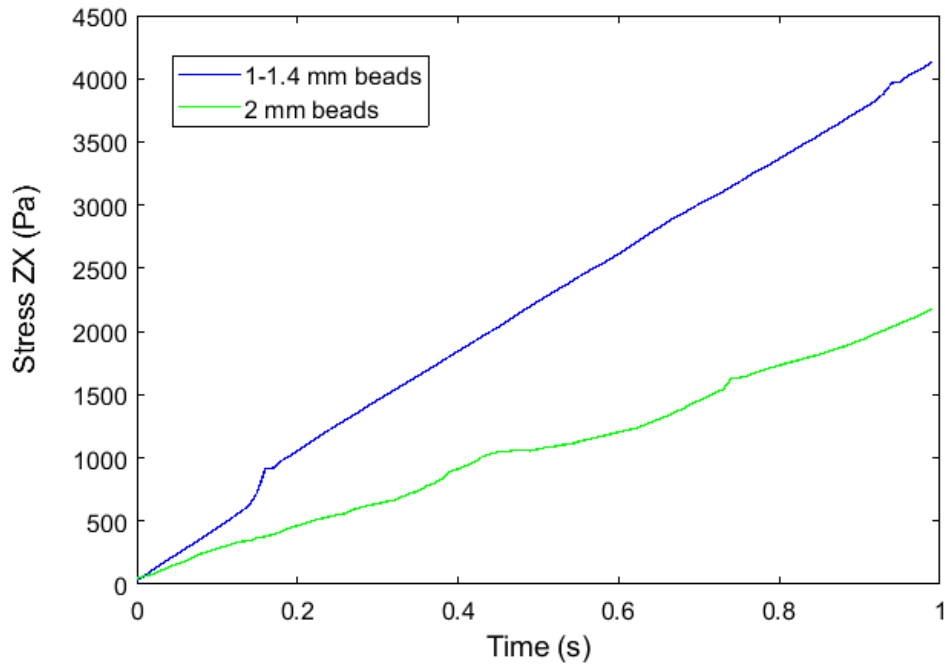


Figure 6.29 Stress σ_{zx} over time for ballotini 10cSt pellets with variation of size of background beads, shear rate of 40.21/s and top plate pressure of 2000 Pa

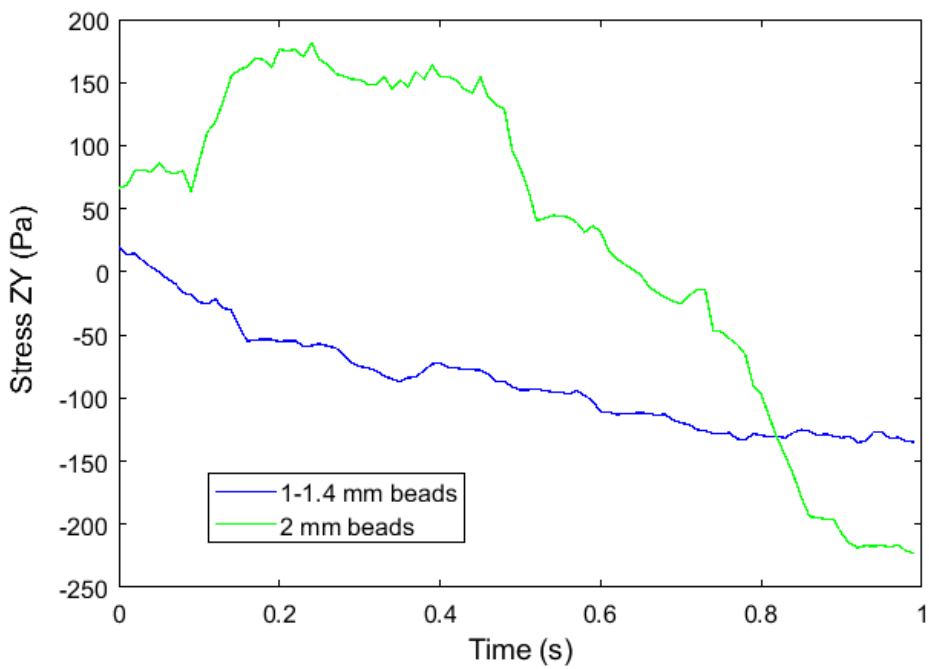


Figure 6.30 Stress σ_{zy} over time for ballotini 10cSt pellets with variation of size of background beads, shear rate of 40.21/s and top plate pressure of 2000 Pa

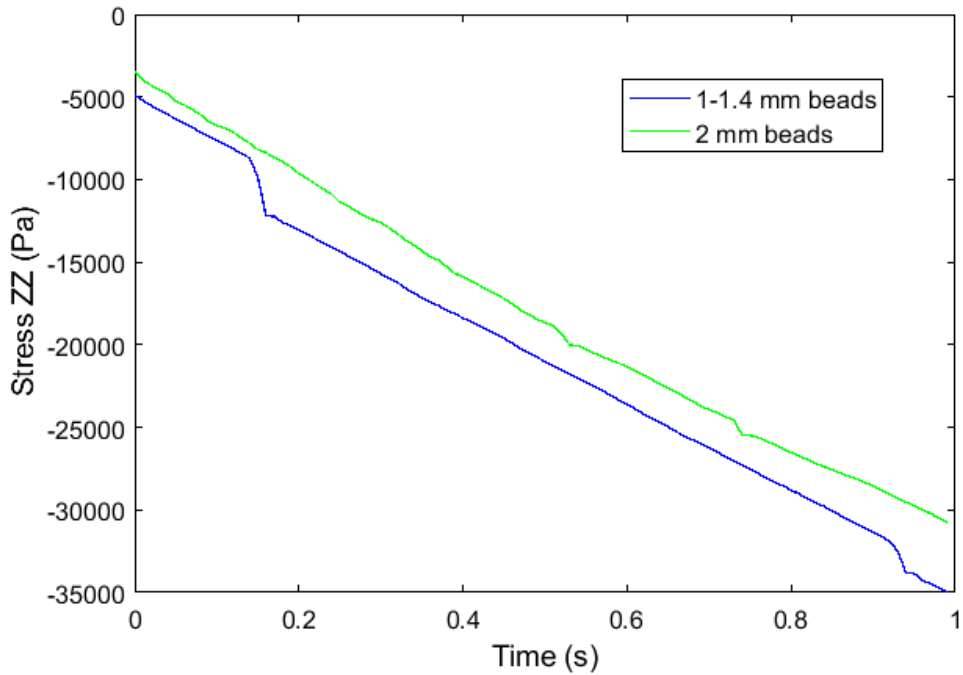


Figure 6.31 Stress σ_{zz} over time for ballotini 10cSt pellets with variation of size of background beads, shear rate of 40.21/s and top plate pressure of 2000 Pa

6.12.2.1 Effect of shear rate

In Figure 6.32, the deviatoric stress of lactose 10cSt pellets as a function of shearing time was evaluated for different shear rates between 5.03/s and 40.21/s. The shearing conditions chosen were 2000 Pa and 1-1.4 mm background beads. An increase the deviatoric stress over shearing time was observed and the trend was similar to the previous deviatoric stress for lactose pellets with different background beads in Figure 6.12, Section 6.12.2.1.

Shear rates of 5.03/s, 10.05/s and 30.16/s did not show large differences in the deviatoric stress of the lactose pellet. However, the shear rate of 40.11/s resulted in the higher deviatoric stress of the lactose pellets after 0.4 s. The highest deviatoric stress was obtained for pellets sheared with a shear rate of 40.21/s. This was as expected, as the highest shear rate of 40.21/s results in the higher rate of shear flow in comparison to the lower shear rates, however the effect was surprisingly small.

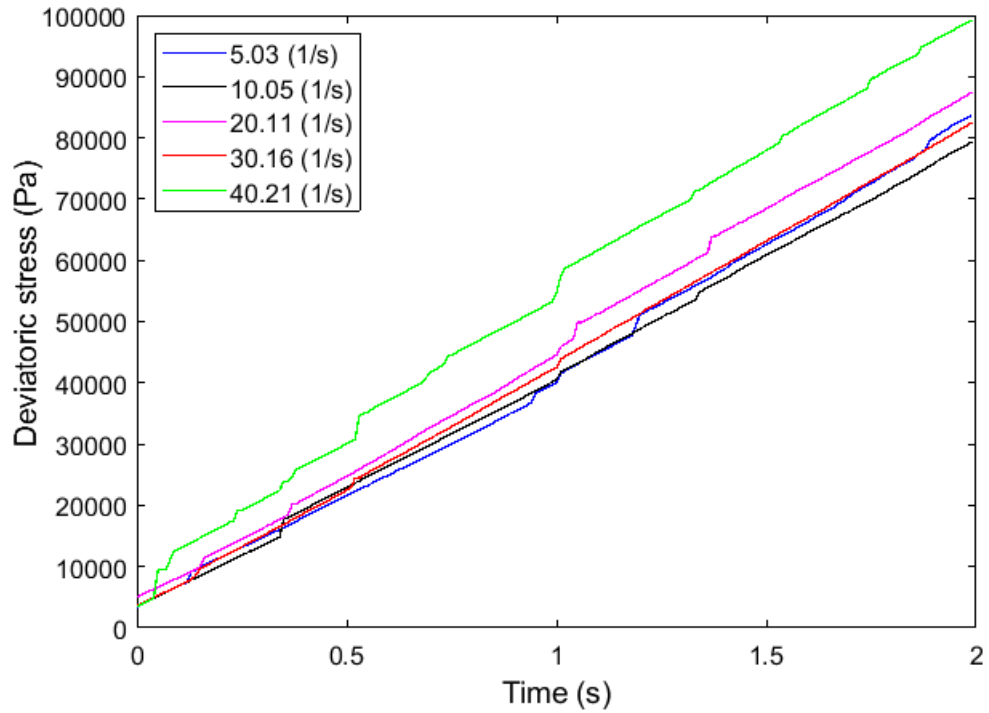


Figure 6.32 Deviatoric stress versus time for lactose 10cSt pellets with different shear rates, top plate pressure of 2000 Pa and 1-1.4 mm background beads

In Figure 6.33, the effect of shear rate on deviatoric stress of ballotini 10cSt pellets was studied for the conditions of top plate pressure of 2000 Pa and 1-1.4 mm background beads. An increase of deviatoric stress of the ballotini pellets as a function of shearing time was observed and the increase of deviatoric stress over the time was similar to the previous deviatoric stress for ballotini pellets with different background beads in Figure 6.22, Section 6.12.2.1. It can be seen that the three different shear rates between 5.03/s and 40.21/s showed only small differences in the deviatoric stress of the ballotini pellets.

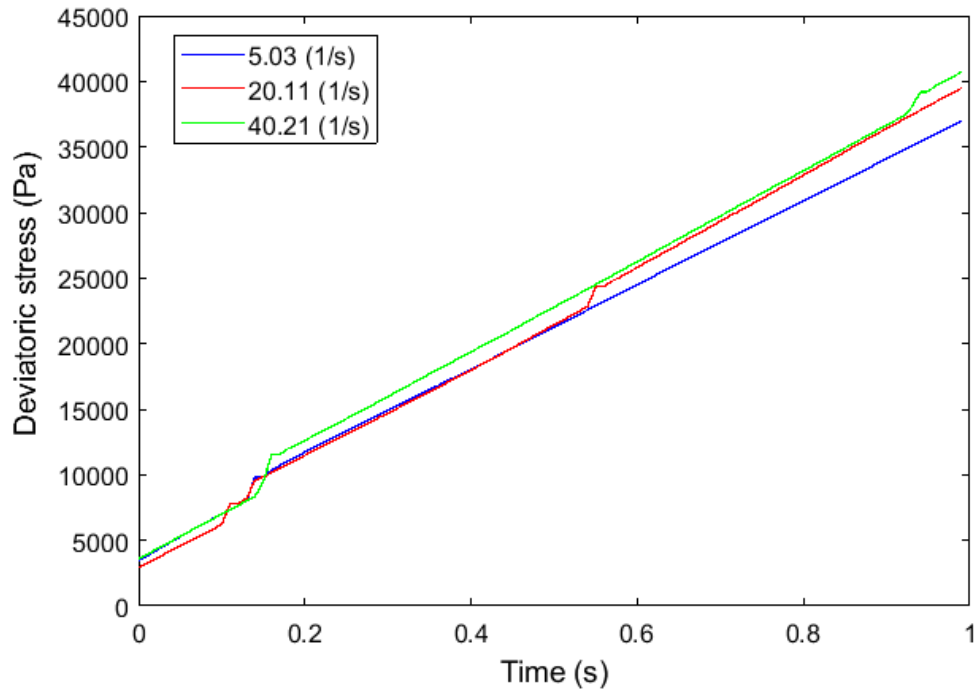


Figure 6.33 Deviatoric stress versus time for ballotini 10cSt pellets with different shear rates, top plate pressure of 2000 Pa and 1-1.4 mm background beads

6.12.2.2 Effect of normal pressure

In Figure 6.34, the deviatoric stress of the lactose pellets versus time for different normal pressures between 383 Pa and 2000 Pa, shear rate of 40.21/s and 1-1.4 mm background beads was evaluated. The deviatoric stress increases with increasing shearing time. The increase of deviatoric stress over time for the lactose pellets with different normal pressures was similar to the trend of deviatoric stress for lactose pellets with different background beads in Figure 6.12, Section 6.12.2.1.

The rate of increase of deviatoric stress for different normal pressures is greatest for 2000 Pa followed by 600 Pa and 383 Pa (the lowest). A fluctuation of deviatoric stress was observed for lactose pellets sheared with a pressure of 2000 Pa over the shearing time. This may be due to the simultaneous movement occurring between the constantly applied highest pressure from the top plate and the bumping shear flow of the bed particles.

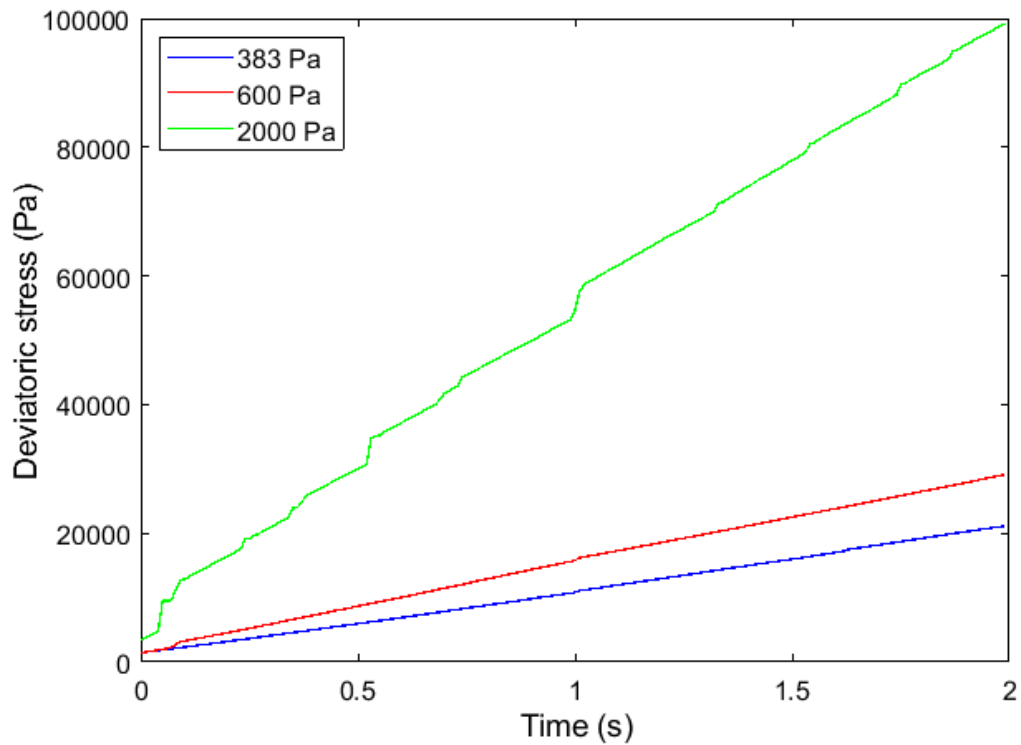


Figure 6.34 Deviatoric stress versus time for lactose 10cSt pellets with different normal pressures, shear rate of 40.21/s and 1-1.4 mm background beads

In Figure 6.35, the deviatoric stress of ballotini 10cSt pellets over time for different normal pressures, shear rate of 40.21/s and 1-1.4 mm background beads was studied. Three normal pressures between 383 and 2000 Pa were chosen for shearing the ballotini pellets. In general, an increase of the deviatoric stress over shearing time was observed and the trend was similar to the deviatoric stress for ballotini pellets with different background beads in Figure 6.22, Section 6.12.2.1. The rate of increase of deviatoric stress of ballotini pellets increased with increasing normal pressure.

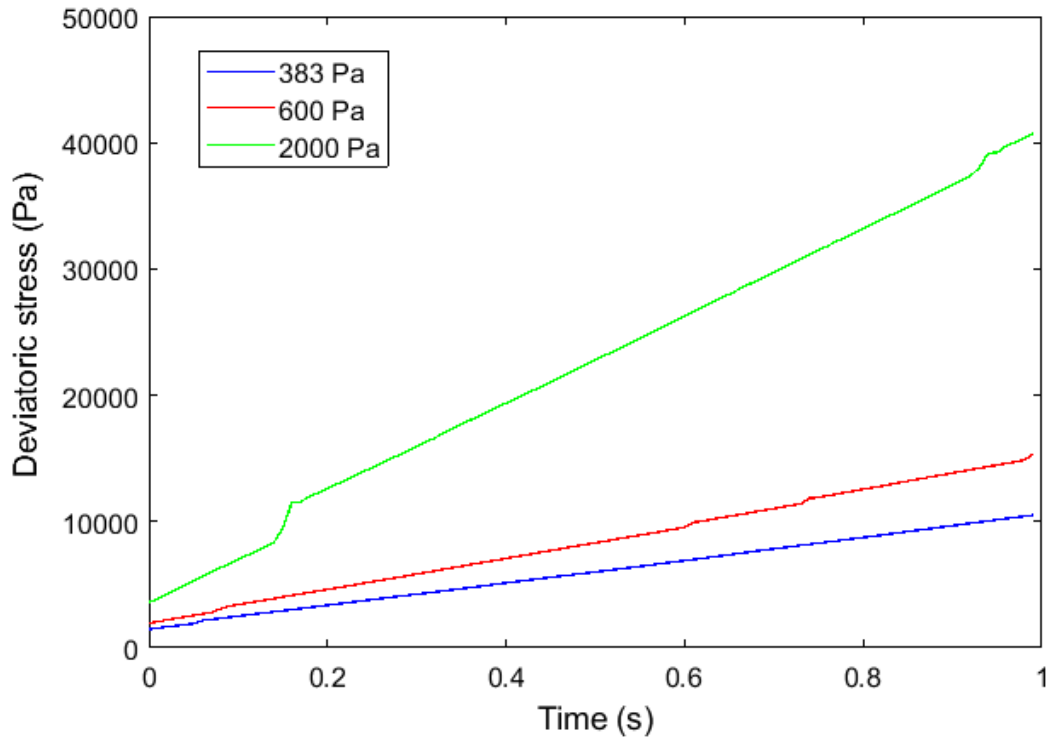


Figure 6.35 Deviatoric stress versus time for ballotini 10cSt pellets with different normal pressures, shear rate of 40.21/s and 1-1.4 mm background beads

6.12.2.3 Effect of viscosity of silicone oils

Figure 6.36, shows the deviatoric stress versus time for ballotini pellets made with 0.01 Pa.s, 0.05 Pa.s, 0.1 Pa.s and 1 Pa.s silicone oils. The shearing conditions chosen were shear rate of 5.03/s, top plate pressure of 2000 Pa and surrounded by 2 mm beads. An increase of deviatoric stress of the ballotini pellets over the shearing time was observed for all silicone oil viscosities. The increase of deviatoric stress over the time was similar to the deviatoric stress for ballotini pellets with different background beads in Figure 6.22, Section 6.12.2.1. The rate of increase of deviatoric stress of ballotini pellets made with different viscosity silicone oils can be arranged as follows: 0.01 Pa.s < 0.05 Pa.s < 0.1 Pa.s. However, for ballotini pellet made with 1 Pa.s silicone oil, a lower of deviatoric stress after 0.4 s of shearing was observed.

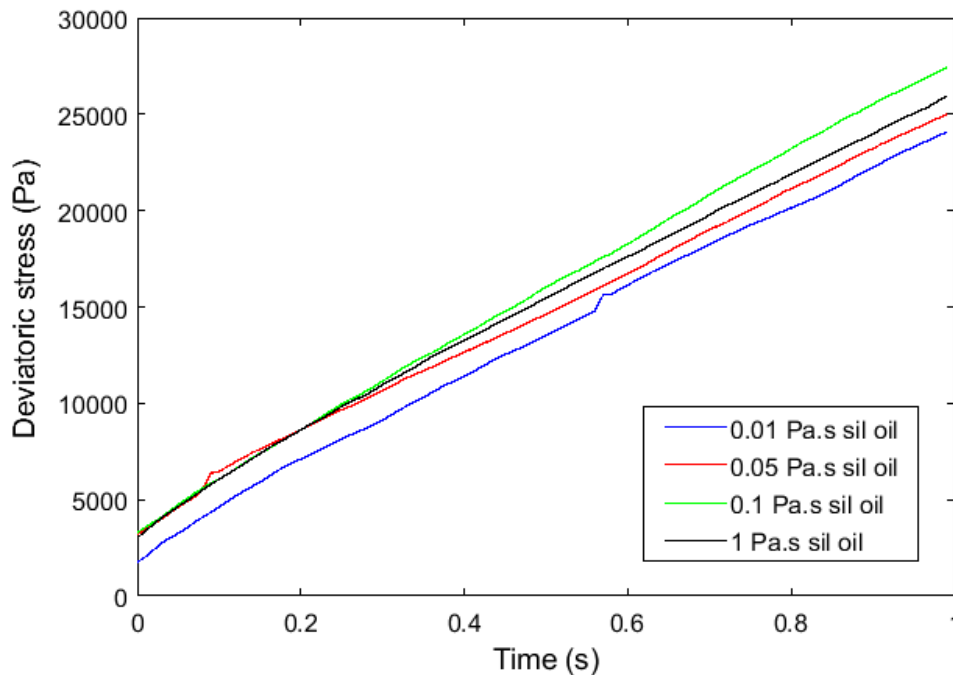


Figure 6.36 Deviatoric stress versus time for ballotini powder and different viscosity silicone oils, shear rate of 5.03/s, top plate pressure of 2000 Pa and 2 mm background beads

6.12.2.4 Effect of types of powders

In Figure 6.37, deviatoric stress over time for pellets made with 0.01 Pa.s silicone oil and two different types of powders were evaluated. These are termed lactose 10cSt and ballotini 10cSt pellets. The shearing conditions were a shear rate of 40.21/s, top plate pressure of 2000 Pa and 1-1.4 mm background beads. An increase of deviatoric stress over the shearing time was observed for pellets made with both types of powders. The increase of deviatoric stress over the time was similar to the previous deviatoric stress results for lactose and ballotini pellets with different background beads (refer to Figures 6.12 and 6.22, Section 6.12.2.1). Pellets made with lactose powder had a higher deviatoric stress in comparison to ballotini powder at all shearing times. The reason for this difference can be further observed from the images of the powders. Ballotini particles have regular and smooth surfaces (refer to Figure 3.4) while the lactose particles had an irregular shape and rough surfaces (refer Figure 3.6). These differences in morphology contribute to the differences in the properties of the pellets such as Young's modulus and plastic stiffness. Lactose 10cSt pellets possessed a higher Young's modulus and plastic stiffness compared to ballotini 10cSt pellets, and therefore experienced a higher deviatoric stress.

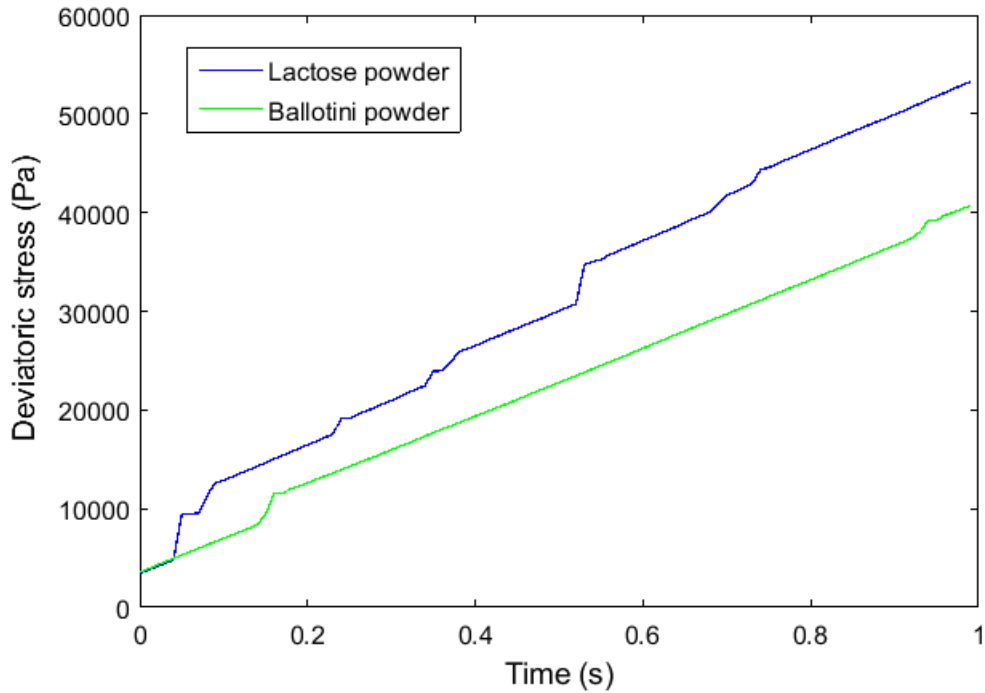


Figure 6.37 Deviatoric stress versus time for 0.01 Pa.s silicone oil and two types of powders, shear rate of 40.21/s, top plate pressure of 2000 Pa and 1-1.4 mm background beads

6.12.3 Analysis of von Mises failure theory

In this section, an attempt is made to predict the yielding time of the pellets in DEM simulations using the von Mises failure theory. The von Mises stresses are calculated from the component stresses generated in the DEM simulations (refer to Equation 2.62, Chapter 2), and the times at which the values of von Mises stresses exceed the yield stresses of the pellets (measured experimentally in Chapter 4) are found.

Tables 6.14 and 6.15 list the yield stresses of the lactose 10cSt and ballotini 10cSt pellets measured at different compression speeds between 1 and 125.7 mm/s. The intersection between the von Mises stress and the measured values of yield stresses of the pellets for compression speeds between 1 and 125.7 mm/s are plotted on the same graph in the y-axis. The scales of the y-axis are set to be on the order of the range of values of yield stresses of the pellets for a clear viewing and comparison. The effect of several operating parameters of the DEM simulations such as size of background beads, shear rate and normal pressure are chosen for the analysis of von Mises failure theory.

Table 6.14 Yield stresses of lactose 10cSt pellets for different compression speeds

Yield stress at 1 mm/s (Pa)	Yield stress at 10 mm/s (Pa)	Yield stress at 50 mm/s (Pa)	Yield stress at 125.7 mm/s (Pa) ^a
37244	59654	79131	35491

^a Compression load of 100 N

Table 6.15 Yield stresses of ballotini 10cSt pellets for different compression speeds

Yield stress at 1 mm/s (Pa)	Yield stress at 10 mm/s (Pa)	Yield stress at 50 mm/s (Pa)	Yield stress at 125.7 mm/s (Pa)
2274	2451	3220	4490

6.12.3.1 Effect of size of background beads

Figure 6.38 shows the von Mises stress versus time for lactose 10cSt pellets sheared with two sizes of background beads, a shear rate of 40.21/s and top plate pressure of 2000 Pa. In Table 6.16, the intersection times for von Mises stress of lactose pellets with different sizes of background beads exceed yield stresses of lactose pellets are listed and they represent the predicted yielding time for the lactose pellets. The von Mises failure theory predicted lower yielding times for lactose pellets sheared with 1-1.4 mm background beads compared to 2 mm background beads, based on the comparison with all the yield stresses of lactose pellets at different compression speeds. As would be expected, as the yield stress of the lactose pellets increased (refer to Tables 6.14 and 6.16), the predicted yielding time for the lactose pellets increased.

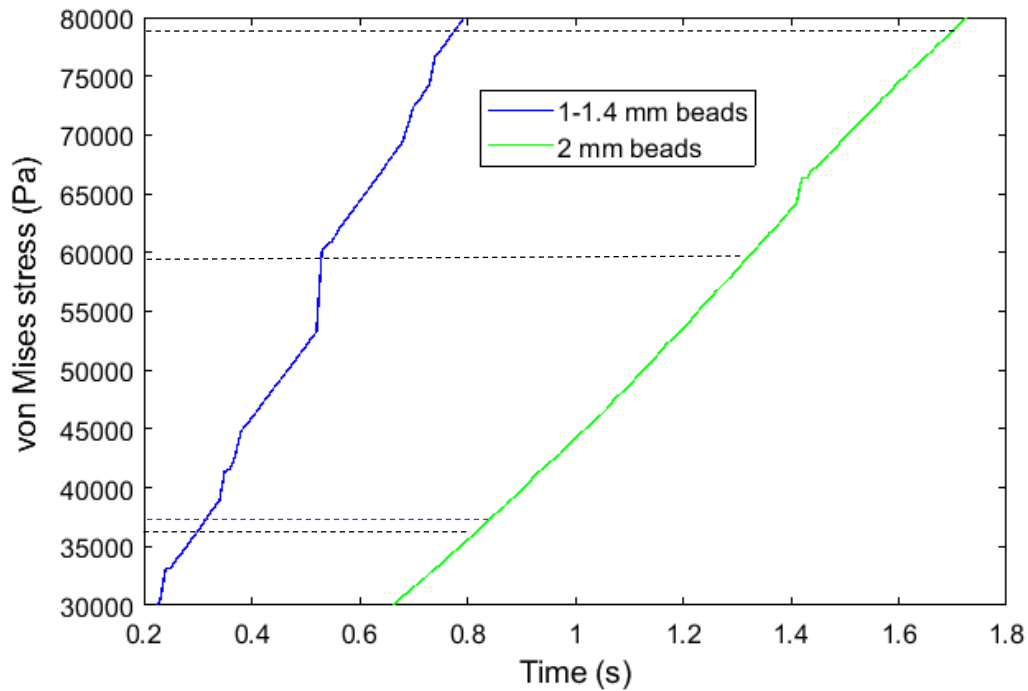


Figure 6.38 von Mises stress versus time for lactose 10cSt pellets with different sizes of background beads, shear rate of 40.21/s and top plate pressure of 2000 Pa

Table 6.16 Intersection times for von Mises stress and yield stresses of lactose pellets with different sizes of background beads, shear rate of 40.21/s and top plate pressure of 2000 Pa

	Intersection times at which von Mises stress exceeds yield stress at 1 mm/s	Intersection times at which von Mises stress exceeds yield stress at 10 mm/s	Intersection times at which von Mises stress exceeds yield stress at 50 mm/s	Intersection times at which von Mises stress exceeds yield stress at 125.7 mm/s
Background beads (mm)	Predicted yielding time (s)	Predicted yielding time (s)	Predicted yielding time (s)	Predicted yielding time (s)
1-1.4	0.315	0.53	0.781	0.287
2	0.84	1.321	1.706	0.798

Figure 6.39 shows the von Mises stress versus time for ballotini 10cSt pellets sheared with different background beads, a shear rate of 40.21/s and top plate pressure of 2000 Pa. The yield stress of ballotini pellets was exceeded the von Mises stress for the 1-1.4 mm background beads simulation, and is therefore not shown. Table 6.17 lists the intersection times at which the von Mises stress exceed the yield stresses of ballotini pellets. From this analysis, it is predicted that all scenarios would deform prior to the start of shearing, due only to the compression from the top plate, with the exception of 2 mm background beads, using the yield stress measured at 125.7 mm.

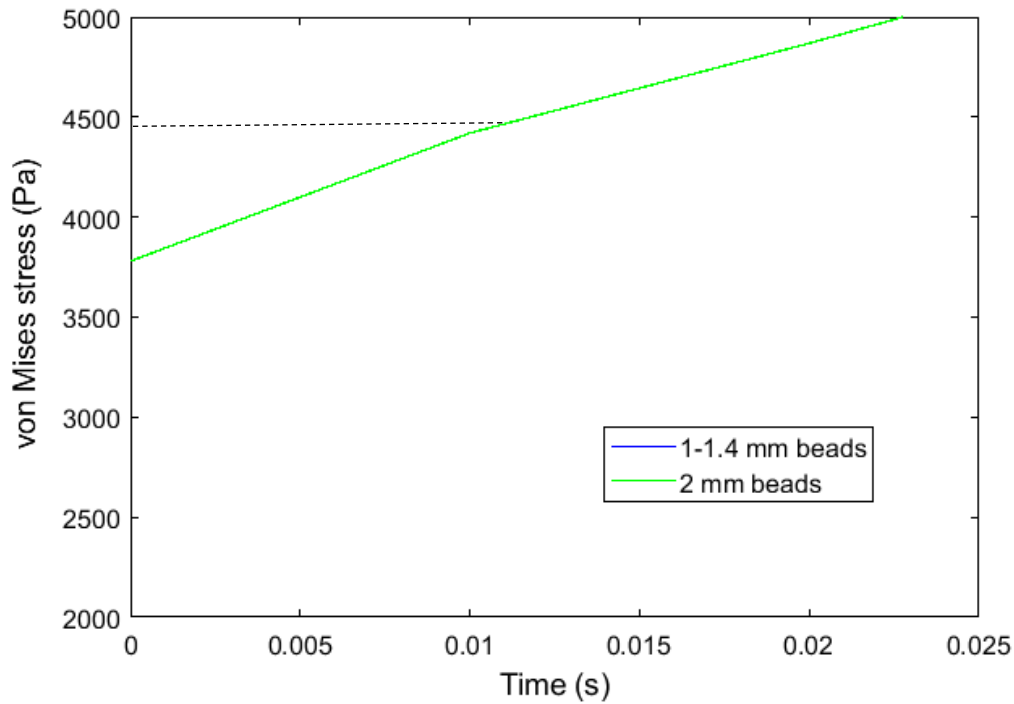


Figure 6.39 von Mises stress versus time for ballotini 10cSt pellets with different background beads, shear rate of 40.21/s and top plate pressure of 2000 Pa

Table 6.17 Intersection times for von Mises stress and yield stresses of ballotini 10cSt pellets with different size of background beads, shear rate of 40.21/s and top plate pressure of 2000 Pa

	Intersection times at which von Mises stress exceeds yield stress at 1 mm/s	Intersection times at which von Mises stress exceeds yield stress at 10 mm/s	Intersection times at which von Mises stress exceeds yield stress at 50 mm/s	Intersection times at which von Mises stress exceeds yield stress at 125.7 mm/s
Background beads (mm)	Predicted yielding time (s)	Predicted yielding time (s)	Predicted yielding time (s)	Predicted yielding time (s)
1-1.4	0	0	0	0
2	0	0	0	0.012

6.12.3.2 Effect of shear rate

In Figure 6.40, the von Mises stress versus time for lactose pellets sheared with different shear rates, a top plate pressure of 2000 Pa and 1-1.4 mm beads was evaluated. In Table 6.18, the times at which the von Mises stress exceeds the measured yield stresses of the lactose pellets are listed. Lower yielding times were predicted for lactose pellets sheared with a shear rate of 40.21/s, followed by lactose pellets sheared with shear rate of 20.11/s (for comparison with yield stresses at compression speeds of 1 and 125.7 mm/s). Further, small differences in yielding times were observed for lactose pellets sheared with shear rates of 10.05/s, 30.16/s and 5.03/s (the highest yielding time) (for comparison with yield stresses at compression speeds of 1 and 125.7 mm/s).

For a compression speed of 10 mm/s, the yielding times for the lactose pellets decreased as the lactose pellets sheared with shear rate of: 40.21/s (the lowest yielding time) < 20.11/s < 30.16/s < 10.05/s < 5.03/s (the highest yielding time).

For a compression speed of 50 mm/s, the yielding times for the lactose pellets decreased as the lactose pellets sheared with shear rate of 40.21/s, followed by lactose pellets sheared with shear rate of 20.11/s and followed by lactose pellets sheared with shear rate of 30.16/s. However, very small differences in yielding times were observed for lactose pellets sheared with shear rates of 5.03/s and 10.05/s (highest yielding times).

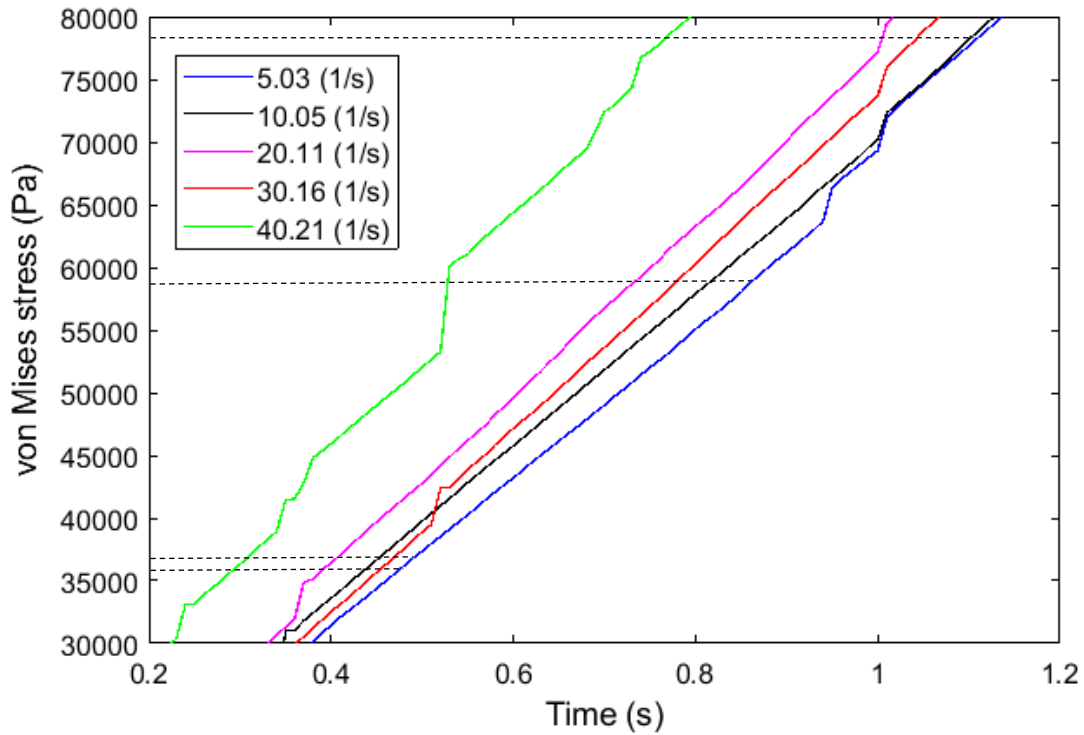


Figure 6.40 von Mises stress versus time for lactose 10cSt pellets with different shear rates, top plate pressure of 2000 Pa and 1-1.4 mm background beads

Table 6.18 Intersection times for von Mises stress and yield stresses of lactose 10cSt pellets with different shear rates, top plate pressure of 2000 Pa and 1-1.4 mm background beads

	Intersection times at which von Mises stress exceeds yield stress at 1 mm/s	Intersection times at which von Mises stress exceeds yield stress at 10 mm/s	Intersection times at which von Mises stress exceeds yield stress at 50 mm/s	Intersection times at which von Mises stress exceeds yield stress at 125.7 mm/s
Shear rate (1/s)	Predicted yielding time (s)	Predicted yielding time (s)	Predicted yielding time (s)	Predicted yielding time (s)
5.03	0.498	0.874	1.123	0.469
10.05	0.46	0.83	1.115	0.431
20.11	0.413	0.746	1.002	0.387
30.16	0.475	0.792	1.055	0.448
40.21	0.315	0.53	0.781	0.287

In Table 6.19, the von Mises stress was calculated for ballotini pellets with different shear rates, a top plate pressure of 2000 Pa and 1-1.4 mm background beads. However, the measured yield stress of all compression speeds was exceeded by all of the shear rates investigated (5.03 /s, 20.11 /s and 40.21/s) at the start of the simulation. Therefore, it is predicted that the ballotini pellets would deform prior to shearing. As shown in Table 6.19, the yielding time for the ballotini pellets was predicted to start at 0 s for all the shear rates.

Table 6.19 Intersection times for von Mises stress and yield stresses of ballotini 10cSt pellets with different shear rates, top plate pressure of 2000 Pa and 1-1.4 mm background beads

	Intersection times at which von Mises stress exceeds yield stress at 1 mm/s	Intersection times at which von Mises stress exceeds yield stress at 10 mm/s	Intersection times at which von Mises stress exceeds yield stress at 50 mm/s	Intersection times at which von Mises stress exceeds yield stress at 125.7 mm/s
Shear rate (1/s)	Predicted yielding time (s)	Predicted yielding time (s)	Predicted yielding time (s)	Predicted yielding time (s)
5.03	0	0	0	0
20.11	0	0	0	0
40.21	0	0	0	0

6.12.3.3 Effect of normal pressure

In Figure 6.41, the von Mises stress versus time for lactose pellets sheared with three normal pressures, a shear rate of 40.21/s and 1-1.4 mm background beads was evaluated. In Table 6.20, the times at which the von Mises stress of the lactose pellets exceeded the yield stresses of lactose pellets for compression speeds between 1 and 125.7 mm/s are given.

For a compression speed of 1 mm/s, the lactose pellet sheared with 383 Pa did not exceed the yield stress of the lactose pellet at the timescale of the simulation, 2 s. Therefore, the yielding time for the lactose pellet sheared with 383 Pa was predicted greater than 2 s. Interestingly, a lower yielding time was predicted for lactose pellets sheared with 2000 Pa than with 600 Pa.

A similar result was observed for yield stresses of lactose pellets at compression speeds of 10 and 50 mm/s. Lactose pellets with normal pressures of 383 and 600 Pa are predicted to yield at greater than 2 s for the reason the von Mises stresses did not exceed the yield stresses of lactose pellets at

compression speeds of 10 and 50 mm/s. Yielding times of 0.53 and 0.781 Pa, respectively, were observed for lactose pellets with a pressure of 2000 Pa.

For a compression speed of 125.7 mm/s, a decrease in yielding time was predicted for the lactose pellets with increasing normal pressures from 383 to 2000 Pa.

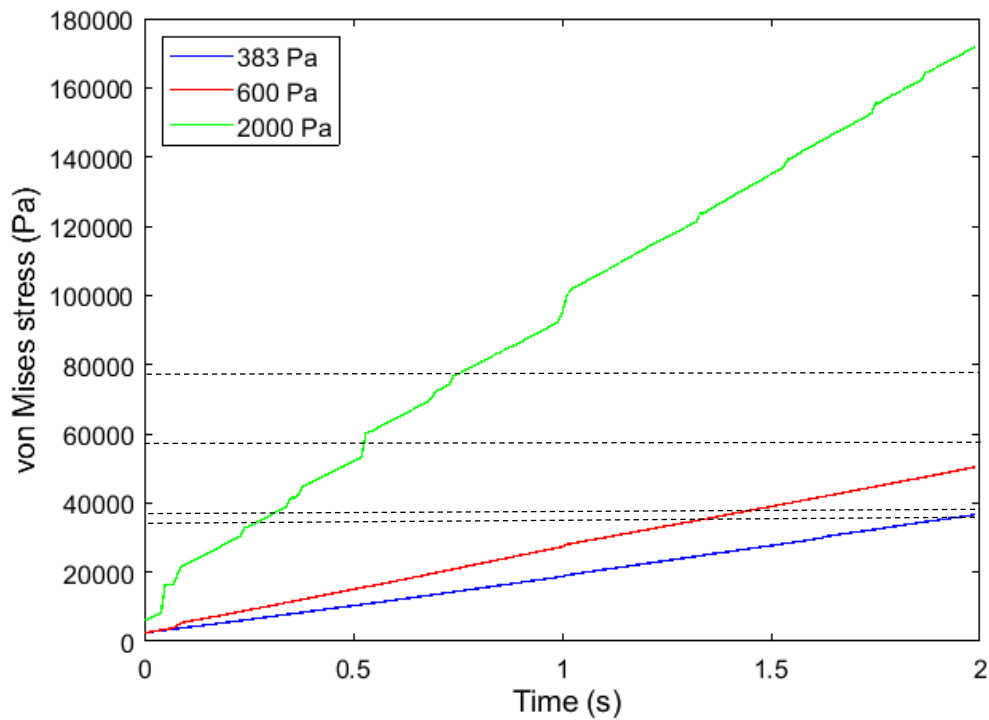


Figure 6.41 von Mises stress versus time for lactose 10cSt pellets with different normal pressures, shear rate of 40.21/s and 1-1.4 mm background beads

Table 6.20 Intersection times for von Mises stress and yield stresses of lactose 10cSt pellets with different normal pressures, shear rate of 40.21/s and 1-1.4 mm background beads

	Intersection times at which von Mises stress exceeds yield stress at 1 mm/s	Intersection times at which von Mises stress exceeds yield stress at 10 mm/s	Intersection times at which von Mises stress exceeds yield stress at 50 mm/s	Intersection times at which von Mises stress exceeds yield stress at 125.7 mm/s
Normal pressure (Pa)	Predicted yielding time (s)	Predicted yielding time (s)	Predicted yielding time (s)	Predicted yielding time (s)
383	> 2 s	> 2 s	> 2 s	1.926
600	1.425	> 2 s	> 2 s	1.348
2000	0.315	0.53	0.781	0.287

In Figure 6.42, the von Mises stress versus time for ballotini pellets sheared with different normal pressures, shear rate of 40.21/s and 1-1.4 mm background beads was evaluated. The data for ballotini pellets with a normal pressure of 2000 Pa was not within the range values of the four yield stresses of ballotini pellets at different compression speeds. Therefore, the data was not plotted in the figure.

The intersection times for von Mises stress and yield stresses of the ballotini pellets with different normal pressures are given in Table 6.21. As shown in Table 6.21, for yield stresses at compression speeds of 1 and 10 mm/s, yielding is predicted prior to the start of shearing for all pressures.

For compression speeds of 50 mm/s, a very small yield time of 0.044 s for ballotini pellets with a normal pressure of 383 Pa was predicted. Yielding was predicted to start at 0 s for the 600 Pa and 2000 Pa cases. For compression speeds of 125.7 mm/s, the predicted the yielding times for the ballotini pellets decreased as the normal pressures increased from 383 to 600 Pa, and was 0 s for 2000 Pa.

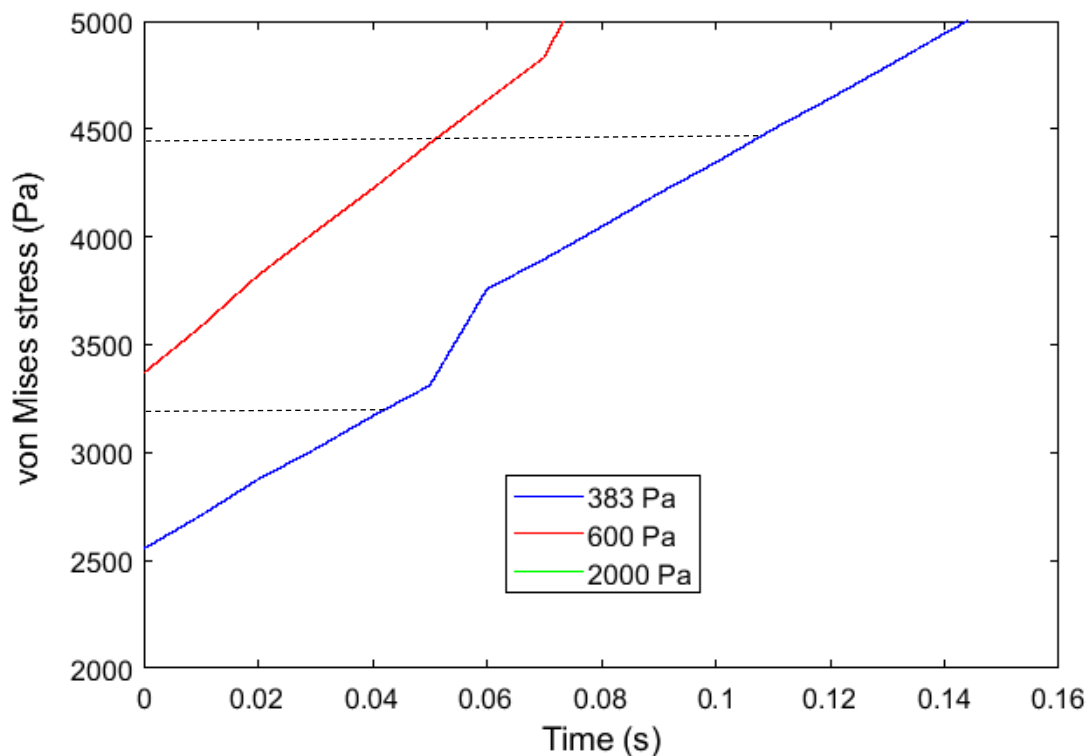


Figure 6.42 von Mises stress versus time for ballotini 10cSt pellets with different normal pressures, shear rate of 40.21/s and 1-1.4 mm background beads

Table 6.21 Intersection times for von Mises stress and yield stresses of ballotini 10cSt pellets with different normal pressures, shear rate of 40.21/s and 1-1.4 mm background beads

	Intersection times at which von Mises stress exceeds yield stress at 1 mm/s	Intersection times at which von Mises stress exceeds yield stress at 10 mm/s	Intersection times at which von Mises stress exceeds yield stress at 50 mm/s	Intersection times at which von Mises stress exceeds yield stress at 125.7 mm/s
Normal pressure (Pa)	Predicted yielding time (s)	Predicted yielding time (s)	Predicted yielding time (s)	Predicted yielding time (s)
383	0	0	0.044	0.11
600	0	0	0	0.053
2000	0	0	0	0

6.13 Summary

The conditions for designing and building the DEM unit shear cell has been discussed in this chapter. The material properties and operating parameters for DEM simulations have been explained. The results from the DEM simulations and the failure theory were presented and discussed. The pellet deformation in the DEM unit shear cell was predicted by considering these material properties and operating parameters, based on the experimental work in the annular shear cell. The pellet deformation is simulated by means of Discrete Element Method (DEM) and von Mises failure theory. The DEM simulations were used as a tool to compute both the deviatoric and von Mises stresses. The von Mises failure theory was used to attempt to predict pellet deformation. The von Mises failure theory states that a pellet is deformed if the von Mises stress exceeds the yield stress of the pellet. In this study, the computed von Mises stress was compared to several yield stresses of the pellets and the intersection times between these von Mises stress and yield stresses were determined. Different pellets, effect of operating parameters and material properties were considered for predicting the pellet deformation through the deviatoric stress and the yielding times through von Mises failure theory.

The results presented here suggest that background beads of 1-1.4 mm to 4 mm, rather than the 6 mm background beads, may be a major effector to higher deviatoric stresses of lactose 10cSt pellets. Based on von Mises failure theory, a lower yielding time was predicted for 1-1.4 mm background beads compared to 2 mm background beads, as compared with all the yield stresses of lactose 10cSt pellets at different compression speeds. Similarly, smaller size of background beads 1-1.4 mm resulted in higher deviatoric stress of ballotini 10cSt pellets compared to 2 mm background beads. Based on von Mises failure theory, a lower yielding time was predicted for ballotini pellets sheared with 1-1.4 mm background beads than the 2 mm background beads, as compared with yield stress at compression speed of 125.7 mm/s.

There would be no point in studying shear rates of 5.03/s, 10.05/s and 30.16/s, as they all share the same deviatoric stress for lactose 10cSt pellets. However, shear rates of 20.11/s and 40.21/s resulted in higher deviatoric stress. For comparison with yield stresses at compression speeds of 1 and 125.7 mm/s, lower yielding times were predicted for lactose 10cSt pellets sheared with a shear rate of 40.21/s, followed by lactose 10cSt pellets sheared with shear rate of 20.11/s and small differences in yielding times were observed for lactose 10cSt pellets sheared with shear rates of 10.05/s, 30.16/s and 5.03/s (the highest yielding time). For comparison with yield stress at a compression speed of 10 mm/s, the yielding times for lactose 10cSt pellets sheared with different shear rates can be arranged as follows: 40.21/s (lowest yielding time) < 20.11/s < 30.16/s < 10.05/s < 5.03/s (the highest yielding time). For comparison with yield stress at a compression speed of 50 mm/s; a lower yielding time for lactose 10cSt pellets with the highest shear rate of 40.21/s, followed by shear rates of 20.11/s and shear rates of 30.16/s. Lactose 10cSt pellets with shear rates of 5.03/s and 10.05/s showed very little differences in yielding time and the highest yielding time. The three different shear rates between 5.03/s and 40.21/s have a minor role in influencing the deviatoric stress change over time for ballotini 10cSt pellets. Based on von Mises failure theory, the yielding times for the ballotini 10cSt pellets were predicted to start at 0 s for all the shear rates.

As we have shown, the normal pressure has a major role in influencing the deviatoric stress change over time for lactose 10cSt pellets. The normal pressure of 2000 Pa resulted in the highest deviatoric stress of lactose 10cSt pellets followed by 600 Pa and 383 Pa. Based on prediction by von Mises failure theory, the lowest yielding time was predicted for lactose pellet sheared with pressure of 2000 Pa, followed by normal pressures of 600 and 383 Pa (highest yielding time). An increase of normal pressures from 383 to 2000 Pa increases the deviatoric stress of the ballotini 10cSt pellets. The von

Mises failure theory predicts that increasing the normal pressures from 383 to 2000 Pa results in decreasing the yielding time for the ballotini 10cSt pellets.

The deviatoric stress of ballotini 10cSt pellets was increased with increasing viscosity of silicone oils for 0.01 Pa.s, 0.05 Pa.s and 0.1 Pa.s silicone oils. Whereas, the results for 1 Pa.s silicone oil did not fit this trend. We believe that higher viscosity silicone oils may play an important role in deforming the ballotini 10cSt pellets, especially in cases of 0.01 Pa.s, 0.05 Pa.s and 0.1 Pa.s silicone oils. The effect of types of powders indicates that pellets made with lactose powder had higher deviatoric stress in comparison to ballotini powder.

In this chapter both the results of deviatoric stress and von Mises failure theory were in line and have been shown to be capable of predicting the deformation of pellets under different operating parameters. In general, pellet deformation was predicted by increasing normal pressure, high shear rates, smaller background beads, increasing viscosity of silicone oils and using lactose powder.

7 Relationship between experiment and prediction

7.1 Introduction

In this chapter, indirect correlation has been made between the experimental shear cell deformation results presented in Chapter 5 (Sections 5.3.1 and 5.3.2) and the predicted yielding times generated in Chapter 6 (Section 6.12.3).

Two types of pellets, lactose 10cSt and ballotini 10cSt pellets were chosen as the formulations for correlation. The experimental shear cell deformation results were based on the analysis of pellet elongation (%) and deformation fraction (%) (by averaging the data at different shearing times between 30 and 100 s). The predicted yielding time from DEM simulations was found using von Mises theory, based on the yield stress of the lactose and ballotini pellets at a compression speed of 125.7 mm/s. If the simulations are a good prediction of the experiments, low values of predicted yielding times would be expected to correspond with high values of pellet elongation or deformation fraction, and high values of predicted yield times to correspond with little observed deformation behaviour.

All available data is presented, where simulation and experimental conditions match. Operating parameters such as shear rate, normal pressure and size of background beads are chosen for correlation between the experimental and predicted results for lactose 10cSt pellets. However, only operating parameters of shear rate and normal pressure are available for ballotini 10cSt pellets. Table 7.1 lists the operating parameters.

Table 7.1 List of operating parameters for correlation between experimental data analysis from annular shear cell experiments and predicted from DEM simulations

Operating parameters	Description
Shear rate (1/s)	5.03 and 40.21
Normal pressure (Pa)	383, 600 and 2000
Size of background beads (mm)	1-1.4 and 2

7.2 Results and discussion

7.2.1 Strongest pellets (lactose 10cSt pellets)

7.2.1.1 Effect of shear rate

Figure 7.1 shows predicted yielding time versus shear rate for lactose pellets with normal pressure of 2000 Pa and 1-1.4 mm background beads. von Mises theory predicted a lower yielding time for a shear rate of 40.21/s compared to the 5.03/s, indicating the lactose pellets with shear rate of 40.21/s were predicted to yield in a shorter period of time. This prediction of yielding time was further correlated with the experimental elongation results for lactose pellets with different shear rates, shown in Figure 7.2. The higher shear rate of 40.21/s resulted in a higher % of pellet elongation compared to the lower shear rate of 5.03/s. A lower yielding time was expected for lactose pellets sheared with 40.21/s. This indicates that the results between the simulation and experiment for lactose pellets with different shear rates, conditions of normal pressure of 2000 Pa and 1-1.4 mm background beads showed some correlation.

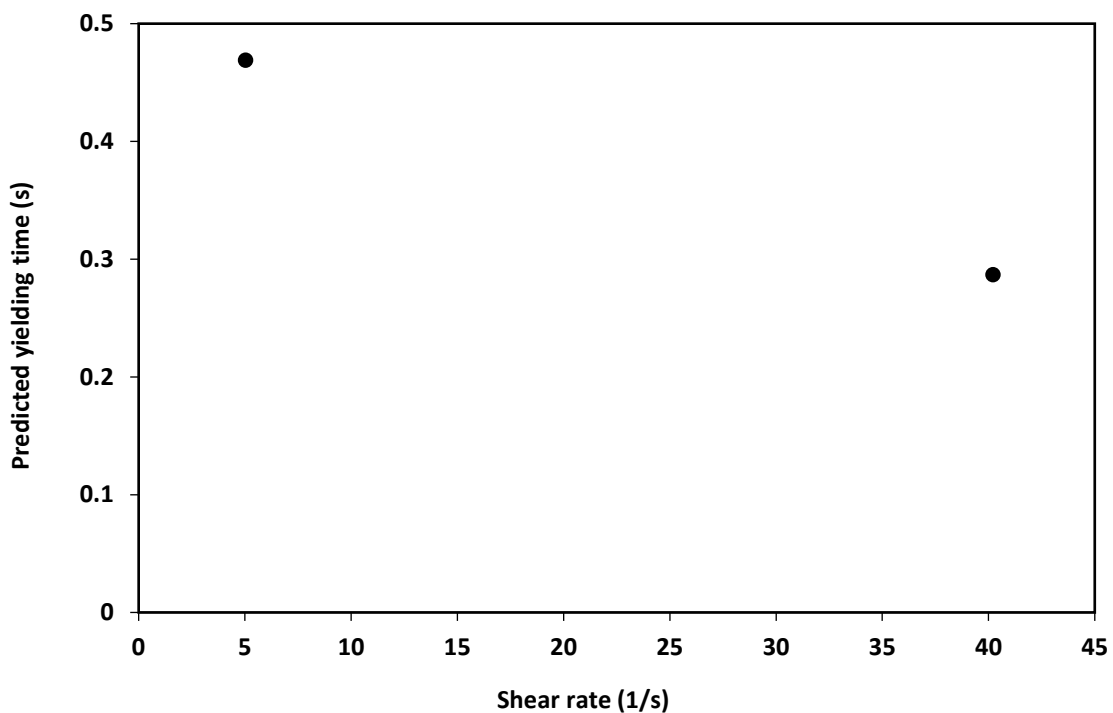


Figure 7.1 Predicted yielding time versus shear rate for lactose 10cSt pellets with a top lid pressure of 2000 Pa and 1-1.4 mm background beads.

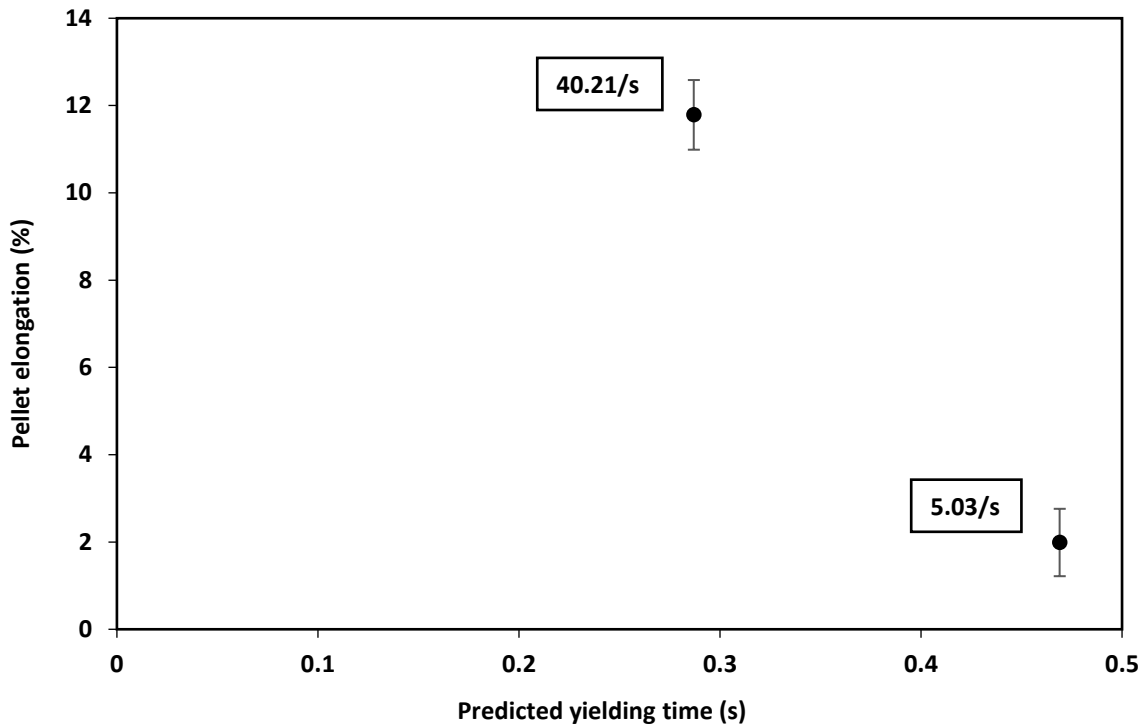


Figure 7.2 Pellet elongation versus predicted yielding time for lactose 10cSt pellets with different shear rates, normal pressure of 2000 Pa and 1-1.4 mm background beads. Error bars represent the standard error of 4 measurements.

7.2.1.2 Effect of normal pressure

Figure 7.3 shows the predicted yielding time versus normal pressure for lactose pellets with shear rate of 40.21/s and 1-1.4 mm background beads. The von Mises theory predicts that lactose pellets sheared with highest pressure of 2000 Pa would yield in a short time followed by 600 Pa and 383 Pa. In Figure 7.4, the experimental elongation results of lactose pellets with different normal pressures supported this prediction. Based on the experiments, the % of pellet elongation increased as increasing the normal pressure from 383 to 2000 Pa, with small values of pellet elongation for normal pressures of 383 and 600 Pa. The increase of the % of pellet elongation gave a shorter predicted yielding time. There appears to be some correlation between predicted and experimental yielding for the effect of normal pressure.

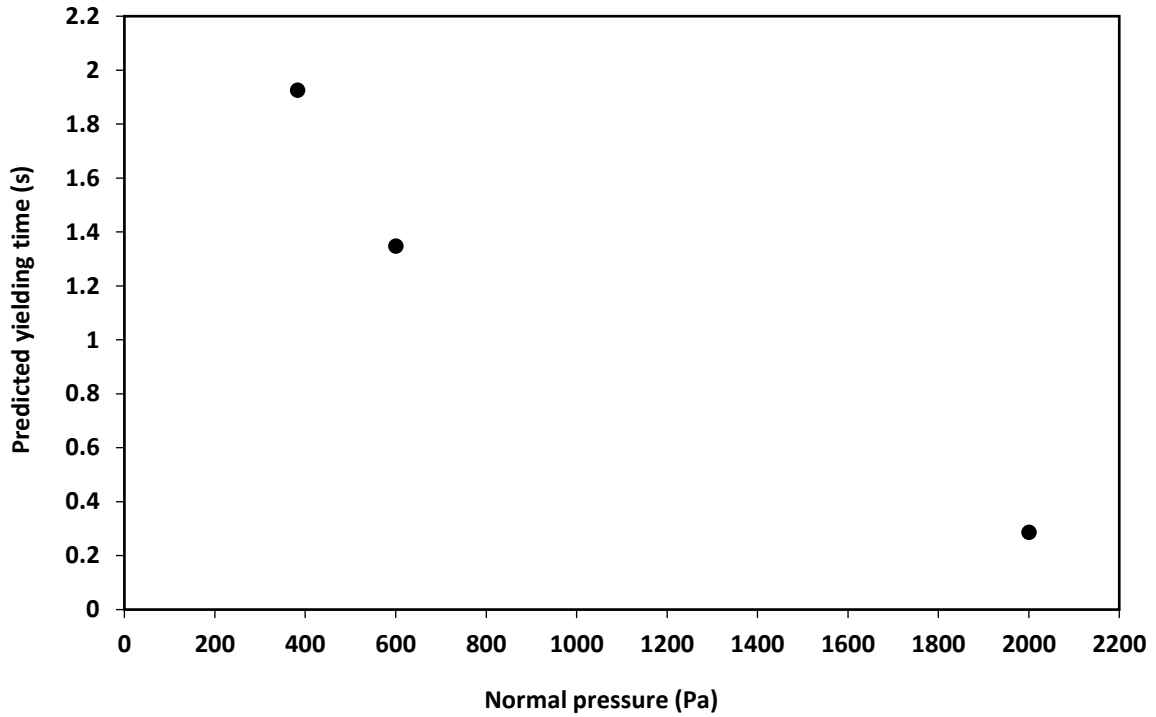


Figure 7.3 Predicted yielding time versus normal pressure for lactose 10cSt pellets with a shear rate of 40.21/s and 1-1.4 mm background beads.

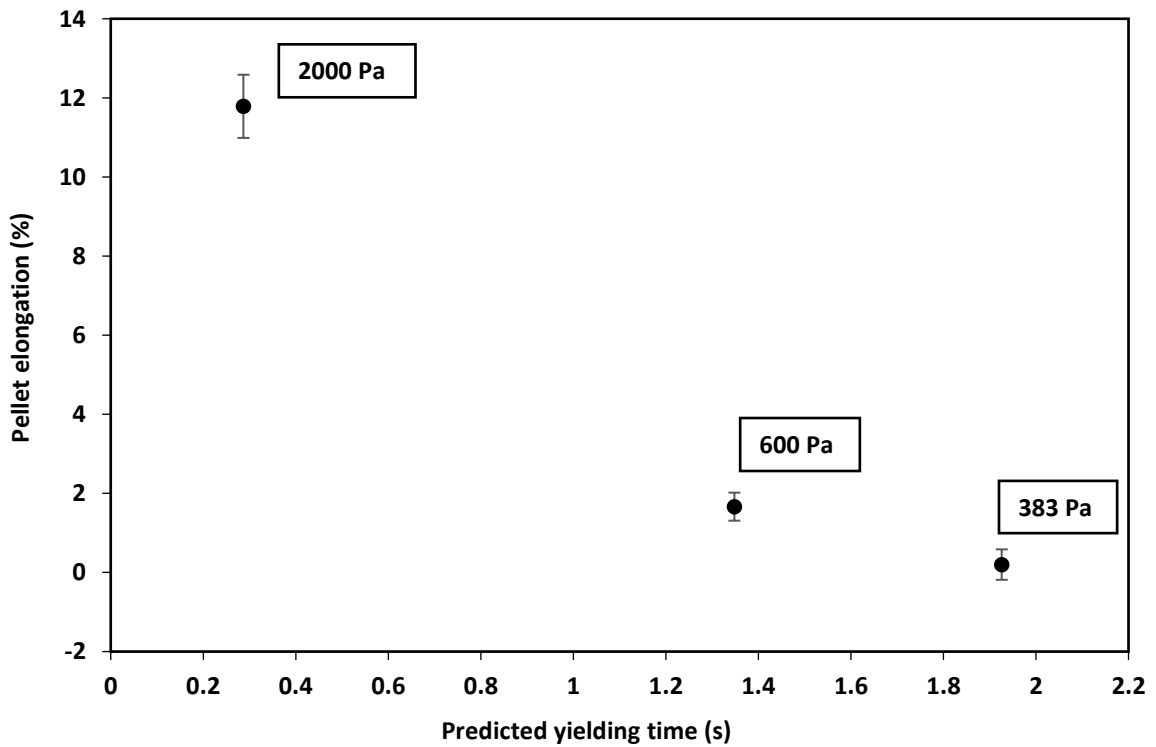


Figure 7.4 Pellet elongation versus predicted yielding time for lactose 10cSt pellets with different normal pressures, shear rate of 40.21/s and 1-1.4 mm background beads. Error bars represent the standard error of 4 measurements

7.2.1.3 Effect of size of background beads

Figure 7.5 shows the predicted yielding time versus sizes of background beads for lactose pellets with shear rate of 40.21/s and normal pressure of 2000 Pa. The 1-1.4 mm condition shows a low predicted yielding time of approximately 0.3 s. For the 2 mm condition, a higher value of 0.8 s was found for the predicted yielding time. In Figure 7.6, the experimental elongation results for both sizes of background beads and the predicted yielding time were plotted. The 1-1.4 mm beads showed a lower pellet elongation (11.8 %) and a lower yield of time. Whereas, the 2 mm beads gave 100 % of elongation and a longer predicted yielding time.

It is clear that in this case, the simulated yielding time does not provide a good prediction for the experimental behaviour. Changing from 1-1.4 mm to 2 mm beads gave longer predicted yielding times, but greater deformation was found experimentally for the 2 mm beads.

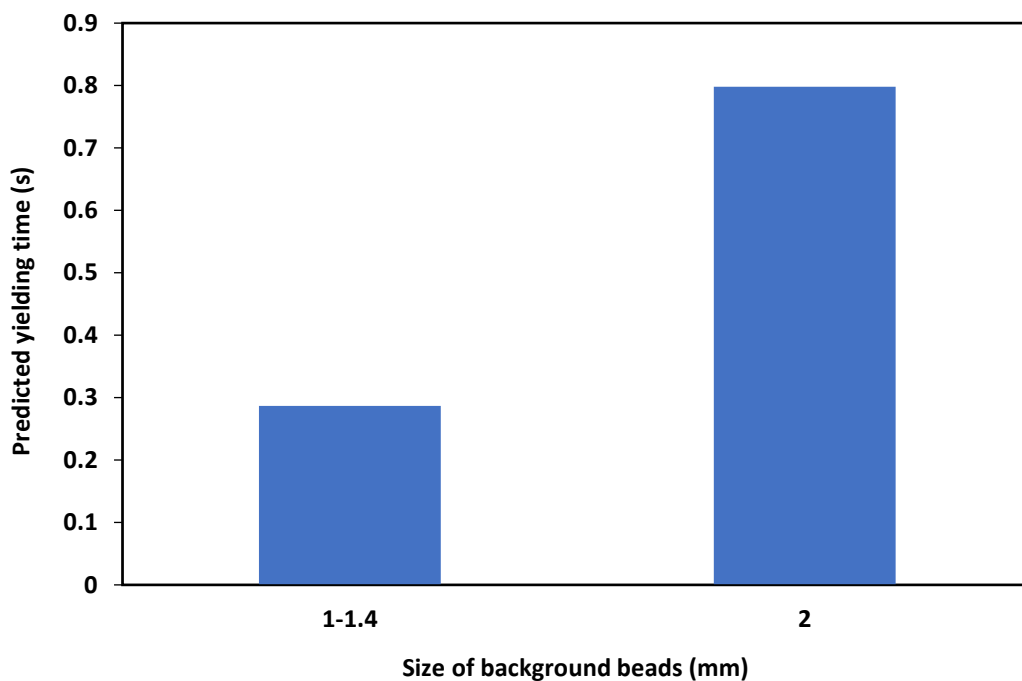


Figure 7.5 Predicted yielding time versus size of background beads for lactose 10cSt pellets with a shear rate of 40.21/s and a top lid pressure of 2000 Pa.

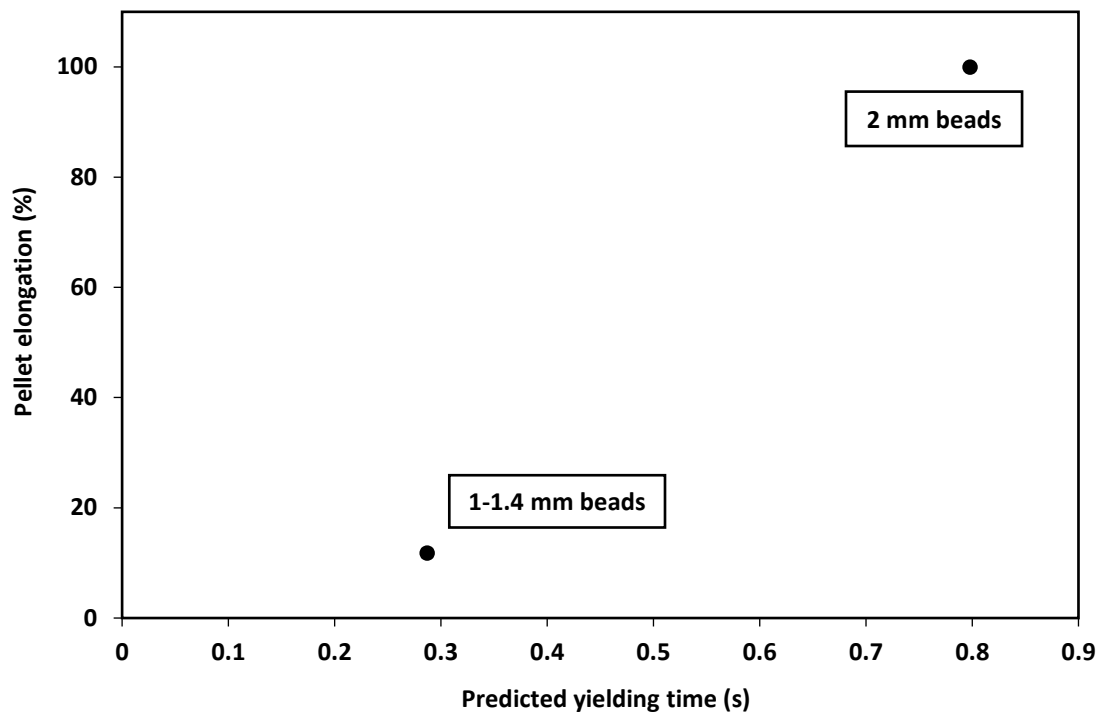


Figure 7.6 Pellet elongation versus predicted yielding time for lactose pellets with different size of background beads, shear rate of 40.21/s and normal pressure of 2000 Pa. Error bars represent the standard error of 4 measurements

7.2.2 Weakest pellets (ballotini 10cSt pellets)

7.2.2.1 Effect of shear rate

Figure 7.7 shows predicted yielding time versus shear rate for ballotini pellets with normal pressure of 2000 Pa and 1-1.4 mm background beads. For both shear rates, all predicted yielding times are 0 s, i.e. yielding before the beginning of shearing. However, the experiments range from minimal to substantial pellet deformation, as shown in Figure 7.8. There is a clear discrepancy between the predicted yielding time and the experimental deformation behaviour. For this case, no correlation could be made for both the simulation and experiments.

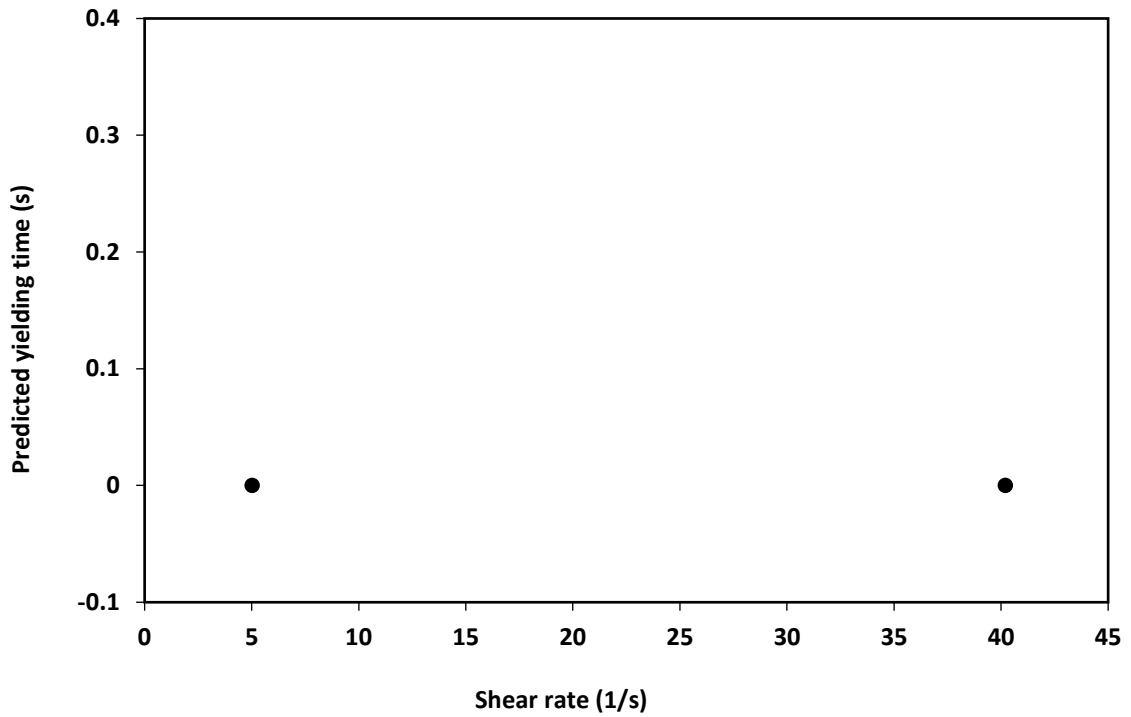


Figure 7.7 Predicted yielding time versus shear rate for ballotini 10cSt pellets with a top lid pressure of 2000 Pa and 1-1.4 mm background beads.

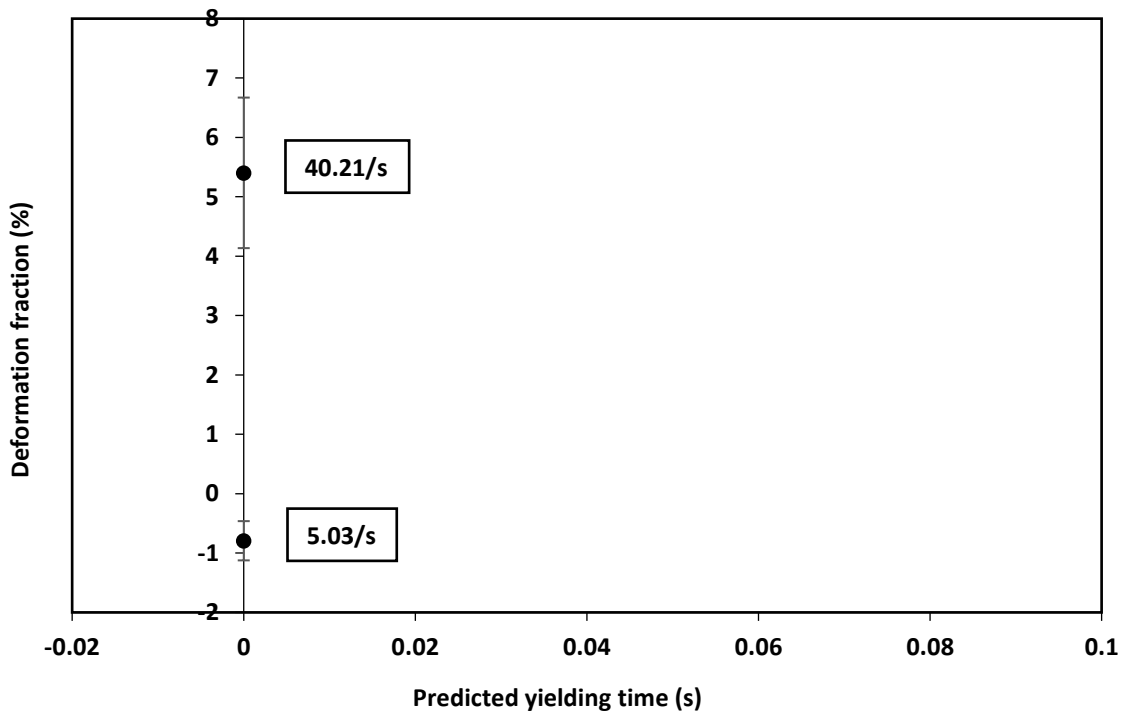


Figure 7.8 Deformation fraction versus predicted yielding time for ballotini 10cSt pellets with different shear rates, normal pressure of 2000 Pa and 1-1.4 mm background beads. Error bars represent the standard error of 4 measurements

7.2.2.2 Effect of normal pressure

Figure 7.9 shows the predicted yielding time versus normal pressure for ballotini pellets with a shear rate of 40.21/s and 1-1.4 mm background beads. Increasing the normal pressure from 383 Pa to 2000 Pa has decreased the predicted yielding time. The predicted yielding time was lowest for the pressure of 2000 Pa, followed by the 600 Pa and the highest yielding time for normal pressure of 383 Pa. The predicted results were further compared to the experimental results of ballotini pellets with different normal pressures. As shown in Figure 7.10, the experiments for ballotini pellets with normal pressure of 383 Pa resulted a higher % of deformation fraction compared to normal pressure of 600 Pa, however the von Mises theory predicts a longer yielding time for 383 Pa. This observation from experiment was not in line with prediction for normal pressure of 383 Pa. Additionally, the experimental deformation fractions for the 383 Pa and 2000 Pa cases were very similar in values, but the predicted yielding times were quite different. There is a clear discrepancy between the predicted and experimental deformation behaviour.

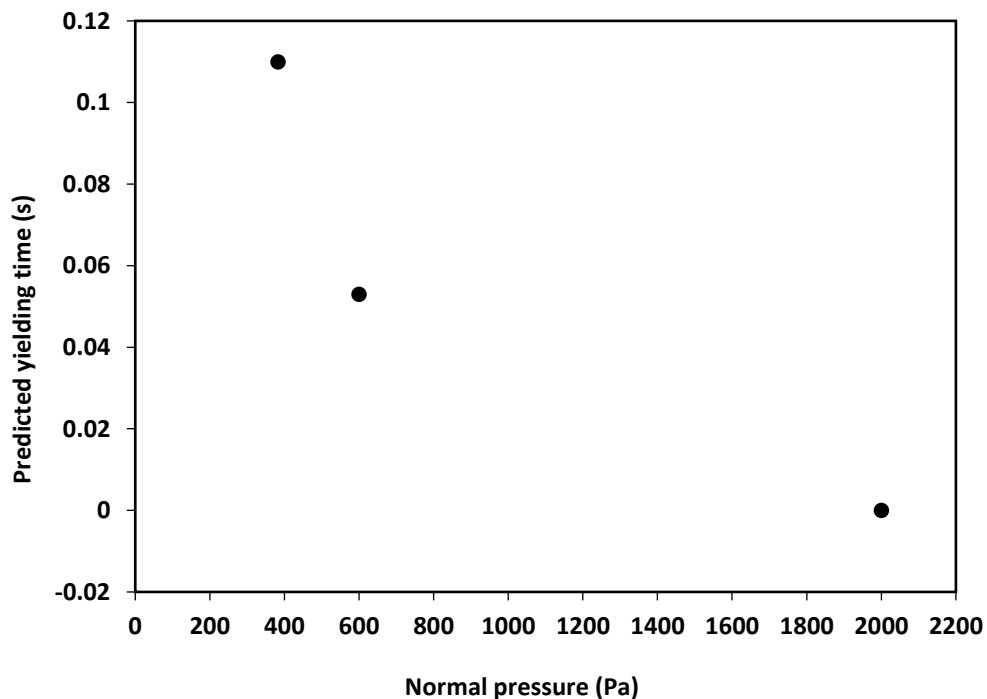


Figure 7.9 Predicted yielding time versus normal pressure for ballotini 10cSt pellets with a shear rate of 40.21/s and 1-1.4 mm background beads.

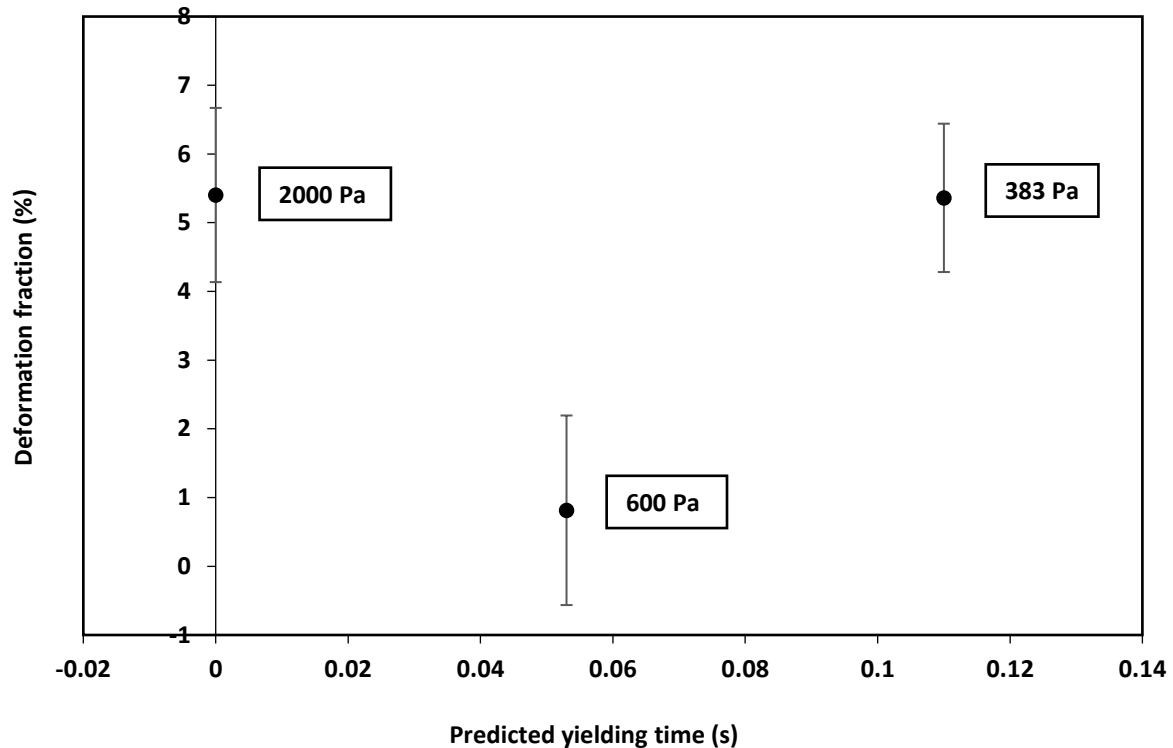


Figure 7.10 Deformation fraction versus predicted yielding time for ballotini 10cSt pellets with different normal pressures, shear rate of 40.21/s and 1-1.4 mm background beads. Error bars represent the standard error of 4 measurements

7.3 Summary

In this section, the predicted from the yielding time of the pellet during shearing in DEM simulations was indirectly correlated to the experimental data analysis in the annular shear cell experiments, e.g. pellet elongation (%) and deformation fraction (%). Although the timescales were different for the simulations and experiments, there is some correlation in the trends observed for the effect of shear rate and normal pressure on lactose pellets. However, the experimental results did not correlate with the predicted results from DEM simulations for three cases; effect of size of background beads on the lactose pellets and effect of shear rate and normal pressures of 383 and 600 Pa on ballotini pellets. While there was some agreement between the predicted and experimental deformation behaviour, overall, a correlation with experiment is about a semi-empirical prediction capability. There may be many reasons for this, including choices made in constructing the DEM simulations and the experimental methods used. Due to the large number of potential causes for this disagreement, it has not been possible to locate the source(s) within the scope of this project. Further work is proposed to investigate these discrepancies in Chapter 8.

8 Conclusions and Recommendations

8.1 Introduction

This research of study was inspired by previous works investigating granule breakage in high shear mixer granulators. Among the three rate processes in granulation, the third mechanism; breakage and attrition were less studied and the way the granules break under shear condition and the effect of other parameters needs further study.

The key research of this study was to attempt to develop a predictive model for granular pellet deformation in an annular shear cell to give a better understanding of the contributing factors of granule deformation. The deformation of pellets made of different formulations and surrounding by background beads were carried out in the annular shear cell. A method for predicting pellet deformation was developed, incorporating DEM simulations and von Mises failure theory. Many material properties were obtained experimentally and used as the input properties in the DEM simulations. A model of the pellet was created in DEM simulations to represent the 6 pellets in the annular shear cell experiments.

A “DEM unit shear cell” model consisting the pellet of interest and background beads were generated and the simulation was performed within the “DEM unit shear cell”. Comparable shearing set-ups in the annular shear cell were implemented, e.g., the pellet surrounding by background beads was sheared between a stationary bottom plate and a moving top plate. Similar operating parameters and material properties from the experiments were applied for prediction of pellet deformation. Relationship between the experiments and the predictions was made by correlating the measured pellet elongation and deformation fraction from experiments and the predicted yielding time of the pellets. This chapter summarises the research findings and contributions for predicting pellet deformation. In addition, suggestions are proposed for future works.

8.2 Research conclusion

The findings of this research are summarised below.

In Chapter 4, the mechanical properties of selected pellets made of different formulations were determined based on both quasi-static and dynamic compression tests. It was found that lactose 10cSt pellets consisting of lactose and 0.01 Pa.s silicone oil were identified as the 'hard' pellets due to their higher values of Young's modulus, plastic and elastic stiffness. Ballotini 1000cSt pellets composed of ballotini glass beads and 1 Pa.s silicone oil possessed the lowest values of Young's modulus, plastic and elastic stiffness, indicating the pellets as the 'soft' pellets. Dynamic yield stresses for all types of pellets increased linearly with the compression speeds. Moreover, ballotini 10cSt pellets and lactose 10cSt pellets possessed the lowest and highest yield stresses respectively, regardless of the compression speed.

In Chapter 5, experimental deformation of lactose 10cSt and ballotini 10cSt pellets were performed in annular shear cell and compared with the Stokes deformation number, St_{def} . Different types of deformation for lactose 10cSt and ballotini 10cSt pellets were identified; elongation and a combination of fragmentation and compression, under different shearing conditions. For lactose 10cSt pellets, pellet elongation (%) increased for with increasing shear rate, increasing normal pressure and increasing size of the background beads. The results of deformation fraction (%) for ballotini 10cSt pellets increased for higher shear rate and increasing the normal pressure. Based on St_{def} theory, St_{def} shows some promise to be used as a predictive tool for predicting the pellet deformation for operating parameter of shear rate.

Deformation of lactose 10cSt and ballotini 10cSt pellets under different shearing conditions was predicted through deviatoric stress and von Mises failure theory (Chapter 6). The conditions for designing and building the DEM unit shear cell and setup for DEM simulations were presented in this chapter. The effect of viscosity of silicone oils and effect of types of powders were also investigated. For lactose 10cSt pellets sheared with smaller sizes of beads (1-1.4 to 4 mm beads), at the highest shear rate of 40.21/s, increasing the normal pressure from 383 to 2000 Pa resulted in a higher deviatoric stresses. A similar effect was found for ballotini 10cSt pellets sheared with 1-1.4 mm beads, where the deviatoric stress increased with increasing normal pressure from 383 to 2000 Pa. Only small changes in deviatoric stress were found for ballotini pellets sheared with shear rates between 5.03/s and 40.21/s. For ballotini pellets made of different viscosity of silicone oils, increasing the viscosity of

silicone oils from 0.01 and 0.1 Pa.s increased the deviatoric stress of the ballotini pellets. The highest viscous property of 1 Pa.s unexpectedly lowered the deviatoric stress. Pellets made with lactose powder had higher deviatoric stresses in comparison with ballotini powder. The von Mises failure theory predicted that for lactose 10cSt pellets sheared with shear rate of 40.21/s, increasing normal pressure from 383 to 2000 Pa and 1-1.4 mm background beads would result in a lower yielding time. The von Mises failure theory predicted that ballotini 10cSt pellets sheared with normal pressures from 383 to 2000 Pa using 1-1.4 mm background beads would result in a lower yielding time.

Finally, the experiments and prediction results were correlated in (Chapter 7). In this analysis, the predicted yielding times from Chapter 6 were correlated with the experimentally measures pellet elongation and deformation fraction from Chapter 5. For the effect of shear rate and normal pressure on lactose pellets, increasing predicted yielding time showed decreasing pellet deformation, as expected, although on quite different timescales. Several other parameters investigated did not show this correlation however, and it is concluded overall that the simulated yielding time as calculated here is able to semi-predict the pellet deformation in the shear cell.

8.3 Future works

Preliminary works for predicting pellet deformation in the annular shear cell has been studied. The following suggestions are proposed for future work:

- In this study, the operating parameters chosen such as shear rates, normal pressures and size of background beads were based on previous studies. However, the experimental results show that the lactose 10cSt and ballotini 10St pellets did not deform completely for certain conditions: the highest normal pressure and shear rate, e.g., 40.21/s and 2000 Pa. Therefore, it is suggested to use higher normal pressures and shear rates than these ranges.
- The annular shear cell experimental works have been performed for two different types of pellets, lactose 10cSt and ballotini 10cSt pellets, for different operating parameters. The effect of the formulation of the pellets can be further investigated in the future. Prediction results have been done in this study for different viscosity of silicone oils, but not for the experimental works. Moreover, lactose and ballotini glass beads were tested for both experiments and modelling. Therefore, future works for experiments and modelling can be extended for other commonly used pharmaceutical powders or food materials that have different characteristics and might behave differently under shearing conditions. For example, the use of

microcrystalline cellulose (MCC) and corn starch powders would be a promising avenue of research.

- In this study, both deviatoric and von Mises stresses obtained from DEM simulations increases as increasing the shearing time for all the shearing conditions. The nine stress components of the pellet might contribute to this result; however, this reason was still unclear. This requires further investigation.
- The model for the pellets was created using a simple technique, e.g., by agglomerating an amount of multi-sphere particles within a cylindrical geometry. This model of pellets was intact together throughout the simulation and the stresses experienced by the pellet were computed over the shearing time. It is suggested in the future to implement the bonding contact model so that the agglomerate of multi-sphere particles can be dispersed/detached during shearing. For this reason, the pellet deformation can be investigated by observing the dispersion/detach of the agglomerate of multi-sphere particles from the cylindrical geometry.
- The effect of the size of the DEM unit shear cell is likely to be important to the deviatoric stress and von Mises stress results. Due to the required simulation times, there was insufficient time in this project to investigate the effect of the size of the DEM unit shear cell. It is recommended that this study be performed in the future.

9 References

- Alenzi, A., Marinack, M., Higgs, C. F., & McCarthy, J. J. (2013). DEM validation using an annular shear cell. *Powder Technology*, 248, 131–142. <https://doi.org/10.1016/j.powtec.2013.05.003>
- Ali Hassanpour, M. P. (2015). Discrete Element Method Applications in Process Engineering. In M. M. Martin (Ed.), *Introduction to Software for Chemical Engineers*. CRC Press Taylor & Francis Group.
- Antony, S. J., & Ghadiri, M. (2001). Size Effects in a Slowly Sheared Granular Media. *Journal of Applied Mechanics*, 68(5), 772. <https://doi.org/10.1115/1.1387443>
- Antonyuk, S., Khanal, M., Tomas, J., Heinrich, S., & M??rl, L. (2006). Impact breakage of spherical granules: Experimental study and DEM simulation. *Chemical Engineering and Processing: Process Intensification*, 45(10), 838–856. <https://doi.org/10.1016/j.cep.2005.12.005>
- Bagherzadeh, K. A., Mirghasemi, A. A., & Mohammadi, S. (2011). Numerical simulation of particle breakage of angular particles using combined DEM and FEM. *Powder Technology*, 205(1–3), 15–29. <https://doi.org/10.1016/j.powtec.2010.07.034>
- Baran, O., & Kondic, L. (2006). On velocity profiles and stresses in sheared and vibrated granular systems under variable gravity. *Physics of Fluids*, 18(12). <https://doi.org/10.1063/1.2397007>
- Bednarek, X., Martin, S., Ndiaye, A., Peres, V., & Bonnefoy, O. (2017). Calibration of DEM parameters on shear test experiments using Kriging method. *EPJ Web of Conferences*, 140, 15016. <https://doi.org/10.1051/epjconf/201714015016>
- Bharadwaj, R., Ketterhagen, W. R., & Hancock, B. C. (2010). Discrete element simulation study of a Freeman powder rheometer. *Chemical Engineering Science*, 65(21), 5747–5756. <https://doi.org/10.1016/j.ces.2010.04.002>
- Bouwman, A. M., Visser, M. R., Meesters, G. M. H., & Frijlink, H. W. (2006a). The use of Stokes deformation number as a predictive tool for material exchange behaviour of granules in the “equilibrium phase” in high shear granulation. *International Journal of Pharmaceutics*, 318(1–2), 78–85. <https://doi.org/10.1016/j.ijpharm.2006.03.038>
- Bouwman, A. M., Visser, M. R., Meesters, G. M. H., & Frijlink, H. W. (2006b). The use of Stokes deformation number as a predictive tool for material exchange behaviour of granules in the “equilibrium phase” in high shear granulation. *International Journal of Pharmaceutics*, 318(1–2), 78–85. <https://doi.org/10.1016/j.ijpharm.2006.03.038>
- Bridgwater, J., Utsumi, R., Zhang, Z., & Tuladhar, T. (2003). Particle attrition due to shearing-the effects of stress, strain and particle shape. *Chemical Engineering Science*, 58(20), 4649–4665. <https://doi.org/10.1016/j.ces.2003.07.007>
- Cavarretta, I., Coop, M., & O’Sullivan, C. (2010). The influence of particle characteristics on the

- behaviour of coarse grained soils. *Géotechnique*, 60(6), 413–423.
<https://doi.org/10.1680/geot.2010.60.6.413>
- Cavinato, M., Artoni, R., Bresciani, M., Canu, P., & Santomaso, A. C. (2013). Scale-up effects on flow patterns in the high shear mixing of cohesive powders. *Chemical Engineering Science*, 102, 1–9.
<https://doi.org/10.1016/j.ces.2013.07.037>
- Cavinato, M., Franceschinis, E., Cavallari, S., Realdon, N., & Santomaso, A. (2010). Relationship between particle shape and some process variables in high shear wet granulation using binders of different viscosity. *Chemical Engineering Journal*, 164(2–3), 292–298.
<https://doi.org/10.1016/j.cej.2010.08.029>
- Chandrashekar, N., Hashemi, J., Slauterbeck, J., & Beynon, B. D. (2008). Low-load behaviour of the patellar tendon graft and its relevance to the biomechanics of the reconstructed knee. *Clinical Biomechanics*, 23(7), 918–925. <https://doi.org/10.1016/j.clinbiomech.2008.03.070>
- Chen, W.-F., & Saleeb, A. F. (1994). *Studies in Applied Mechanics 37A. Constitutive Equations for Engineering Materials, Vol 1: Elasticity and Modelling*. Elsevier.
- Cheng, H. J., Hsiao, S. S., & Liao, C. C. (2012). Influence of the initial volume fill ratio of the granulator on melt agglomeration behavior in a high-shear mixer. *Advanced Powder Technology*, 23(1), 46–54. <https://doi.org/10.1016/j.apt.2010.12.006>
- Chitu, T. M., Oulahna, D., & Hemati, M. (2011a). Wet granulation in laboratory-scale high shear mixers: Effect of chopper presence, design and impeller speed. *Powder Technology*, 206(1–2), 34–43.
<https://doi.org/10.1016/j.powtec.2010.07.016>
- Chitu, T. M., Oulahna, D., & Hemati, M. (2011b). Wet granulation in laboratory scale high shear mixers: Effect of binder properties. *Powder Technology*, 206(1–2), 25–33.
<https://doi.org/10.1016/j.powtec.2010.07.012>
- Cleary, P. W. (2010). DEM prediction of industrial and geophysical particle flows. *Particuology*, 8(2), 106–118. <https://doi.org/10.1016/j.partic.2009.05.006>
- Clyens, S., & Johnson, W. (1977). A shear cell for the determination of the dynamic shear strength and flow behaviour of particulate materials. *International Journal of Mechanical Sciences*, 19(12), 745–752. [https://doi.org/10.1016/0020-7403\(77\)90059-5](https://doi.org/10.1016/0020-7403(77)90059-5)
- Cundall, P. A., & Strack, O. D. L. (1979). A Discrete Numerical Model for Granular Assemblies. *Geotechnique*, 29, 47–65.
- Das, N. (2007). *Modeling Three-Dimensional Shape of Sand Grains Using Discrete Element Method* [University of South Florida]. <https://doi.org/10.1017/CBO9781107415324.004>
- Davis, N. J. (2016). *Mechanical Dispersion of Semi-Solid Binders in High Shear Granulation*. Purdue University.

- Eliassen, H., Kristensen, H., & Schaefer, T. (1999). Growth mechanisms in melt agglomeration with a low viscosity binder. *International Journal of Pharmaceutics*, *186*, 149–159.
- Eliassen, H., Schaefer, T., & Kristensen, H. (1998). Effects of binder rheology on melt agglomeration in a high shear mixer. *International Journal of Pharmaceutics*, *176*, 73–83.
- Elliott, D. M., & Setton, L. A. (2001). Anisotropic and Inhomogeneous Tensile Behavior of the Human Annulus Fibrosus: Experimental Measurement and Material Model Predictions. *Journal of Biomechanical Engineering*, *123*(3), 256. <https://doi.org/10.1115/1.1374202>
- Ennis Litster, J.D., B. J. (1997). Particle size enlargement. In R. Perry Green, D. (Ed.), *Perry's Chemical Engineers' Handbook* (7th ed., pp. 20–89). McGraw-Hill.
- Flores, P. (2011). Compliant contact force approach for forward dynamic modeling and analysis of biomechanical systems. *Procedia IUTAM*, *2*, 58–67. <https://doi.org/10.1016/j.piutam.2011.04.006>
- Franceschinis, E., Santomaso, A. C., Trotter, A., & Realdon, N. (2014). High shear mixer granulation using food grade binders with different thickening power. *Food Research International*, *64*, 711–717. <https://doi.org/10.1016/j.foodres.2014.08.005>
- Gantt, J. A., & Gatzke, E. P. (2005). High-shear granulation modeling using a discrete element simulation approach. *Powder Technology*, *156*(2–3), 195–212. <https://doi.org/10.1016/j.powtec.2005.04.012>
- Ghadiri, M., Ning, Z., Kenter, S. ., & Puik, E. (2000a). Attrition of granular solids in a shear cell. *Chemical Engineering Science*, *55*(22), 5445–5456. [https://doi.org/10.1016/S0009-2509\(00\)00168-8](https://doi.org/10.1016/S0009-2509(00)00168-8)
- Ghadiri, M., Ning, Z., Kenter, S. J., & Puik, E. (2000b). Attrition of granular solids in a shear cell. *Chemical Engineering Science*, *55*(22), 5445–5456. [https://doi.org/10.1016/S0009-2509\(00\)00168-8](https://doi.org/10.1016/S0009-2509(00)00168-8)
- Goh, W. P., Ghadiri, M., Muller, F., Sinha, K., Nere, N., Ho, R., Bordawekar, S., & Sheikh, A. (2017). Stress analysis of an agitated particle bed with different particle aspect ratios by the discrete element method. *EPJ Web of Conferences*, *140*, 4–7. <https://doi.org/10.1051/epjconf/201714006022>
- Halidan, M., Chandratilleke, G. R., Chan, S. L. I., Yu, A. B., & Bridgwater, J. (2014). Prediction of the mixing behaviour of binary mixtures of particles in a bladed mixer. *Chemical Engineering Science*, *120*, 37–48. <https://doi.org/10.1016/j.ces.2014.08.048>
- Hanes, D. M., & Inman, D. L. (1985). Observations of rapidly flowing granular-fluid materials. *Journal of Fluid Mechanics*, *150*, 357–380. <https://doi.org/10.1017/S0022112085000167>
- Hare, C., & Ghadiri, M. (2015). Attrition of paracetamol and aspirin under bulk shear deformation. *Chemical Engineering Science*, *125*, 13–19. <https://doi.org/10.1016/j.ces.2014.10.027>
- Hare, C., & Ghadiri, M. (2017). Stress and strain rate analysis of the FT4 Powder Rheometer. *EPJ Web*

- of Conferences*, 140, 3034. <https://doi.org/10.1051/epjconf/201714003034>
- Hare, C., Ghadiri, M., & Dennehy, R. (2011a). Prediction of attrition in agitated particle beds. *Chemical Engineering Science*, 66(20), 4757–4770. <https://doi.org/10.1016/j.ces.2011.06.042>
- Hare, C., Ghadiri, M., & Dennehy, R. (2011b). Prediction of attrition in agitated particle beds. *Chemical Engineering Science*, 66(20), 4757–4770. <https://doi.org/10.1016/j.ces.2011.06.042>
- Hare, C. L., & Ghadiri, M. (2013). Influence of measurement cell size on predicted attrition by the Distinct Element Method. *Powder Technology*, 236, 100–106. <https://doi.org/10.1016/j.powtec.2012.04.061>
- Hare, C., Zafar, U., Ghadiri, M., Freeman, T., Clayton, J., & Murtagh, M. J. (2015). Analysis of the dynamics of the FT4 powder rheometer. *Powder Technology*, 285, 123–127. <https://doi.org/10.1016/j.powtec.2015.04.039>
- Hare, Colin, & Ghadiri, M. (2013). Prediction of bulk particle breakage due to naturally formed shear bands. *AIP Conference Proceedings*, 1542(1), 487–490. <https://doi.org/10.1063/1.4811974>
- Hassanpour, A., Ding, Y., & Ghadiri, M. (2004). Shear deformation of binary mixtures of dry particulate solids. *Advanced Powder Technology*, 15(6), 687–697. <https://doi.org/10.1163/1568552042456214>
- Hassanpour, A., Kwan, C. C., Ng, B. H., Rahmanian, N., Ding, Y. L., Antony, S. J., Jia, X. D., & Ghadiri, M. (2009). Effect of granulation scale-up on the strength of granules. *Powder Technology*, 189(2), 304–312. <https://doi.org/10.1016/j.powtec.2008.04.023>
- Hassanpour, Ali, Antony, S. J., & Ghadiri, M. (2007). Modeling of agglomerate behavior under shear deformation: Effect of velocity field of a high shear mixer granulator on the structure of agglomerates. *Advanced Powder Technology*, 18(6), 803–811. <https://doi.org/10.1163/156855207782515094>
- Hassanpour, Ali, Joseph Antony, S., & Ghadiri, M. (2008). Influence of interface energy of primary particles on the deformation and breakage behaviour of agglomerates sheared in a powder bed. *Chemical Engineering Science*, 63(23), 5593–5599. <https://doi.org/10.1016/j.ces.2008.08.008>
- Hassanpour, Ali, Tan, H., Bayly, A., Gopalkrishnan, P., Ng, B., & Ghadiri, M. (2011). Analysis of particle motion in a paddle mixer using Discrete Element Method (DEM). *Powder Technology*, 206(1–2), 189–194. <https://doi.org/10.1016/j.powtec.2010.07.025>
- Hsiau, S.-S., & Shieh, Y.-M. (1999). Fluctuations and self-diffusion of sheared granular material flows. *Journal of Rheology*, 43(5), 1049. <https://doi.org/10.1122/1.551027>
- Hsiau, S.-S., & Yang, W.-L. (2005). Transport property measurements in sheared granular flows. *Chemical Engineering Science*, 60(1), 13. <https://doi.org/10.1016/j.ces.2004.07.079>
- Hsiau, S. S., Lu, L. S., Chen, J. C., & Yang, W. L. (2005). Particle mixing in a sheared granular flow.

- International Journal of Multiphase Flow*, 31(7), 793–808.
<https://doi.org/10.1016/j.ijmultiphaseflow.2005.02.007>
- Hsiao, S. S., & Yang, W. L. (2002). Stresses and transport phenomena in sheared granular flows with different wall conditions. *Physics of Fluids*, 14(2), 612–621. <https://doi.org/10.1063/1.1428324>
- Hu, S., & Guo, X. (2015). A dissipative contact force model for impact analysis in multibody dynamics. *Multibody System Dynamics*, 35(2), 131–151. <https://doi.org/10.1007/s11044-015-9453-z>
- Iveson, S M, & Litster, J. D. (1998). Growth regime map for liquid-bound granules. *AIChE Journal*, 44(7), 1510–1518. <https://doi.org/10.1002/aic.690440705>
- Iveson, Simon M., Litster, J. D., Hapgood, K., & Ennis, B. J. (2001). Nucleation, growth and breakage phenomena in agitated wet granulation processes: A review. *Powder Technology*, 117(1–2), 3–39. [https://doi.org/10.1016/S0032-5910\(01\)00313-8](https://doi.org/10.1016/S0032-5910(01)00313-8)
- Iveson, Simon M., Page, N. W., & Litster, J. D. (2003). The importance of wet-powder dynamic mechanical properties in understanding granulation. *Powder Technology*, 130(1–3), 97–101. [https://doi.org/10.1016/S0032-5910\(02\)00233-4](https://doi.org/10.1016/S0032-5910(02)00233-4)
- Iveson, Simon M., Wauters, P. A. L., Forrest, S., Litster, J. D., Meesters, G. M. H., & Scarlett, B. (2001). Growth regime map for liquid-bound granules: Further development and experimental validation. *Powder Technology*, 117(1–2), 83–97. [https://doi.org/10.1016/S0032-5910\(01\)00317-5](https://doi.org/10.1016/S0032-5910(01)00317-5)
- Ji, S., Hanes, D. M., & Shen, H. H. (2009). Comparisons of physical experiment and discrete element simulations of sheared granular materials in an annular shear cell. *Mechanics of Materials*, 41(6), 764–776. <https://doi.org/10.1016/j.mechmat.2009.01.029>
- Jiang, M., Shen, Z., & Wang, J. (2015). A novel three-dimensional contact model for granulates incorporating rolling and twisting resistances. *Computers and Geotechnics*, 65, 147–163. <https://doi.org/10.1016/j.compgeo.2014.12.011>
- Jim Litster and Bryan Ennis. (2004). *the Science and Engineering of Granulation Process* (L. X. Liu (ed.); 1st ed.). Kluwer Academic Publishers.
- Johansen, A., & Schafer, T. (2001). Effects of physical properties of powder particles on binder liquid requirement and agglomerate growth mechanisms in a high shear mixer. *European Journal of Pharmaceutical Sciences*, 14(2), 135–147. [https://doi.org/10.1016/S0928-0987\(01\)00164-6](https://doi.org/10.1016/S0928-0987(01)00164-6)
- Kano, T., Yoshihashi, Y., Yonemochi, E., & Terada, K. (2014). Clarifying the mechanism of aggregation of particles in high-shear granulation based on their surface properties by using micro-spectroscopy. *International Journal of Pharmaceutics*, 461(1–2), 495–504. <https://doi.org/10.1016/j.ijpharm.2013.12.013>
- Kayrak-Talay, D., Dale, S., Wassgren, C., & Litster, J. (2013). Quality by design for wet granulation in

- pharmaceutical processing: Assessing models for a priori design and scaling. *Powder Technology*, 240, 7–18. <https://doi.org/10.1016/j.powtec.2012.07.013>
- Keningley, S. T., Knight, P. C., & Marson, A. D. (1997). An investigation into the effects of binder viscosity on agglomeration behaviour. *Powder Technology*, 91(2), 95–103. [https://doi.org/10.1016/S0032-5910\(96\)03230-5](https://doi.org/10.1016/S0032-5910(96)03230-5)
- Khan, M. I., & Tardos, G. I. (1997). Stability of wet agglomerates in granular shear flows. *Journal of Fluid Mechanics*, 347(1997), 347–368. <https://doi.org/10.1017/S002211209700668X>
- Kheiripour Langroudi, M., Sun, J., Sundaresan, S., & Tardos, G. I. (2010). Transmission of stresses in static and sheared granular beds: The influence of particle size, shearing rate, layer thickness and sensor size. *Powder Technology*, 203(1), 23–32. <https://doi.org/10.1016/j.powtec.2010.03.028>
- Knight, P. C., Instone, T., Pearson, J. M. K., & Hounslow, M. J. (1998). An investigation into the kinetics of liquid distribution and growth in high shear mixer agglomeration. *Powder Technology*, 97(3), 246–257. [https://doi.org/10.1016/S0032-5910\(98\)00031-X](https://doi.org/10.1016/S0032-5910(98)00031-X)
- Knight, P. C., Johansen, A., Kristensen, H. G., Schæfer, T., & Seville, J. P. K. (2000a). An investigation of the effects on agglomeration of changing the speed of a mechanical mixer. *Powder Technology*, 110(3), 204–209. [https://doi.org/10.1016/S0032-5910\(99\)00259-4](https://doi.org/10.1016/S0032-5910(99)00259-4)
- Knight, P. C., Johansen, A., Kristensen, H. G., Schæfer, T., & Seville, J. P. K. (2000b). An investigation of the effects on agglomeration of changing the speed of a mechanical mixer. *Powder Technology*, 110(3), 204–209. [https://doi.org/10.1016/S0032-5910\(99\)00259-4](https://doi.org/10.1016/S0032-5910(99)00259-4)
- Knight, P. C., Seville, J. P. K., Wellm, A. B., & Instone, T. (2001). Prediction of impeller torque in high shear powder mixers. *Chemical Engineering Science*, 56(15), 4457–4471. [https://doi.org/10.1016/S0009-2509\(01\)00114-2](https://doi.org/10.1016/S0009-2509(01)00114-2)
- Le, P. K., Avontuur, P., Hounslow, M. J., & Salman, A. D. (2009). The kinetics of the granulation process: Right from the early stages. *Powder Technology*, 189(2), 149–157. <https://doi.org/10.1016/j.powtec.2008.04.018>
- Lekhal Girard, K.P., Brown, M.A., Kiang, S., Glasser, B.J., Khinast, J.G., A. (2003). Impact of agitated drying on crystal morphology: KCl–water system. *Powder Technology*, 132, 119–130.
- Lekhal Girard, K.P., Brown, M.A., Kiang, S., Khinast, J.G., Glasser, B.J., A. (2004). The effect of agitated drying on the morphology of l-threonine (needle-like) crystals. *International Journal of Pharmaceutics*, 270, 263–277.
- Liao, C. C., Hsiao, S. S., & Chang, P. S. (2015). Bottom wall friction coefficients on the dynamic properties of sheared granular flows. *Powder Technology*, 270(Part A), 348–357. <https://doi.org/10.1016/j.powtec.2014.10.043>
- Liao, C., Hsiao, S., & Hu, Y. (2017a). Density-driven sinking dynamics of a granular ring in sheared

- granular flows. *Advanced Powder Technology*.
- Liao, C., Hsiao, S., & Hu, Y. (2017b). *Density-driven sinking dynamics of a granular ring in sheared granular flows*.
- Litster, J. D., Hapgood, K. P., Michaels, J. N., Sims, A., Roberts, M., & Kameneni, S. K. (2002). Scale-up of mixer granulators for effective liquid distribution. *Powder Technology*, *124*(3), 272–280. [https://doi.org/10.1016/S0032-5910\(02\)00023-2](https://doi.org/10.1016/S0032-5910(02)00023-2)
- Liu, L. X., Smith, R., & Litster, J. D. (2009). Wet granule breakage in a breakage only high-shear mixer: Effect of formulation properties on breakage behaviour. *Powder Technology*, *189*(2), 158–164. <https://doi.org/10.1016/j.powtec.2008.04.029>
- Liu, Y., Scharf, D., Graule, T., & Clemens, F. J. (2014). Granulation processing parameters on the mechanical properties of diatomite-based porous granulates. *Powder Technology*, *263*, 159–167. <https://doi.org/10.1016/j.powtec.2014.04.094>
- Luding, S. (2008). Constitutive relations for the shear band evolution in granular matter under large strain. *Particuology*, *6*(6), 501–505. <https://doi.org/10.1016/j.partic.2008.07.020>
- Lynch, H. A. (2003). Effect of Fiber Orientation and Strain Rate on the Nonlinear Uniaxial Tensile Material Properties of Tendon. *Journal of Biomechanical Engineering*, *125*(5), 726. <https://doi.org/10.1115/1.1614819>
- MacHado, M., Moreira, P., Flores, P., & Lankarani, H. M. (2012). Compliant contact force models in multibody dynamics: Evolution of the Hertz contact theory. *Mechanism and Machine Theory*, *53*(January 2016), 99–121. <https://doi.org/10.1016/j.mechmachtheory.2012.02.010>
- MacKaplou, M. B., Rosen, L. A., & Michaels, J. N. (2000). Effect of primary particle size on granule growth and endpoint determination in high-shear wet granulation. *Powder Technology*, *108*(1), 32–45. [https://doi.org/10.1016/S0032-5910\(99\)00203-X](https://doi.org/10.1016/S0032-5910(99)00203-X)
- Mangwandi, C., JiangTao, L., Albadarin, A. B., Dhenge, R. M., & Walker, G. M. (2015). High shear granulation of binary mixtures: Effect of powder composition on granule properties. *Powder Technology*, *270*, 424–434. <https://doi.org/10.1016/j.powtec.2014.06.021>
- Marigo, M. (2012). *Discrete element method modelling of complex granular motion in mixing vessels: evaluation and validation*. 1–341. <http://core.kmi.open.ac.uk/download/pdf/8821055.pdf>
- Mattucci, S. F. E., & Cronin, D. S. (2015). A method to characterize average cervical spine ligament response based on raw data sets for implementation into injury biomechanics models. *Journal of the Mechanical Behavior of Biomedical Materials*, *41*, 251–260. <https://doi.org/10.1016/j.jmbbm.2014.09.023>
- McCarthy, J. J., Jasti, V., Marinack, M., & Higgs, C. F. (2010). Quantitative validation of the discrete element method using an annular shear cell. *Powder Technology*, *203*(1), 70–77.

<https://doi.org/10.1016/j.powtec.2010.04.011>

- Midi, G. D. R. (2004). On dense granular flows. *European Physical Journal E*, 14(4), 341–365. <https://doi.org/10.1140/epje/i2003-10153-0>
- Mills, P. J. T., Seville, J. P. K., Knight, P. C., & Adams, M. J. (2000). The effect of binder viscosity on particle agglomeration in a low shear mixer/agglomerator. *Powder Technology*, 113(1–2), 140–147. [https://doi.org/10.1016/S0032-5910\(00\)00224-2](https://doi.org/10.1016/S0032-5910(00)00224-2)
- Mishra, B. K. (2003). A review of computer simulation of tumbling mills by the discrete element method: Part I-contact mechanics. *International Journal of Mineral Processing*, 71(1–4), 73–93. [https://doi.org/10.1016/S0301-7516\(03\)00032-2](https://doi.org/10.1016/S0301-7516(03)00032-2)
- Moreno, R., Ghadiri, M., & Antony, S. J. (2003). Effect of the impact angle on the breakage of agglomerates: a numerical study using DEM. *Powder Technology*, 130, 132–137.
- Mort, P., & Tardos, G. (1999). Scale-up of agglomeration processes using transformations. *Kona*, 17(17), 64–75. http://www.kona.or.jp/search/17_064.pdf
- Nakamura, H., Fujii, H., & Watano, S. (2013). Scale-up of high shear mixer-granulator based on discrete element analysis. *Powder Technology*, 236, 149–156. <https://doi.org/10.1016/j.powtec.2012.03.009>
- Nakamura, H., Miyazaki, Y., Sato, Y., Iwasaki, T., & Watano, S. (2009). Numerical analysis of similarities of particle behavior in high shear mixer granulators with different vessel sizes. *Advanced Powder Technology*, 20(5), 493–501. <https://doi.org/10.1016/j.apt.2009.05.006>
- Neil, A. U., & Bridgwater, J. (1994). Attrition of particulate solids under shear. *Powder Technology*, 80(3), 207–219. [https://doi.org/10.1016/0032-5910\(94\)02849-4](https://doi.org/10.1016/0032-5910(94)02849-4)
- Neil, A. U., & Bridgwater, J. (1999). Towards a parameter characterising attrition. *Powder Technology*, 106(1–2), 37–44. [https://doi.org/10.1016/S0032-5910\(99\)00064-9](https://doi.org/10.1016/S0032-5910(99)00064-9)
- Ning, Z., Boerefijn, R., Ghadiri, M., & Thornton, C. (1997). Distinct element simulation of impact breakage of lactose agglomerates. *Advanced Powder Technology*, 8, 15–37. <https://doi.org/10.1017/CBO9781107415324.004>
- Ning, Zemin, & Ghadiri, M. (2006). Distinct element analysis of attrition of granular solids under shear deformation. *Chemical Engineering Science*, 61(18), 5991–6001. <https://doi.org/10.1016/j.ces.2006.03.056>
- Orlando, A. D., & Shen, H. H. (2012). Effect of particle size and boundary conditions on the shear stress in an annular shear cell. *Granular Matter*, 14(3), 423–431. <https://doi.org/10.1007/s10035-012-0313-8>
- Orlando, A. D., & Shen, H. H. (2013). Using the annular shear cell as a rheometer for rapidly sheared granular materials: A DEM study. *Granular Matter*, 15(2), 183–194.

<https://doi.org/10.1007/s10035-013-0401-4>

- Osborne, J. D., Sochon, R. P. J., Cartwright, J. J., Doughty, D. G., Hounslow, M. J., & Salman, A. D. (2011). Binder addition methods and binder distribution in high shear and fluidised bed granulation. *Chemical Engineering Research and Design*, 89(5), 553–559. <https://doi.org/10.1016/j.cherd.2010.08.006>
- Padrós, C. B. (2014). Discrete Element Simulations with LIGGGHTS. In *College of Engineering: Vol. Master of*. Swansea University.
- Pandey, P., Tao, J., Chaudhury, A., Ramachandran, R., Gao, J. Z., & Bindra, D. S. (2013). A combined experimental and modeling approach to study the effects of high-shear wet granulation process parameters on granule characteristics. *Pharmaceutical Development and Technology*, 18, 210–224. <https://doi.org/10.3109/10837450.2012.700933>
- Pantaleev, S., Yordanova, S., Janda, A., Marigo, M., & Ooi, J. Y. (2017). An experimentally validated DEM study of powder mixing in a paddle blade mixer. *Powder Technology*, 311, 287–302. <https://doi.org/10.1016/j.powtec.2016.12.053>
- Paramanathan, B. K., & Bridgwater, J. (1983a). Attrition of solids—I Cell Development. *Chemical Engineering Science*, 38(2), 197–206. [https://doi.org/10.1016/0009-2509\(83\)85003-9](https://doi.org/10.1016/0009-2509(83)85003-9)
- Paramanathan, B. K., & Bridgwater, J. (1983b). Attrition of solids—II Material Behaviour and Kinetics of Attrition. *Chemical Engineering Science*, 38(2), 207–224. [https://doi.org/10.1016/0009-2509\(83\)85003-9](https://doi.org/10.1016/0009-2509(83)85003-9)
- Pasha, M., Hare, C., Hassanpour, A., & Ghadiri, M. (2015). Numerical analysis of strain rate sensitivity in ball indentation on cohesive powder Beds. *Chemical Engineering Science*, 123, 92–98. <https://doi.org/10.1016/j.ces.2014.10.026>
- Pasha, Massih, Dogbe, S., Hare, C., Hassanpour, A., & Ghadiri, M. (2013). A new contact model for modelling of elastic-plastic-adhesive spheres in distinct element method. *AIP Conference Proceedings*, 1542, 831–834. <https://doi.org/10.1063/1.4812060>
- Pasha, Massih, Dogbe, S., Hare, C., Hassanpour, A., & Ghadiri, M. (2014a). A linear model of elasto-plastic and adhesive contact deformation. *Granular Matter*, 16(1), 151–162. <https://doi.org/10.1007/s10035-013-0476-y>
- Pasha, Massih, Dogbe, S., Hare, C., Hassanpour, A., & Ghadiri, M. (2014b). A linear model of elasto-plastic and adhesive contact deformation. *Granular Matter*, 16(1), 151–162. <https://doi.org/10.1007/s10035-013-0476-y>
- Pathare, P. B., Baş, N., Fitzpatrick, J. J., Cronin, K., & Byrne, E. P. (2011). Effect of high shear granulation process parameters on the production of granola cereal aggregates. *Biosystems Engineering*, 110(4), 473–481. <https://doi.org/10.1016/j.biosystemseng.2011.10.004>

- Pearson, J. M. K., Hounslow, M. J., & Instone, T. (2001). Tracer studies of high-shear granulation: I. Experimental results. *AIChE Journal*, *47*(9), 1978–1983. <https://doi.org/10.1002/aic.690470909>
- Quapp, K. M., & Weiss, J. A. (1998). Material Characterization of Human Medial Collateral Ligament. *Journal of Biomechanical Engineering*, *120*(6), 757. <https://doi.org/10.1115/1.2834890>
- Ramaker, J. S., Jelgersma, M. A., Vonk, P., & Kossen, N. W. F. (1998). Scale-down of a high shear pelletisation process: Flow profile and growth kinetics. *International Journal of Pharmaceutics*, *166*, 89–97.
- Rathbone, D., Marigo, M., Dini, D., & van Wachem, B. (2015). An accurate force-displacement law for the modelling of elastic-plastic contacts in discrete element simulations. *Powder Technology*, *282*, 2–9. <https://doi.org/10.1016/j.powtec.2014.12.055>
- Realpe, A., & Velázquez, C. (2008). Growth kinetics and mechanism of wet granulation in a laboratory-scale high shear mixer: Effect of initial polydispersity of particle size. *Chemical Engineering Science*, *63*(6), 1602–1611. <https://doi.org/10.1016/j.ces.2007.11.018>
- Reynolds, G. K., Fu, J. S., Cheong, Y. S., Hounslow, M. J., & Salman, A. D. (2005). Breakage in granulation: A review. *Chemical Engineering Science*, *60*(14), 3969–3992. <https://doi.org/10.1016/j.ces.2005.02.029>
- Saito, Y., Fan, X., Ingram, A., & Seville, J. P. K. (2011). A new approach to high-shear mixer granulation using positron emission particle tracking. *Chemical Engineering Science*, *66*(4), 563–569. <https://doi.org/10.1016/j.ces.2010.09.028>
- Savage, S. B., & Sayed, M. (1984). Stresses developed by dry cohesionless granular materials sheared in an annular shear cell. *Journal of Fluid Mechanics*, *142*, 391–430. <https://doi.org/10.1017/S0022112084001166>
- Schæfer, T., Johnsen, D., & Johansen, A. (2004). Effects of powder particle size and binder viscosity on intergranular and intragranular particle size heterogeneity during high shear granulation. *European Journal of Pharmaceutical Sciences*, *21*(4), 525–531.
- Schaefer, T., Taagegaard, B., Thomsen, L. J., & Kristensen, H. G. (1993). Melt pelletization in a high shear mixer. V. Effects of apparatus variables. *European Journal of Pharmaceutical Sciences*, *1*(3), 133–141.
- Schwarze, R., Gladkyy, A., Uhlig, F., & Luding, S. (2013). Rheology of weakly wetted granular materials: A comparison of experimental and numerical data. *Granular Matter*, *15*(4), 455–465. <https://doi.org/10.1007/s10035-013-0430-z>
- Schwedes, J. (2003). Review on testers for measuring flow properties of bulk solids. *Granular Matter*, *5*(1), 1–43. <https://doi.org/10.1007/s10035-002-0124-4>
- Seyedi Hosseini, E., & Mirghasemi, A. A. (2006). Numerical simulation of breakage of two-

- dimensional polygon-shaped particles using discrete element method. *Powder Technology*, 166(2), 100–112. <https://doi.org/10.1016/j.powtec.2006.05.006>
- Seyedi Hosseininia, E., & Mirghasemi, A. A. (2007). Effect of particle breakage on the behavior of simulated angular particle assemblies. *China Particuology*, 5(5), 328–336. <https://doi.org/10.1016/j.cpart.2007.06.005>
- Šibanc, R., Kitak, T., Govedarica, B., Srčić, S., & Dreu, R. (2013). Physical properties of pharmaceutical pellets. *Chemical Engineering Science*, 86, 50–60. <https://doi.org/10.1016/j.ces.2012.04.037>
- Smith, R M. (2007). Wet Granule Breakage in High Shear Mixer Granulators. In *School of Engineering: Vol. Doctor of*. University of Queensland.
- Smith, Rachel M., & Litster, J. D. (2012). Examining the failure modes of wet granular materials using dynamic diametrical compression. *Powder Technology*, 224, 189–195. <https://doi.org/10.1016/j.powtec.2012.02.053>
- Smith, Rachel M., Liu, L. X., & Litster, J. D. (2010). Breakage of drop nucleated granules in a breakage only high shear mixer. *Chemical Engineering Science*, 65(21), 5651–5657. <https://doi.org/10.1016/j.ces.2010.06.037>
- Snow, R. H., Allen, T., Ennis, B. J., & Litster, J. D. (1997). Size Reduction and Size Enlargement. In D. G. R. Perry (Ed.), *Perry's Chemical Engineers' Handbook*. McGraw-Hill.
- Tan, B. M. J., Loh, Z. H., Soh, J. L. P., Liew, C. V., & Heng, P. W. S. (2014). Distribution of a viscous binder during high shear granulation - Sensitivity to the method of delivery and its impact on product properties. *International Journal of Pharmaceutics*, 460(1–2), 255–263. <https://doi.org/10.1016/j.ijpharm.2013.11.020>
- Tan, M. X. L., & Hapgood, K. P. (2012). Foam granulation: Effects of formulation and process conditions on granule size distributions. *Powder Technology*, 218, 149–156. <https://doi.org/10.1016/j.powtec.2011.12.006>
- Tardos, G. I., Khan, M. I., & Mort, P. R. (1997). Critical parameters and limiting conditions in binder granulation of fine powders. *Powder Technology*, 94(3), 245–258. [https://doi.org/10.1016/S0032-5910\(97\)03321-4](https://doi.org/10.1016/S0032-5910(97)03321-4)
- Tardos, G. I., McNamara, S., & Talu, I. (2003). Slow and intermediate flow of a frictional bulk powder in the Couette geometry. *Powder Technology*, 131(1), 23–39. [https://doi.org/10.1016/S0032-5910\(02\)00315-7](https://doi.org/10.1016/S0032-5910(02)00315-7)
- Thornton, C., & Antony, S. J. (2000). Quasi-static shear deformation of a soft particle system. *Powder Technology*, 109(1–3), 179–191. [https://doi.org/10.1016/S0032-5910\(99\)00235-1](https://doi.org/10.1016/S0032-5910(99)00235-1)
- Thornton, C., & Yin, K. K. (1991). Impact of elastic spheres with and without adhesion. *Powder Technology*, 65(1–3), 153–166. [https://doi.org/10.1016/0032-5910\(91\)80178-L](https://doi.org/10.1016/0032-5910(91)80178-L)

- Thornton, Colin. (2015). *Granular Dynamics, Contact Mechanics and Particle System Simulations A DEM study* (Particle T). Springer.
- Van Den Dries, K., De Vegt, O. M., Girard, V., & Vromans, H. (2003a). Granule breakage phenomena in a high shear mixer; influence of process and formulation variables and consequences on granule homogeneity. *Powder Technology*, *133*(1–3), 228–236. [https://doi.org/10.1016/S0032-5910\(03\)00106-2](https://doi.org/10.1016/S0032-5910(03)00106-2)
- Van Den Dries, K., De Vegt, O. M., Girard, V., & Vromans, H. (2003b). Granule breakage phenomena in a high shear mixer; influence of process and formulation variables and consequences on granule homogeneity. *Powder Technology*, *133*(1–3), 228–236. [https://doi.org/10.1016/S0032-5910\(03\)00106-2](https://doi.org/10.1016/S0032-5910(03)00106-2)
- Vedachalam, V. (2011). Discrete Element Modelling Of Granular Snow Particles Using LIGGGHTS. In *Edinburgh Parallel Computing Centre: Vol. MSc in Hig*. The University of Edinburgh.
- Vidyapati, V., Kheiripour Langroudi, M., Sun, J., Sundaresan, S., Tardos, G. I., & Subramaniam, S. (2012). Experimental and computational studies of dense granular flow: Transition from quasi-static to intermediate regime in a Couette shear device. *Powder Technology*, *220*, 7–14. <https://doi.org/10.1016/j.powtec.2011.09.032>
- Vonk, P., Guillaume, C. P. F., Ramaker, J. S., Vromans, H., & Kossen, N. W. F. (1997). Growth mechanisms of high-shear pelletisation. *International Journal of Pharmaceutics*, *157*(1), 93–102.
- Wade, J. B., Martin, G. P., & Long, D. F. (2015). Controlling granule size through breakage in a novel reverse-phase wet granulation process; The effect of impeller speed and binder liquid viscosity. *International Journal of Pharmaceutics*, *478*(2), 439–446. <https://doi.org/10.1016/j.ijpharm.2014.11.067>
- Wade, Jonathan Brett. (2013). *The development and characterisation of a novel reverse-phase wet granulation process*. King's College London.
- Wang, J. Y., Mesquida, P., & Lee, T. (2011). Young's modulus measurement on pig trachea and bronchial airways. *Proceedings of the Annual International Conference of the IEEE Engineering in Medicine and Biology Society, EMBS*, 2089–2092. <https://doi.org/10.1109/IEMBS.2011.6090388>
- Wang, L. G. (2016). *Particle Breakage Mechanics in Milling Operation*. The University of Edinburgh.
- Wang, X., Zhu, H. P., & Yu, A. B. (2012a). Flow properties of particles in a model annular shear cell. *Physics of Fluids*, *24*(5). <https://doi.org/10.1063/1.4710539>
- Wang, X., Zhu, H. P., & Yu, A. B. (2012b). Microdynamic analysis of solid flow in a shear cell. *Granular Matter*, *14*(3), 411–421. <https://doi.org/10.1007/s10035-012-0311-x>
- Weerasekara, N. S., Liu, L. X., & Powell, M. S. (2016). Estimating energy in grinding using DEM modelling. *Minerals Engineering*, *85*, 23–33. <https://doi.org/10.1016/j.mineng.2015.10.013>

Zhou, Y. C., Yu, A. B., Stewart, R. L., & Bridgwater, J. (2004). Microdynamic analysis of the particle flow in a cylindrical bladed mixer. *Chemical Engineering Science*, 59(6), 1343–1364.
<https://doi.org/10.1016/j.ces.2003.12.023>

